ELECTROCHEMICAL PROPERTIES OF NANOPOROUS BASED MATERIALS DOPED WITH METAL OXIDE NANOPARTICLES FOR POTENTIAL APPLICATION AS SENSORS

OMOLOLA ESTHER FAYEMI

ELECTROCHEMICAL PROPERTIES OF NANOPOROUS BASED MATERIALS DOPED WITH METAL OXIDE NANOPARTICLES FOR POTENTIAL APPLICATION AS SENSORS

OMOLOLA ESTHER FAYEMI

B.Sc (UNAAB), MSc (RU)

A thesis submitted in fulfilment of the requirements for the degree of

Doctor of Philosophy (Chemistry) in the

Department of Chemistry

Faculty of Agriculture Science and Technology,

North-West University, (Mafikeng Campus)

Supervisor: Prof. Eno E. Ebenso

Co-Supervisor: Dr. A. S. Adekunle

November 2015

DECLARATION

I, the undersigned, hereby declare that the dissertation which is hereby submitted to the Department of Chemistry, Faculty of Agriculture Science and Technology, North-West University, is my work with the exception to the citations and that this work has not been submitted by me for a degree at any other University.

Name: Omolola Esther Fayemi

Signature:.....

Date: .....

DEDICATION

This dissertation is dedicated to the Almighty God for His loving kindness and tender mercies. He gave free life to me and enables me to complete this work. May His name be praised forever Amen.

ACKNOWLEDGEMENTS

I would like to express my appreciation to my mentor and supervisor Prof. Eno E. Ebenso. He has the attitude and substance of a genuis: he continually and convincingly convey a kind spirit of adventure in regards to research and scholarship and an excitement in regards to mentoring. Also my co-supervisor Dr. A. S Adekunle, indeed you are great. Thank you for your patience, motivation, enthusiasm, and immense knowledge and contributions that made tremedious remark in my research.

Dr. Damian Onwudiwe is hereby acknowledged for assistance in characterization of my samples with the SEM, TEM, XRD and EDX. I would like to appreciate my colleague Mr. Lukman, he is a noble partner. My sincere thanks goes to all the support staff of the Department of Chemistry including; Peter, Kagizo, Sizwe, Millicent and Nomfundu, for all their help and support in making sure I get the materials needed at the right time. Thanks to all my colleagues in the group of sensor, thermodynamics of solution and corrosion.

North-West University is acknowledged for giving me the opportunity to study and also financial support towards a PhD degree in Chemistry. I also acknowledge with honour and gratitude NRF/Sasol Inzalo for bursary/scholarship award towards my PhD degree.

Special thanks go to my husband (Olutope Peter Fayemi, lovely girls Boluwatife, Beatrice and Busayo. I will not fail to mention members of Deeper Life Campus fellowship at NWU Mafikeng, University of Fort Hare Alice, University of Pretoria, South-Africa and DLCF LUTH Lagos Nigeria.

I will also like to extend my profound gratitude to Dr. Adebayo's family, Pastor Amoni, Prof. Remi Adewunmi, Prof. Oyero, Pastor Nicolas, Pastor Mike, Prof and Mrs. Oladele and

family, Prof and Mrs Salawu and family, Prof and Mrs Tidings, Prof and Mrs Reju, Prof. John T. Agee, Prof. Zenixole Tshentu, Dr. Sasikumar, Dr. Baska, Dr. Indra, Dr. Kabanda, and never to forget the wonderful mama in the faculty Mrs Maggy Medupe, she is a lovely fellow.

Thanks to my friends who have been of great help and comfort to me during my PhD journey: Mr and Mrs Aremu, Ruth, Seun, Florence, Dayo, Tomiwa, Aloo, Mr. Daniel, Jane, Dr. Bolaji, Sister Caroline, Favour, Mercy, Grace, Tomiwa Junior, Victoria, Bisola, Bisayo, Neo, Demilade, Damilola, and Emmanuel and lastly, my ultimate thanks to my father Benjamin Alabi Ogunbona and my family, for their unwavering love and support.

ABSTRACT

This work describes successful synthesis of three metal oxides nanoparticles (MO = NiO, ZnO and Fe_3O_4) obtained by chemical synthesis, and modified with multiwalled carbon nanotubes (MWCNT), polyaniline (PANI) and MWCNT functionalized nylon 6,6 nanofibers on glassy carbon electrode (GCE). Successful characterization of the electrodes with the MO (NiO, ZnO and Fe_3O_4), MWCNT/MO, PANI/MO and Nylon 6,6/MWCNT/MO nanocomposites were confirmed by field emission scanning electron microscopy (FESEM), high resolution scanning electron microscopy (HRSEM), high resolution transmission electron microscopy (HRTEM), x-ray diffraction spectroscopy (XRD), electron dispersive x-ray spectroscopy (EDX), Fourier transformed infra-red spectroscopy (FTIR) and ultraviolet-visible (UV-vis) spectroscopy. Electron transport (ET) properties of the modified electrodes was explored using cyclic voltammetry (CV) and electrochemical impedance spectroscopic techniques (EIS) with ferricyanide/ferrocyanide ($[Fe(CN)_6]^{3-/4-}$) as the redox probe. The mechanism of electron transport between the MO nanomaterial, their nanocomposites`and the electrocatalytic oxidation or reduction of the analyte at the modified electrode was extensively studied and discussed using electrochemical impedance spectroscopy (EIS). The electron transfer constant differs in terms of materials and electrical equivalent circuits used in the fitting or modelling process. The presence of MWCNT, PANI and Nylon 6, 6 also enhances the MO modified electrodes ET compared with electrodes without CNTs, PANI and Nylon 6,6. The electrocatalytic properties of the modified electrodes were explored using the following analytical probes: dopamine, serotonin, phenanthrene and lindane.

Electrochemical oxidation of dopamine and serotonin on a glassy carbon electrode (GCE) modified with multi-walled carbon nanotubes doped with metal oxides (GCE/MWCNT/NiO,

GCE/MWCNT/ZnO, GCE/MWCNT/Fe_3O_4) was examined by cyclic voltammetry, EIS and square wave voltammetry in 0.1 M phosphate buffer solution PBS at pH 7 and results discussed. The results were compared with those obtained on bare GCE, GCE/MWCNT and MO GCE modified electrodes (GCE/NiO, GCE/ ZnO, GCE/ Fe_3O_4). The nanocomposite modified electrodes exhibit excellent electrocatalytic activity towards the electrochemical oxidation of serotonin at large peak current and lower oxidation potentials compared to other electrodes investigated. It was found that the multi-walled carbon nanotubes improve remarkably the reactivity of NiO, ZnO and Fe_3O_4 for dopamine and serotonin oxidation. The GCE/MWCNT/NiO, GCE/MWCNT/ZnO, GCE/MWCNT/Fe_3O_4 electrodes exhibited good linear properties in the concentration range studied with a limit of detection of 0.00799 nM, 374.2 nM and 1386 nM respectively for dopamine; and 50.8 nM, 60.6 nM and 1090 nM respectively for serotonin. GCE-MWCNT-NiO was the best electrode in terms of dopamine and serotonin current response, electrode stability, resistance to fouling and limit of detection towards the analytes. The interference study also revealed no AA interference signal to DA at AA concentration 1000 times that of DA.

Similar results were obtained for GCE/Nylon6,6/MWCNT/NiO, GCE/Nylon6,6/MWCNT/ZnO, GCE/Nylon6,6/MWCNT/Fe_3O_4 for electrochemical detection of dopamine with a limit of detection of 0.0176 nM, 0.0149 nM and 0.0428 nM respectively towards DA; and 339 nM, 0.117 nM, and 1160 nM respectively towards serotonin. GCE/Nylon6,6/MWCNT/ZnO modified electrode gave the best limit of detection towards both DA and serotonin.

In the same vein, GCE-PANI-NiO, GCE-PANI-ZnO, GCE-PANI-Fe_3O_4 electrodes exhibited good electrocatalytic properties towards DA with a limit of detection of 11.5 nM, 63.3 nM and 1110 nM respectively.

The electrocatalytic oxidation of phenanthrene on PANI-NiO on modified glassy carbon electrode (GCE-PANI-NiO) was studied using cyclic voltammetry, square wave voltammetry and impedance spectroscopy and discussed. Results showed that detection of phenanthrene was enhanced by the nanostructure of PANI-NiO film on GCE. The square wave voltammetry analysis shows a very low detection limit of 0.732 x 10^{-3} nM for phenanthrene with the linear range of 7.6 x 10^{-3} nM – 1.4 x 10^{-2} nM. The Tafel value of 227 $mVdec^{-1}$ suggests adsorption of phenanthrene oxidation intermediates on the GCE-PANI-NiO electrode. The GCE-PANI-NiO modified electrodes gave better performance towards phenanthrene in terms current response, oxidation potential, current recovery, stability and resistance to electrode fouling effects PANI-MO and Nylon6,6/MWCNT/MO modified glassy carbon electrodes were prepared and used for the electrochemical reduction of lindane. The modified electrodes offer a high sensing current for lindane, and highly stable with respect to time, so that the single electrode can be used for the multiple analysis of the lindane sample. Cyclic voltammetry and square wave voltammetry were used as the sensing techniques. The dynamic range for the lindane determination was between 9.9×10^{-12} mol/L to 5×10^{-6} mol/L with detection limits 51 and 32 nM for Nylon6,6/MWCNT/ZnO and Nylon6,6/MWCNT/Fe_3O_4 sensors respectively, and 239 nM, 44.7 nM for PANI/ZnO and PANI/Fe_3O_4 sensors respectively. The LoD value reveals that the best electrode is Nylon6,6/MWCNT/Fe_3O_4. The analytical utility of the proposed method was checked with drinking water samples.

TABLE OF CONTENTS

LIST OF ABBREVIATION

PANI:	Polyaniline
MWCNT;	Multi-walled carbon nanotube
NiO:	Nickel oxide
ZnO:	Zinc oxide
Fe_3O_4:	Iron oxide
PBS:	Phosphate buffer solution
GCE:	Glassy carbon electrode
MO:	Metal oxide
EIS:	Electrochemical impedance spectroscopy
UV-Vis:	Ultraviolet-visible spectrophotometry
EDX:	Energy dispersive x-ray spectra
FESEM:	Field emission scanning electron microscope
TEM:	Transmission electron microscopy
XRD:	X-ray diffraction
GPES:	General purpose electrochemical system software.
TBAB:	Tetrabutylammonium bromide
Ip,c	Cathodic peak current
SWV	Square wave voltammetry
Rs	Solution resistance
Rct	Charge transfer resistance
CPE	Constant phase element
UV-vis	Ultraviolet visible
FTIR	Fourier transform infrared
Ag/AgCl	Silver-silver chloride

CE	Counter electrode
WE	Working electrode
RE	Reference electrode
ΔEp	Peak separation
Ep,a	Anodic peak potential
Ep,c	Cathodic peak potential
Ip,a	Anodic peak current
DA	Dopamine
SE	Serotonin

LIST OF FIGURES

LIST OF SCHEMES

LIST OF SELECTED SYMBOLS

υ	Scan rate
A	Area
α	Charge transfer coefficient
D	Diffusion coefficient
k_s	Charge transfer rate constant
Γ	Electroactive surface coverage area
b	Tafel value
δ	Relative standard deviation of the intercept of the y-coordinates from the line that best fit
m	Slope of the same line that best fit
λ	Wavelength
d	Average crystal size
n	Number of moles of electron transfer
i_0	Exchange current
F	Faraday constant
R	Gas constant
T	Absolute temperature
μM	Micro mole (10^{-6})
nM	Nano mole (10^{-9})
pM	Pico mole (10^{-12})

LIST OF TABLES

.

CHAPTER 1

●●●●●

INTRODUCTION

1.0 SENSOR

Sensors are described as devices that can respond to stimulus by the provision of a functional link [1]. On exposure to environment or analyte it converts its properties such as optical, electrical, and mass to a quantifiable signal that carries information about the analyte [1]. Sensors are regarded as devices with active sensing material and signal transducer. These two important characteristics play a role transmitting signal without any amplification from a selective compound or from a change in a reaction. One of the signals is produced as electrical, thermal or optical output signals which could be converted into digital signals for further processing. The sensor's output signal may be in the form of voltage, current, or charge. These may be further described in terms of amplitude, polarity, frequency, phase, or digital code. This set of characteristics is called the output signal format. Therefore, a sensor has input properties (of any kind) and electrical output properties. The classification of sensor is, therefore, based on the fact about these output signals [2]. Among these, electrochemical sensors have more advantage over the others because; in these, the electrodes can sense the materials which are present within the host without doing any damage to the host system. In summary, there are two types of sensors; direct and complex. A direct sensor converts a stimulus into an electrical signal or modifies an electrical signal by using an appropriate physical effect, whereas a complex sensor in addition needs one or more transducers of energy before a direct sensor can be employed to generate an electrical output [3].

1.1 Classification of sensors

1.1.1 Chemical sensors

A chemical sensor is a device that transforms chemical information, ranging from the concentration of a specific sample component to total composition analysis, into an analytically useful signal [4]. The chemical information, mentioned above, may originate from a chemical reaction of the analyte or from a physical property of the system

investigated. It is also an essential component of an analyzer. In addition to the sensor, the analyzer may contain devices that perform the following functions: sampling, sample transport, signal processing, data processing. An analyzer may be an essential part of an automated system. The analyzer working according to a sampling plan as a function of time acts as a monitor [4].

The two basic functional units in chemical sensors are: a receptor part and a transducer part. In the receptor part of a sensor the chemical information is transformed into a form of energy which may be measured by the transducer. The transducer part is a device capable of transforming the energy carrying the chemical information about the sample into a useful analytical signal. The transducer as such does not show selectivity [5]. Hence, it is not always necessary that a sensor responds specifically to a certain analyte. Under carefully controlled operating conditions, the analyte signal may be independent of other sample components, thus allowing the determination of the analyte without any major preliminary treatment of the sample.

Chemical sensors may be classified according to the operating principle of the transducer.

1. Optical devices transform changes of optical phenomena, which are the result of an interaction of the analyte with the receptor part.

2. Electrochemical devices transform the effect of the electrochemical interaction analyte – electrode into a useful signal. Such effects may be stimulated electrically or may result in a spontaneous interaction at the zero-current condition. The following subgroups may be distinguished:

a) Voltammetric sensors, including amperometric devices, in which current is measured in the d.c. or a.c. mode. This subgroup may include sensors based on chemically inert electrodes, chemically active electrodes and modified electrodes. In this group are included sensors with and without (galvanic sensors) external current source.

b) Potentiometric sensors, in which the potential of the indicator electrode (ion-selective electrode, redox electrode, metal-metal oxide electrode) is measured against a reference electrode.

c) Chemically sensitized field effect transistor in which the effect of the interaction between the analyte and the active coating is transformed into a change of the source-drain current. The interactions between the analyte and the coating are, from the chemical point of view, similar to those found in potentiometric ion-selective sensors.

d) Potentiometric solid electrolyte gas sensors, differing from potentiometric sensors because they work in high temperature solid electrolytes and are usually applied for gas sensing measurements.

3. Electrical devices based on measurements, where no electrochemical processes take place, but the signal arises from the change of electrical properties caused by the interaction of the analyte.

4. Mass sensitive devices transform the mass change at a specially modified surface into a change of a property of the support material. The mass change is caused by accumulation of the analyt [6-8].

1.1.2 Biosensors

These can be defined in terms of sensing ability, where these sensors can sense biochemical compounds such as biological proteins, nucleotides and even tissues [9-11]. The active sensing materials on the electrode modified with this sensor act as a catalyst and catalyze the reaction of the biochemical chemical compounds to obtain the output signals [12, 13]. The combination of these two different ways of classifications has given rise to a new type of sensors which are called electrochemical biosensors, A sensor is often defined as a “device that receives and responds to a signal or where the electrochemical methods are applied for the construction and working of a biosensor [14-16].

Electrochemical sensors therefore are essentially an electrochemical cell which employs a two or three-electrode arrangement. The measurement can be made at steady-state or transient. The applied current or potential for electrochemical sensors may vary according to the mode of operation, and the selection of the mode is often intended to enhance the sensitivity and selectivity of a particular sensor [17]. The general principles of electrochemical sensors have been extensively discussed in many electroanalytic references. However, many electroanalytic methods are not practical in biomedical sensing applications. For instance, dropping mercury electrode polarography is a well-established electroanalytic method, yet its usefulness in biomedical sensor development, particularly for potential in vivo sensing, is rather limited. In this chapter, we shall focus on the electrochemical methodologies which are useful in biomedical sensor development. Electrochemical sensors can be applied for solid, liquid, or gaseous analytes with the latter two most common. High temperatures can be accommodated using solid electrolytes and high temperature materials for sensor device construction [17].

1.2 Application of electrochemical sensors

Sensors enable us to monitor our environment properly. Parameters such as volume, concentration, temperature, humidity, pressure, vibration, fluid flow, and position are monitored by sensors. Large manufacturing and processing industries depend mostly on sensors to remotely monitor their production process for an optimized plant performance, centralized control and equipment health diagnostics. Sensor technology is thriving as the need for recognizing complex chemical, biological or physical phenomena [18]. Electrochemical sensors can be used as follows:

1.2.1 Detection of drugs

Electrochemical methods have been used to determine the concentration of benzodiazepines, phenothiazines and paracetamol types of drugs [19-22]. These drugs were widely tested, and their electrode reactions, dependences on the medium parameters and metabolism are known. Effects of drugs on a patient depend on the dose and the regimen of its application. Nowadays, a lot of drugs are used, some of them being not quite neutral or harmless for human organism. Therefore, monitoring of the serum drug concentration is necessary during the period of the drug application. The effect of medication has been confirmed to be dependent mostly on the concentration of the active drug in blood [22].

1.2.2 Detection of pesticides

Organic pollutants have been investigated widely in the laboratory, particularly pesticides. This has usually been following separation of complex mixtures, and, if electrochemically, usually by oxidation at carbon electrodes; problems of electrode fouling can be acute. The use of biosensors, i.e., a modified electrode in which the modifier is a biologically active molecule, can lead to other possibilities [23].

1.3 Problem statement

Neuro degeneration of dopamine-containing neurons contributes to late-onset neurological diseases, including Parkinson's and Alzheimer's diseases, and possibly to normal ageing of the brain [24] and report also show its coexistence in biological systems [25, 26]. Therefore investigation of neurological behaviour and also simultaneous determination of dopamine is of great importance for the elucidation of its precise physiological functions. Serotonin (5-Hydroxytryptamine) is also an important and major biogenic monoamine neurotransmitter as well as neuromodulator [27], widely distributed in human brain and makes an important contribution in wide variety of biological, physical, psychopathological processes including sleep regulation, depression, eating disorder, alcoholism, infantile autism, anxiety disorders,

muscle contraction, liver regeneration, endocrine regulation, obsessive – compulsive disorder and psychosis [28-29]. The determination of serotonin is instructive in the diagnosis of various diseases and hence makes it the subject of biologically and pharmacologically oriented research [30]. A range of analytical techniques such as chromatographic methods [31], mass spectroscopy [32], spectrophotometry [33] and chemiluminesence [31] are reported in the literature for detection of DA. However, these methods suffer from some disadvantages including long analysis times, high costs, the requirement for sample pretreatment, and in some cases low sensitivity and selectivity. These disadvantages probably make them unsuitable for routine analysis.

On the other hand, there has been a great concern about the public health because of the environmental pollution caused by the polyaromatic hydrocarbon (i.e phenanthrene) and organochlorine pesticides (i.e lindane). They have toxic effect such as being carcinogenic, mutagenic and tetrogenic. Some of the methods reported are the use of immunoassay, gas chromatography, high performance liquid chromatograhphy with UV-vis absorbance or fluorescence and capillary electrophoresis equipped with laser-induced fluorescence. These methods allow high accuracy and low detection limit but the major drawbacks of these methods is the fact that they are expensive, time consuming, required large sample volumes as well as large amount of organic solvent with separation and extraction procedures.

These, therefore, necessitate the use of electrochemical sensors for the detection and monitoring of the concentration of the biological and environmental analytes. The electrochemical method has been found as a cheap and less time consuming methods other than the various methods used for the monitoring of their concentration in the environment.

Nanotechnology is playing an increasing important role in the development of biosensor. Recently, electrochemical biosensors based on nanostructured metal oxides gained much attention in the field of health care for the management of various important analyte in a

biological system. This work provides a literature search of current research activities that concentrate on nanostructured metal oxide based electrochemical biosensors. The unique properties of nanostructured metal oxides offer excellent prospects for interfacing biological recognition events with electronic signal transduction and for designing a new generation of bioelectronic devices. In this work, we address various nanostructured metal oxides are for fabrication of electrochemical biosensor and assembling procedures of these nanosensors. The evaluation and how they have been used for detection of various biological and enviromental molecules and how such devices have enabled the achievement of high sensitivity and selectivity with low detection limits is investigated. It has been observed that the sensitivity and performance of nanostructured metal oxide based biosensors is improved. The use of these metal oxide nanostructured materials has allowed the introduction of many new signal transduction technologies in biosensors.

1.4 Aim and objectives

The aim of this study is to investigate a comparative study of the electrochemical properties of metal oxide doped multi-walled carbon nanotubes, polyaniline and nylon 6, 6 nanofibers and also verify their electro activity towards biological and environmental analytes such as dopamine, serotonin, phenanthrene, and lindane.

- Fabrication of metal oxide (ZnO, Fe_3O_4 and NiO) doped nylon 6,6 into nanofibers,
- Functionalization of the electrospun Nylon 6, 6/MO nanofibers with MWCNT.
- Doping of carbon nanotubes with metal oxides nanoparticles (ZnO, Fe_3O_4 and NiO) respectively,
- Characterization of materials using microscopic and spectroscopic techniques: FT-IR spectrometer, Field emission scanning electron microscopy (FESEM) high resolution scanning electron microscopy (HRSEM), energy dispersive x-ray spectra (EDX).

TEM experiment will be performed using a Model JEOL JEM-2100F field emission transmission electron microscope. The electrochemical properties of the functionalized nanomaterials to understand their heterogenous electron transfer kinetics will be carried out using the cyclic voltammetry (CV) and electrochemical impedance spectroscopy (EIS);

- Comparative study of the sensing activity of the material towards some biological and environmental analytes will be investigated.

CHAPTER 2

●●●●●

LITERATURE REVIEW

2.1 Nanotechnology

Nanotechnology is defined as the study of structures between 1 nanometre and 100 nanometres in size. Integration of nano-scale technologies could lead to tiny, low-power, smart sensors that could be manufactured cheaply in large numbers, sensing the interaction of a small number of molecules, processing and transmitting the data with a small number of electrons, and storing the information in nano meter scale structure [34].

2.1.1 Classification of Nanomaterials

Nanomaterials can be nanoscale in one dimension (eg. surface films), two dimensions (eg. strands or fibres), or three dimensions (eg. particles) [35]. They can exist in single, fused, aggregated or agglomerated forms with spherical, tubular, and irregular shapes. Common types of nanomaterials include nanotubes, dendrimers, quantum dots and fullerenes. This classification is based upon different properties it holds such as scattering of light, absorbing x rays, transport electric current or heat. Nanomaterials can be created with various modulation dimensionalities as defined by Richard W. Siegel: zero (atomic clusters, filaments and cluster assemblies), one (multilayers), two (ultrafine-grained overlayers or buried layers), and three (nanophase materials consisting of equiaxed nanometer sized grains) [36] as shown in the above Figure 2.1, Figure is below..

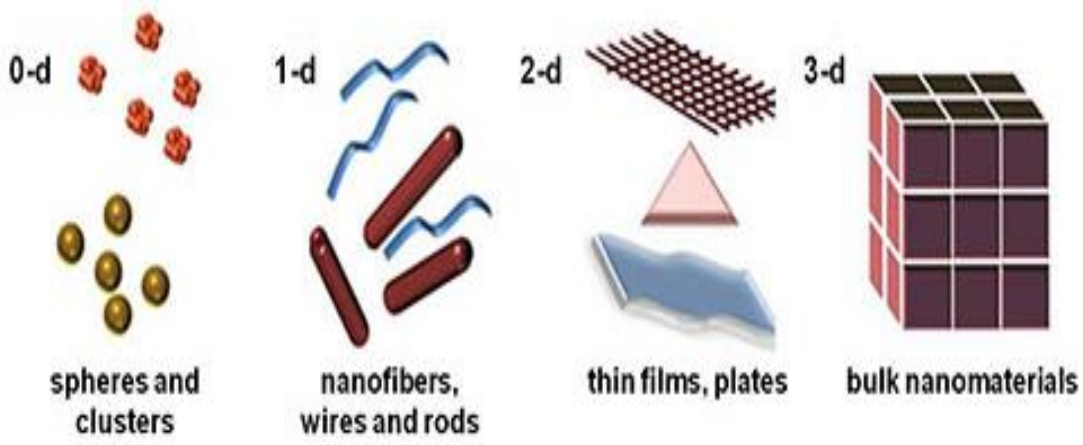

Figure 2.1: Classification of Nanomaterials (a) 0D spheres and clusters, (b) 1D nanofibers, wires, and rods, (c) 2D films, plates, and networks, (d) 3D nanomaterials [35].

2.1.2 Application of Nanomaterials

Nanoscale materials can also be used for bulk applications; for medical applications; nanoscale materials such as nanopillars are sometimes used in solar cells which conflicts with the cost of traditional Silicon solar cells. The incorporation of semiconductor nanoparticles to be used in the next generation of products, such as display technology, lighting, solar cells and biological imaging cannot be over emphasized. Recent application of nanomaterials include a range of biomedical applications, such as tissue engineering, drug delivery, and biosensors [37].

2.2 Nanofibers

Nanofibers are an exciting new class of materials used for several value added applications such as medical, filtration, barrier, wipes, personal care, composite, garments, insulation, energy storage [35, 38,] sample clean-up [39, 40] and catalysis [41]. An advantage of nanofibers is the ease of surface chemistry modification in order to accommodate various functionalities. They also possess unique characteristics such as high surface area per unit

mass, high porosity, excellent structural mechanical properties and high axial strength combined with extreme flexibility [42, 43]. The last and one of the most preferred methods for fabrication of fibers in nano and low micro-scale is electrospinning. Since 1980s and especially in the last 10 years there has been an increase in the attention paid by researchers to this method due to increase in interest in nanotechnology.

2.2.1 The Electrospinning Process

Electrospinning is an effective method for producing nanofibers under the influence of electrical charges [44 47]. A number of techniques have been employed in the production of fibrous scaffolds. These are self-assembly, drawing, template synthesis, phase separation, wet spinning, electrospinning and combinations of these [48, 49].

2.2.2 Self-assembly

This method is also called 'bottom-up'. It produces fibers of small diameters. It involves the arrangement of atoms and molecules via weak non-covalent interactions (H-bonding, hydrophobic forces, electrostatic interactions) forces producing a stable structures [50]. Its major disadvantage is that it is a complex, long, and extremely elaborates technique with low productivity [50].

2.2.3 Dry spinning

This is a method used to form polymeric fibers from solution. It involves the dissolution of polymer in a volatile solvent and the solution is pumped through a spinneret composed of numerous holes. Stretching of the fibers provides for orientation of the polymer chains along the fiber axis. Dry spun fibers typically have lower void content than wet spun fibers. This technique is used only for polymers that cannot be melt spun [51].

2.2.4 Drawing

Drawing method is similar to dry spinning and single nanofibers can be produced. It requires a minimum amount of equipment, and is a discontinuous process. A micropipette is dipped into a droplet near the solution solid surface contact line *via* a micromanipulator. Then the micropipette is withdrawn from the liquid at a certain speed, yielding a nanofiber. These steps are repeated many times on each droplet. The solution viscosity, however, increases with solvent evaporation and some fiber breaking occurs due to instabilities that occur during the process [52]. Drawing process is disadvantageous since it requires solutions of only viscoelastic materials, which can undergo strong deformations that are cohesive enough to withstand the stresses developed during pulling. The fiber size is dependent on the orifice size of the extrusion mould and it is difficult to obtain fibers diameters less than 100 nm.

2.2.5 Phase separation

This process has five steps, namely polymer dissolution, gelation, solvent extraction, freezing, and freeze-drying. The polymer is first dissolved in an appropriate solvent at the desired concentration and stirred at a required temperature for a period of time until a homogeneous solution is obtained. The solution is then transferred into a refrigerator for gelation. The resultant gel is immersed in water several times to allow solvent exchange. Finally, the gel is removed from water, transferred to a freezer (-70^{o}C), and then the frozen gel is lyophilized [53]. Phase separation occurs due to physical incompatibility and yields nanofibers. The disadvantage of this method is that no long continuous fibers are produced and only the polymers that have gelation capability can be used to produce the nanofibrous structure.

2.2.6 Wet spinning

This method is based on precipitation, which starts by dissolving the polymer in a suitable organic solvent or in a weak inorganic solvent in order to prepare the spinning dope. The polymer solution is then transferred to a reservoir of a (glass) spinneret. The solution is then allowed to flow under gravity through the spinneret into the non-solvent and precipitation or coagulation occurs. This results in fibers with a diameter range varying from 10 to 100 nm [54].

2.3 Electrospinning

The most preferred method for fabrication of fibers in nano and low micro-scale is electrospinning. Since the 1980s and especially in the last 10 years there has been an increase in the attention paid by researchers to this method due to an increased interest in nanotechnology. The electrospinning apparatus and the schematic representation of the electrospinning process are shown in Figures 2.2 and 2.3. An electric field is subjected to the end of a capillary tube that contains the polymer fluid held by its surface tension. This induces a charge on the surface of the liquid and the mutual charge repulsion causes a force directly opposite to the surface tension [55]. As the intensity of the electric field is increased, the hemispherical surface of the fluid at the tip of the capillary tube elongates to form a conical shape known as the Taylor cone (the base region). With increasing field, a critical value is attained when the repulsive electrostatic force overcomes the surface tension and a charged jet of fluid is ejected from the tip of the Taylor cone. The discharged polymer solution jet undergoes a whipping process wherein the solvent evaporates, leaving behind a charged polymer fiber, which is highly stretched and reduced in diameter as it travels before it lays itself randomly on a grounded collecting metal screen (the jet region). The rapidly whipping jet (the fluid instability) is an essential element of the process that cause bending and stretching of the jet. In the case of the melt the discharged jet solidifies when it travels in

the air and is collected on the grounded metal screen. Spraying occurs in a region in which the radical forces from the electrical charges carried by the jet, become larger than the cohesive forces within the jet, and the single jet divides into many charged jets (with approximately equal diameters and charge per unit length) before fibers 'land' on the collector (the collection region).

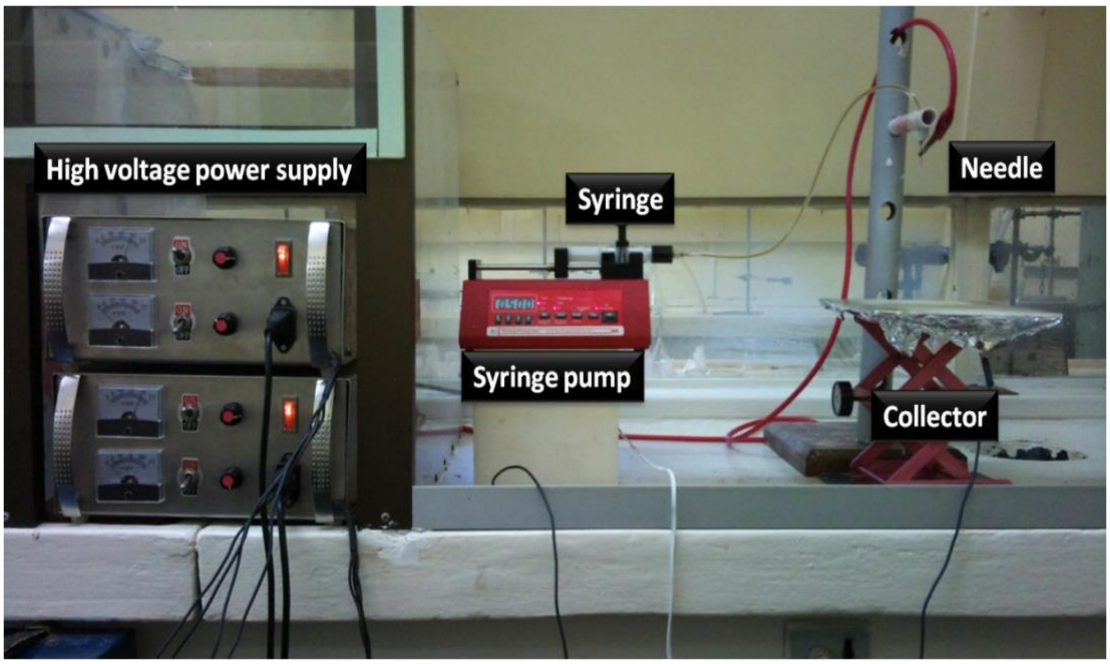

Figure 2.2: The picture of the electrospinning set-up used in this study.

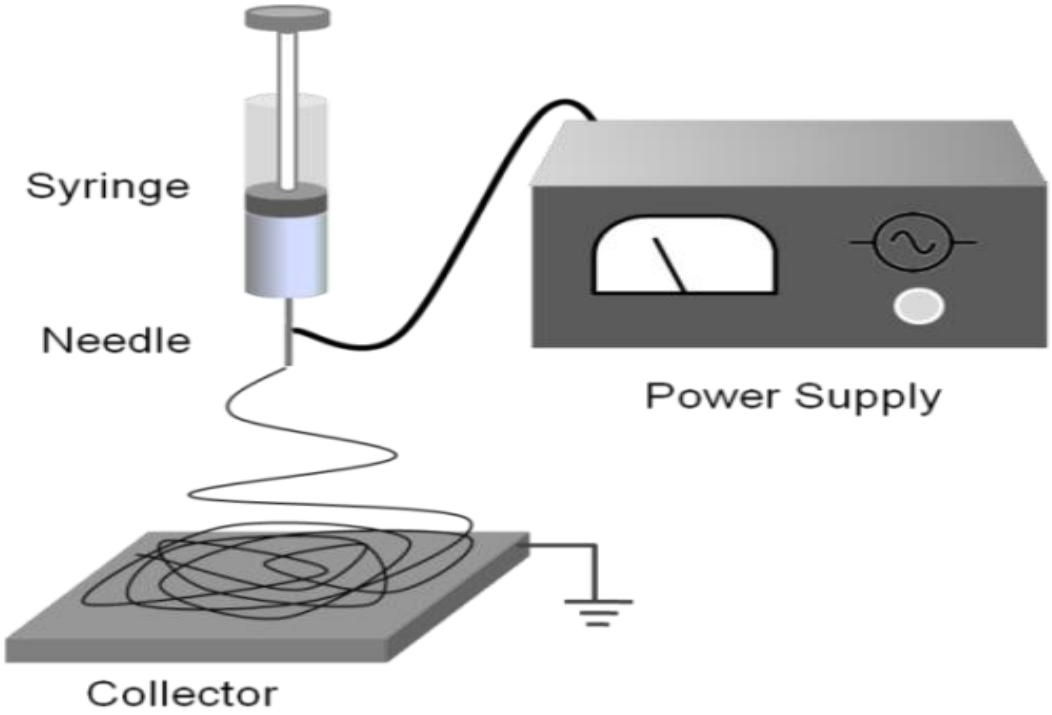

Figure 2.3: Schematic diagram of an electrospinning set-up [56].

2.3.1 Parameter of the Electrospinning Process

Electrospinning and fiber morphology can be influenced by the following factors; polymer properties (e.g. polymer structure, molecular weight, solubility), solvent (e.g. boiling point and dielectric properties), solution properties (e.g. viscosity, concentration, conductivity and surface tension), operating conditions (e.g. applied voltage, collecting distance and flow rate), and ambient environment (e.g. temperature, gas environment and humidity).

2.3.1.1 Process parameter

Higher potentials generally give rise to fibers with thinner diameters. Pore size also has been reported to decrease with an increase in potential because the drawing rate and fiber crossings increase [57]. The hydrostatic pressure in the capillary tube of the needle can also affect the

results. The polymer solution is forced out of the needle orifice by the applied electric field [58], gravity [59], or a pump [60]. Flow rate and needle size has also been found to influence the electrospinning process. Higher flow rates result in larger fiber diameters, and smaller needle orifices have been reported to contribute to thinner fiber formation [61]. Another parameter is the distance between needle and collector. Decrease in distance, regardless of the concentration of the polymer solution, results in the formation of wet fibers and beaded structures [62, 63].

2.3.1.2 Ambient parameters

The followings are the three major environment-related parameters that should be taken into consideration; solution temperature, medium humidity, and air velocity in the electrospinning chamber. An increase in solution temperature results in solution chain formation, decrease in solution viscosity and an increase in solvent evaporation. All these factors influence fiber morphology. An increase in humidity leads to an increase in diameter, number, shape and distribution of pores. A relative humidity higher than 30% has been reported to lead to micro- and nano-structured pores on the surface of fibers [64].

2.3.1.3 Polymer and solvent-related parameters

The structure of a polymer has a great impact on its solubility. A polymer with higher molecular weight is less soluble and takes longer time to dissolve than polymers with lower molecular weights using the same solvent. This is because the intermolecular forces between longer chain molecules are stronger and the solvent molecule takes longer time to diffuse into the bulk. The architecture of the polymer also affects processing; for instance, branched polymers seem to need a higher concentration than linear polymers in order to form defect-free nanofibers [65].

The properties of a polymer solution such as surface tension and viscosity determine its stretching potential. The rate of evaporation will influence the viscosity of the solution. Viscosity appears to be very important factor in this configuration. It is related to the extent of polymer molecule chains entanglement within the solution. At lower viscosity polymer chain entanglements are lower and this leads to formation of beaded fibers and this can also result into electrospraying. Electrospraying occurs, when entanglement of polymer chains does not occur but still undergoes a bending instability that causes a whip-like motion between the capillary tip and the grounded target. Very high viscosities, on the other hand, prevent ejection of the solution from the syringe tip due to a high surface tension and this is called suppression [66- 69]. An appropriate solution viscosity is important for an efficient electrospinning process.

To achieve nanofibers in the range of 100 to 2000 nm diameter appropriate polymer solvent system must be chosen [70]. Table 2.1 gives list of some of polymer solvent systems used in electrospinning.

Table 2.1 Polymer solvent systems for electrospinning [70].

POLYMER	**SOLVENTS**
Nylon 6 and nylon 66	Formic Acid
Polyacrylonitrile	Dimethyl formaldehyde
PET	Trifluoroacetic acid/Dimethyl chloride
PVA	Water
Polystyrene	DMF/Toluene
Nylon-6-co-polyamide	Formic acid
Polybenzimidazole	Dimethyl acetamide
Polyramide	Sulfuric acid
Polyimides	Phenol

2.4 Functionalization of nanofibers

An exciting feature about nanofibers is the ease of surface modification in order to accommodate various functionalities [71, 72]. Functionalization can be achieved before

electrospinning process which is termed pre-electrospinning functionalization. This involves the introduction of functional groups into the polymer solution before spinning. The next is post-electrospinning functionalization. In this case the nanofibers are functionalized after the electrospinning process.

2.5 Electrochemical methods

Electrochemistry affords some of the most sensitive and informative analytical techniques in the chemists arsenal. Electroanalytical methods such as cyclic voltammetry, stripping voltammetry, differential pulse polarography, square wave and chronoamperometry complements other analytical techniques such as chromatography and spectroscopy and are not only capable of assaying trace concentrations of an electroactive analyte, but also supply useful information concerning its physical and chemical properties.

Electrochemical methods of analysis include all methods of analysis that measure current, potential and resistance and relate them to analyte concentration. Quantities such as oxidation potentials, diffusion coefficients, electron transfer rates, and electron transfer numbers are readily obtained using electroanalytical methods, and are difficult to obtain using other techniques. Arguably, the most popular electroanalytical techniques are cyclic voltammetry and square wave.

Electrochemical detection of biological and environmental analytes using metal and metal oxide modified electrode was found to be very cheap and convenient over other methods of determination. Not only that, metal and metal oxides have been used to modify electrodes for use as electrocatalysts and sensors [73, 74]. These materials act as electron mediators, increasing the rate of electron transfer at the electrode-solution interface and also lowering the over-potentials for redox processes. The modification introduce some chemical and electrochemical properties which the bare electrode do not possess. Electrocatalysis can be observed by comparing the cyclic voltammogramm (CV) of an analyte on modified electrode

with that on bare electrodes; higher catalytic current, and a shift to less positive peak potential in the CV of the former compared to the latter is an indication of electrocatalytic oxidation of the analyte. A wide variety of metals and metal oxides nanoparticles, especially metal oxides nanoparticles with different properties have found wide applications in various fields of biomedical sciences [75, 76]. A large number of nanostructured metal oxides such as cerium oxide (CeO_2) [77, 78], iron oxide (Fe_3O_4) [79-81], manganese di oxide (MnO_2) [82, 83], niobium oxide (Nb_2O_5) [84], nickel oxide (NiO) [85], praseodymium oxide (Pr_2O_6) [86, 87], tin oxide (SnO_2) [88, 89], titanium oxide (TiO_2) [90-96], zinc oxide (ZnO) [97-102] and zirconium oxide (ZrO_2) [103-111] have been used for their application in electrochemical biosensors.

Several analytical techniques have been developed over the years for the detection and quantification of arrays of biological and environmentally important analytes. Among these is titrimetric [112], flourimetry [113], high performance liquid chromatography (HPLC) [114], mass spectroscopy [115] among others. However, these methods require a lot of chemical derivatization procedures and are time consuming. Some are very cumbersome and expensive and not even portable enough for field analysis. Therefore recently, the properties and the application of these electrodes for analytical purposes have been investigated using electrochemical techniques.

2.5.1 Component of electrochemical techniques

In electrochemical techniques the aim of the experiments is to obtain a current response which is related to the concentration of the target analyte. This objective is accomplished by monitoring the transfer of electron(s) during the redox process of the analyte:

$$O + ne^- \rightleftharpoons R \qquad (2.1)$$

O and R are the oxidized and the reduced forms, respectively, of the redox couple. These reactions are called Faradaic processes as electrons are transferred across the electrode-solution interface. Figure 2.4 represents a Faradaic process during an electrochemical measurement.

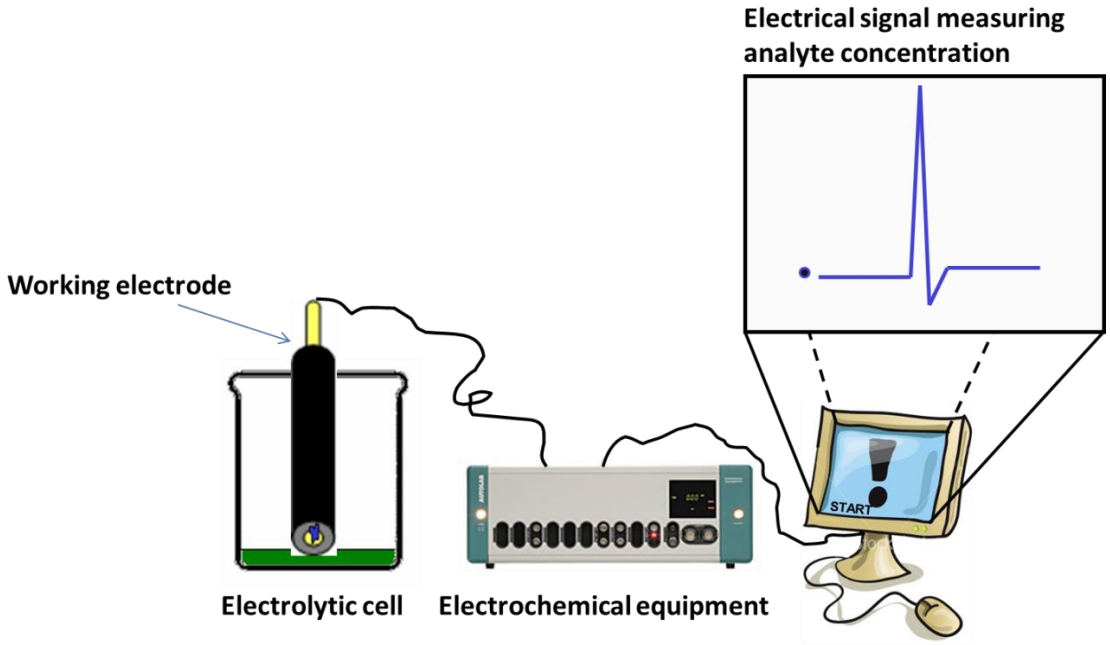

Figure 2.4: A typical electrochemical set-up showing the Faradaic process [118].

A typical electrochemical cell for electrochemical measurement is made up of three electrode systems as shown in Figure 2.5. The working electrode, which makes contact with the analyte, must apply the desired potential in a controlled way and facilitate the transfer of electrons to and from the analyte. The reference electrode is a half cell with a known reduction potential. Its only role is to act as reference in measuring and controlling the working electrode's potential and at no point does it pass any current. The auxiliary electrode passes all the current needed to balance the current observed at the working electrode. To achieve this current, the auxiliary will often swing to extreme potentials at the edges of the

solvent window, where it oxidizes or reduces the solvent or supporting electrolyte. These electrodes, the working, reference, and auxiliary make up the modern three electrode system.

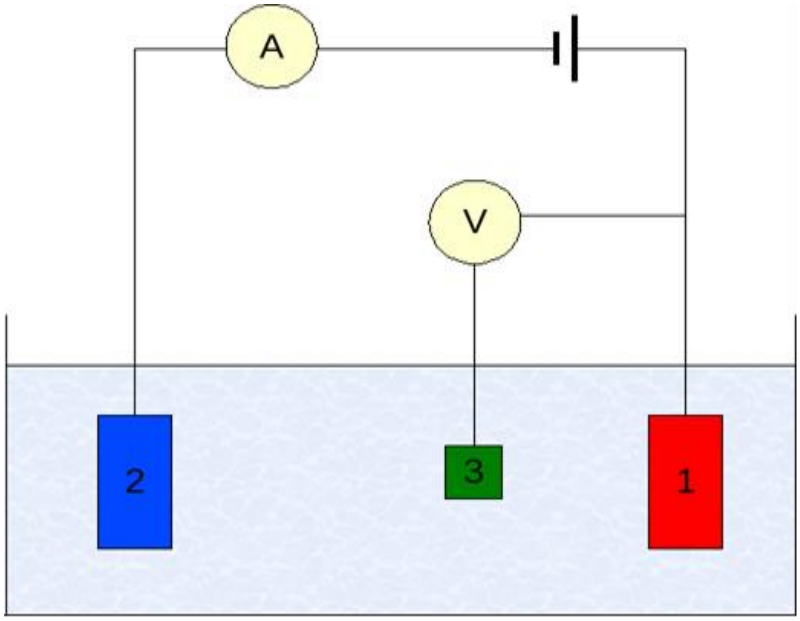

Figure 2.5: Three electrode set-up: (1) working electrode (2) auxillary electrode (3) reference electrode [118].

The arrangement of the electrodes within the cell is important. The reference electrode is placed close to the working electrode, stationed between the working and the auxiliary electrode. A glass cell is used which has a close fitting lid containing ports for electrodes and a purging line. The choice of electrolytes solution depends basically on the application. Generally the solution is expected to be conducting, be chemically and electrochemically inert. It must not react or undergo electrochemical reactions while in use.

2.5.1.1 The reference electrode (RE)

The reference electrode is an electrode with a steady and recognizable electrode potential. It is used as point of reference to control and measure the potential of the other electrodes. The

saturated calomel electrodes (SCE), silver/silver chloride (Ag/AgCl) electrode are the most commonly used reference electrode for aqueous solutions.

2.5.1.2 Counter electrode (CE)

The counter electrode (also known as auxiliary electrode) is usually made of an inert material of platinum (Pt) or metallic foil, gold (Au), graphite or sometimes glassy carbon may be used. Counter electrode does not usually take part in the electrochemical reaction, but the total surface act as source of electron so that current can flow between the working electrode and counter electrode which make it not to be isolated from the reaction. The surface area must however be higher than that of the working electrode so that it will not be a limiting factor in the kinetics of the process under investigation [118].

2.5.1.3 Working electrode (WE)

The working electrode is where the reaction or transfer of interest is taking place. At an appropriate potential, oxidation or reduction of a substance on the surface of the working electrode will bring about a mass transport of a new material along with current been produced. The commonly used materials for working electrodes are glassy carbon (GC), platinum (Pt), gold (Au). Others include small mercury drop and film electrodes. The size and shape also varies and depends on application. The quality of an ideal working electrode includes a wide potential range, low resistance as well as a surface that is reproducible [118].

2.5.2 Cyclic voltammetry (CV)

Cyclic voltammetry is a widely used electrochemical techniques that uses microelectrodes and unstirred solution so that the measured current is limited by the analyte diffusion at the surface of the electrode. It has been widely applied in the study of redox processes, electrochemical properties of analytes in solution and for the understanding of reaction intermediates as well as for obtaining the stability of reaction products [119]. The technique

operates by varying the applied potential at the working electrode at some scan rate (ν) in both forward and backward direction while monitoring the current. The potential is usually measured between the reference and the working electrode and the current is measured between the working electrode and the auxiliary electrode. The plot of current peak versus potential as shown in Figure 2.6 shows the forward scan of current peak for any analyte that can be reduced or oxidized depending on the initial scan direction over the range of potential scanned.

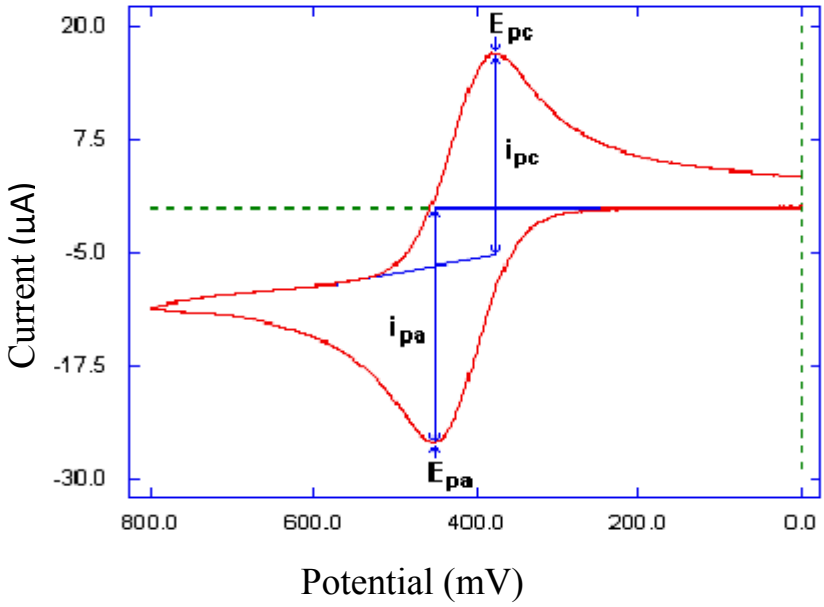

Figure 2.6: A typical cyclic voltammogramm

The current increases as the current reaches the reduction potential of the analytes, but decreases as the concentration of the analytes is depleted close to the electrode surface.

Important parameters that can be obtained from cyclic voltammograms includes peak potentials E_{pc}, E_{pa} and peak current I_{pc}, I_{pa} for both the cathodic and anodic peaks respectively. Likewise, the number of electron involved in the electrochemical process can be determined by using the equation below derived from the peak potentials;

$$\Delta E_p = [E_{pa} - E_{pc}] = 2.303RT/nF \quad (2.2)$$

Where ΔE_p is the peak separation potential (V), E_{pa} is the anodic peak potential (V), E_{pc} is the cathodic peak potential (V), n is the number of electrons, F is Faraday constant (96486 C mol^{-1}), R is the gas constant (8.314 J mol^{-1} K^{-1}) and T is the absolute temperature of the system (298 K). Therefore, for a reversible redox reaction at 25 ° C (298 K) with n number of electrons, ΔE_p is 59 mV/n or 60 mV for one electron. While for irreversibility due slow electron transfer results in ΔE_p > 59 mV/n, possibly, greater than 70 mV for a one-electron reaction [120]. For reversible reaction, the concentration is related to peak current by the Randles Sevcik equation.

$$I_p = 2.69 \times 10^5 n^{\frac{3}{2}} A D^{\frac{1}{2}} v^{\frac{1}{2}} C_o \quad (2.3)$$

Where I_p is the peak current in amperes (pa and pc represent the anodic and cathodic peak current respectively), ν is the scan rate in V s^{-1}, A is the area (cm^2), n is the number of electrons tranfered, D is the diffusion coefficient (cm^2 s^{-1}), Co is the concentration in mol/L. When the peak current is plotted against the square root of the scan rate, the slope of the linear plot can be used to determine the diffusion coefficient according to the Randles Sevcik equation, equation 2.3. Also the plot of the Log I_p versus log ν is linear, with slope of 0.5 for diffusion peak and slope of 1 for an adsorption peak. Intermediate values of the slope are sometimes observed, and these suggest a mixed diffusion-adsorption peak [120].

The surface concentration of adsorbed materials for chemically modified electrodes can be estimated by using the Brown-Anson equation model;

$$I_p = \frac{n^2 F^2 \Gamma^* A v}{4RT} \quad (2.4)$$

Where I_p, n, F, A, R, v and T are described in equations 2 and 3 and Γ^* is the surface concentration of the adsorbed species of the electrode modifier.

2.5.3 Square Wave voltammetry (SWV)

Square wave voltammetry has received growing attention as a voltammetric technique for routine quantitative analyses. Square wave voltammetry can be used to perform an experiment much faster than normal and differential pulse techniques, which typically run at scan rates of 1 to 10 mV/sec. Square wave voltammetry employs scan rates up to 1 V/sec or faster, allowing much faster determinations. The current is sampled twice during each square wave cycle, one at the end of the forward pulse, and again at the end of the reverse pulse. The technique discriminates against charging current by delaying the current measurement to the end of the pulse. The difference current between the two measurements is plotted vs. the potential staircase. Square wave voltammetry yields peaks for faradaic processes, where the peak height is directly proportional to the concentration of the species in solution. Due to the rapid scan rates possible with square wave voltammetry, the entire voltammogram is recorded on a single mercury drop. Frequencies used for square wave voltammetry typically range from approximately 1 Hz to 120 Hz. This frequency range allows square wave experiments to be up to 100 times faster than other pulse techniques. a typical square wave voltammogram is shown in Figure 2.7 [121].

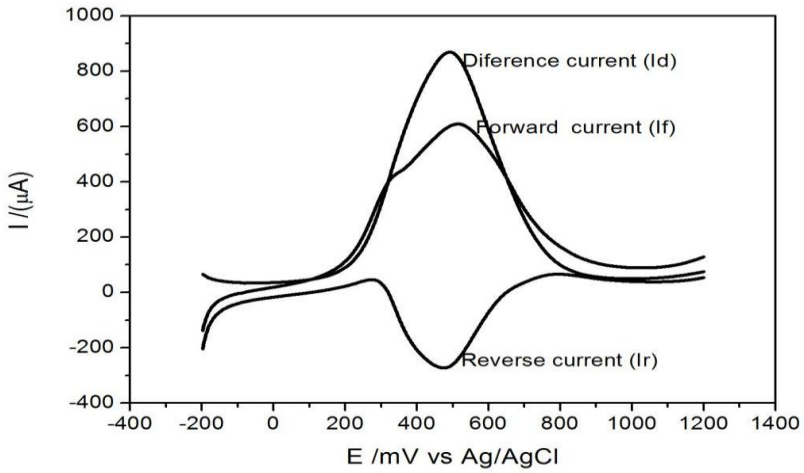

Figure 2.7: A typical SWV showing forward, reverse and difference current [94].

2.5.4 Differential Pulse voltammetry

This is an electrochemical technique where the cell current is measured as a function of time and as a function of the potential between the indicator and reference electrodes. The potential is varied using pulses of increasing amplitude and the current is sampled before and after each voltage pulse. These measurements can be used to study the redox properties of extremely small amounts of chemicals.

2.5.5 Chronoamperometric

Chronoamperometric is very powerful method for the quantitative analysis of a nucleation process. This useful technique leads to obtain the initial information about nucleation and growth mechanism in a studied system. Additionally, the amount of charge for deposition (dissolution) can be determined. Also, this method can be applied for the determination of a nucleation rate constant and an adsorption isotherm. With the chronoamperometry, the current is measured versus time as a response to a (sequence of) potential pulse. The recorded current can be analysed and its nature can be identified from the variations with time. For example: at short times the capacitive current is dominant, while at longer time scales, the diffusion limited faradaic current might prevail [122].

Chronoamperometry experiments are most commonly either single potential step, in which only the current resulting from the forward step as described above is recorded, or double potential step, in which the potential is returned to a final value (Ef) following a time period, usually designated as τ, at the step potential (Es).

2.6 Electrochemical impedance spectroscopy

Impedance is known as the measure of the total opposition to flow of a sinusoidal electric current when using AC circuit. To understand what impedance actually is, one can use Ohms law to explain how it's measured. Ohm's law applies directly to simple resistors (and

conductors) in both DC and AC circuits. However, in more complex AC circuits, the form of the current-voltage relationship defined by Ohms law must be changed from I=V/R to I = V/Z where V is voltage, I is the resulting current, and R is resistance. The quantity Z for the modified formula is denoted as impedance, which is measured in ohms, and for a pure resistor Z = R. Impedance is commonly represented as Z = R + iX, where R is the ohmic resistance and X is the reactance. Circuit elements such as inductors and capacitors have a frequency dependent opposition to current flow and increase or decrease current opposition as AC frequency changes. The opposition to current flow caused by inductance or capacitance is known as reactance. The term reactance refers to the imaginary part of the impedance measurement (iX) due to it being a function of the frequency. Commonly speaking, a capacitor would have an impedance measurement that would decrease with increasing frequency supplied to the circuit. An inductor would have an impedance value that increases with increasing frequency. Also, a pure resistor would have the same impedance measurement at any frequency applied to the circuit. When capacitors or inductors are involved in an AC circuit, the current and voltage do not peak at the same time. The period difference between the peaks, expressed in degrees, is known as the phase difference. The contributions of capacitors and inductors differ in phase from resistive components by 90 degrees. For inductive circuits, this results in a positive phase because current lags behind the voltage while for a capacitive circuit, the current leads the voltage for a negative phase. A resistor does not cause a phase shift. Since the C/V behavior of capacitors and inductors are 180^{o} out-of-phase, the impedance in a given circuit using both elements will have phase-angle dependence. Impedance spectroscopy (IS) can provide accurate evaluation of material characteristics by measuring impedance values for a range of circuit elements whose capacitance or inductance characteristics depend in some way on their chemical environment. Impedance vs. frequency data for different electrode configurations is typically collected by

connecting the electrode to an impedance analyzer and then graphically presenting the data as either a Bode or Nyquist plot.

The Bode graph plots absolute values of impedance (Z) or phase angle (degrees) vs. the frequency range used while Nyquist plots depict the imaginary number Z" (reactance) vs. the real number value Z'. The experimental data collected from an impedance experiment is often represented as Nyquist plot of Z' versus Z'' over a wide range of frequency (100 KHz to 0.1 Hz) Figure 2.8.

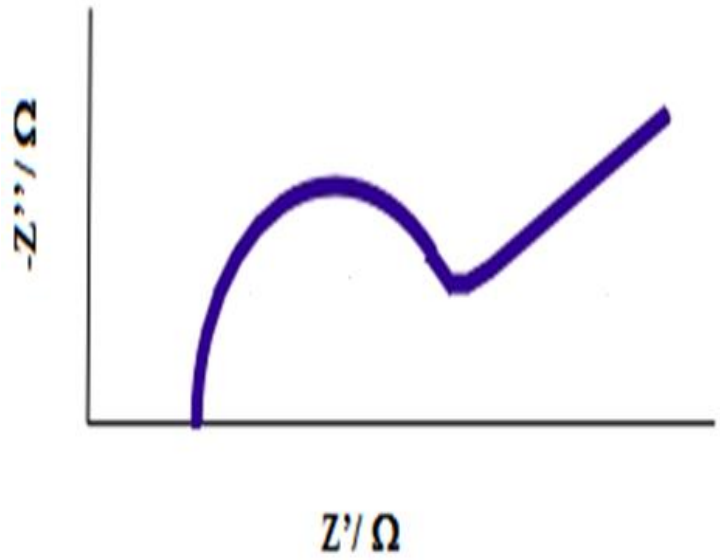

Figure 2.8: A typical Nyquist plot.

The Nyquist plot of impedance spectra include a semicircle portion and a linear portion, with the former at high frequencies corresponding to the electron transfer process and the latter at lower frequencies corresponding to the diffusion process. The electron transfer resistance (Rct) at the electrode surface is equal to the semicircle diameter, which can be used to describe the interface properties of the electrode [123].

Measuring impedance over a wide range of frequencies allows different scales such as electron transfer, mass transport and chemical reaction to be detected within the same experiment. Impedance data is commonly analyzed by fitting it to an equivalent circuit model. The commonly used circuit Randles equivalent circuit used for fitting the impedance data is shown in Figure 2.9.

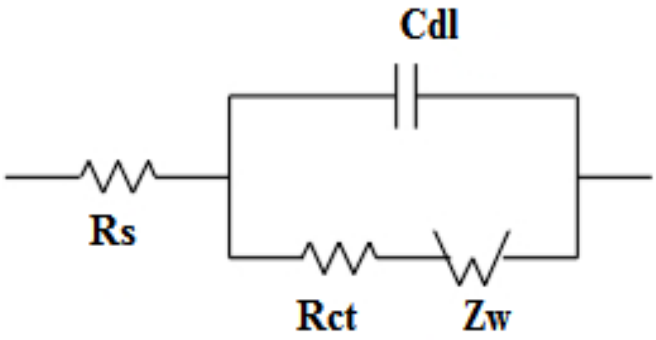

Figure 2.9: Randles equivalent circuit for a simple electrochemical cell.

The circuit is composed of elements such as capacitance (C) which is the ability of an electrochemical system to store or retain charge, Warburg impedance (Zw) which is associated with the resistance as a result of the diffusion of ions across the electrode/electrolyte interface, solution resistance (Rs) and charge transfer resistance (Rct). Therefore, EIS can provide information on the impedance changes on the electrode surface before and after modification. Figure 2.10 shows a typical diagram for impedance spectra with real impedance (x-axis) and imaginary impedance (y-axis) and low and high frequencies on the right and left side of the plot respectively [124].

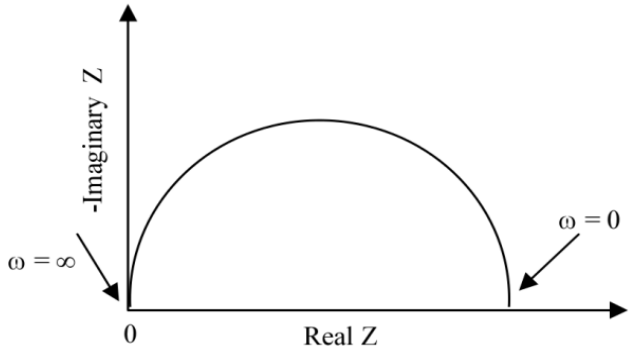

Figure 2.10: A typical impedance diagram.

EIS is a useful tool in studying the kinetics of electrochemical reactions. Redox reactions usually involve charge transfer kinetics and mass transfer. The slower of this two determines the rate of the reaction. The mass transfer in EIS is limited to diffusion (concentration gradient) by the steady state condition. Figure 2.11 shows the Nyquist plot indicating the kinetically controlled (higher frequency) and the mass controlled (low frequency) parts of the plot.

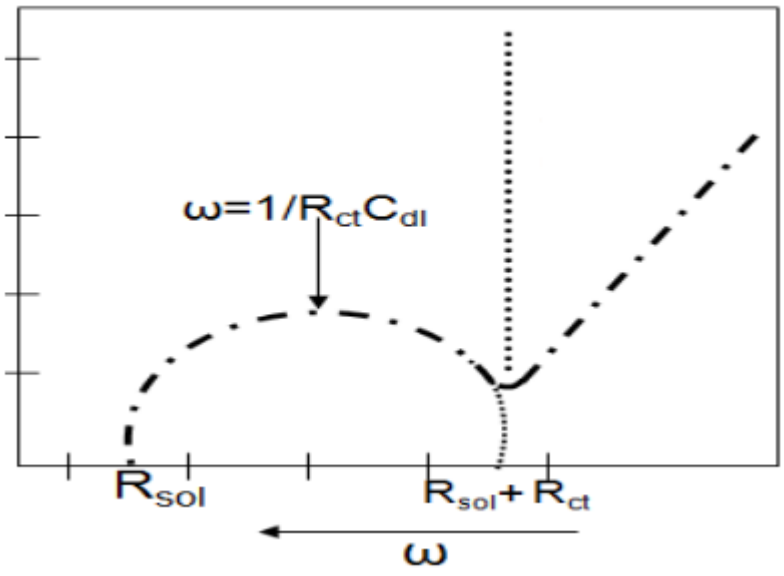

Figure 2.11 A typical Nyquist plot.

From ω_{max} (frequency at maximum imaginary impedance of the semicircle) useful kinetic parameters such as double layer capacitance (C_{dl}), (obtained using equation 2.5), time constant (cycle life) τ, (calculated using equation 2.6), exchange current I_o , (Calculated using equation 2.7) and heterogeneous rate constant K_{et} (calculated using equation 2.8) can be evaluated:

$$\omega_{max} = \frac{1}{R_{ct}C_{dl}} \quad (2.5)$$

$$\boldsymbol{\tau} = R_{ct}\, C_{dl} \quad (2.6)$$

$$I_o = \frac{RT}{nF\, R_{ct}} \quad (2.7)$$

$$k_{et} = \frac{I_o}{nFAC_o} \quad (2.8)$$

where ω_{max} = 2 π f, Rs is the solution resistance, R_{ct} is the charge transfer resistance, C_{dl} is the double layer capacitance, R is the gas constant (8.314 J K^{-1} mol^{-1}), F is the Faradays constant (96 486 C mol^{-1}), n is the number of electrons, τ is the time constant or cycle life (relates to the time required for the proton to completely move across the electrolyte layer from one side to the other), I_o is the exchange current (relates to rate constant to electron transfer at zero overpotential), Co is the concentration (mol cm^{-3}) and et k is the heterogeneous rate constant.

2.7 Metal oxides nanoparticles

Metal oxides form an important group of functional materials with diverse structural, electronic, magnetic and optical properties. At room temperature, these materials exhibit metallic, semiconducting or insulating behavior depending upon their band gap. Controlled synthesis of metal oxide nanoparticles is essential for their successful applications because the physico-chemical properties of metal oxides are highly influenced by their particle sizes, especially if they are in the 'nano' domain (10^{-9} m). As the particle size decreases from bulk to tens of nanometers, the ratio of surface to bulk atoms increases. This results in a larger

surface area with respect to the volume of the material, higher number of chemically active sites and modified density of electronic states at the surface of the particles [125].

Some of the applications of metal oxides include microelectronic circuits, sensors, piezoelectric devices, fuel cells, corrosion-resistant coatings, catalysis, field emission, magnetic memory and photoelectrochemical cells. Amongst the applications that benefit specifically from these properties is the area of 'sensors' which is the focus of this thesis. Below is more on the properties and applications of some selected metal oxides nanoparticles used in this work.

2.7.1 Nickel oxide nanoparticles (NiO)

Nickel oxide is a transition metal oxide; NiO has recently received a great deal of attention due to its applications in various fields such as fabrication of p–n heterojunctions [126], energetic material [127], magnetic properties [128-130], catalysis [131, 132], solar cells [133], gas sensors [134, 135], lithium ion battery [136, 137].

2.7.2 Zinc oxide nanoparticles (ZnO)

Zinc oxide, with its unique physical and chemical properties, such as high chemical stability, high electrochemical coupling coefficient, broad range of radiation absorption and high photostability, is a multifunctional material [138, 139]. In materials science, zinc oxide is classified as a semiconductor in group II-VI, whose covalence is on the boundary between ionic and covalent semiconductors. A broad energy band (3.37 eV), high bond energy (60 meV) and high thermal and mechanical stability at room temperature make it attractive for potential use in electronics, optoelectronics and laser technology [140, 141]. The piezo- and pyroelectric properties of ZnO mean that it can be used as a sensor, converter, energy generator and photocatalyst in hydrogen production [142, 143]. Because of its hardness, rigidity and piezoelectric constant it is an important material in the ceramics industry, while

its low toxicity, biocompatibility and biodegradability make it a material of interest for biomedicine and in pro-ecological systems [144-146]. The variety of structures of nanometric zinc oxide means that ZnO can be classified among new materials with potential applications in many fields of nanotechnology. Zinc oxide can occur in one- (1D), two- (2D), and three-dimensional (3D) structures. One-dimensional structures make up the largest group, including nanorods [147-149], -needles [150], -helixes, -springs and -rings [151], -ribbons [152], -tubes [153-158] -belts [159], -wires [160-162] and -combs [163]. Zinc oxide can be obtained in 2D structures, such as nanoplate/nanosheet and nanopellets [164, 165]. Examples of 3D structures of zinc oxide include flower, dandelion, snowflakes, coniferous urchin-like, etc. [166-169].

Application of Zinc Oxide is found in many areas due to its diverse properties, both chemical and physical. It plays an important role in wide range of applications, ranging from tyres to ceramics, from pharmaceuticals to agriculture, electronic, photocatalysis and gas sensor [170-181].

2.7.3 Iron oxide nanoparticles (Fe_3O_4)

Iron oxides are one of the most important transition metal oxides of technological importance. Sixteen pure phases of iron oxides, i.e., oxides, hydroxides or oxy-hydroxides are known to date. These are $Fe(OH)_3$, $Fe(OH)_2$, $Fe_5HO_8{\cdot}4H_2O$, Fe_3O_4, FeO, five polymorphs of FeOOH and four of Fe_2O_3. Characteristics of these oxide compounds include mostly the trivalent state of the iron, low solubility and brilliant colors (Cornell and Schwertmann, 1996) [182]. All the iron oxides are crystalline except Schwertmannite and ferrihydrite which are poorly crystalline. These oxides can be synthesized by all known wet chemical methods but to tailor the particle size in nano range and morphology towards a particular application still remains a challenging task. Some of the synthesis techniques include chemical precipitation,

sol-gel, hydrothermal, surfactant mediated-precipitation, emulsion-precipitation, microemulsion -precipitation, electro-deposition, and micro wave assisted hydrothermal technique. These oxides find applications as catalysts, sorbents, pigments, flocculants, coatings, gas sensors, ion exchangers and for lubrication [183-190]. Iron oxide nano-composites have potential applications in areas such as magnetic recording, magnetic data storage devices, toners and inks for xerography, and magnetic resonance imaging, wastewater treatment, bioseparation, and medicine [191-199]. Careful control of the preparation process of transparent iron oxide pigments results in the formation of pigments with very small primary particle sizes. When fully dispersed, they do not scatter light and are hence completely transparent. Magnetite (Fe_3O_4) is a black, ferromagnetic mineral containing both Fe (II) and Fe (III). In stoichiometric magnetite Fe (II)/Fe(III) = 0.5 but magnetite is often non-stoichiometric resulting in a cation deficient Fe (III) layer. The crystal structure of magnetite is inverse spinel with a unit cell consisting of 32 oxygen atoms in a face-centered cubic structure and a unit cell edge length of 0.839 nm. In this crystal structure Fe (II) ions and half of the Fe (III) ions occupy octahedral sites and the other half of the Fe (III) occupies tetrahedral sites. Divalent iron atoms prefer to occupy octahedral sites to have a higher Crystal Field Stabilization Energy (CFSE), whilst the trivalent iron atoms has a CFSE=0 in both octahedral and tetrahedral sites. The crystal forms of magnetite include octahedron and rhombodecahedron and the specific surface area ranges from 4 - 100 m^2/g [200].

2.8 Polymer nanocomposites

A polymer nanocomposite can be defined as a polymer-nanofiller system in which the inorganic filler is on a nanometric scale at least in one dimension and it can be a polymer/nanoparticle blend or a hybrid. The composite interconnection can be based on a secondary force or physical entanglement [201, 202]. The polymer/nanofiller-hybrid, in turn, is formed when the polymer and the nanoparticle are covalently bonded. The covalent bond

can be formed during the in situ polymerization (the monomer or the growing polymer chain can react with the filler particle), or during the composite processing.

2.8.1 Application of nanocomposites of MWCNT doped with metal oxides nanoparticles

Carbon nanotube/metal oxide (CNT-MO) nanocomposites are new generation materials with interesting properties that not only combine the properties of CNTs and MOx but also hold new properties caused by the interaction between them. In addition, combine these materials in a composite can overcome some disadvantages. For example, metal oxide nanoparticles have a tendency to agglomerate because of their dangling bonds. In the composite, dispersion of the nanoparticles on the surface of the nanotube prevents their agglomeration. It should be noticed that the aggregation of nanotubes in aqueous media is solved by functionalization. As a result, the composites attractive wide applications compared with the isolated nanoparticles because CNTs act as carrier to stabilize the nanoparticles, maintaining their integrity.

In recent years, there has been great consideration in the research and development of carbon nanotubes (CNTs) and its composites due to their unique physical and chemical properties [203-207], which is not only widely used in catalysts [208], nanoelectronic devices [209-212], solar cells [213], displays [211], hydrogen storage materials [214], supercapacitors, but also has potential applications in sensors [215, 216]. The following are examples of the nanocomposites that can be prepared are Ti_2O_3, ZnO, NiO, WO_3, Fe_2O_3, SnO_2, CeO_2, Al_2O_3, ZrO_2, SiO_2, V_2O_4 and Fe_3O_4 on CNTs. The enhancement in photocatalytic performance of the CNT/MO nanocomposites can be explained in a mechanism based on two criteria. The first is adsorption ability of the nanotubes since the adsorption is a key process in the catalytic destruction of organic pollutants. Secondly is the electron transfer process from nanoparticels into the nanotubes. In general, irradiation of metal oxide semiconductor with a photon of

sufficient energy, greater or equal to band gap energy could promote an electron from valence band (VB) to conduction band (CB). The promoted electron leaves a vacancy in the valence band creating positive hole which can react with hydroxyl forming a powerful oxidant or a hydroxyl radical. The promoted electrons reduce dissolved oxygen to produce superoxide anion radical. The hydroxyl radical ($^{\cdot}OH$) and superoxide anion radical ($O_2^{\cdot -}$) therefore oxidize the target. CNTs can adsorb CNT/MO composites and by being CNTs relatively good electron acceptors while semiconductors as good electron donor under illumination [217, 218]. Oxygen molecule on its surface thus the promoted electrons in CB might directly react with the adsorbed oxygen molecule and form superoxide anion radical. This will increase the number of radicals ready for reacting with the target. Also CNTs can adsorb the target which is considered to be the first step in the degradation since the pre-adsorption of the target on the surface of catalyst particles is a prerequisite for efficient photo-degradation [219]. On the other hand, the strong interaction and formation of ester bonds between the metal and the nanotube leading in a close contact which offers an effective route of electron transfer from the conduction band into the nanotube. This can reduce the recombination of photogenerated electron-hole pairs.

2.8.2 Application of nanocomposites of PANI doped with metal oxides nanoparticles

PANI a conducting polymer has increasing scientific and technological interests in the synthesis of a broad variety of promising materials due to its unique electrical and optical properties [220, 221]. PANI is widely used in the area of electrochemical materials, light-emitting diodes, biosensors, chemical sensors, and battery electrodes [222-224]. The relatively high environmental stability and excellent electrical properties, together with the fact that it can be made from inexpensive raw materials, make PANI an ideal electronically conducting polymer for sensing applications. Much attention has been reported on both electrochemical and chemical oxidative syntheses of PANI. Generally, PANI falls into a class

of organic polymers, which exhibit different oxidation states. Leucoemeraldine base (LEB) is the fully reduced form of PANI, pernigranilene base (PB) is the fully oxidized form of PANI, and emeraldine base (EB) is the half oxidized form of PANI. All of these states, except leucoemeraldine, can be protonated. After protonation, the polymer is denoted as "salt". For instance, protonation of the emeraldine base form with HCl yields emeraldine hydrochloride (Figure 2.12).

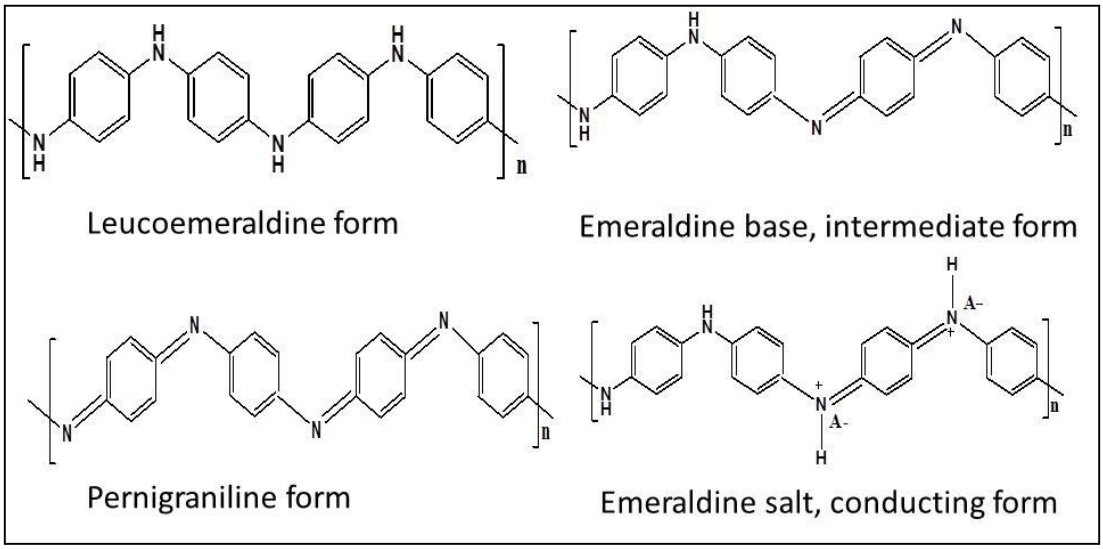

Figure 2.12: Different possible equilibrium states of PANI.

Numerous efforts have been made to successfully prepare nanocomposites by chemical and electrochemical preparation methods using nanostructured metal oxides namely TiO_2, SnO_2, SiO_2, CeO_2, and Fe_2O_3 due to their unique electrocatalytic, piezoelectric and photonic properties and tunable size that make them suitable for solar cell applications [225-229].

2.8.3 Application of nanocomposites of Nylon 6,6 nanofiber functionalized with MWCNT and metal oxides nanoparticles

Nylon 6,6 is a semicrystalline polymer which has good thermal stability and mechanical strength and it is an important engineering thermoplastic [230-232]. This polymer is suitable

for electrospinning processing due to its poly-electrolytic behaviour in acid solution [233]. The nanofibres obtained from electrospinning offer the possibility to incorporate active components on a nanoscale [234, 235]. Furthermore, it is well known that the addition of carbon nanomaterials can promote the crystallisation process of polymers due to their nucleating effects [236-238]. The enhancement of the nanocomposite mechanical properties due to functionalisation of 1D and 2D carbon has been widely studied [238, 239]. Rong et al. found that functionalised CNTs have a better performance in improving the mechanical properties of poly (ether ether ketone) when compared to pristine CNTs [236].

The possibility of combining a variety of polymers, particulate nanofillers, and biological agents through electrospinning leads to development of nanocomposite/hybrid nanofibrous membranes with a more optimum filtration efficiency and a much broader domain of environmental applications than their neat counterparts. The nanocomposite synthesis could be conventionally done through blending of insoluble nanoparticles and the polymer solution to be electrospun. In such a manner, the nanoparticles are encapsulated in the solidified nanofibers [240-244].

2.9 Biological analytes: Neurotransmitters

Neurotransmitters are the brain chemicals that communicate information throughout our brain and body. They relay signals between nerve cells, called “neurons.” The brain uses neurotransmitters to tell your heart to beat, your lungs to breathe, and your stomach to digest. Neurotransmitters are critical to the regulation of the central and peripheral nervous systems and command a number of functions such as learning, memory, sleep, and movement [245, 246]. Discerning the machinery involved in vesicular fusion, the spatiotemporal mechanisms of synaptic release, and the chemical activity of neurotransmitters is vital to understanding both normal and a typical cellular processes.

They can also affect mood, sleep, concentration, weight, and can cause adverse symptoms when they are out of balance. The neurotransmitter is a ligand that binds to a receptor protein. It must be removed to end the signal and clear the way for the next signal. Neurotransmitter can therefore be removed by diffusion and can be re-uptake by the presynaptic neuron which can actively transport the neurotransmitter back into itself.

2.9.1 Dopamine

Dopamine's synthetic precursor is 3,4-dihydroxyphenylalanine (L-DOPA) shown in Figure 2.13. Dopamine is a special neurotransmitter because it is considered to be both excitatory and inhibitory. Dopamine helps with depression as well as focus, which you will read about in the excitatory section. When dopamine is either elevated or low – we can have focus issues such as not remembering where we put our keys, and other side effects as shown in Figure 2.14. Dopamine is also responsible for our drive or desire to get things done – or motivation. Stimulants such as medications for ADD/ADHD and caffeine cause dopamine to be pushed into the synapse so that focus is improved. Unfortunately, stimulating dopamine consistently can cause a depletion of dopamine over time

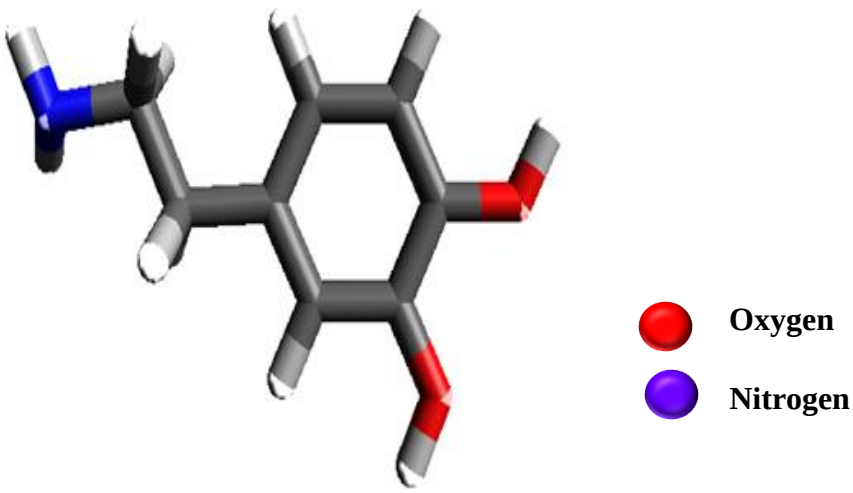

Figure 2.13: Structure of dopamine.

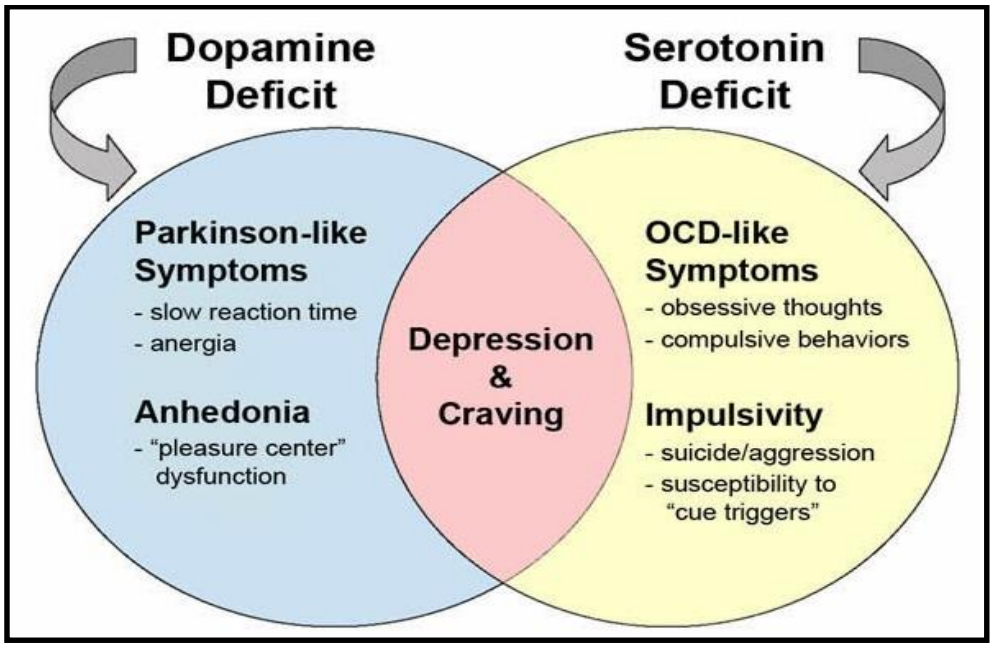

Figure 2.14: Effects of imbalance in dopamine and serotonin.

2.9.2 Serotonin

Serotonin structure is derived from the amino acid L-tryptophan as shown in Figure 2.14.

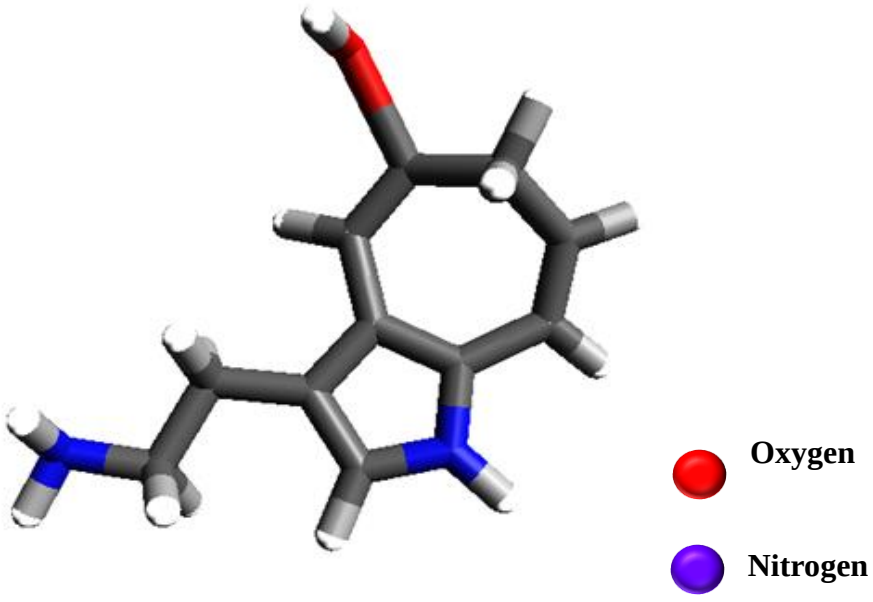

Figure 2.15: Structure of serotonin.

Serotonin is an inhibitory neurotransmitter – which means that it does not stimulate the brain. Adequate amounts of serotonin are necessary for a stable mood and to balance any excessive excitatory (stimulating) neurotransmitter firing in the brain. Inadequacy in the concentration of serotonin can have a negative effect on the human body as shown in Figure 2.15. Serotonin also regulates many other processes such as carbohydrate cravings, sleep cycle, and pain control.

2.10 Environmental analytes: Polyaromatic compounds (PAHs)

Polycyclic aromatic hydrocarbons (PAHs) also known as polyarenes are a diverse group of organic compounds composed of hydrogen and carbon atoms arranged in two or more fused benzene rings. They are widespread ubiquitous environmental contaminants of anthropogenic or natural origin usually occurring in mixtures. The natural sources of PAHs include natural fires, volcanic eruptions, thermal geological reactions etc. [247]. Anthropogenic sources are the major sources of PAHs and this include fuel oil or gasoline spills, natural seeps as well as the combustion of fossil fuels such as coal, oil, and natural gas. The main source of PAHs is the incomplete combustion of coal, oil and petrol as well as in processes involving the petrochemical industries. They can also be found airborne, in the gas phase or adsorbed to airborne particles, in aqueous phases, such as groundwater, wastewater or drinking water, and

adsorbed to solids in soil or sediments [248]. Crude oil and coal have also been identified as sources of PAHs. The adverse effects of PAHs are as a result of their persistence, hydrophobic character, bioaccumulation and carcinogenic properties. Hence, due to their ubiquitous distribution, PAHs detection in water and soils has arose a lot of concern and thus of ongoing interest to analytical chemists. They are emitted in the atmosphere, adsorbed to particles, and may then be transported over long distances [248].

2.10.1 Phenanthrene

Phenanthrene is a polycyclic aromatic hydrocarbon (PAH) composed of three fused benzene rings and with the chemical formula, $C_{14}H_{10}$. It is a colourless, crystal- like solid but can also look yellow as well as a white powder and has a bluish fluorescence. It is derived from coal tar, melts at 99 °C, boils at 340 °C and is insoluble in water but soluble in most organic solvents such as toluene, carbon tetrachloride, ether, chloroform, acetic acid, acetonitrile and benzene. It is a composite of phenol and anthracene [249] and its oxidation reactions occur at the 9 and 10 positions to form phenanthrenequinone. The structure of phenanthrene is shown in Figure 2.16.

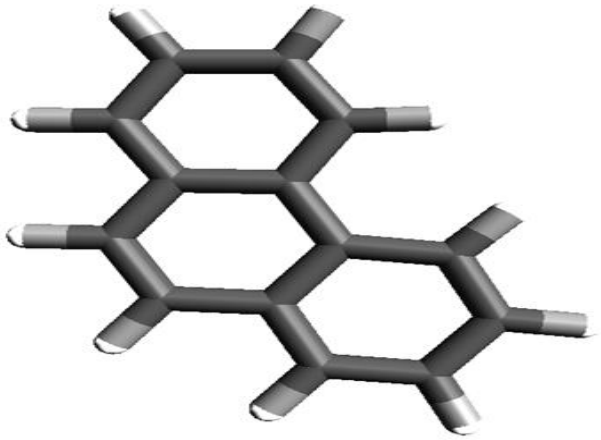

Figure 2.16: Structure of phenanthrene.

One of the most common ways through which phenanthrene gets into the body of human beings is through the breathing of contaminated air. This can be either through breathing it or working in a hazardous waste site where PAHs are disposed. Eating food or drinking water that is contaminated with PAHs can also lead to the exposure of the body to phenanthrene. Exposure to phenanthrene can also occur if ones skin comes into contact with contaminated soil or products like soils, coal, coal tar, roofing tar or creosote where PAHs are found [250].

It has also been found that breathing cigarette and tobacco smoke, eating foods grown in contaminated soils or eating grilled meat can expose one to phenanthrene [250]. Once it gets into the body, it spreads and targets the fat tissues. The major target organs in the body include the kidneys and the liver. However, in a matter of days, it leaves the body through urine and feaces [250]. It has been identified as one of the priority pollutant by the United States Environmental Protection Agency (USEPA) [251]. Other sources of PHE include incomplete combustion of fossil fuels, vehicular emissions, municipal incinerators and coke plants. Oil and petrol spillage into water bodies also results in the release of PHE to the environment [252-254]. It is widely distributed throughout the environment and is one of the most frequent and abundant PAHs found at contaminated sites [254].

2.11 Environmental analytes: organochlorine pesticides (OCPs)

An organochlorine compound is an organic compound containing at least one covalently bonded atom of chlorine as the dominant functionality, of which chloroalkane and chlorinated solvent as examples are major members. Their wide structural variety and divergent chemical properties lead to a broad range of names and applications. Many such compounds are controversial because of the effects of these compounds on the environment and on human and animal health. Organochlorine pesticides are chlorinated hydrocarbons used extensively from the 1940s through the 1960s in agriculture and mosquito control. Representative compounds in this group include DDT, methoxychlor, dieldrin, chlordane, toxaphene, mirex, kepone, lindane, and benzene hexachloride. As neurotoxicants, many organochlorine pesticides were banned in the United States, although a few are still registered for use in this country.

Exposure to organochlorine pesticides can be through accidental inhalation. The chemicals can also be ingested in fish, dairy products, and other fatty foods that are contaminated.

Organochlorine pesticides accumulate in the environment. They are very persistent and move long distances in surface runoff or groundwater. Prior to the mid-1970s, organochlorines resulted in widespread reproductive failure among birds because birds laid eggs with thin shells that cracked before hatching. Exposure to organochlorine pesticides over a short period may produce convulsions, headache, dizziness, nausea, vomiting, tremors, confusion, muscle weakness, slurred speech, salivation and sweating. Long-term exposure to organochlorine pesticides may damage the liver, kidney, central nervous system, thyroid and bladder. Many of these pesticides have been linked to elevated rates of liver or kidney cancer in animals [255 -260].

2.11.1 Lindane

Lindane is also known as gamma-hexachlorocyclohexane, (γ-HCH) gammaxene, Gammallin and sometimes incorrectly called benzene hexachloride (BHC) [261] with structural formular illustrated in Figure 2.17. Lindane is the active ingredient of some pest control products used in the home and garden, on the farm, and in forestry and animal husbandry. It is also the active agent in the medicine Kwell®, used for human ectoparasitic disease. Lindane has been reported on numerous occasions to be associated with acute neurological toxicity either from ingestion or in persons treated for scabies or lice [262-267]. Lindane has a documented 9.3% dermal absorption rate and is absorbed even more efficiently across abraded skin [262, 268].

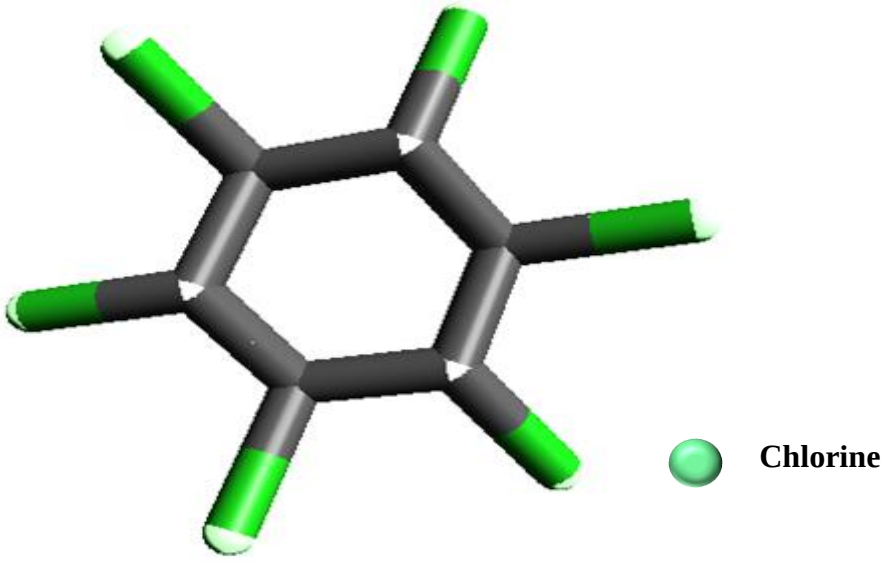

Figure 2.17: Structure of Lindane.

This becomes especially important when taking into account its use on children with severe dermatitis associated with scabies. Fat and fat solvents enhance gastrointestinal, and probably dermal, absorption of organochlorines. While most of the solid organochlorines are not highly volatile, pesticide-laden aerosols or dust particles trapped in respiratory mucous and subsequently swallowed may lead to significant gastrointestinal absorption.

2.12 Spectroscopic techniques

2.12.1 Raman spectrometry

Raman scattering spectra of the CNF mat, CNF mat containing Ag nanoparticles, and Ag coated CNF mat were determined in backscattering geometry with Jobin Yvon T64000 triple monochromator (Horiba Jobin Yvon, Inc., Edison, New Jersey). An argon laser with a wavelength of 514.5 nm and power of 4 mW under ambient conditions was used as an excitation source. The scattered light was collected in the backscattering configuration and the first-order (1000-2000 cm^{-1}). Raman spectra were recorded at a 2.0 cm^{-1} resolution. The

spectra were averaged over three scans to improve the signal-tonoise ratio and the data were corrected for the spectral response of the instrument.

Raman spectroscopy is a spectroscopic technique that can be used to observe, rotational, vibrational and other low-frequency modes in a system [269]. The technique is based on inelastic scattering of monochromatic light, generally from a laser in the visible, near infrared range, or near ultraviolet range. The interaction of the laser light with molecular vibration, phonons or other excitation in the system results in the Raman shifted photon. This Raman shifted photon could either be higher or lower in energy; it however depends upon the vibrational state of the molecule under study. The shift in wavelength of the inelastically scattered radiation provides the chemical and structural information [270]. Typically, a sample is illuminated with a laser beam and this produces a light spot that is collected with a lens and made to pass through a monochromator. Wavelengths nearer to the laser line owing to elastic Rayleigh scattering are filtered out while the rest of the collected light is dispersed onto detector. Theoretically, when light impinges upon a molecule and interacts with the electron cloud and the bond of the molecule, a spontaneous raman effect will occur inform of lights scattering and the molecule is then excited by a photon from the ground state to a virtual energy state. At this stage, the molecule relaxes and emits a photon in return to a different rotational or vibrational state. The energy difference between the states leads to a shift in the emitted photon's frequency away from the excitation wavelength.

However, Raman Effect is a light scattering phenomenon where excitation of molecule is to a virtual energy level not absorption as with fluorescence where excitation is to a discrete energy level. The emitted photon's shift actually depends on the energy of the vibrational state as regards the molecule under study as earlier mentioned. The photon will shift to a lower frequency if the final vibration state of the molecule is more energetic than the initial state, creating a balance in energy of the system. This shift in frequency is designated as a

strokes shift, and anti-strokes, if it is reversed. The observed raman shift of the stokes and anti-stokes features are a direct measure of the vibrational energies of the molecule [269]. However, during Raman Effect, about 99.999% of all incident photons in spontaneous Raman undergo elastic Rayleigh scattering while only 0.001% of the incident light produces inelastic raman signal, rendering the spontaneous raman scattering very weak. As such, measures are made by introducing the use of instruments such as tunable filters, laser stop aperture and double or triple spectrometric systems so as to reduce Rayleigh scattering and produce a high-quality and Raman spectral [268].

Raman shifts are typically in wavenumbers with a unit of inverse length. To convert between spectral wavelength and wavenumbers of shift in the Raman spectrum, then expression in equation 3.1 [271] can be used.

$$\Delta W = \left(\frac{1}{\lambda_o} - \frac{1}{\lambda_1}\right) \quad (3.1)$$

Where ΔW is the raman shift expressed in wavenumber, λ_0 is the excitation wavelength and λ1 is the raman spectrum wavelength. The unit commonly use for expressing wavenumber in raman spectra is the inverse of centimetre (cm^{-1}), and wavelength is often expressed as nanometre, therefore, the equation can be scaled for unit conversion, thus, [271].

$$\Delta W\ (cm^{-1}) = \left(\frac{1}{\lambda_o(nm)} - \frac{-1}{\lambda_1(nm)}\right) \times \frac{(10^7\ nm)}{(cm)} \quad (3.2)$$

2.12.2 Fourier transform infrared spectroscopy (FT-IR)

The chemical structure of the metal oxides and nanocomposites used in this work were identified by FT-IR (Perkin Elmer 16PC, Perkin Elmer, Inc., Boston Massachusetts) with 16 scans per sample at a resolution of 4 cm^{-1}. The sample was scanned in the range of 4400 to 350 cm^{-1}. Infrared spectroscopy is an important technique that provides easy way to identify the presence of certain functional groups in a molecule. Also, the unique collection of

absorption bands can be used to confirm the identity of a pure compound or to sense the presence of specific impurities [272]. In infrared spectroscopy, IR radiation is passed through a sample where some of the radiation is absorbed by the sample and some of it is passed through (transmittance). The resulting spectrum represents the molecular absorption and transmission, producing a molecular fingerprint of the sample. Similar to a fingerprint, two unique molecular structures cannot produce the same infrared spectrum. As a result, infrared spectroscopy can result in a positive identification (qualitative analysis) of every diverse kind of material. Additionally, the size of the peaks in the spectrum is a direct indication of the amount of material present. This makes infrared spectroscopy a useful technique for several types of analysis in terms of identifying an unknown materials, determining the quality or consistency of a sample and the amount of component in a mixture [273].

2.12.3 UV-visible spectroscopy

UV-vis is a spectroscopic technique that involves the spectroscopy of photons in the UVvisible region. It uses light in the visible and adjacent (ultraviolet) and near infrared. In UV-visible spectroscopy, the colour of a material and current can be monitored at the same time. The colour monitored is the wavelength at which the maximum of the absorption band occurs, λmax, together with the absorbance at each of these wavelengths. The absorption spectrum tells us the nature of the material generated. It is a major technique that is used in the quantitative determination of solutions of transition metal ions and highly conjugated compounds. For example, if a material absorbs UV-visible light, then we can monitor its concentration using Beer-Lambert relationship;

$$A = \varepsilon c l \qquad (3.3)$$

where A is absorbance (determined at fixed wavelength λ), ε is the extinction coefficient (cited at the same value of λ), and l is the optical path length. If the magnitude of the

extinction coefficient at λ is known, then the amount of analyte (c) can be quantified simply by determining the optical absorbance and inserting the values into equation 3.3. Most of the analytical techniques are not particularly useful for telling us what 'something' is, but are excellent at telling us how much of that 'something' is present, or has been formed or has been changed. However, UV-visible spectroscopy is one of the best ways of identifying an analyte. This is because each specific analyte absorbs energy in the form of photons at different wavelengths [274]. Hence, one is able to identify a certain analyte by the application of UV-vis spectroscopy. It is a complementary technique to fluorescence spectroscopy in that it deals with transitions from the ground state to the excited state while fluorescence spectroscopy measures transitions from excited state to the ground state [275].

2.13 Surface characterization techniques

2.13.1 Scanning electron microscopy

Samples were prepared for scanning electron microscopy (SEM) by mounting on the SEM stubs using double-sided graphite tape and then sputter coated with gold using a Balzers' union sputtering device [276]. The samples were viewed using a TESCAN Vega TS 5136LM typically at 20 kV at a working distance of 20 mm.

A scanning electron microscope (SEM) is a form of electron microscope used for producing images of a sample by scanning it with a beam of electrons in form of raster scan patterns. The electrons are made to interact with the atoms of the samples thereby producing signals that contain information about the sample's surface topography as well as its composition [277]. Electron beam which possess energy ranging from 0.2 k eV to 40 k eV, is focused by one or two condenser lenses to a spot about 0.4 nm to 5 nm in diameter. As the beam of electron passes through pairs of scanning coils or pairs of deflector plates in the electron column in the final lens, the beam is deflected so that it scans in a rectangular fashion over an

area of the sample surface. As the primary beam interacts with the sample, the electrons lose energy by repeated random scattering and absorption within a teardrop-shaped volume of the specimen known as the interaction volume, which extends from less than 100 nm to around 5 µm into the surface [278]. The electron's landing energy, the atomic number of the specimen and the specimen's density are all determining factors of the size of the interaction volume [279]. The high-energy electron is as a result of the reflection energy exchange between the electron beam and the sample and this can be detected by specialized detectors. The specimen absorbs the beam current which can be detected and used to create images. SEM micrograph is known to have magnification of a range of up to six orders of magnitude from about 10 to 500,000 times [280].

2.13.2 Transmission electron microscopy (TEM).

Transmission electron microscopy (TEM) is a microscopic technique whereby a beam of electrons is transmitted through an ultra thin specimen, interacting with the specimen as it passes through [281]. An image is formed from the interaction of the electrons transmitted through the specimen; the image is magnified and focused onto an imaging device, such as a fluorescent screen on a layer of photographic film, or to be detected by a sensor such as a CCD camera. Transmission electron microscopes are capable of imaging at a significantly higher resolution than light microscopes, owing to the small de Broglie wavelength of electrons. This enables the instrument's user to examine fine detail-even as small as a single column of atoms, which is tens of thousands times smaller than the smallest resolvable object in a light microscope.

TEM is a major analysis method in a range of scientific fields, in both physical and biological sciences. TEMs find application in cancer research, virology, materials science as well as pollution and semiconductor research.

2.13.3 X-ray diffraction (XRD)

X-ray diffraction scans of samples were obtained using a Bruker X-ray diffractometer (Bruker-AXS, Madison, Wisconsin), at 40 kV and 40 mA. WAXD device was equipped with a copper target tube, and a graphite crystal monochrometer. X-ray photographs were taken by using Ni-filtered CuKα radiation (λ = 1.5418 Å). X-ray diffraction was applied to determine the crystal structure. The scan range of 2θ was from 20-90^{o} for each sample.

X-ray diffraction is a non-destructive analytical technique which can yield the unique fingerprint of bragg reflections associated with a crystal structure. It is reflected such that, the angle of reflection is equal to the angle of incidence, and this is referred to as diffraction which can be described by Bragg's law [282].

$$2dsin\theta = n\lambda \quad (3.4)$$

At this satisfaction, a constructive interferences of the diffraction X-ray beams occurred and a detector scanning picked up the Bragg's reflection at this angle. It is the position of these reflection that give information about the inter-layer spacing of atoms in the crystal structure [282]. Therefore, a phenomenon, whereby, x-ray crystallographic method is used to determine the atomic and molecular structure of a crystal, in which the crystalline atoms caused a beam of x-rays to diffract into many specific directions (term referred to as reflection) with a wavelength similar to the distance between the atomic or molecular structure of interest, is called X-ray diffraction. As such, two-dimensional images taken at different rotations are converted into a three-dimensional model of density of the electrons within the crystal while measuring the angle and intensities of the diffraction beam. The mean position of the atom in the crystal can be determined, in addition to their chemical bonds, theirs disorder and various other information can also be gathered through the electron density. However, Poor resolution (fuzziness) or even errors may result if the crystals are too

minimal, or not consistent enough in their internal makeup [283]. The following information is expected of a very effective and reliable x-ray diffraction pattern:

1. The ability to measure the average spacing between layers or rows of atoms
2. It must be able to determine the orientation of a single crystal of grain
3. The crystal structure of unknown crystal can be found with x-ray diffraction.
4. Measurements of the size, shape and internal stress of small crystalline regions of a sample must be possible [284].

2.13.4 Energy dispersive X-ray spectroscopy (EDS)

Energy dispersive X-ray spectroscopy (EDS) is an analytical technique used for the elemental analysis of a sample. As a type of spectroscopy, it relies on the investigation of a sample through interactions between electromagnetic radiation and matter, analyzing X-rays emitted by the matter in response to being hit with charged particles. The characteristic X-rays of an element's atomic structure to be identified is unique and can be separated from others [285, 286].

CHAPTER 3

●●●●●

EXPERIMNENTAL SECTION

3.1 Materials

A working Glassy carbon electrode (GCE, 3 mm diameter), Ag/AgCl, sat'd KCl reference electrode and a platinum disk counter electrode (99.999%) were purchased from CH Instrument Inc., US. The salts of the metals, iron (II) chloride (97%), nickel (II) chloride (98%), sodium nitrite (97%), copper (II) nitrate (98-103%), iron (III) chloride hexahydrate (99%), zinc nitrate hexahydrate (98%), nickel (II) nitrate hexahydrate (98.5%) also other chemicals such as multi-walled carbon nanotube MWCNT (98%), ammonium persulphate (98%), lithium perchlorate (95%), phananthrene (98%), lindane (99.8%), serotonin hydrochloride (98%), tetrabutylammonium bromide (98%), hydrated potassium hexacyano ferrate(II) (98.5-102%), dopamine-hydrochloride (98%), ascorbic acid (99.5%) and nylon 6,6 were purchased from Sigma-Aldrich. Merck-chemicals is hereby acknowledged for the supply of the following chemicals used for these work; Sodium dihydrogen orthophosphate di-hydrate (98-100.5%), and di-sodium hydrogen phosphate di-hydrate (98.5-101%), Other reagents such as *N*,*N*-dimethylformamide (99.8), ethanol (99.8%), acetonitrile (99.8%), hydrochloric acid (32%), tetraoxosulphate (IV) acid (95-99%), aniline (99.5%), formic acid (85%), ammonia solution (25%), acetone (97%) and methanol (99.9%) were of analytical grade and were obtained from and Merck, GlassWorld Chemicals and Sigma Aldrich respectively.

3.2 Preparation of Metal Oxides

3.2.1 Nickel oxide nanoparticle

In a typical procedure, 291 mg Ni $(NO_3)_2 \cdot 6\,H_2O$ was dissolved in 10 mL water. Then, concentrated ammonia solution was added until formation of Ni $(OH)_2$. The precipitate colour was light green. Addition of ammonia solution was continued just to dissolve Ni (OH)

$_2$ and form dark blue nickel-ammonia complex with a solution pH of ≈10. This solution was then placed near a baker containing 10 mL concentrated sulfuric acid in a closed polyethylene container for 48 h at room temperature. A light green powder was so precipitated. The product was washed with distilled water and ethanol and dried at 40 °C to obtain the nickel oxide nanostructure [287].

3.2.2 Zinc oxide nanoparticle

The production unit of ZnO nanostructures consists basically of a jacketed three-neck glass flask and of a magnetic stirrer with temperature control. In the three-neck glass flask, NaOH was dissolved in deionized water to a concentration of 1.0 M and the resulting solution was heated, under constant stirring, to the temperature of 70°C. After achieving this temperature, solution of 0.5 M Zn $(NO_3)_2.6H_2O$ was added slowly (dripped for 60 minutes) into the three-neck glass flask containing the NaOH aqueous solution under continual stirring. In this procedure the reaction temperature was constantly maintained in 70°C.

The suspension formed with the dropping of 0.5 M Zn $(NO_3)_2.6H_2O$ solution to the alkaline aqueous solution was kept stirred for 2h in the temperature of 70°C. The material formed was filtered and washed several times with deionized water. The washed sample was dried at 65°C in oven for several hours [288].

3.2.3 Iron (III) oxide nanoparticle

About 30 mL of 2 mol dm^{-3} $FeCl_3$ stock solutions, 20 mL of 1 mol dm^{-3} Na_2SO_3 stock solution, and 50.8 mL of concentrated ammonia diluted to a total volume of 800 L were used. Just after the mixing of $FeCl_3$ and Na_2SO_3, the color of the solution in the smaller beaker could be seen to change from light yellow to red, indicating formation of complex ions. This solution was poured quickly into the diluted ammonia solution under vigorous stirring when the colour changed from red to yellow again. A black precipitate formed. Stirring was continued for 30 min. After the reaction, the beaker containing the suspension was placed on

a permanent magnet. Black powders could be seen to quickly settle on the bottom of the beaker. The supernatant was discarded and fresh water was added to the beaker; this procedure was repeated several times until most of the ions in the suspension were removed. Dry powders were obtained by filtering and drying at room temperature [289].

3.2.4 Synthesis of polyaniline

Polyaniline nanofibers (PANI) were synthesized according to the procedure reported in literature [290]. About 0.298 g aniline was added to 10 mL of 1.0 M HCl aqueous solution. 0.186 g APS was dissolved in 10 mL of 1.0 M HCl aqueous solution. The initiator solution (APS in 1.0 M HCl) was added into the monomer solution (aniline in 1.0 M HCl) all at once. The initial ratio of APS/aniline was 1:4. The polymerization reaction was carried out under static conditions for 10 min at room temperature. The resulting polyaniline precipitate was filtered, washed with de-ionized water several times, and dried at vacuum condition (50 ^{o}C) for 24 h.

3.2.5 Treatment of MWCNT

The pre-treatment of the MWCNT was done by a method decribed as follows [291]: 110 mg of MWCNT was oxidized with a mixture of 120mL of H_2SO_4/ HNO_3 (3:1, v/v) Mixture was sonicated for 3h at 40^{o} C and cooled to room temperature. The mixture was added dropwise to 300mL of cold deionized water. It was afterward filtered and washed with deionized water until pH is neutral, then dried at 70^{o}C overnight.

3.3 Preparation of catalysts

3.3.1 Preparation of MWCNT-MO catalysts

About 2 mg of MWCNT was weighed and doped with 2.5 mg of metal oxides NiO nanoparticles in 2 mL DMF. The mixture was stirred for 72 h at room temperature. The

known volume of the putty formed of the MWCNT-NiO nanocomposites was dried at 25 °C for overnight for the solvent to evaporate.

3.3.2 Preparation of PANI-MO catalysts

Approximately 2 mg of PANI nanofibers was weighed and 2.5 mg of metal oxides MO nanoparticles were mixed together in 2 mL DMF. The mixture was stirred for 72 h at room temperature. The PANI-MO nanocomposite was dried at 25 °C for the solvent to evaporate. The obtained PANI based nanocomposites were PANI-NiO, PANI-ZnO, and PANI-Fe_3O_4.

3.3.3 Preparation of Nylon 6,6/MWCNT/MO catalysts

10 wt % nylon 6,6 was dissolved in the formic acid at room temperature, and clear solution was obtained by stirring for 3 h.

About 2.5mg of metal oxides Fe_3O_4 and ZnO nanoparticles were added respectively into the 10 % (w/v) nylon 6,6 in formic acid. The resulting nylon 6,6/MO solutions were stirred for 5 h and sonicated for 1 h at the ambient conditions to obtain homogeneous solutions. Each resulting solution was loaded to a syringe fitted with a metallic needle. The electrospinning setup consisted of a high voltage supply and an aluminum collecting plate. The flow rate of the polymer solution was controlled using a programmable syringe pump (Model NE-1010, New Era Pump Systems Inc. USA). The solution was electrospun at a positive voltage of 20 kV, the tip-to-collector distance was 10 cm and the flow rate was 0.2 mL/h. All procedures were carried out at room temperature. The schematic diagram of the electrospinning set-up used in this work is shown in Figure 2.2. The nanofibers of Nylon 6,6/Fe_3O_4 and Nylon 6,6/ZnO are respectively functionalized with MWCNT in formic acid by sonicating for several hours to yield Nylon 6,6/MWCNT/Fe_3O_4 and Nylon 6,6/MWCNT/ZnO nanocomposites.

3.3.4 Preparation of analytes solutions

The analytes used in this study were grouped as biological and environmental. The biological analytes used are the neurotransmitters (i.e dopamine and serotonin), while the environmental analytes further classified are respectively the polyaromatic compound (PAHs), i.e. phenanthrene and the organochlorine pesticides (OCP) i.e lindane.

(a) 1 mM of dopamine was prepared in 0.1 M PBS at pH 7, by weighing dopamine hydrochloride in 50 mL 0.1 M PBS.

(b) 1 mM of serotonin was prepared in 0.1 M PBS at pH 7, by weighing serotonin hydrochloride in 50 mL 0.1 M PBS.

(c) Phenanthrene stock solution of 3×10^{-6} M was prepared by dissolving in 100 cm^3 of acetonitrile to attain solubility and later made up to 500 cm^3 with distilled water. 10 mL solution of acetonitrile (acetonitrile: water = 80:20) containing 0.1 M $LiClO_4$ was used as the working electrolyte.

(d) 500 mM of lindane stock solution was also prepared by dissolving 0.0072 g of lindane in 50 mL of 60:40 methanol/water containing 0.05 M TBAB.

3.3.5 Preparation of the dopamine hydrochloride injection solution

A 2 mL of the drug (dopamine hydrochloride injection- Dopamine HCl-Fresenius®) sample was diluted to 100 mL with distilled de-ionised water. About 2 mL of the diluted solution was pipette into five 50 mL volumetric flask and all except one were spiked with different concentration of standard dopamine solution, and made to volume with phosphate buffer pH 7.0. The concentration of each test aliquot solution was determined using square wave voltammetry. Four different injections from the same batch were analysed using the same procedure. The experiment was repeated 3 times for each sample.

3.4 Electrode Pre-treatment and Modification

3.4.1 Electrode pre-treatment

Electrodes were prepared using the following procedures. The GCE surface was cleaned by gentle polishing in aqueous slurry of alumina oxide nanopowder on a SiC-emery paper and then to a mirror finish on a Buehler felt pad. The electrode was then subjected to ultrasonic vibration in ethanol to remove residual alumina particles that might be trapped at the surface.

3.4.2 Electrode modification

3.4.2.1 Drop-dry / electrodeposition method

About 20 μL drop of the nanocomposites of MWCNT, MO, PANI, Nylon 6,6, and Nylon 6,6/MWCNT solution were droped on the bare glassy carbon electrode respectively and dried in an oven at 50 ^{o}C for 5 min [292, 293]. The modified electrodes obtained are denoted as GCE-MWCNT-MO, GCE-PANI-MO and Nylon 6,6/MWCNT/MO (where MO = NiO, ZnO and Fe_3O_4).

3.4.3 Electrochemical Studies

The unmodified GC and modified GC electrodes were characterized by cyclic voltammetry and electrochemical impedance spectroscopy (EIS). For the CV characterization, the electrodes were examined by cyclic voltammetry using 5 mM potassium ferricyanide solution prepared in 0.1 M PBS at pH 7 (by evaluating the oxidation peak current and peak potential). The voltammograms were performed between −0.2 V and 1.2 V at 25 mV/s. The electrodes were electrochemically pre-treated by cycling the potential scan between −0.2 V and 1.2 V in 1 mM potassium ferricyanide solution at the scan rate of 25 mV/s to 1000 mV/s. While the EIS was conducted for the electrodes in 0.1 mol/L PBS at pH 7 containing 5 mM $Fe(CN)_6^{3-/4-}$; the potential was set at 0.2 V in the frequency range from 10 kHz to 1Hz.

3.4.3.1 Electron Transport Experimental Procedure

The electron transport (ET) of the redox-active nanomaterials (MWCNTs, PANl and Nylon 6,6/MWCNT), MO (ZnO, Fe_3O_4 and NiO) and MWCNT/MO, PANI/MO and Nylon 6,6/MWCNT/MO nanocomposites were interrogated in a solution containing an outer-sphere redox probe 5 mM $[Fe(CN)_6]^{3-}/[Fe(CN)_6]^{4-}$ using cyclic voltammetry (CV) and electrochemical impedance spectroscopy (EIS). This usually represents a preliminary experiment conducted to establishing the successful modification and the electrical properties of the redox active nano materials on the modified electrodes. Bare and modified GCE electrodes were used as the working electrodes. Ag|AgCl, sat'd KCl and platinum electrodes were employed as reference and counter electrodes respectively. From the voltammogram obtained, the following electrochemical parameters were determined for the electrodes:

$E_{1/2}$ = Formal potential

ΔE = Change in potential

Ep = Peak potential

Ip= Peak current

Ic = Catalytic current

Ip/Ic = Ratio of peak current to catalytic current

These parameters are envisaged to give insight into the electron transport properties of the respective fabricated sensors. The EIS experiment was conducted by running the bare and the modified GCE electrodes in $[Fe(CN)_6]^{3-}/[Fe(CN)_6]^{4-}$ solution ($E_{1/2}$ 0.2 vs. Ag|AgCl in sat'd KCl) between 10 mHz and 1 kHz using a 5 mV rms sinusoidal modulation. The data points generated were fitted with a particular equivalent circuit and the charge transfer resistant (Rct) which controls the electron transfer kinetics of the redox probe at the electrode interface will be determined from the EIS fitting.

3.4.4 Electrocatalytic and Electroanalysis Experiment

3.4.4.1 Electrocatalytic procedure

Experiments for electrocatalytic oxidation of the analytes (e.g. dopamine, serotonin, phenanthrene, and lindane,) were carried out using nitrogen purged supporting electrolytes. Cyclic voltammetry (CV) and electrochemical impedance (EIS) experiments were conducted to investigate the electrocatalytic behaviour of the electrodes towards the analyte. For CV, the experiment will be carried out at scan rate of 25 mVs^{-1} and within the oxidation potential window at which maximum oxidation of the analyte is visible. A comparative study of the electrocatalytic behaviour of the modified electrodes towards the analyte was investigated. From CVs experiment, electrochemical parameters such as peak current (Ip), peak potential (Ep), ΔE and formal potential ($E_{1/2}$) were measured. In addition, square wave voltammetry (SWV) and differential pulse voltammetry (DPV) was carried out for the analytes to monitor their kinetic at the electrode, and to monitor the interfering effect of ascorbic acid (AA) on dopamine (DA) and serotonin at the best modified electrodes. In every case of measurement, the bare or modified electrode is the working electrode while Ag|AgCl, sat'd KCl and platinum electrodes are the reference and counter electrodes respectively. EIS experiment was done by fixing the peak potential (Ep) at which the analyte was best catalyzed (vs Ag|AgCl, sat'd KCl) or its half potential ($E_{1/2}$) especially for a reversible electrocatalytic process.

3.4.4.2 Electroanalysis procedure

The effect of scan rate (25 to 1000 mVs^{-1}) on the electrode kinetics during analyte oxidation was investigated using the best electrode from the electrocatalytic experiment. Several kinetic parameters such as Ep, Ip, and the peak-to-peak separation (ΔEp) were obtained. The plot of

the anodic (Ipa) peak current against square root of scan rate ($\nu^{1/2}$) which is an indication of diffusion-controlled reaction, was investigated.

As part of the analysis experiment, concentration study on each analyte was carried out using square wave voltammetry or differential pulse voltammetry experiment. Analysis of the analytes was carried out at their respective peak potential of catalysis. Different aliquots of the stock analyte solution (corresponding to different concentrations) were injected into 50 or 100 mL of supporting electrolyte solution and the mixture stirred thoroughly for 5 min. The modified electrode was run in both the supporting electrolytes and the analyte solutions. From the plot of peak current response Ip versus different analyte concentration [analyte], sensitivity and the limit of detection (LoD =3.3 s/m [294] where s is the relative standard deviation of the intercept and m, the slope of the linear current versus the concentration of analyte) were estimated.

CHAPTER 4

●●●●●

RESULT AND DISCUSSION

4.1 METAL OXIDE NANOPARTICLES / MULTI-WALLED CARBON NANOTUBE NANOCOMPOSITE MODIFIED ELECTRODE FOR THE DETECTION OF DOPAMINE

There is significant interest in developing electrochemical techniques for determination of neurotransmitters such as dopamine (DA). DA is ever-present neurotransmitter in mammalian brain tissues that plays an important physiological role in the functioning of central nervous, renal, hormonal and cardiovascular systems as an extra cellular chemical messenger [295, 296]. DA belongs to the family of inhibitory neurotransmitters; its function is to regulate neural interactions by reducing the permeability of gap junctions between adjacent neurons of the same type. In addition, neuro degeneration of DA-containing neurons contributes to late-onset neurological diseases, including Parkinson's and Alzheimer's diseases, and possibly to normal ageing of the brain [297]. Besides, numerous reports have shown its coexistence in biological systems [298, 299]. Therefore, investigation of neurological behavior and also simultaneous determination of DA is of great importance for the elucidation of its precise physiological functions.

4.1.1 Characterization of the electrodes

4.1.1.1 Morphological characterization

The surface morphology of the material was examined with SEM and transmission electron microscope (TEM).

The TEM images for the nanocomposites as shown in Figure 4.1a (i-iv) The MWCNT showed disperse spiral tubes (Figure 4.1 a (i)), whilt the TEM images of the metal oxide nanoparticles were porous, crystalline and somewhat aggregated, possibly due to strong electrostatic interactions between the oxide molecules. TEM image of ZnO nanoparticles (Figure 4, 1 a (iv)) shows dark layers of several nanoparticles on top of one another and they have either spherical or rod-like structure. The average diameter of MWCNT nanoparticles is

about 8–11 nm. The relatively mono disperse Fe_3O_4 particles have an average diameter of 10 nm. The sizes of ZnO NP were 50 ± 15 nm.

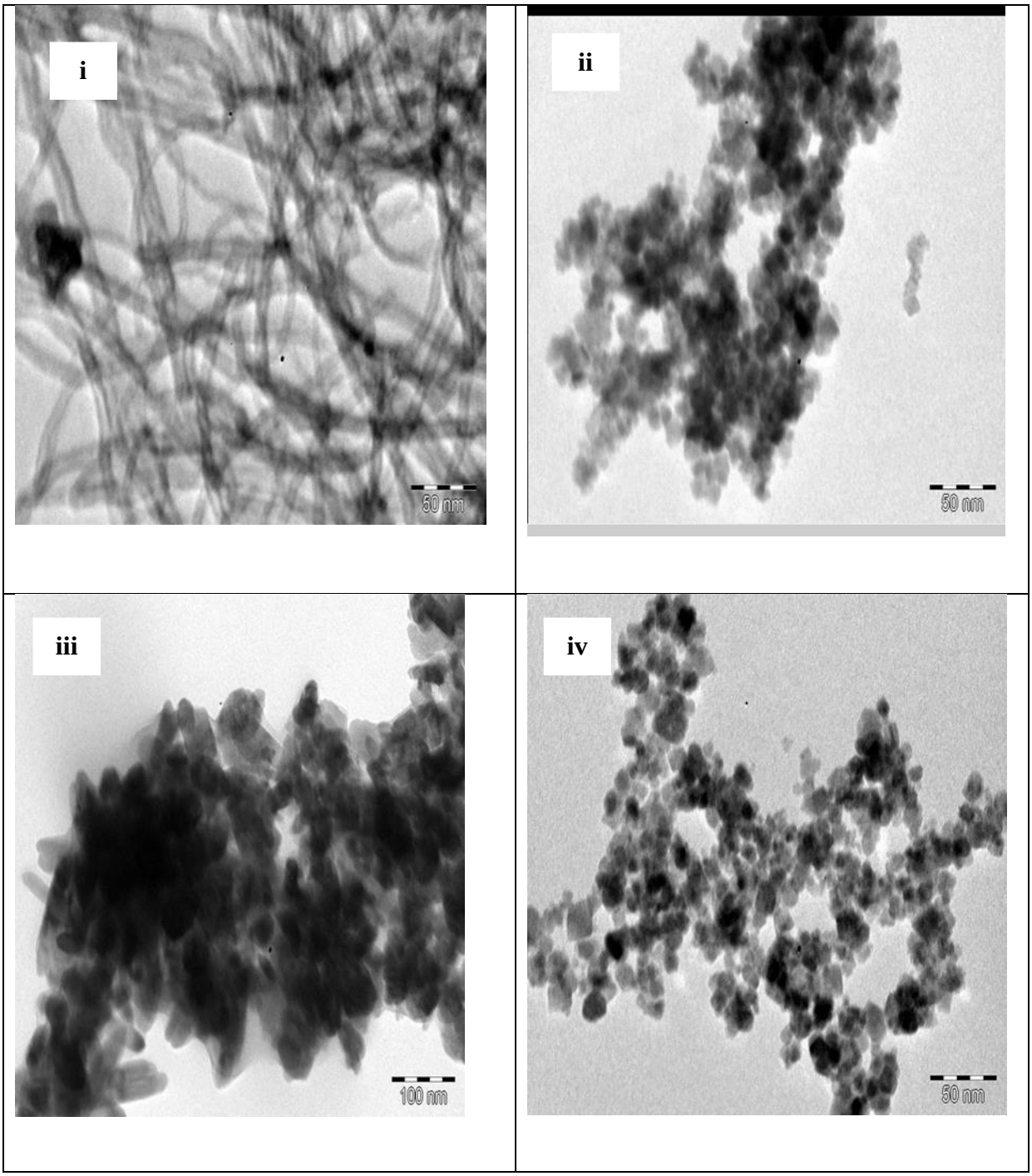

Figure 4.1a: Typical TEM images of (i) MWCNT (ii) NiO (iii) Fe_3O_4 and (iv) ZnO nanoparticles.

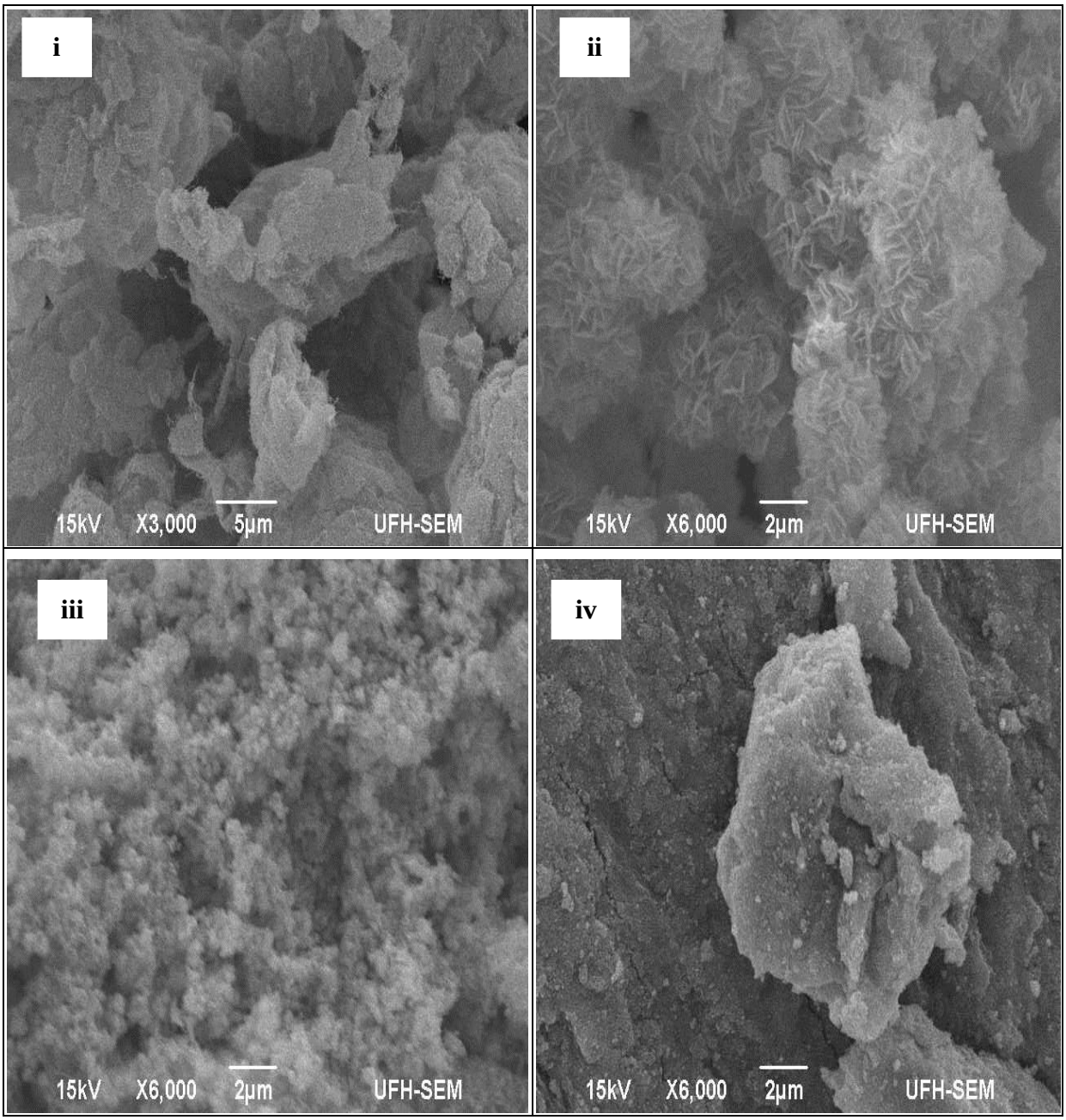

Figure 4.1b: Typical SEM images of (i) MWCNT (ii) NiO (iii) Fe_3O_4 and (iv) ZnO nanoparticles.

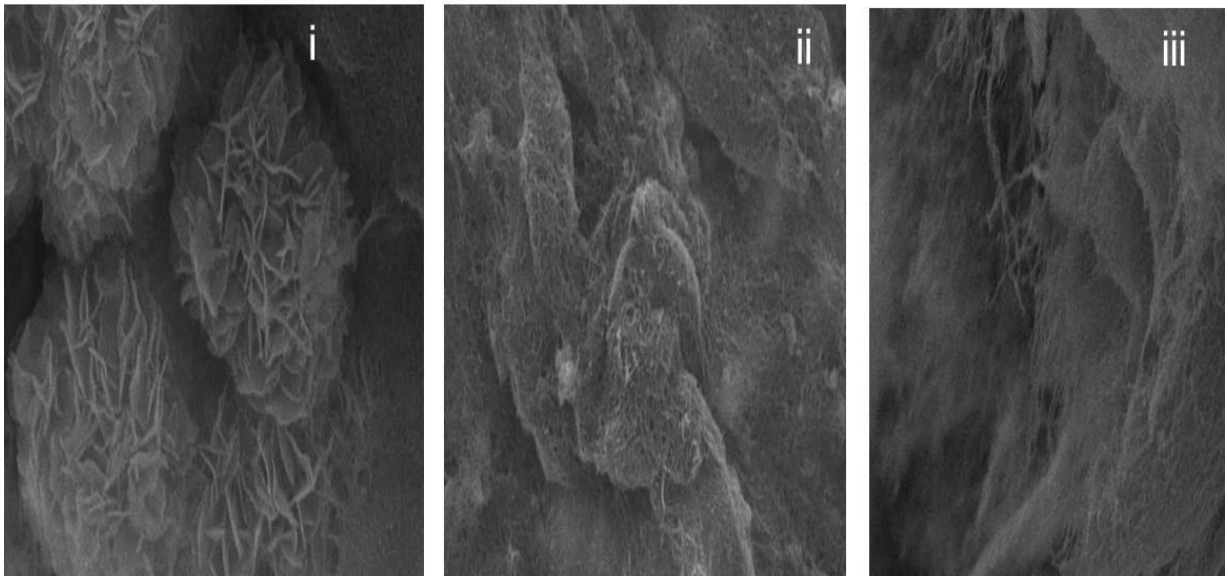

Figure 4.1c: The typical SEM images of (i) MWCNT-NiO (ii) MWCNT-ZnO and (iii) MWCNT-Fe_3O_4 nanocomposites.

Samples were prepared for scanning electron microscopy (SEM) by mounting on the SEM stubs using double-sided graphite tape and then sputter coated with gold using a Balzers' union sputtering device. The samples were viewed using a TESCAN Vega TS 5136LM typically at 20 kV at a working distance of 20 mm. The SEM images of MWCNT and the synthesised metal oxide nanoparticles were represented in Figure 4.1b (i-iv). Figure 4.4.1b (i) show the SEM image for the carbon nanotube materials, showing the appearance of loose curly CNTs together with some amorphous-like particles. These nanotubes seemingly have a broad length distribution. The nanotube diameters range from 20 to 60 nm. The SEM image Figure 4.1b (ii) indicates the formation of a flower-like conglomerate structures nickel oxide nanoparticles. Figure 4.1b (iii) shows aggregated ZnO microstructures. It can be clearly seen that the flower is made of taper shape rods that are 400 - 500 nm long and 100 - 150 nm thick. The Fe_3O_4 particle (Figure 4.1b (iv)) showed an aggregated film probably due to the method of preparation. The average sizes of Fe_3O_4 nanoparticles are estimated to be 40-100 nm. Figure 4.1c show the SEM images of MWCNT doped with NiO, ZnO and Fe_3O_4 oxide

nanoparticles respectively. There was also a change in morphology of the MWCNT after been doped with synthesized nickel, zinc and iron oxide nanoparticles. The SEM image Figure 4.1ci indicates the formation of flower-like hierarchical structure MWCNT-nickel oxide nanocomposites and nanofibers like structure was observed in the case of MWCNT-Fe_3O_4.

4.1.1.2 Ultraviolet-Visible Spectroscopy

The optical absorption spectrum of nickel oxide nanoparticle is shown in Figure 4. 2. It can be seen that the strongest absorption peak of the NiO sample appears at around 330 nm, which is closer to 355 and 320 nm reported for NiO nanoparticles [300, 301]. The different in absorption bands can be attributed to the different methods of preparation of the nanoparticles. The absorption bands at 330 nm for the NiO shifted to lower absorption band at around 280 nm in the presence of MWCNT suggesting the successful formation of MWCNT-NiO nanocomposite.

The Uv-vis absorption spectrum of ZnO sample shows excitonic peak with absorbance intensity at wavelength of 280 nm. Another absorption peak observed at around 350 nm is characteristic of ZnO nanoparticles [302]. For ZnO of wide band Gap of 3.37 eV, an absorption peak is expected at ~358 nm [303]. In the MWCNT-ZnO nanocomposite, aside the ZnO absorption bands at 350 nm two new absorption bands emerged at around 530 and 650 nm respectively and a reduction in the ZnO band intensity also confirming successful transformation of ZnO to MWCNT-ZnO nanocomposite. The Uv-vis absorption spectrum of Fe_3O_4 sample shows broad absorption peak ranging from 350 to 400 nm and was suggested to originate primarily from the absorption and scattering of light by magnetic nanoparticles. This observed absorption peak is in accordance with the literatures [304]. The high absorption band at 385 nm could indicate the formation of a least agglomerated nanosize

particle which was observed at 410 nm in a related study [305]. However, in the MWCNT-Fe_3O_4 nanocomposite, a shift in the absorption band of Fe_3O_4 at 350 nm to 280 nm, plus reduction in the Fe_3O_4 band intensity further confirm the transformation of Fe_3O_4 to MWCNT-Fe_3O_4 nanocomposite. From the results, it can be observed that the UV absorption ability of MWCNT-MO nanocomposite decreased as demonstrated by reduction in the band intensity of the MO nanoparticles after incorporated into MWCNT. This behaviour has been described previously by authors as the characteristic of the adsorption of the assembled CNTs [306]. It can also be attributed to the smooth and pure nature of the MWCNTs, with the absence of other light absorbing groups that may lead to an increased absorption band.

4.1.1.3 Raman spectroscopy

Figure 4.3a shows the Raman spectra of MWCNT and the metal oxide nanoparticles synthesized in this study. The Raman spectra of MWCNTs showed two charateristics sharp peaks at 1600 and 1380 cm^{-1} respectively. The sharp band at 1600 cm^{-1} (G band) is attributed to the in-plane vibration of the C–C bond [307], while the band at 1380 cm^{-1} (D band) is attributed to activation by the presence of disorder in carbon systems [308]. The Raman spectrum of NiO nanoparticles exhibited a strong, broad peak at 550 to 600 cm^{-1} which is due to the NiO stretching mode, also reported at 518 cm^{-1} for NiO in another study [309]. The Raman spectrum of Fe_3O_4 showed a strong band at 667 cm^{-1} which is characteristic of Fe_3O_4 nanoparticles [310]. The Raman spectrum of ZnO nanoparticles showed ZnO stretching modes at 442, 571 and 1103 cm^{-1} characteristic of ZnO nanoparticles [311].

There was a successful incorporation of the metal oxide nanoparticles into MWCNT which is confirmed by the first-order transverse optical (TO, ~ 340 cm^{-1}), longitudinal optical (LO, ~ 670 cm^{-1}), and two two-photon (2TO at 877 cm^{-1} , 2LO at 1086 cm^{-1}) peaks belonging to NiO and ZnO nanoparticles, while the first-order transverse optical (TO, 301 cm^{-1}),

longitudinal optical (LO, 491 cm^{-1}) [309, 311], and two two-photon (2TO at 808 cm^{-1} , 2LO at 1014 cm^{-1}) peaks belonging to Fe_3O_4 nanoparticles [310].

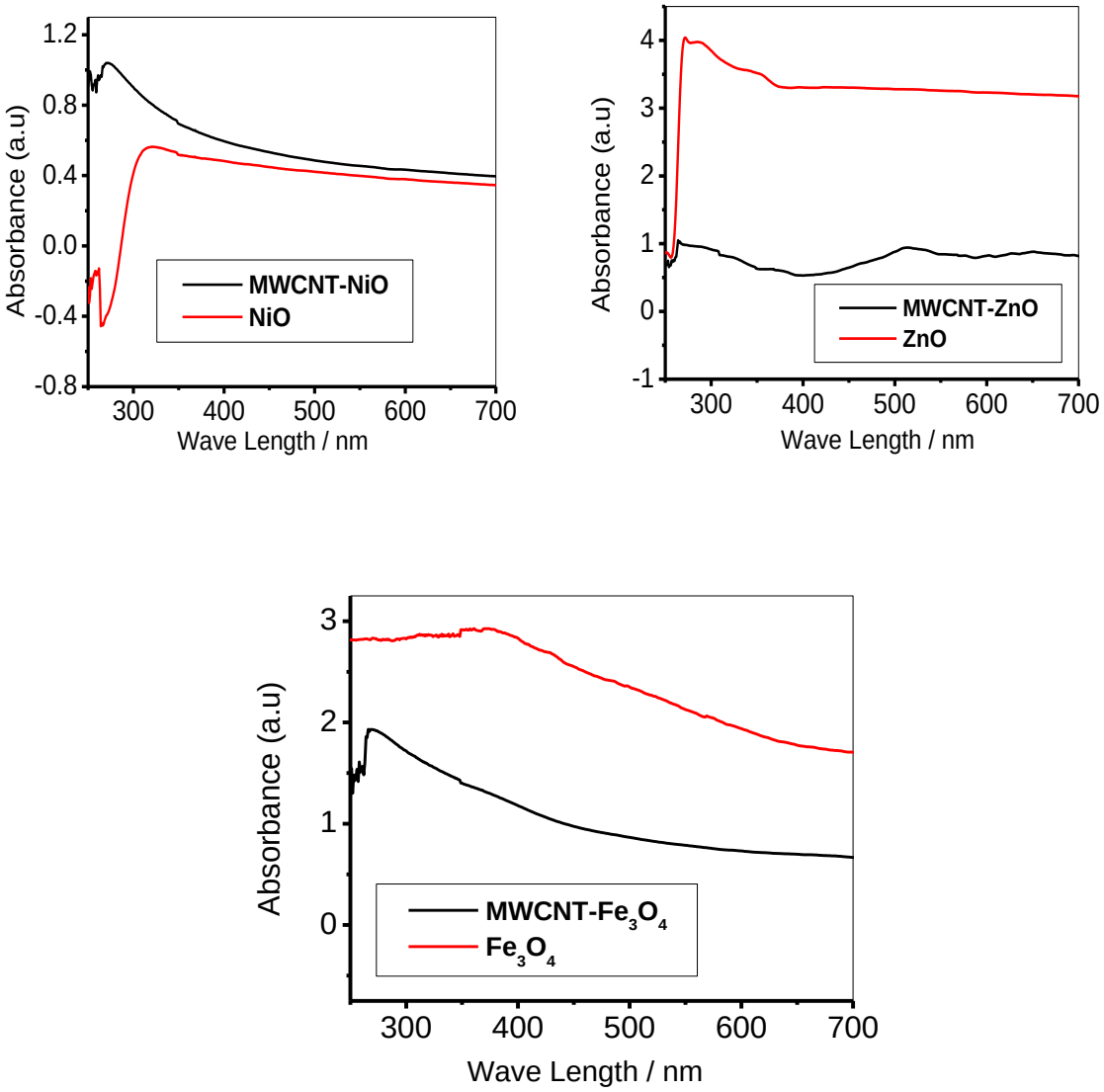

Figure 4.2: The UV-vis spectra of MWCNT, MO metal oxide nanoparticles, and MWCNT-MO nanocomposites.

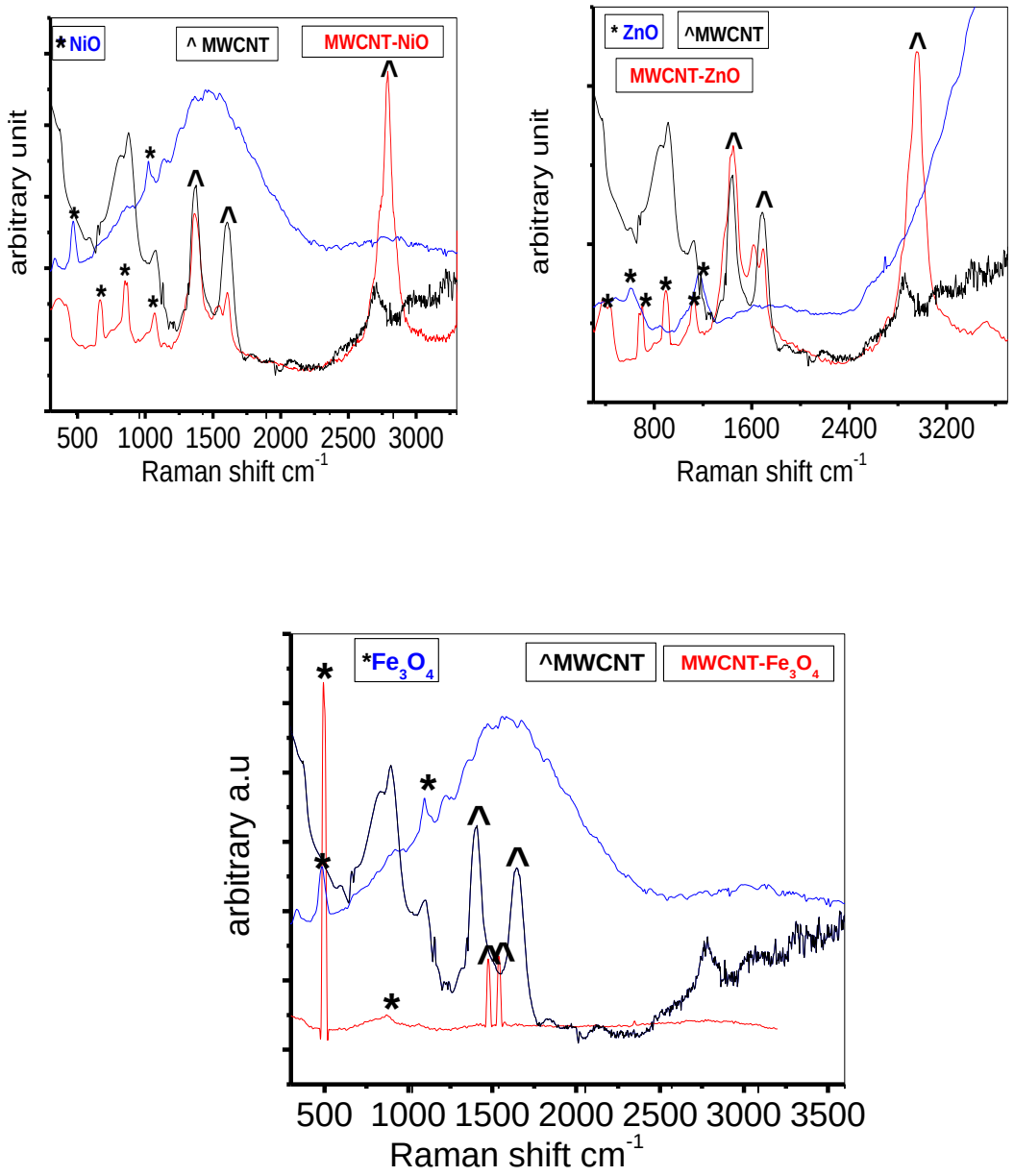

Figure 4.3a: The Raman Spectra of MWCNT, MO metal oxide nanoparticles, and MWCNT-MO nanocomposites.

4.1.1.4 Fourier Transform Infra-red spectroscopy

The FTIR spectra showed several significant absorption peaks Figure 4.3b. The broad absorption band in the region of 500–600 cm^{-1} is assigned to Ni–O, Zn-O and Fe-O stretching vibration mode; the broadness of the absorption band indicates that the metal oxide powders are nanocrystals [312]. The weak band near 1635 cm^{-1} is assigned to H–O–H bending vibrations mode due to the adsorption of water in air during FTIR sample preparation. These observations provided the evidence to the effect of hydration in the structure. The serrated absorption bands in the region of 1000 – 1500 cm^{-1} are assigned to the O–C=O symmetric and asymmetric stretching vibrations and the C–O stretching vibration, but the intensity of the band has weakened, which indicated that the ultrafine powers tend to strong physically adsorbed H_2O and CO_2 [313]. There are distinct absorption peaks at 1582, 2920, 2850 and 3446 cm^{-1}. The spectra show a band around 3446 cm^{-1} which can be attributed to the hydroxyl group (νOH) of adsorbed water molecules. The band between 1582 – 1653 cm^{-1} can be attributed to vibration mode of C=C bonds of graphite in MWCNTs, while bands around 2920 and 2850 cm^{-1} are due to asymmetric and symmetric C–H stretching in the MWCNTs. In the MWCNT-MO spectra, upon modification of the MO nanoparticles with MWCNT, the peaks around 500 - 600 cm^{-1} becomes more pronounced due to drastic reduction in the intensities of the MO peaks indicating that the MO have now been transformed to MWCNT-MO. There are also evidences of new peaks around 1200 – 1600 cm^{-1} in the MWCNT-MO nanocomposite but absent in MO nanoparticles alone. This is also an evidence of the successful formation of the MWCNT-MO nanocomposite through electrostatic interactions.

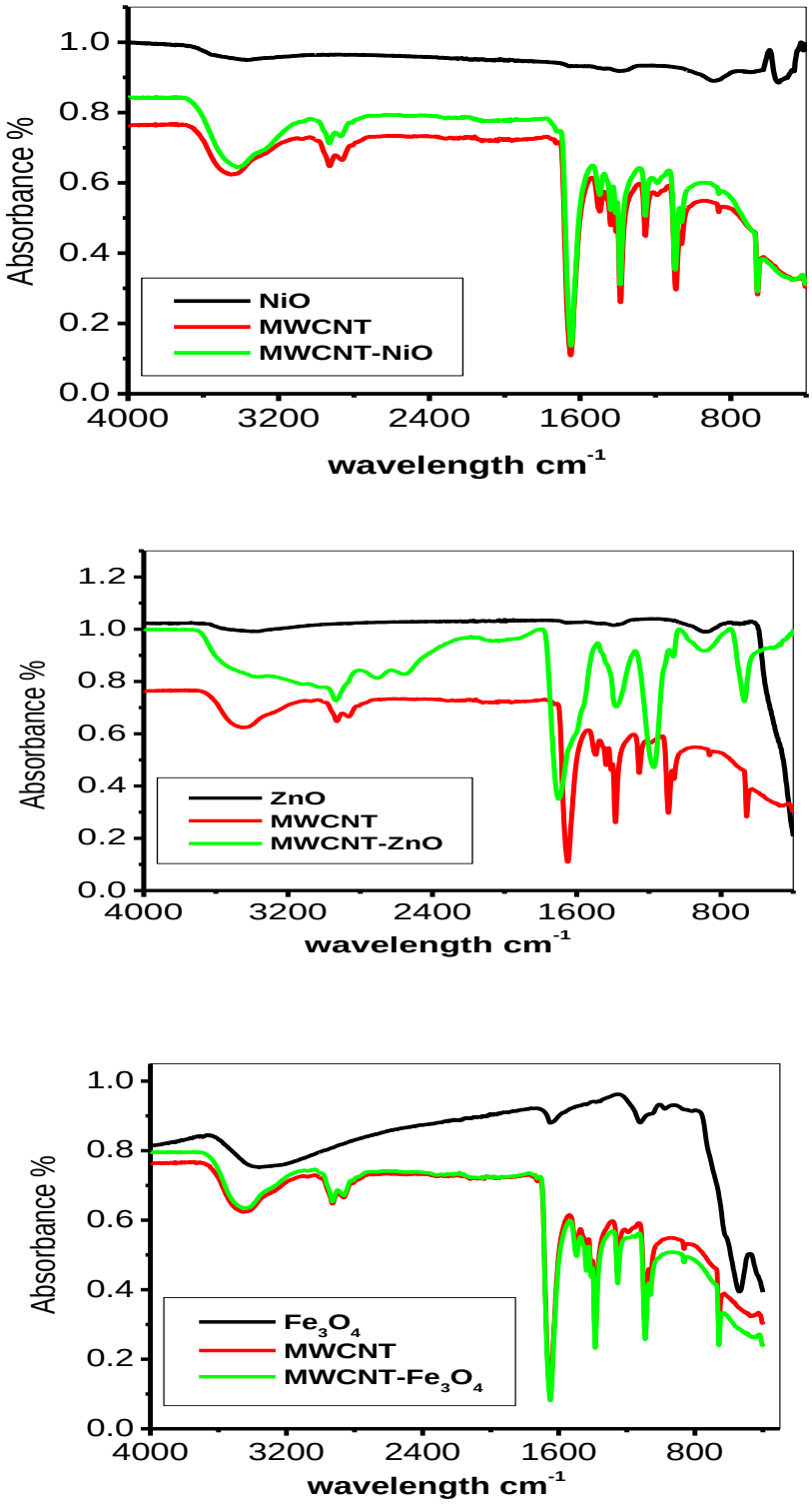

Figure 4.3b: Comparative FTIR Spectra of MWCNT, MO and MWCNT-MO nanocomposites.

4.1.1.5 Energy Dispersed X-ray spectroscopy

EDX spectra in Figure 4.4 show the elemental compositions of the MWCNT (i) and the synthesised metal oxide nanoparticles (ii – iv). The MWCNT spectrum is predominantly characterised with prominent carbon peak (C = 92.22 %). The prominence of nickel, zinc, iron and oxygen peaks in the EDX spectra of Figure 4. 4 (ii) to (iv) confirm the successful synthesis of NiO (ii), ZnO (iii), and Fe_3O_4 (iv) nanoparticles. The elemental components for the metal oxides nanoparticles are NiO (Ni = 72.98 %, O = 25.56 %), ZnO (Zn = 87.34 %, O = 11.88 %) and Fe_3O_4 (Fe = 75.58 %, O = 21.70 %).

EDX spectrum Figure 4.4b gives insights to the elemental compositions of nanocomposite formed when the MWCNT was doped with nickel, zinc and iron oxide nanoparticles respectively. The atomic Fe and O ratio obtained by the EDX analyses for MWCNT- Fe_3O_4 was close to 3:4 which further confirms the presence of Fe_3O_4 nanoparticles on the MWCNT surface. On the other hand the appearance of peaks for nickel, zinc, and oxygen proves the successful functionalization of MWCNT with the NiO and ZnO and Fe_3O_4 nanoparticles and prominent peak of carbon further proved successful functionalization of MWCNT with the three metal oxides nanoparticles.

4.1.1.6 X-ray Differaction

XRD analysis was used to determine the crystalline phase and the purity of the metal oxides nanoparticles incorporated into MWCNT. The results revealed that the nanocomposite formed were crystalline. Observed peaks diffraction indicated a high phase purity of metal oxide nanoparticles and also diffraction peaks at $2\Theta = 26.3°$ and 43.2° corresponding to reflections of (002) and (100) crystallographic plates of MWCNT. In Figure 4.5, XRD analysis of the nanocomposites indicates that MWCNT is decorated with the metal oxides nanoparticles. The diffraction lines typical of cubic crystal structures of magnetite are well-defined in the XRD pattern for MWCNT-Fe_3O_4 (Figure 4.5c). The formation of MWCNT-

NiO composites are confirmed by the presence of (002) plane of CNTs and 5 planes of NiO in XRD spectra (Figure 4.5a) and the formation of MWCNT-ZnO composites are characterized by the diffraction peaks situated at 2 Θ =31.8°, 34.5°, 36.2°, 47.5° and 56.7° corresponding to (100), (002), (101), (102) and (110) orientation planes of ZnO.

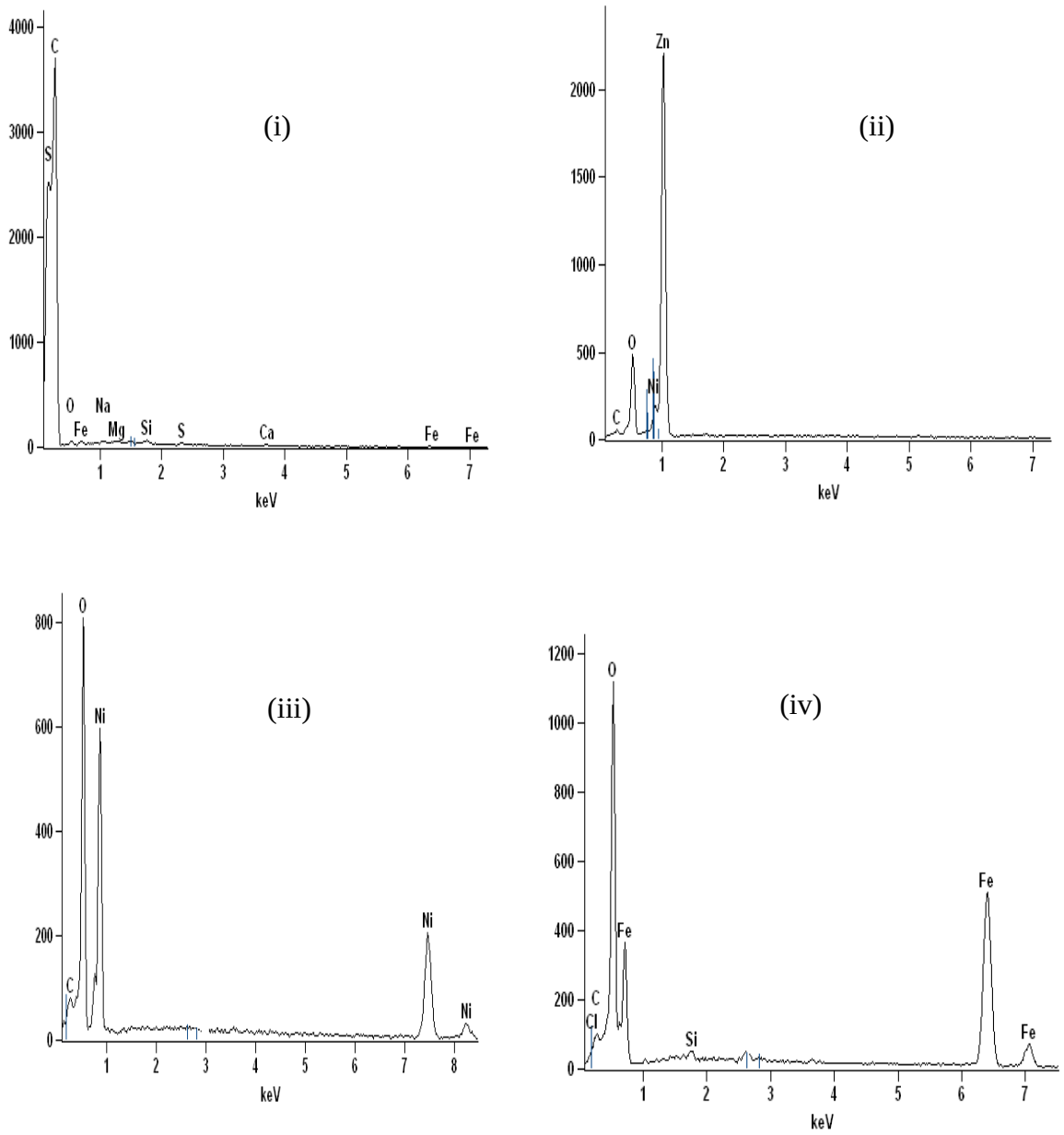

Figure 4.4a: The typical EDX spectra of: (i) MWCNT (ii) NiO (iii) Fe_3O_4 and (iv) ZnO nanoparticles.

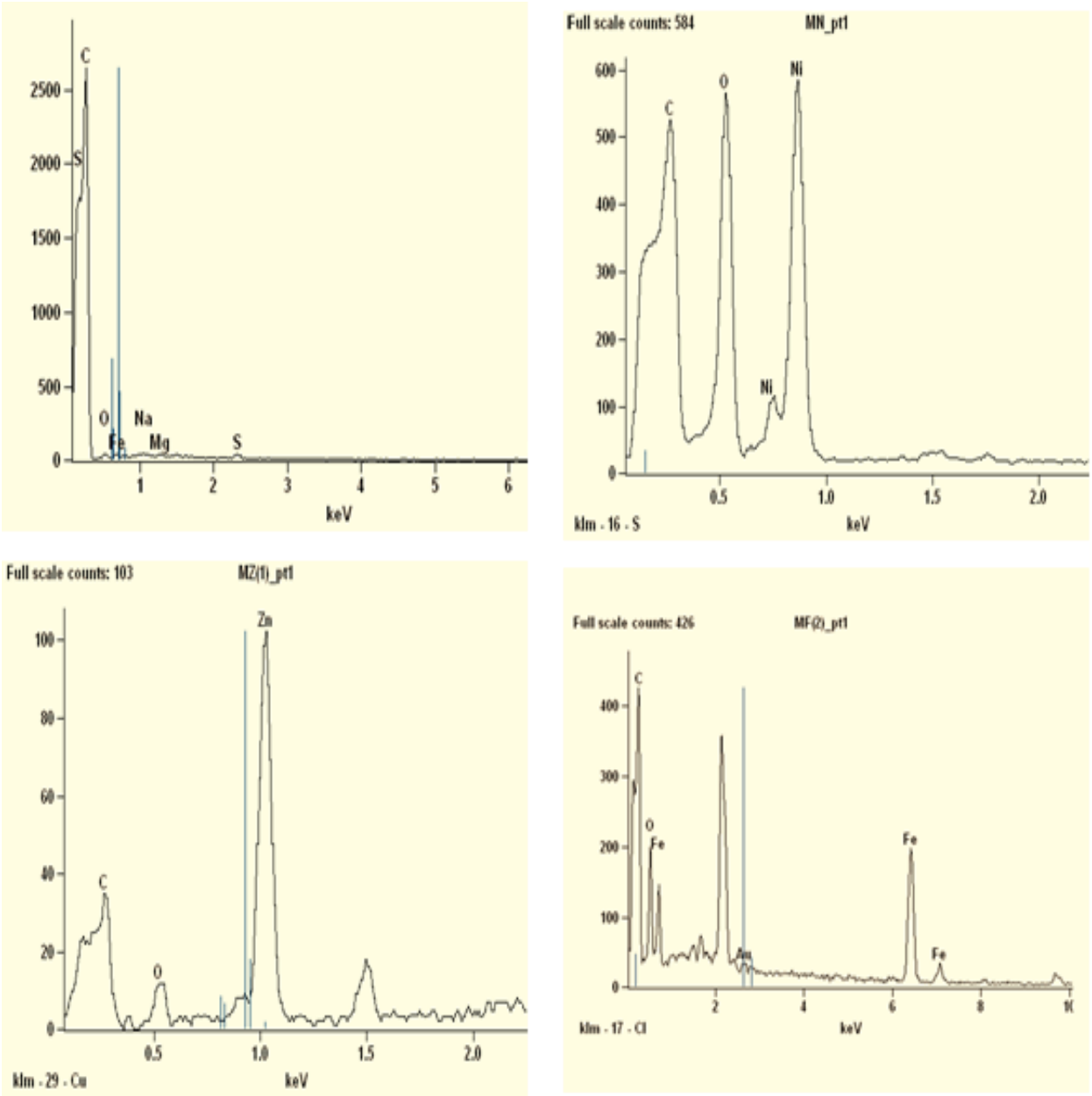

Figure 4.4b: The typical EDX spectra of: (a) MWCNT (b) MWCNT-NiO (b) MWCNT-ZnO and (c) MWCNT-Fe_3O_4 nanocomposites.

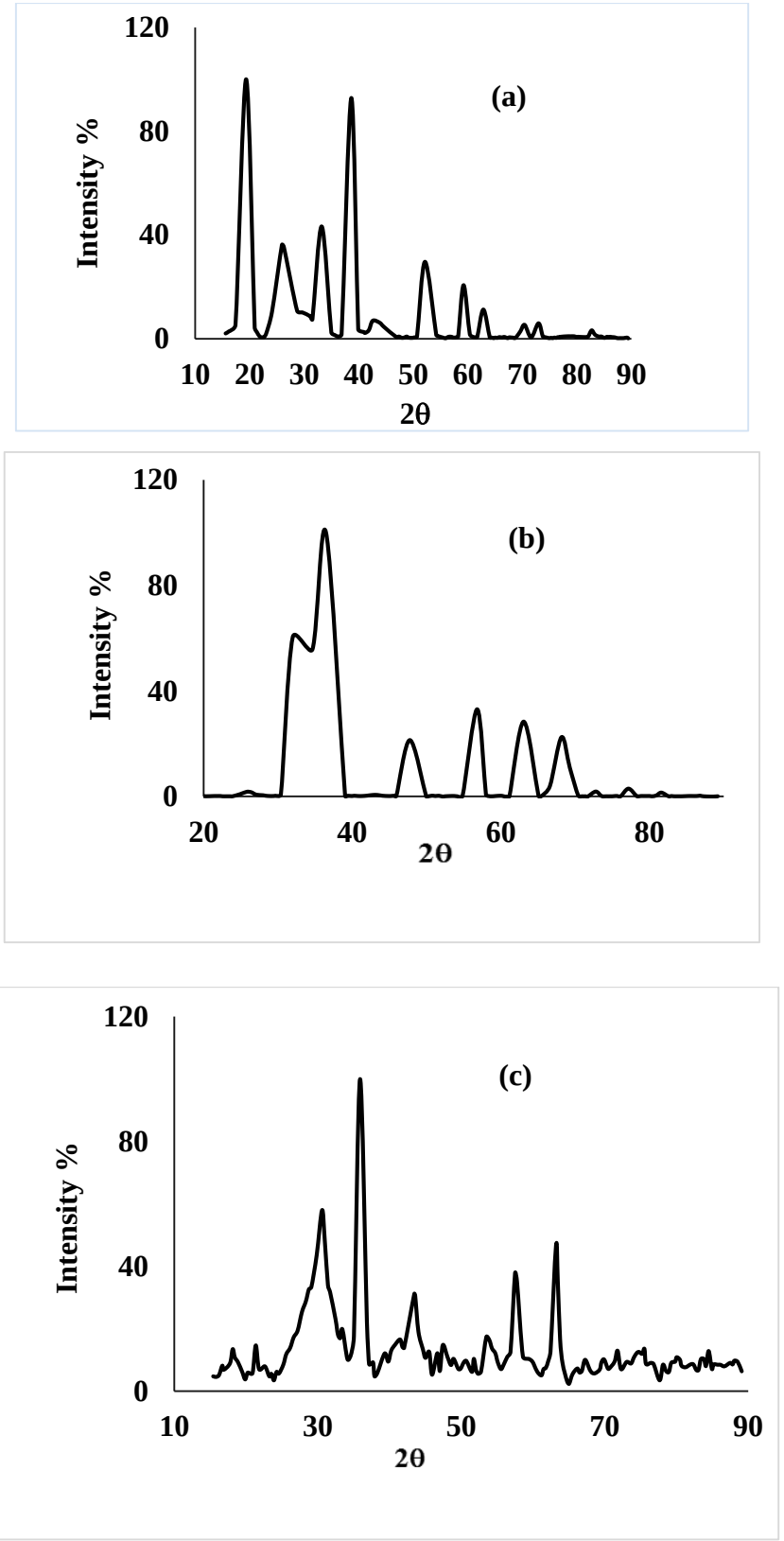

Figure 4.5: The typical XRD spectra of: (a) MWCNT-NiO (b) MWCNT-ZnO and (c) MWCNT-Fe_3O_4 nanocomposites.

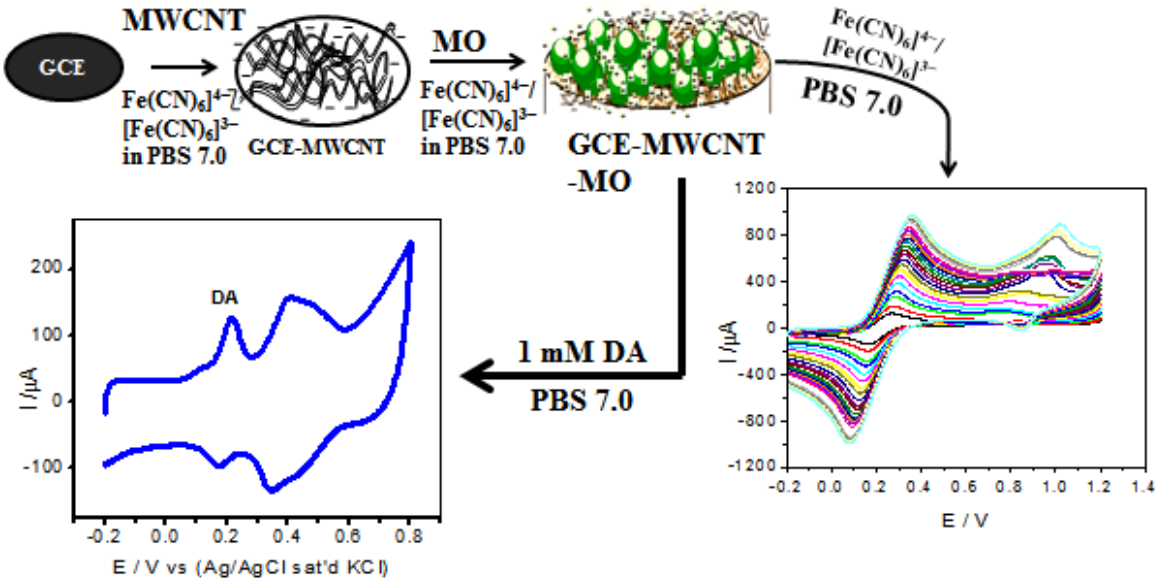

Scheme 4.1: Schematic diagram showing electrode modification procedure and the electrocatalytic behavior of the GCE-MWCNT-MO electrodes towards oxidation of dopamine.

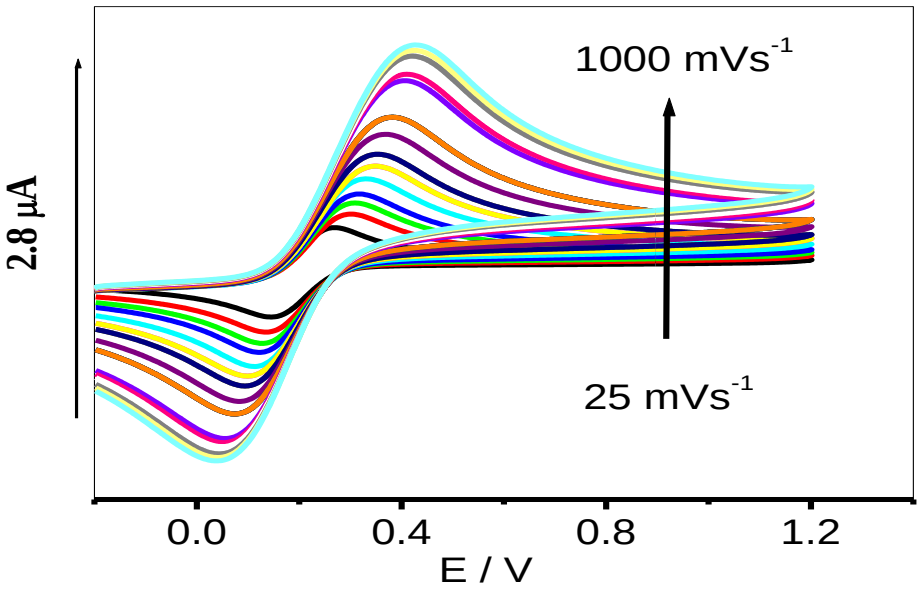

Figure 4.6: Cyclic Voltammograms of Bare GCE in 5mM $Fe(CN)_6]^{4-}/[Fe(CN)_6]^{3-}$ solution prepared in 0.1M PBS (scan rate: 25-1000 mVs^{-1}; inner to outer).

4.1.2 Electrochemical characterization of electrodes

The Schematic diagram showing electrode modification procedure, the electron transport and electrocatalytic behaviour of the GCE-MWCNT-MO electrodes towards oxidation of dopamine is shown in Scheme 4.1. Scheme 4.1 is the schematic diagram summarising the electrochemical response of the GCE-MWCNT-MO electrodes in 5 mM $Fe(CN)_6]^{4-}/[Fe(CN)_6]^{3-}$ redox probe prepared in 0.1 M PBS at pH 7.0 and in 0.1 mM DA prepared in 0.1 M PBS (pH 7.0). The cyclic voltammograms study (scan rate, 25 – 1000 mVs^{-1}) of the bare GCE electrode in 0.1 M PBS and 5 mM $Fe(CN)_6]^{4-}/[Fe(CN)_6]^{3-}$ solution prepared in 0.1M PBS at pH 7 is presented in Figur 4. 6. The bare GCE did not show any peak in PBS (Figure 4.6a) while it showed a pair of redox peaks AA' in the regions of 0.16 and 0.24 V (attributed to the $Fe(CN)_6]^{4-}/[Fe(CN)_6]^{3-}$ redox process ($E_{1/2} \approx 0.2$ V and $\Delta E_p \approx 0.1$ V) as shown in Figure 4. 6b.

To evaluate the charge transfer properties of the GCE-MWCNT-MO modified electrodes where MO represents NiO, ZnO and Fe_3O_4 nanoparticles, we performed the cyclic voltammetry experiment for the modified electrodes in 5 mM $Fe(CN)_6]^{4-}/[Fe(CN)_6]^{3-}$ in 0.1 M PBS (scan rate, 25 mVs^{-1}) and the result is presented in Figure 4.7. Two pairs of redox peaks were observed for the NiO modified electrodes (Figure 4.7a). The first redox peaks AA' ranging from the regions of 0.0 to 400 mV is attributed to the $Fe(CN)_6]^{4-}/[Fe(CN)_6]^{3-}$ redox process. Similar redox peaks was observed in Figures. 4.7b and 4.7c. Another pair of redox peaks BB' in the regions of 543 and 491 mV is attributed to Ni(II)/Ni(III) redox process. Second redox peaks BB' around 879 mV attributed to Zn(II)/Zn(III) redox process was observed on the ZnO modified electrodes (Figure 4.7c). There is no observable peaks corresponding to Fe(II)/Fe(III) redox process on the Fe_3O_4 modified electrodes probably because of the faster electron transfer at the electrode, or overllap between the $Fe(CN)_6]^{4-}/[Fe(CN)_6]^{3-}$ peaks and the Fe_3O_4 redox peaks. Generally, the GCE-MWCNT-NiO,

GCE-MWCNT-ZnO and GCE-MWCNT- Fe_3O_4 electrodes gave higher current response compared with bare GCE, GCE-MWCNT and GCE-MO (MO = NiO, ZnO, Fe_3O_4) modified electrodes electrodes. Thus, the GCE-MWCNT-MO electrodes have demonstrated faster charge transport behaviour in this study.

The synergy between MWCNT and MO nanoparticles in enhancing the electron transport process obtained at the GCE modified electrodes cannot be overemphasised. The conductive nature of the MO nanopartilses and the MWCNTs due to its facile electronic nature, plus the ionic interaction between the MO nanoparticles and MWCNTs are some of the factors responsible for this significant electron transport at the GCE-MWCNT-MO modified electrodes. Similarly, the large surface area created by the porous MWCNT on the electrode for free flow of electrolytes and charges between the base electrode and the electroactive species at the electrode surface is also another important factor for the great feat at the GCE-MWCNT-MO electrode. Similar results have been reported for modified electrodes in literature [314-317]. The peak-to-peak potential separation (ΔE_p) for the three GCE-MWCNT-MO electrodes is $\geqslant$100 mV, which is greater than the theoretical 59.8 mV expected for a fast one-electron transport. Also, the ratios of the anodic to the cathodic peak current response (I_{pa}/I_{pc}) for GCE-MWCNT-NiO electrode is pproximately unity, indicative of reversible electrochemical process, while that of GCE-MWCNT-ZnO and GCE-MWCNT-Fe_3O_4 are less than unity suggesting a quasi-reversible electron transfer process at these electrodes.

Using the Randles-Sevcik equation, $I_p = 2.69 \times 10^5 n^{\frac{3}{2}} A D^{\frac{1}{2}} v^{\frac{1}{2}} C_o$

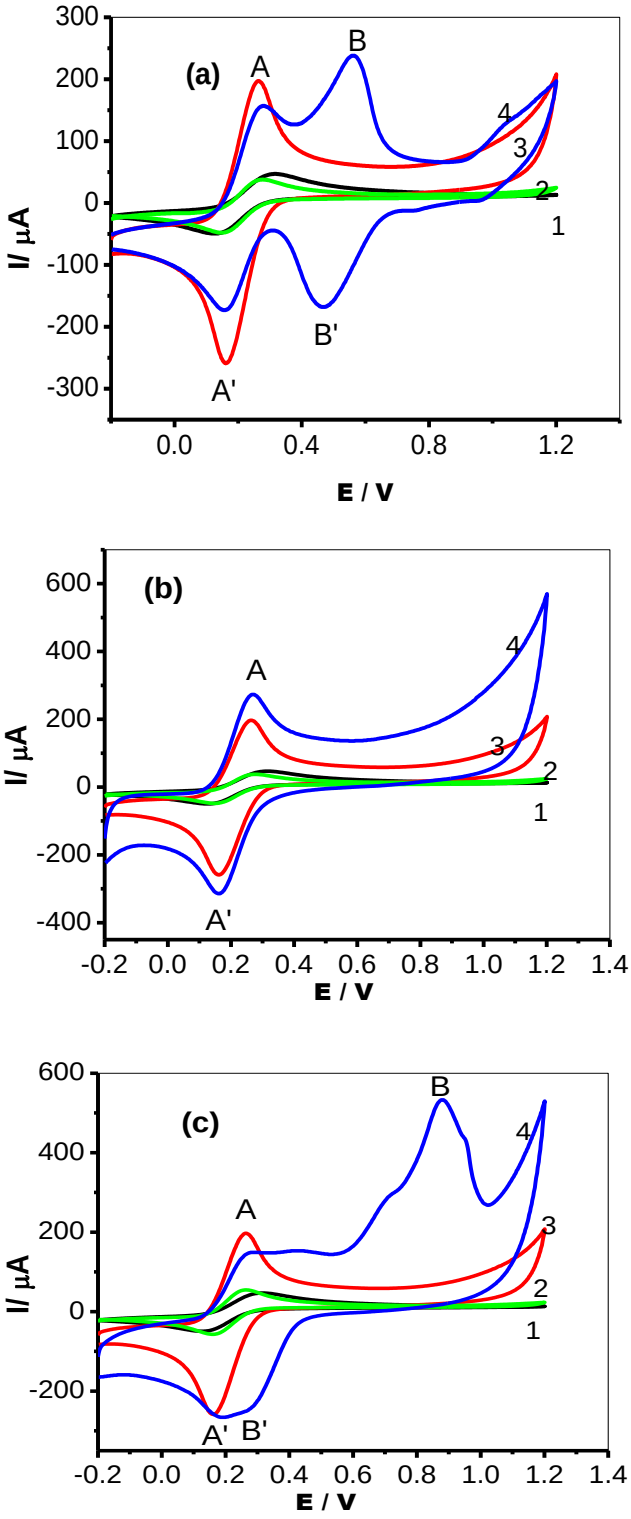

Figure 4.7: Cyclic Voltammograms of (1) GCE-MWCNT-MO, (2) GCE-MWCNT, (3) GCE- MO and (4) GCE in 5mM $Fe(CN)_6]^{4-}/[Fe(CN)_6]^{3-}$ solution prepared in 0.1M PBS at scan rate 25 mVs^{-1}. (MO: (a) NiO, (b) Fe_3O_4, and (c) ZnO nanoparticles.

where n is the number of electron transfer, α is the electron transfer coefficient, A is the electroactive surface area, C is bulk concentration (5 mM) of $Fe(CN)_6]^{4-}/[Fe(CN)_6]^{3-}$ and D is the diffusion coefficient. The electroactive surface area for the electrodes GCE-MWCNT-NiO, GCE-MWCNT-ZnO and GCE-MWCNT-Fe_3O_4 were calculated to be 1.18, 1.50 and 0.5 cm^2 respectively. Therefore, the anodic current response (in current density) of each electrode in $Fe(CN)_6]^{4-}/[Fe(CN)_6]^{3-}$ redox probe follows the order: GCE-MWCNT-Fe_3O_4 (1800 μAcm^{-2}) > GCE-MWCNT-ZnO (366.7 μAcm^{-2}) > GCE-MWCNT-NiO (211.9 μAcm^{-2}). Therefore, GCE-MWCNT-Fe_3O_4 has demonstrated the best electron transport properties with current density approximately 5 and 9 times current produced at GCE-MWCNT-ZnO and GCE-MWCNT-NiO electrodes respectively. This could be attributed to the presence of four (4) oxygen atoms with lone pair of electrons in Fe_3O_4 thereby contributing to the net electron cloud and electron transport process at the GCE-MWCNT-Fe_3O_4 electrode as compared with NiO and ZnO modified electrodes with one oxygen atom each.

The scan rate study (scan rate, 25 – 1000 mVs^{-1}) of the GCE-MWCNT-MO electrode was carried out in 5 mM $Fe(CN)_6]^{4-}/[Fe(CN)_6]^{3-}$ solution prepared in 0.1M PBS (pH 7) using cyclic voltammetry experiment. Both anodic current (I_{pa}) and cathodic current (I_{pc}) increase with increase in scan rates (25 to 1000 mVs^{-1}) (Figure 4.8).

The plot of the anodic peak currents (*Ipa*) varies linearly with square root of scan rate and the regression equation for the different electrodes is given below.

$$I_p(\mu A) = 8x10^{-4}\nu^{1/2} - 3x10^{-5}; r^2 = 0.9931 \text{(GCE-MWCNT-NiO)}$$

$$I_p(\mu A) = 2.1x10^{-3}\nu^{1/2} - 5x10^{-4}; r^2 = 0.9671 \text{(GCE-MWCNT- ZnO)}$$

$$I_p(\mu A) = 5.2x10^{-3}\nu^{1/2} - 6x10^{-4}; r^2 = 0.9980 \text{(GCE-MWCNT- } Fe_3O_4\text{)}.$$

The apparent charge transfer rate constant (k_s) and the charge transfer coefficient (α) of a surface-confined redox couple can be evaluated from the cyclic voltammetric experiments by using the variation of anodic and cathodic peak potentials with logarithm of scan rate. The E_{pa} shifted to more positive values with increasing the scan rate (v). The transfer coefficient (i.e. α) and the number of electrons involved in the rate-determining step can be evaluated. Based on the slope of E_{pa} versus log (v), $(1-\alpha)n\alpha$ was calculated to be 0.74, 0.34 and 0.33 for electrodes GCE-MWCNT-NiO, GCE-MWCNT-ZnO and GCE-MWCNT-Fe_3O_4 respectively. The values of ks were evaluated to be 0.12, 0.17 and 0.15 cms^{-1} for electrodes GCE-MWCNT-NiO, GCE-MWCNT-ZnO and GCE-MWCNT-Fe_3O_4 respectively using equation (4.1).

$$\log ks = \alpha \log (1-\alpha) + (1-\alpha) \log \alpha - \log (RT/nFn) - \alpha(1-\alpha)\, nFE/2.3RT \qquad (4.1)$$

Furthermore, from the slope of the linear plot of I vs. v, the surface concentration of the electroactive species (Γ) can be estimated according to equation 2.4 in chapter 2.where (Γ) is the surface coverage, A is the electrode surface area, F is the Faraday constant. The calculated surface coverage was 5.9, 6.7 and 2.2 $nmol/cm^2$ for GCE-MWCNT-NiO, GCE-MWCNT-ZnO and GCE-MWCNT-Fe_3O_4 respectively. It should be pointed out that the calculated surface coverage is an efficient attribute (per cross section of the electrode) and does not reflect the actual amount of MWCNT-MO per area of exposed glassy carbon.

4.1.2.1 Electrochemical impedance spectroscopic (EIS) studies

EIS is a complex electrochemical process that gives insightful information about reaction at the electrode-electrolyte interface. The result obtained is presented in Nyquist plot, which includes a semi-circular portion corresponding to the electron-transfer-limited process and a linear part resulting from the diffusion process [318]. The diameter of the semicircle

corresponds to the electron transfer resistance (Rct) of the redox probe at the electrode interface. A smaller Rct value implies that the probe has a higher interfacial electron transfer rate.

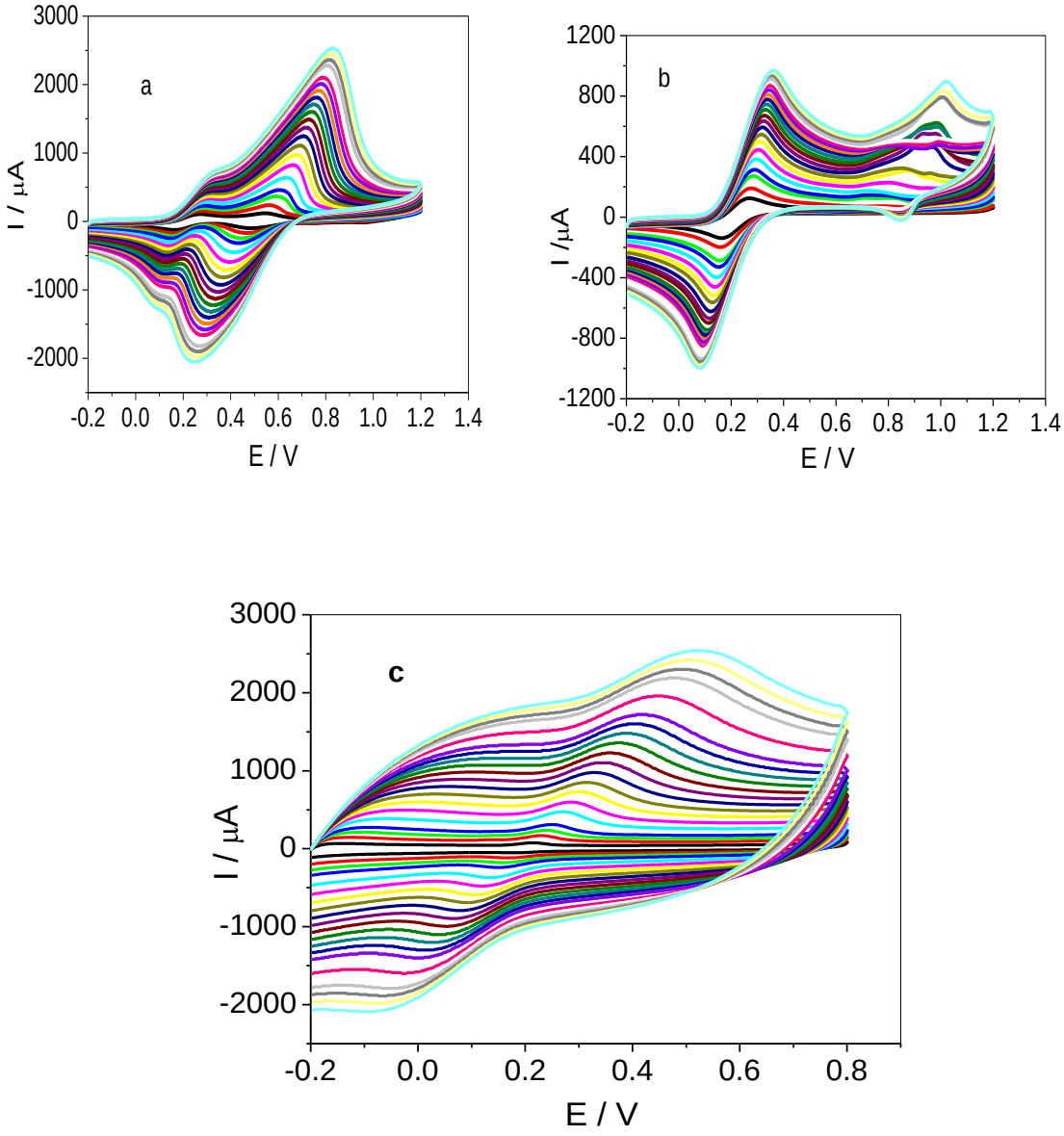

Figure 4.8: Cyclic Voltammograms obtained for (a) GCE-MWCNT-NiO, (b) GCE-MWCNT-ZnO and (c) GCE-MWCNT-Fe_3O_4 in 5 mM $Fe(CN)_6]^{4-}/[Fe(CN)_6]^{3-}$ solution prepared in 0.1 M PBS (scan rate: 25-1000 mVs-1; inner to outer).

The Nyquist plots obtained from the impedance experiment (at fixed potential of 0.2 V vs Ag/AgCl, sat'd KCl) and between 10 KHz and 1 Hz are presented in Figure 4.9a-c, while the circuit model used in the fitting of the impedance data is represented in Figure 4. 8d (i and ii). Where circuit 4.9di represent the EIS data fitting for bare GCE and 4.9dii represent that of the NiO, ZnO, Fe_3O_4, MWCNT, MWCNT-NiO, MWCNT-ZnO and MWCNT-Fe_3O_4 modified GCE electrodes. In this circuit model, R_s is the solution resistance, C_{dl} represents the double layer capacitance, Q or CPE is the constant phase element, and R_{ct} is the charge transfer resistance. The values obtained from the fitting of the raw impedance spectra with this circuit are presented in Table 4.1.

From the R_{ct} values, the electron transport is faster for the GCE–MWCNT–MO electrode compared to others. The bare GCE exhibited a larger semicircle with an Rct value of 1.572 kΩ when compared with MWCNT-ZnO, MWCNT-NiO and MWCNT-Fe_3O_4 modified GCE (38.2, 6.86 and 5.26 Ω) respectively, revealing the fast electron transfer at MWCNT-MO modified electrode. The rapid electron transfer at the nanocomposite can be ascribed to the excellent conductivity of MWCNT, which acts as a good electron conducting wire between MO and the electrode surface. The *n* values are less than the ideal 1.0 expected from an ideal capacitive behaviour, thus suggesting pseudo-capacitive properties for these electrodes.

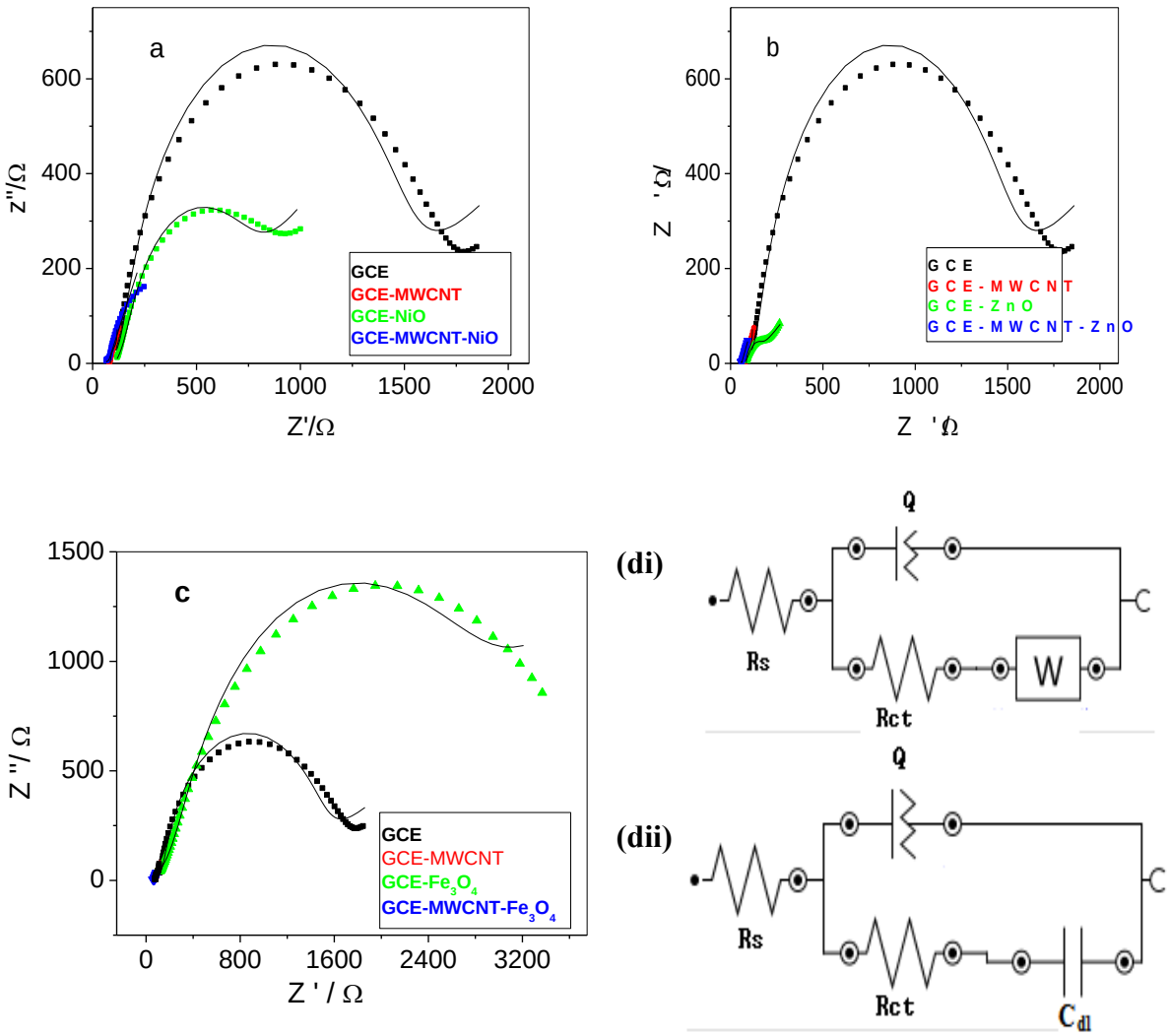

Figure 4.9: Typical Nyquist plots obtained for the electrodes in 5 mM $[Fe(CN)_6]^{4-}/[Fe(CN)_6]^{3-}$ solution (PBS pH 7.0) at a fixed potential of 0.2 V (vs. Ag|AgCl, saturated KCl). The data points are experimental while the solid lines in the spectra represent non-linear squares fits. (Figure 4.9 di and dii) represent the circuit used in the fitting of the EIS data for bare GCE and GCE-MWCNT, GCE-MWCNT-MO, and MO respectively.

Table 4.4.1. Impedance data obtained for the bare GCE and the modified electrodes in 5 mM $Fe(CN)_6]^{4-}/[Fe(CN)_6]^{3-}$ solution at 0.2 V (vs. Ag|AgCl saturated KCl). All values were obtained from the fitted impedance spectra. The values in parentheses are percent errors of data fitting.

Electrodes	**Electrochemical impedance spectroscopy data**			
	R_s (Ω)	Q (x 10^6 nF)	R_{ct} (Ω)	C_{dl} (u F)
GCE	126.60 (0.04)	8.44 (1.19)	1237.00 (0.44)	2.13 (2.25)
GCE-NiO	104.60 (1.62)	940.00 (3.95)	442.00 (2.14)	22.63 (2.42)
GCE-ZnO	70.80 (1.10)	3200.00 (1.38)	38.20 (3.34)	83.30 (4.94)
GCE-Fe_3O_4	55.80 (8.93)	334.00 (9.50)	1915.00 (4.37)	10.61 (3.84)
GCE-MWCNT-NiO	66.60 (2.17)	1410.00 (4.05)	6.86 (23.39)	10.90 (3.81)
GCE-MWCNT-ZnO	53.90 (1.39)	5800.00 (1.89)	5.33 (13.23)	4.06 (30.17)
GCE-MWCNT-Fe_3O_4	60.30 (0.59)	8270.00 (1.99)	5.26 (8.75)	18.12 (17.60)
GCE-MWCNT	85.30 (0.59)	7770.00 (5.94)	73.10 (7.551)	1.73 (7.71)

4.1.3 Electrooxidation of DA at the surface of the Electrodes

Figure 4.10, shows the electrochemical response of dopamine at bare GCE, GCE-MWCNT, GCE-MO and GCE-MWCNT-MO electrodes in 0.1M phosphate buffer solution (pH 7.0). The CV evolution of electrodes in DA is typical for DA oxidation process where the anodic peak corresponds to dopaminoquinone (DA+) (Figure 4.10, scheme 4.2) and the cathodic peak corresponds to reduction of dopaminoquinone to leucodopanoquinone [319]. The results showed that DA was oxidized with well-defined sharp DA oxidation peak at lower potentials and significantly enhanced DA oxidation current at the GCE-MWCNT-MO electrodes compared with other electrodes investigated (Figure 4.10).

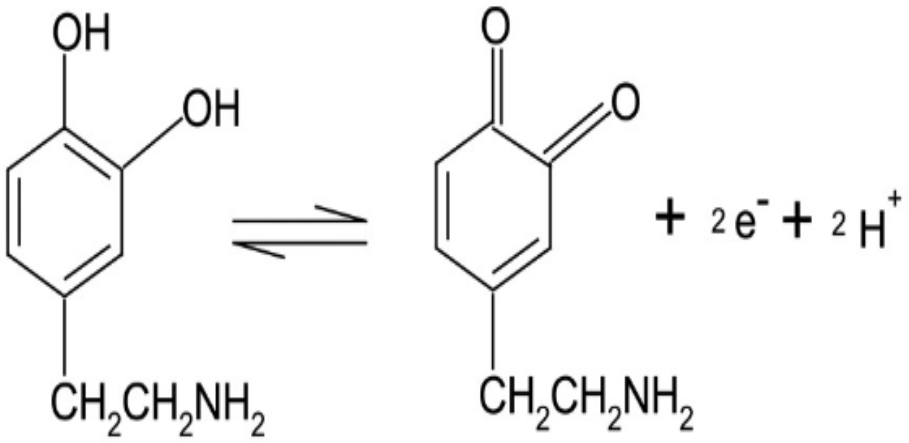

Scheme 4.2: Mechanism of DA oxidation at modified GCE-MWCNT-MO electrodes.

The oxidation peak potentials of DA on the GCE-MWCNT-MO modified electrodes were at around 0.20V vs. Ag/AgCl. On the other hand, the indistinguishable and broad peak at a bare GCE and GCE-MO electrodes indicate a slow electron transfer kinetic at the electrode. In addition, the enhanced DA currents at lower potential at the GCE-MWCNT-MO indicate that the modified electrode plays a catalytic effect on the oxidation of DA. The DA oxidation current at the GCE-MWCNT-MO electrodes follow the order: GCE-MWCNT-NiO (145 μA) > GCE-MWCNT-ZnO (76 μA) and GCE-MWCNT-Fe_3O_4 (72 μA). In terms of current density, the DA oxidation current at the electrode follows the order: GCE-MWCNT-NiO (1557 μAcm^{-2}) > GCE-MWCNT-ZnO (1085.7 μAcm^{-2}) and > GCE-MWCNT-Fe_3O_4 (1028.6 μAcm^{-2}) thus suggesting GCE-MWCNT-NiO electrode as the best electrode for DA oxidation in this study. The higher DA oxidation current at these electrodes indicates that the MWCNT has provided large surface area for effective diffusion of more DA molecules in and out of the electrode surface for maximum electrocatalytic oxidation by the MO nanoparticles compared with the bare GCE and other electrodes investigated. Similar results have been reported for DA oxidation on modified electrodes [320-322].

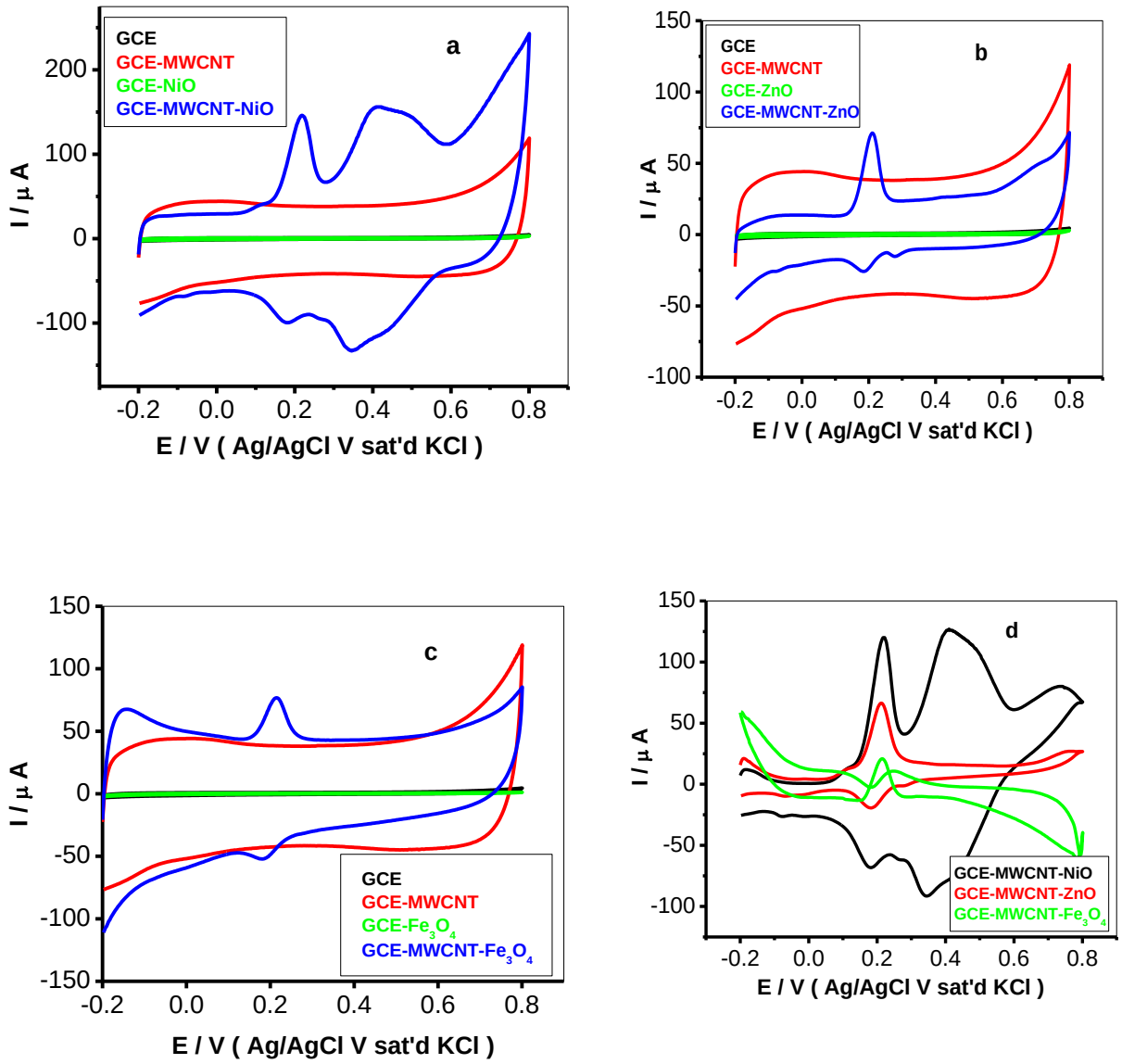

Figure 4.10: Cyclic voltammograms of 1 x 10^{-4} M DA on different electrodes (a) GCE-MWCNT-NiO, (b) GCE-MWCNT-ZnO and (c) GCE-MWCNT-Fe_3O_4 and (d) background subtracted CVs.

4.1.4 Effect of varying scan rate

Cyclic voltammetry experiments were carried out with the GCE-MWCNT-MO to establish the impact of scan rate at constant concentration (10^{-4} M) of dopamine in pH 7.0 PBS solutions. In all cases, we observed a shift in potential with increase in scan rate (Figure 4.11). From the Randles–Sevˇcik equation for an anodic oxidation process equation (2.3, chapter 2), the plot of the peak currents (I_p) against the square root of scan rate ($v^{1/2}$) (Figure 4.11) for scan rate ranging from 25 to 1000 mVs^{-1}, gave a linear relationship with equations;

$I_{pa} = 2697.1\ v^{1/2} - 467.92;\quad R^2 = 0.992,\quad I_{pc} = -2572.4\ v^{1/2} + 551.82;\quad R^2 = 0.991$

$I_{pa} = 2719.2\ v^{1/2} - 487.96;\quad R^2 = 0.9931,\quad I_{pc} = -2574.7\ v^{1/2} + 553.96;\quad R^2 = 0.9931$

$I_{pa} = 3004.8\ v^{1/2} - 656.35;\quad R^2 = 0.9931,\quad I_{pc} = -2454.5\ v^{1/2} + 545.33;\quad R^2 = 0.9931$

and approximately zero intercept, confirming a diffusion-controlled process but with some levels of adsorbed reaction intermediates. The linear relationship of the plot confirmed that the nanocomposites were electroactive, conducting and confined to the surface. This was further confirmed by the plots of log of peak current against log of scan rate (graphs not shown) which gave a slope of 1 as expected for the electrochemistry of surface-absorbed species as shown by relationship below [323].

GCE-MWCNT-NiO: $I_{pa} = 1.0544 \log \nu + 2.5007;\quad R^2 = 0.9907$

GCE-MWCNT-ZnO: $I_{pa} = 1.0827 \log \nu + 2.7936;\quad R^2 = 0.9651$

GCE-MWCNT- Fe_3O_4: $I_{pa} = 1.0721 \log \nu + 2.7727;\quad R^2 = 0.9987$

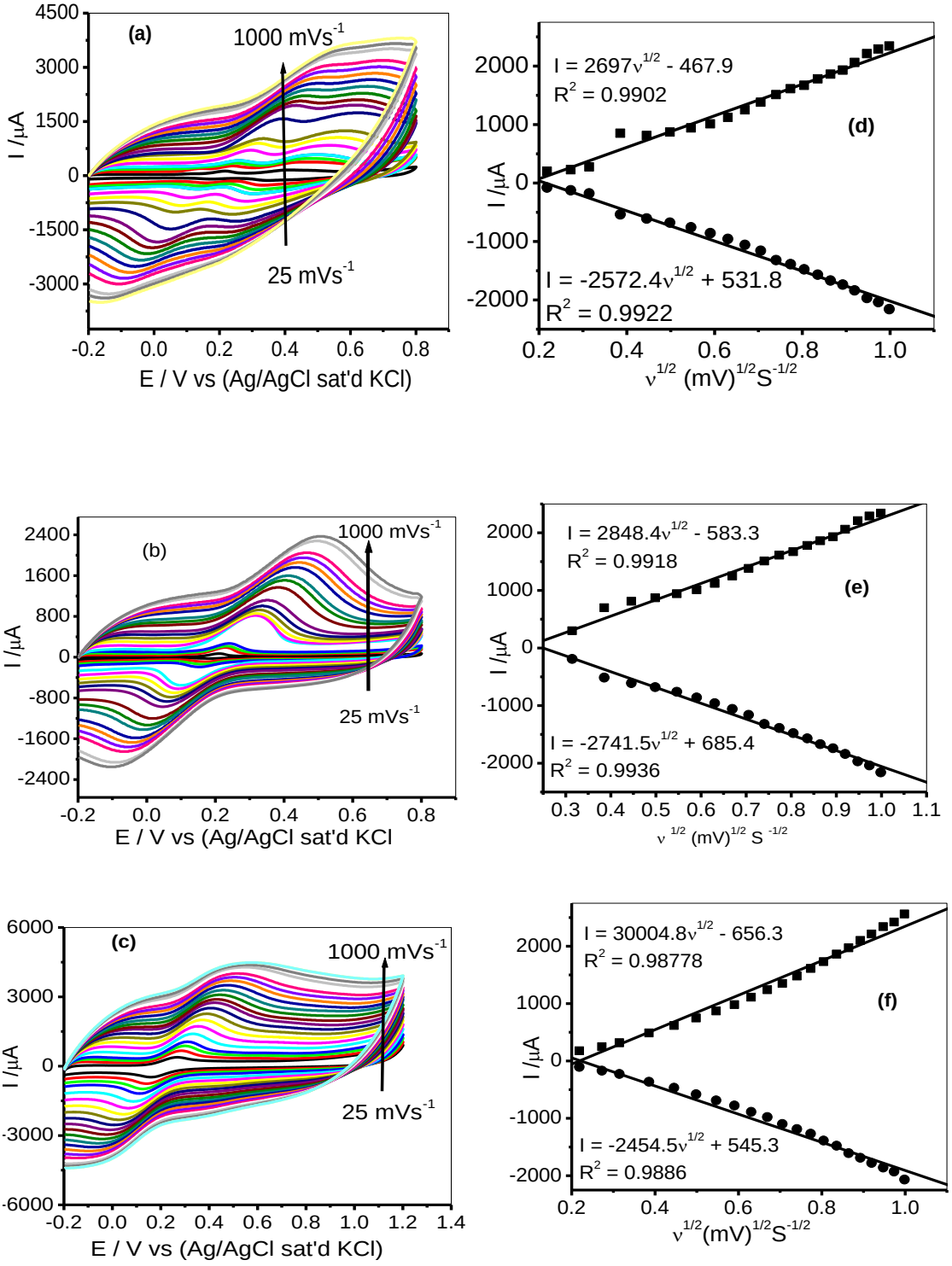

Figure 4.11: Cyclic voltammograms scan rate study of modified electrodes (a) GCE-MWCNT-NiO, (b) GCE-MWCNT-ZnO and (c) GCE-MWCNT-Fe_3O_4 in 1 x 10^{-4} M DA at various scan rates: 25-1000 mVs^{-1} (d-f are the linear plots of current versus square root of scan rate for GCE-MWCNT-NiO, GCE-MWCNT-ZnO and GCE-MWCNT-Fe_3O_4 respectively.

The charge transfer coefficient (α) for the reaction can be evaluated from cyclic voltammetric experiments by using the variation of anodic and cathodic peak potentials with logarithm of scan rate. Based on the slope of E_{pa} with log (v), (1-α)nα was calculated to be 0.86, 0.84 and 0.85 for electrodes GCE-MWCNT-NiO, GCE-MWCNT-ZnO and GCE-MWCNT-Fe_3O_4 respectively. In order to get information on the rate determining step, the peak potential, E_p, is proportional to log ν (graph not shown). The slopes of E_p *vs.* log v for the different electrodes were 0.226, 0.190, and 0.196 V for electrodes GCE-MWCNT-NiO, GCE-MWCNT-ZnO and GCE-MWCNT-Fe_3O_4 respectively. The tafel slopes may be estimated according to the equation (4.2) for the totally irreversible diffusion controlled process [324]. So, the respective values of b for these electrodes were obtained as 0.452, 0.380 and 0.392 $Vdec^{-1}$. These values are higher than the theoretical 0.118 V dec^{-1} for a one-electron process involved in the rate-determining step. Therefore the high Tafel values suggest adsorption of dopamine or its reaction intermediate at the electrode surface since high Tafel values have been attributed to the adsorption of reactants or intermediates on the electrode surfaces and/or reactions occurring within a porous electrode structure [325]. Adsorption process at the electrode can be linked with the porous CNT layer [326].

$$E_p = \left(\frac{b}{2}\right)\log \nu + constant \qquad (4.2)$$

If α was assumed equal to 0.5, nα was 1.7 (approximately 2) for all the electrodes indicating that the redox reaction of DA on the GCE electrodes GCE-MWCNT-NiO, GCE-MWCNT-ZnO and GCE-MWCNT-Fe_3O_4 was two protons coupled two electrons process. Also, the electron transfer rate constant for the GCE-MWCNT-MO electrode can be determined using equation 4.2 above, and assuming (1-α)nα =0.56, v is the sweep rate and all other symbols having their conventional meanings. The value of k_s was evaluated to be equal to 0.65, 0.81 and 0.05 cm s^{-1} for electrodes GCE-MWCNT-NiO, GCE-MWCNT-ZnO and GCE-MWCNT-

Fe_3O_4 respectively. According to the kinetics of electron process, when the rate constant is larger than 10^{-2} cm/s , the electron transfer process is very fast, and the electrode reaction is reversible, and when $10^{-4} < k_s < 10^{-2}$ cm/s, the electrode reaction is a quasireversible process. So the electrode reaction of DA on the proposed electrodes is reversible process.

The stability of electrocatalytic activity of modified GCE towards oxidation of DA was checked by repetitive scanning at scan rate of 25 mV s^{-1}. The results show that the modified electrode has a good stability in aqueous solution after repeated twenty cyclic voltammogram of modified GCE-MWCNT-MO in 1 x 10^{-4} M of DA at pH = 7.0 phosphate buffer solution between -0.2 to 0.8V (scan rate: 25 mVs^{-1}) (graph not shown). The peak current was considered as factors indicating the stability of these electrodes at various conditions of operations. The anodic peak current decrease for about 7, 8 and 4% at electrodes GCE-MWCNT-NiO, GCE-MWCNT-ZnO and GCE-MWCNT-Fe_3O_4 respectively after twenty cyclic voltammogram in the supporting electrolyte.

Impedance studies were also carried out to monitor the mechanism of the electron transfer process during the electrocatalytic oxidation of 10^{-4} M DA at fixed potential 0.2 V and frequencies between 10 kHz and 1.0 Hz. the impedance spectra (Nyquist plots) obtained for the electrodes are presented in Figure 4.12a, while Figure 4.12b shows the equivalent circuits used in the fitting of the impedance data.

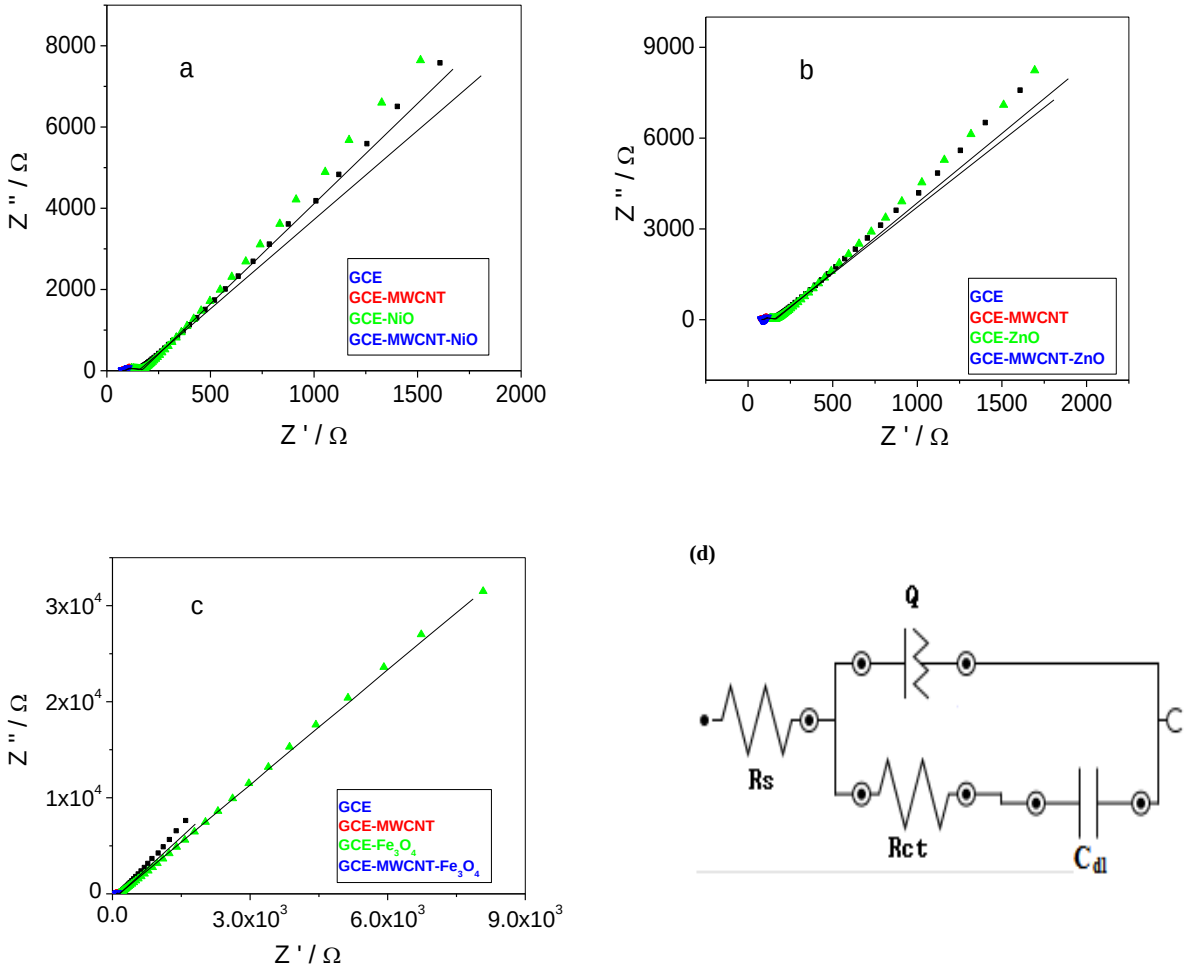

Figure 4.12: Typical Nyquist plots obtained for the electrodes in 1 x 10^{-4} M DA solution (PBS pH 7.0) at a fixed potential of 0.2 V (vs. Ag|AgCl, saturated KCl). The data points are experimental while the solid lines in the spectra represent non-linear squares fits. (d) Represent the circuit used in the fitting of the EIS data in (a-c).

However the GCE-electrodes were successfully fitted with minimum error values especially for the R_{ct} data using circuit model RQ (RC) (Figure 4.12). The charge transfer resistance R_{ct} is lower at GCE MWCNT-MO compared with the bare GCE, GCE-MWCNT and GCE-MO. The finding further confirms the CV data and also indicates that the electron transfer process is faster at GCE-MWCNT-MO electrodes with GCE-MWCNT-NiO > GCE-MWCNT-ZnO and > GCE-MWCNT-Fe_3O_4 as shown in Table 4.2. This was achieved because of the presence of MWCNT on the electrode. The MWCNT creates a porous and large surface area that mediates the analyte/catalyst electrocatalytic process.

Table 4.2: Impedance data obtained electrodes in 1 X 10^{-4} M DA solution in pH 7.0 PBS (at 0.2 V vs. Ag/AgCl saturated KCl). The values in parentheses are percent errors of data fitting.

Electrodes	**Electrochemical impedance spectroscopy data**			
	R_s (Ω)	Q (x10^5 nF)	R_{ct} (Ω)	C (n F)
GCE	54.70 (9.05)	2.77 (1.33)	98.40 (4.63)	163.70 (10.56)
GCE-MWCNT	80.40 (0.50)	307.00 (3.25)	8.50 (7.77)	78.50 (15.72)
GCE-NiO	62.60 (8.53)	2.65 (1.31)	104.80 (4.72)	152.30 (10.72)
GCE-ZnO	81.20 (7.95)	80.30 (3.04)	80.40 (7.47)	180.90 (16.73)
GCE-Fe_3O_4	134.60 (3.18)	80.30 (3.04)	319.00 (2.586)	8.66 (3.54)
GCE-MWCNT-NiO	74.60 (0.57)	350.00 (3.80)	9.50 (7.18)	63.00 (14.82)
GCE-MWCNT-ZnO	80.10 (0.49)	332.00 (3.45)	10.48 (6.59)	72.49 (12.74)
GCE-MWCNT-Fe_3O_4	78.90 (0.65)	235.00 (6.64)	33.30 (5.19)	93.30 (5.15)

4.1.5 Electroanalysis of Dopamine

Since the proposed MWCNT-MO GCE electrodes have demonstrated favourable electrochemical response towards DA, they have been used for determination of DA. To improve the sensitivity of the developed sensors in detection of DA, square wave voltemmetry (SWV) technique has been used. Results showed that the electrochemical oxidation current is linearly proportional to its concentration in the range 4.0×10^{-11} mol/L to 6.25×10^{-6} mol/L for electrodes GCE-MWCNT-NiO, GCE-MWCNT-ZnO and GCE-MWCNT-Fe_3O_4 respectively, (Figure 4.13). The respective detection limit for the electrodes were calculated based on the relationship LoD = 3.3 δ/m [294] where δ is the relative standard deviation of the intercept of the y-coordinates from the line of best fit, and m the slope of the same line to be 7.99 x 10^{-12}, 3.74 x 10^{-7}, and 1.389 x 10^{-6} mol/L (S/N = 3) for electrodes GCE-MWCNT-NiO, GCE-MWCNT-ZnO and GCE-MWCNT-Fe_3O_4 respectively. The nano molar limit of detection obtained for GCE-MWCNT-NiO compared favourably and even better that the limit of detection reported for other electrodes in literature (see Table 4.3).

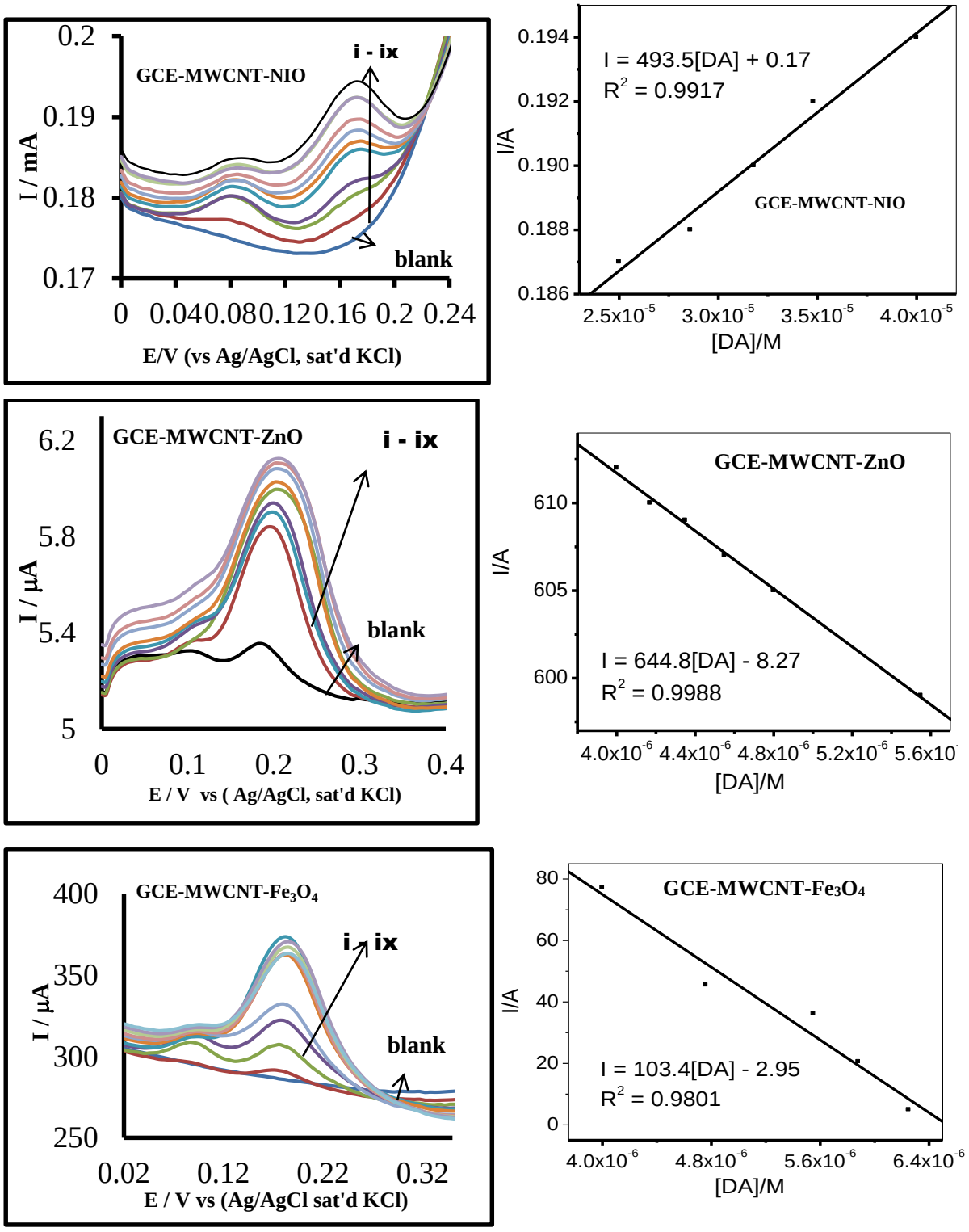

Figure 4.13: SWV of GCE-MWCNT-NiO, GCE-MWCNT-ZnO and GCE-MWCNT-Fe_3O_4 in 1 x 10^{-4} M DA and their respective current vs concentration of DA graphs.

Table 4.3: Comparison of different electrochemical sensors for the determination of dopamine.

Electrode material	Techniques	Interference	Detection Limit ($molL^{-1}$)	References
SWNT/Ppy,Surf.cov.bend	SWV	AA	5.00×10^{-6}	[336]
MWCNT/B-CD modified GCE	SWV	AA	6.70×10^{-6}	[337]
Fe_3O_4/rGO/GO	SWV	AA	1.20×10^{-7}	[338]
GCE/MWCNT-NiO	SWV	AA	7.99×10^{-12}	This work
GCE/MWCNT-ZnO	SWV	AA	3.74×10^{-7}	This work
GCE/MWCNT-Fe_3O_4	SWV	AA	1.39×10^{-6}	This work

4.1.6 Interference study: Detection of DA in the presence of AA

Figure 4,14 is the cyclic voltammetric responses of (a) bare GCE (b) GCE-MWCNT-ZnO, (c) GCE-MWCNT-NiO and (d) GCE-MWCNT-Fe_3O_4 in 0.1 M pH 7.0 PBS containing mixture of 10^{-2} M AA, approximately 1000 times concentration of DA. On the bare electrode the detection of DA in the presence of AA was not successful (Figure 4.14a). That is, AA signal interferes with the DA signal thus no signal separation for the two analytes. However at the GCE-MWCNT-MO modified electrodes, AA signal which was initially observed at 0.05 V in the absence of DA remained at the same potential after the addition of DA, while the DA signal was observed at 0.25 V. The simultaneous detection of AA and DA even at AA concentration (9.09 mM) which is 1000 times as high as DA concentration (9.09 µM) was successful at the GCE-MWCNT-MO electrodes with potential separation of about 170 mV, 190 mV and 150 mV observed at GCE-MWCNT-NiO, GCE-MWCNT-ZnO and GCE-MWCNT-Fe_3O_4 electrodes respectively. The height and amplitude of the peak corresponding to DA signal increases as the concentration DA increases. The simultaneous determination of DA in the presence of AA has also been carried out using more sensitive techniques such as differential pulse voltammetry (DPV) (Figure 4.15), square wave voltammetry (SWV) (Figure 4.16) and chronoamperometric (CA) techniques (Figure 4.17). A well resolved signal difference at large enough potential peak separation was observed for the modified

electrodes using SWV and DPV respectively as compared to CV. For example using SWV, potential peak separation of about 200 mV, 500 mV and 250 mV observed at GCE-MWCNT-NiO, GCE-MWCNT-ZnO and GCE-MWCNT-Fe_3O_4 electrodes respectively, while DPV gave peak separation of 400 mV, 300 mV and 600 mV observed at GCE-MWCNT-NiO, GCE-MWCNT-ZnO and GCE-MWCNT-Fe_3O_4 electrodes respectively. Figure 17 represent the amperometric measurements recorded at an applied potential of +0.20 V vs. Ag/AgCl on MWCNT-NiO, GCE-MWCNT-ZnO and GCE-MWCNT-Fe_3O_4 modified electrodes by continuous addition 1 mL DA and AA respectively. From the chronoamperometric study, there is no significant change in DA current response after addition of different concentration of ascorbic acid (AA). GCE-MWCNT-NiO and GCE-MWCNT-ZnO gave comparable DA recovery current compare with GCE-MWCNT-Fe_3O_4.

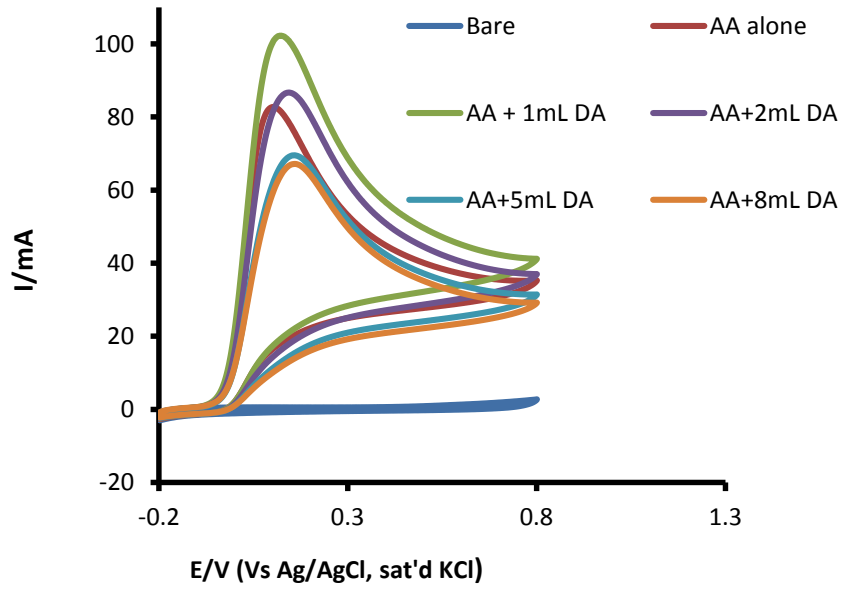

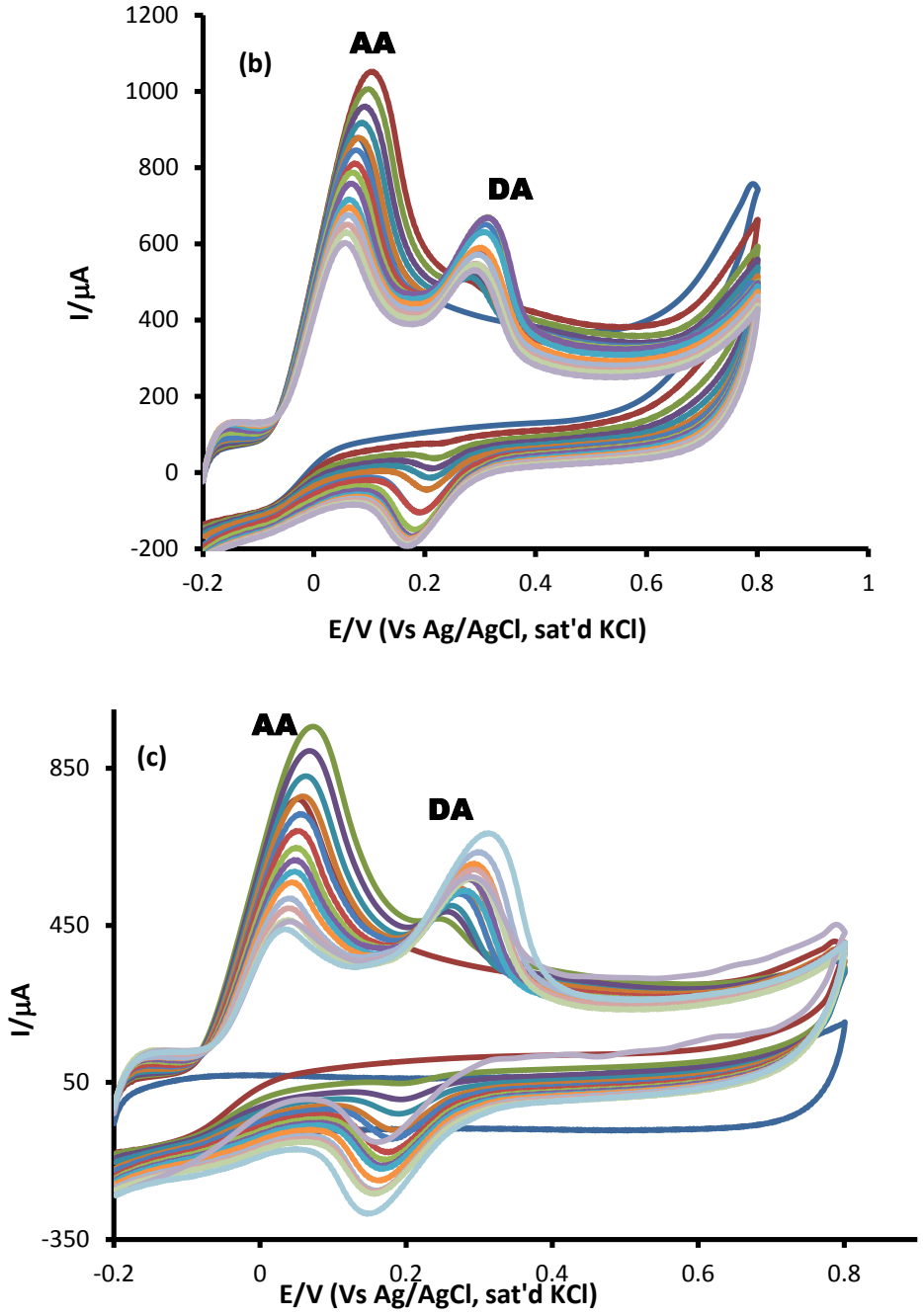

Figure 4.14**:** Cyclic voltammograms responses of: (a) bare GCE in PBS (pH 7.0), 10^{-2} M AA alone and 10^{-2} M AA + different volume of 10^{-4} M DA solutions; (b) GCE-MWCNT-ZnO, and (c) GCE-MWCNT-NiO in (i) 0.1M pH 7.0 PBS (ii) 10^{-2} M AA alone, (iii) mixture of 9.09 mM AA/ 9.09 µM DA, (iv) mixture of 8.33 mM AA /16.7 µM DA (v) mixture of 7.69 mM AA / 23.0 DA µM (vi) 7.14 mM AA/28.6 µM DA (vii) 6.67 mM AA/ 33.0 µM DA (viii) 6.25 mM AA / 37.5 µM DA (ix) 5.88 mM AA/ 41.2 µM DA (x) 5.56 mM AA / 44.0 µM DA (xi) 5.2 mM AA / 47.0 µM DA and (xii) 5 mM AA / 50 µM DA concentrations.

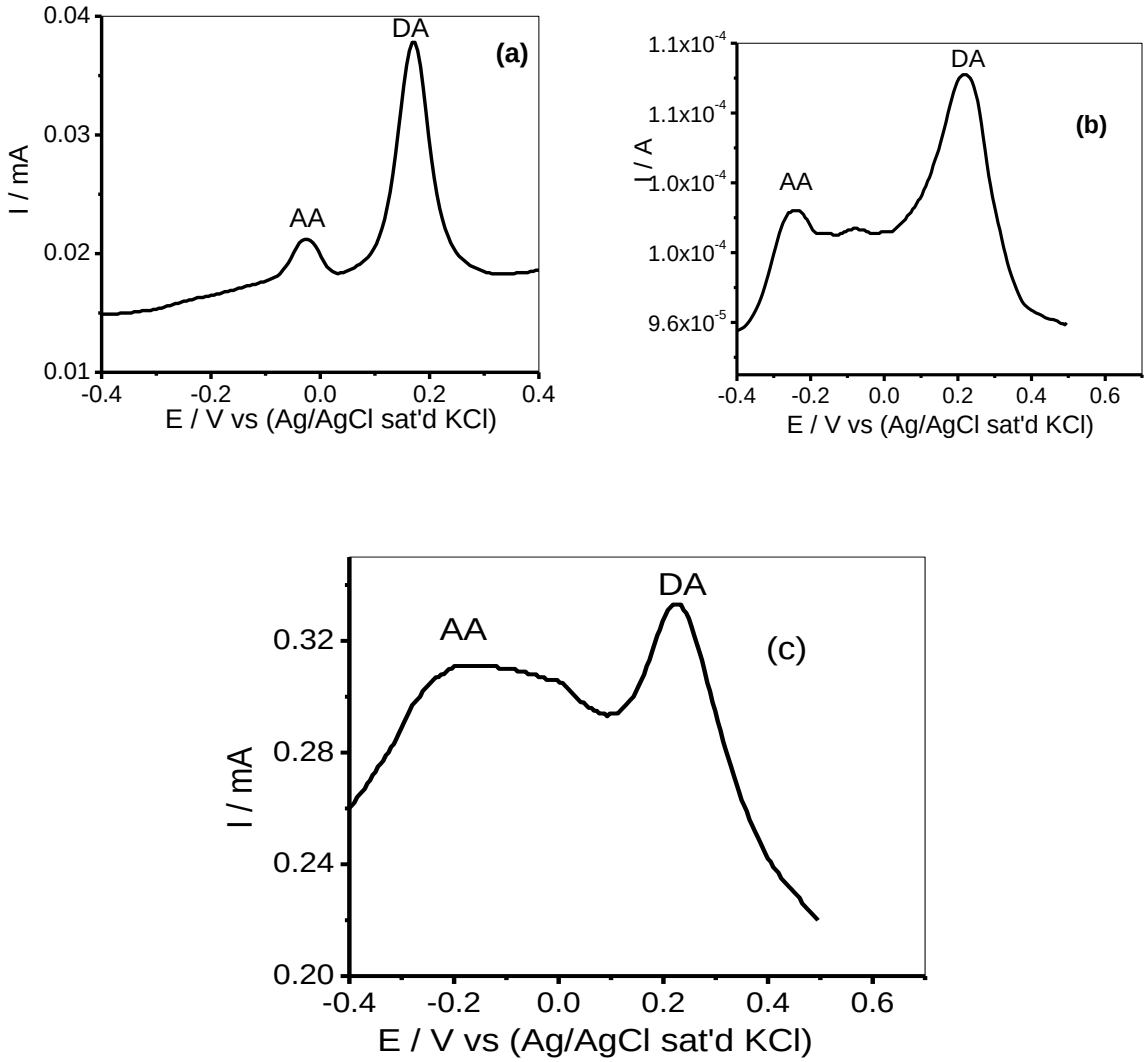

Figure 4.15: DPV profiles of (a) GCE-MWCNT-NiO, (b) GCE-MWCNT-ZnO and (c) GCE-MWCNT-Fe_3O_4 in pH 7.0 PBS containing 10^{-2} M AA and 10^{-4} M DA solutions respectively.

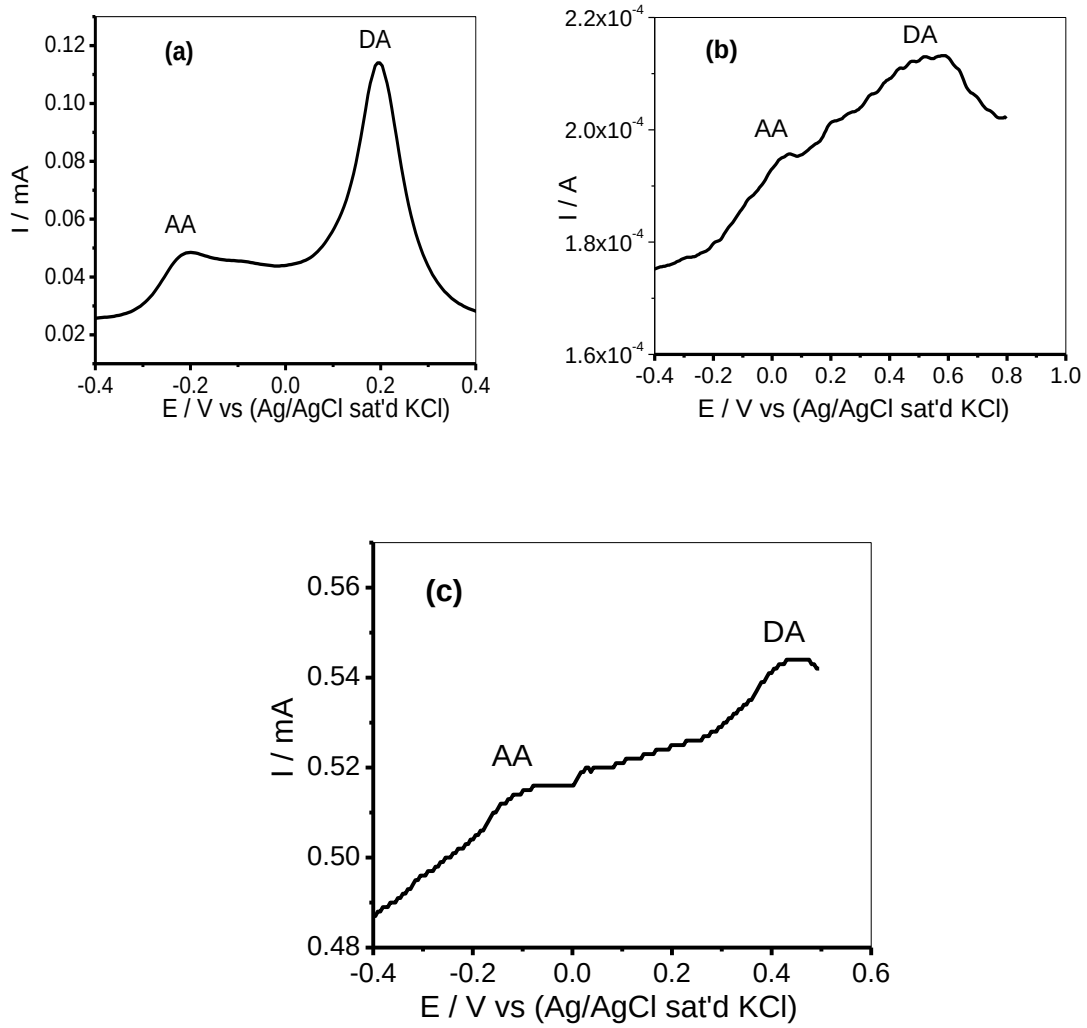

Figure 4.16: SWV profiles of (a) GCE-MWCNT-NiO, (b) GCE-MWCNT-ZnO and (c) GCE-MWCNT-Fe_3O_4 in pH 7.0 PBS containing 10^{-2} M AA and 10^{-4} M DA solutions respectively.

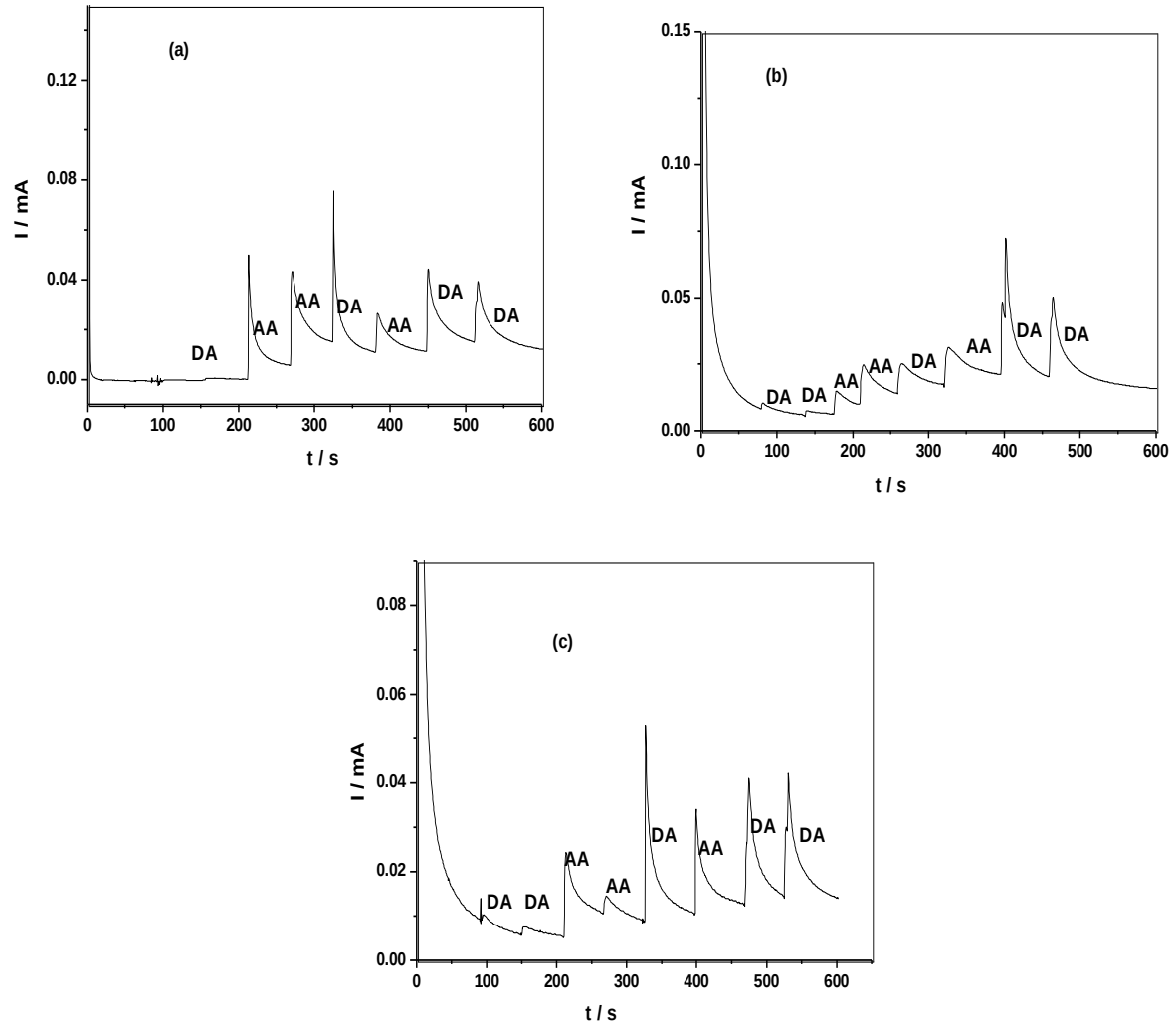

Figure 4.17: Chronoamperometric curves of (a) GCE-MWCNT-NiO, (b) GCE-MWCNT-ZnO and (c) GCE-MWCNT-Fe_3O_4 in pH 7.0 PBS containing 10^{-4} M DA and different concentration of AA (1000 times DA concentration).

4.1.7 Analytical performance of the proposed sensors for determination of DA in pharmaceutical sample

The proposed sensors were tested for determination of DA in dopamine hydrochloride injection samples. The SWV method was used for the determination of DA in Pharmaceutical samples. The samples were prepared and adjusted to 3.5 x 10^{-4} M DA in 0.1 M PBS (pH 7.0), by dilution of DA ampoule contents (2.5 mL of 40 mg/mL DA hydrochloride injection solution). The standard addition experiment was carried out by addition of different concentrations of DA to the drug sample and its DA concentration evaluated using SWV. The obtained equations for the plot of peak current versus concentration of DA (graph not shown) are:

$I_{pa}(\mu A) = 0.0004DA - 0.0008; \quad R^2 = 0.9999$ (GCE-MWCNT-NiO)

$I_{pa}(\mu A) = 0.00005DA - 0.0006; \quad R^2 = 0.9815$ (GCE-MWCNT-ZnO)

$I_{pa}(\mu A) = 0.0004DA - 0.0009; \quad R^2 = 0.9999$ (GCE-MWCNT-Fe_3O_4)

The analytical results obtained are presented in Table 4. 4. The result clearly indicates that dopamine can be reliably assayed from its drug using the proposed GCE-MWCNT-MO sensor.

Table 4.4: Results of detection of DA in dopamine hydrochloride injection (n=5).

Electrode	Added (mg/mL)	Detected (mg/mL)	Recovery (%)	RSD %
GCE-MWCNT-NiO	40	44.9	112.4	0.10
GCE-MWCNT-ZnO	40	39.1	97.8	0.13
GCE-MWCNT-Fe_3O_4	40	36.1	90.3	0.3

4.2 METAL OXIDE NANOPARTICLES / MULTI-WALLED CARBON NANOTUBE NANOCOMPOSITE MODIFIED ELECTRODE FOR THE DETECTION OF SEROTONIN

5-Hydroxytryptamine (serotonin (SE)) is an important and major biogenic monoamine neurotransmitter as well as neuromodulator [327], which are largely distributed in human brain and makes an important contribution in wide variety of biological, physical, psychopathological processes including sleep regulation, depression, eating disorder, alcoholism, infantile autism, anxiety disorders, muscle contraction, liver regeneration, endocrine regulation, obsessive – compulsive disorder and psychosis [328, 329]. Therefore on this note the determination of SE is instructive in the diagnosis of various diseases and hence makes it the subject of biologically and pharmacologically oriented research [330]. To date, a variety of analytical methods such as spectrophotometry [331], fluorometry [332-334], enzyme immunoassay [335, 336], radioimmunoassay [337], capillary electrophoresis (CE) [338] and GC–MS [339], have been developed for the determination of serotonin. Serotonin is usually assayed by HPLC with either electrochemical or fluorometry detection [340, 341]. However, these reported techniques are expensive and require time-consuming derivatization step and also in some cases low sensitivity and selectivity makes them unsuitable for a routine analysis and also with the fact that the concentration of SE is very low in biological systems. The other problem which must be solved in the electrochemical detection of SE is the co-existence of many interfering compounds in biological systems. Among these interfering compounds, ascorbic acid (AA), and dopamine (DA) are particularly important because they can all be oxidized at similar potentials resulting in overlap of voltammetric responses. The oxidation potential of SE (0.38 V at pH 7) is close to that of DA (0.22 V) and AA (0.2 V) on the unmodified glassy carbon electrodes. To overcome these problems, one of the most common ways is using a modified electrode to improve the measuring sensitivity of serotonin (SE) and remove the interference of ascorbic acid (AA) and dopamine (DA) to SE

detection. Therefore, different electrochemical methods using various modified electrodes were also proposed for the determination of (SE).

There are several literatures on the electro-oxidation of serotonin on modified electrodes [342-349]. For example, Rajendra et al. developed a gold nanoparticles modified ITO (Au/ITO) electrode using electrochemical method and used it for the detection of dopamine and serotonin in the presence of a high concentration of ascorbic acid [350]. Kangbing et al. reported a chemically modified electrode based on the carbon nanotube film–coated glassy carbon electrode (GCE) for the simultaneous determination of dopamine (DA) and serotonin (5-HT) and lowers oxidation over potentials [351]. In similar attempt, Zong-hua et al. reported that multiwall carbon nanotube (MWNT) film–coated GCE exhibits a marked enhancement effect on the current response of DA and 5-HT [352].

Despite this huge literature, the use of carbon nanotubes and nylon 6,6 nanofiber nanocomposites decorated with metal oxide nanoparticle is limited and to the best of our knowledge, no consideration has been given to this type of investigation, whereby the synergy between three different metal oxides (NiO, ZnO and Fe_3O_4) and multi-walled carbon nanotubes and nylon 6,6 nanofiber nanocomposites towards serotonin detection in the presence of interfering molecules such as ascorbic acid was investigated.

4.2.1 Electrocatalytic response of the modified electrodes towards the oxidation of serotonin (SE)

Scheme 4.3 shows the schematic diagram of the electrochemical response of the GCE-MWCNT-MO electrodes in 5 mM $Fe(CN)_6]^{4-}$/$[Fe(CN)_6]^{3-}$ prepared in 0.1 M PBS (pH 7.0) and in 0.1 mM SE prepared in 0.1 M PBS (pH 7.0).

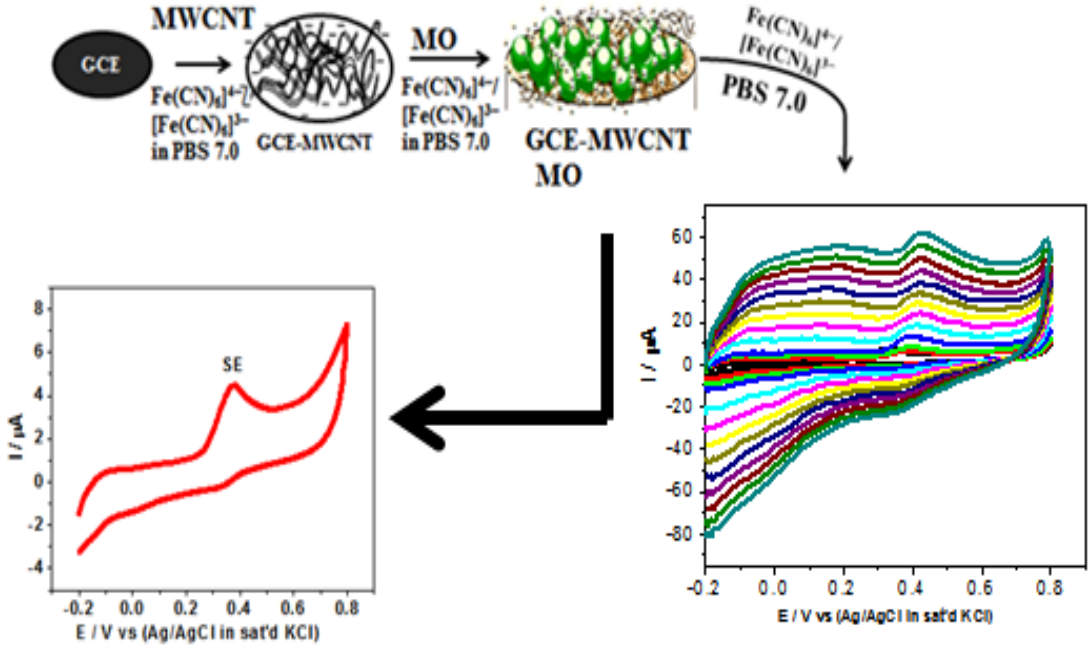

Scheme 4.3. Schematic diagram showing electrode modification procedure and the electrocatalytic behavior of the GCE-MWCNT-MO electrodes towards oxidation of serotonin.

The electrochemical behaviour of different modified electrodes in the presence of 0.1 mM SE in 0.1 M PBS (pH 7.0) was investigated by cyclic voltammetric (CV) technique at a scan rate of 25 mV/s and presented in Figure 4.18. All the electrodes showed well defined serotonin oxidation peak at potential > 0.35 V. From the CV obtained, serotonin oxidation current (and oxidation potential) are 4 μA (0.38 V) at the bare GCE, 5.8 μA (0.36 V) at GCE-NiO, 5 μA (0.38 V) at GCE-ZnO and 5μA (0.38 V) at GCE-Fe_3O_4 electrodes respectively. The result clearly indicate that there is no significant difference in SE oxidation current at bare GCE electrode compared with the GCE-MO (MO = NiO, ZnO and Fe_3O_4) modified electrodes.

However, the GCE-MWCNT-NiO, GCE-MWCNT-ZnO and GCE-MWCNT-Fe_3O_4 showed higher current response (at around 0.38 V) than that of the bare and other modified electrodes and these results indicate that the GCE-MWCNT-MO electrodes have better electrocatalytic activity and demonstrated enhance current response towards SE (Figure 4.18a-c). After background current subtraction (Figure 4.18d), SE current response on the GCE-MWCNT-MO electrodes follow the order: GCE-MWCNT-NiO (309.85 μA) > GCE-MWCNT-ZnO (128.53 μA) > GCE-MWCNT-Fe_3O_4 (118.7 μA). These current are in the order of 77, 32 and 30 times higher than SE current at bare GCE electrode. Thus, GCE-MWCNT-NiO electrode demonstrated the best electrocatalytic behavior towards SE oxidation. Similar results have been obtained and reported in literature for modified electrodes [342-349]. For example, Kangbing et al. reported simultaneous determination of dopamine (DA) and serotonin (5-HT) at lower oxidation over potentials using carbon nanotube film–coated glassy carbon electrode (GCE) [343]. Zong-hua et al. reported that multiwall carbon nanotube (MWNT) film–coated GCE exhibits a marked enhancement effect on the current response of DA and 5-HT [344].

The enhanced SE current at the nanocomposite modified electrodes can be attributed to the high electrical conductivity of the metal oxide nanoparticles and the MWCNT, large porous surface area created by the MWCNT for easy diffusion of the analyte and electrolyte in and out of the electrode surface, uniform structure of the nanocomposite, improved catalytic properties of the surface electroactive materials due to the synergy between MWCNT and the metal oxide nanoparticles and biocompatibility of the nanocomposite with the analyte [362, 363-365]. It is believed that the existence of MWCNT is an ideal support material and acts as an effective electron promoter for electrocatalytic oxidation of SE [343, 344]. Since GCE-MWCNT-MO electrodes gave better SE electrochemical response, further studies are carried out using this electrodes platform.

Impedance studies were also carried out to monitor the mechanism of the electron process at the electrode-electrolytes interface during the electrocatalytic oxidation of 10^{-4} M SE at fixed potential 0.2 V and frequencies between 10 kHz and 1.0 Hz. The impedance spectra (Nyquist plots) obtained for the electrodes are presented in Figures 4.19a-c, while Figure 4.19d shows the equivalent circuits used in the fitting of the impedance data. The GCE modified electrodes were successfully fitted with minimum error values (Table 4.5). In the circuit model (Figure 4.19d), R_s is the solution resistance, C_{dl} is the double layer capacitance, R_{ct} is the charge transfer resistance and Q is the constant phase element. The R_{ct} value is lower at GCE-MWCNT-NiO (54.2 Ω), GCE-MWCNT-ZnO (57.2 Ω) and GCE-MWCNT-Fe_3O_4 (63.4 Ω) electrodes compared with the bare GCE (100.2 Ω), GCE-NiO (115.2 Ω), GCE-ZnO (144.4 Ω) and GCE-Fe_3O_4 electrodes. The result further confirms that MWCNT-MO nanocomposite can form a good electron pathway between electrode and electrolyte/analyte during electrocatalytic oxidation of serotonin compared with the bare GCE or GCE-MO modified electrodes. Therefore, the electron transfer process is fastest at GCE-MWCNT-NiO electrode and follow the order, GCE-MWCNT-NiO > GCE-MWCNT-ZnO > GCE-MWCNT-Fe_3O_4 for the GCE-MWCNT-MO modified electrodes. This results is also in good agreement with SE oxidation peak current values obtained from the CVs experiment discussed above where GCE-MWCNT-NiO > GCE-MWCNT-ZnO (57.2 Ω) > GCE-MWCNT-Fe_3O_4. The MWCNT creates a porous and large surface area that mediates the analyte /catalyst electrocatalytic process. Similar results have been reported for chemically modified electrodes [353]. Since GCE-MWCNT-MO electrodes gave better SE electrochemical response, further studies are carried out using this electrodes platform.

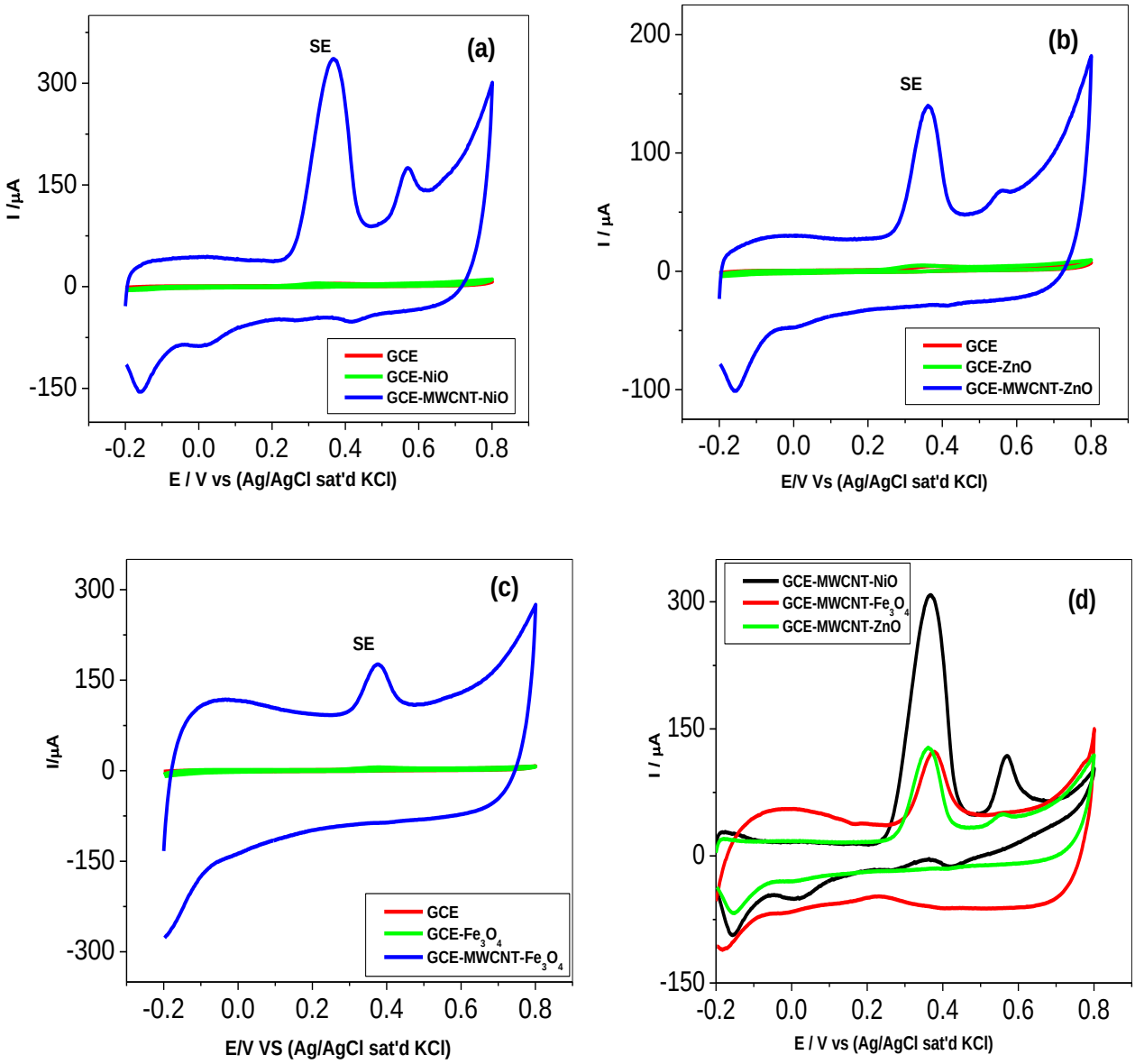

Figure 4.18: Cyclic voltammograms of GCE and (a) GCE-NiO, GCE-MWCNT-NiO, (b) GCE-ZnO, GCE-MWCNT-ZnO and (c) GCE-Fe_3O_4, GCE-MWCNT-Fe3O4 in pH 7.0 PBS containing 0.1 mM SE at a scan rate of 25 mV/s. (d) Comparative current response of GCE-MWCNT-NiO, GCE-MWCNT-ZnO and

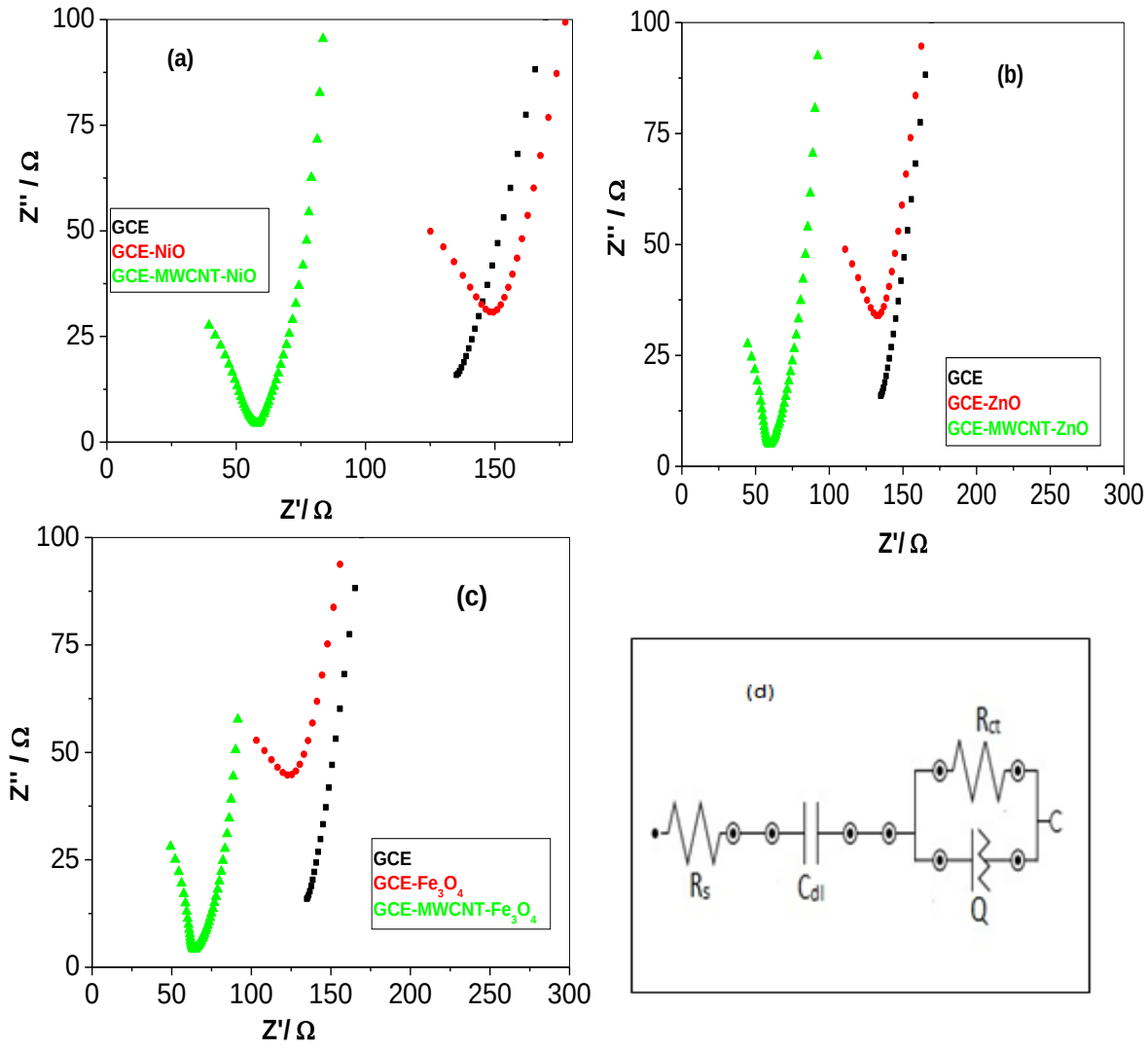

Figure 4.19: Typical Nyquist plots (a-c) obtained for the electrodes in 0.1 mM SE solution (PBS pH 7.0) at a fixed potential of 0.2 V (vs. Ag|AgCl, saturated KCl) (d) represents the circuit used in the fitting of the EIS data (a-c).

Table 4.5: Charge transfer resistance values for the electrodes in 0.1 mM SE in pH 7.0 PBS (at Ag/AgCl saturated KCl). Note that the values in parenthesis are percentage errors of the data fitting.

Electrodes	**Electrochemical impedance spectroscopy data**			
	R_s (Ω)	Q (x10 nF)	R_{ct} (Ω)	C (n F)
GCE	134.70 (1.28)	1.19(2.52)	100.2 (16.23)	1.99 (8.39)
GCE-NiO	59.40 (12.36)	1.89(1.08)	115.2 (8.912)	123.30 (16.28)
GCE-ZnO	49.60 (14.05)	1.73 (1.13)	144.4 (11.64)	134.70 (16.51)
GCE-Fe_3O_4	45.10 (12.79)	1.21 (1.01)	99.2 (4.59)	149.30 (14.17)
GCE-MWCNT-NiO	2.28 (100)	2.65 (4.36)	54.2 (7.19)	234.80 (15.58)
GCE-MWCNT-ZnO	6.62 (0.00)	2.12 (4.19)	57.2 (10.46)	184.20 (22.26)
GCE-MWCNT-Fe_3O_4	19.99 (100)	5.16 (4.09)	63.4 (8.56)	144.40 (18.09)

4.2.1.1 Effect of scan rate on the electrocatalytic oxidation of serotonin (SE) at modified electrode

The influence of scan rate on the electrochemical response of SE at GCE-MWCNT-MO electrodes was investigated by cyclic voltammetry, and the results are shown in Figure 4.20. The oxidation peak currents gradually increased with increasing scan rate in the range of 25-500 mV/s (Figures 4.20a-c). When the peak current (I_{pa}) was plotted against the square root of scan rate ($v^{1/2}$), a linear relationship with a regression coefficient > 0.98 was obtained for the GCE-MWCNT-MO electrodes (Figures 4.20d-f). This behaviour suggests that the oxidation of SE at the modified electrodes GCE-MWCNT-NiO, GCE-MWCNT-ZnO and GCE-MWCNT-Fe_3O_4 is diffusion controlled. A positive shift of the anodic peak potential (E_{pa}) with increase in scan rate was also observed in Figure 4.20. The apparent charge transfer rate constant (k_s) and the charge transfer coefficient (α) of a surface-confined redox couple can be evaluated from cyclic voltammetric results, and by using the variation of anodic peak potentials with logarithm of scan rate. It was found that E_{pa} increased linearly

with ln (scan rate) (graph not shown). The number of electrons involved in the reaction can be calculated according to the Laviron's equation [354]. Accordingly, the slope (b) of the E_p vs. ln(v) plot is represented in equation 4.2,

$$b = 2.3RT/n\alpha F \qquad (4.2)$$

Where b is the slope. The values of the charge transfer coefficient (α) of GCE-MWCNT-NiO, GCE-MWCNT-ZnO and GCE-MWCNT-Fe_3O_4 electrodes were calculated as 0.55 0.96 and 0.49 respectively. The obtained value for n is approximately 1, which indicates that one electron is involved in the oxidation of serotonin. The electrode reaction standard rate constant (ks) for the modified electrodes were obtained by using equation 4.1 to be equal to 0.27, 0.47 and 0.52 cms^{-1} for GCE-MWCNT-NiO, GCE-MWCNT-ZnO and GCE-MWCNT-Fe_3O_4 electrodes respectively.

According to the kinetics of electron process, when the rate constant is larger than 10^{-2} cm/s, the electron transfer process is very fast, and the electrode reaction is reversible, and when $10^{-4} < k_s < 10^{-2}$ cms^{-1}, the electrode reaction is a quasireversible process [354]. So the electrode reaction of SE on the proposed electrodes is reversible process.

In order to get information on the rate determining step. The peak potential, E_p, is proportional to log v (graph not shown). The slopes of E_p *vs.* log *v* for the different electrodes are 0.0617, 0.1083, and 0.1217 V for electrodes GCE-MWCNT-NiO, GCE-MWCNT-ZnO and GCE-MWCNT-Fe_3O_4 respectively. The Tafel slopes (b) may be estimated according to the equation (4.4, chapter 4) for totally irreversible diffusion controlled process [324]. So, the values of *b* for GCE-MWCNT-NiO, GCE-MWCNT-ZnO and GCE-MWCNT-Fe_3O_4 electrodes are 123, 216 and 243 $mVdec^{-1}$ respectively.

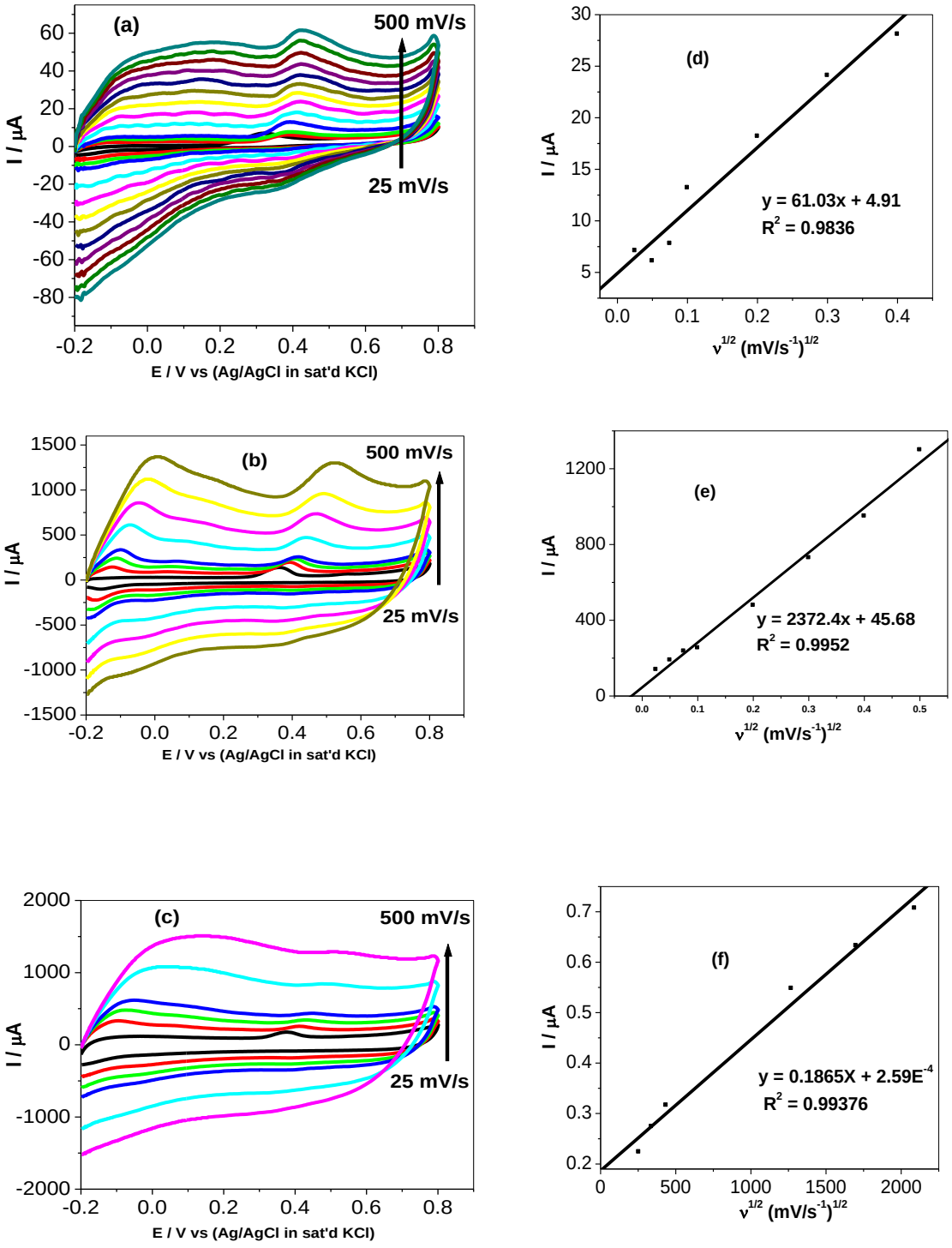

Figure 4.20: Effect of scan rate (25 – 500 mVs^{-1}) on the cyclic voltammograms of (a) GCE-MWCNT-NiO (b) GCE-MWCNT-ZnO and (c) GCE-MWCNT-Fe_3O_4 in 0.1 mM SE. The plots of current (I) against square root of scan rate (ν^2) are presented in Figure 8(d-f) for GCE-MWCNT-NiO, GCE-MWCNT-ZnO and GCE-MWCNT-Fe_3O_4 electrodes respectively.

These Tafel values are higher than the theoretical value of 118 $mVdec^{-1}$ for a one-electron process involved in the rate-determining step. Therefore, higher Tafel values are attributed to the adsorption of reactants or intermediates on the electrode surfaces, or reaction occurring within porous electrode structure [325]. The result further confirm the porous nature of the GCE-MWCNT-MO modified electrodes which despite their porous and adsorptive nature gave better performance towards SE oxidation in terms of oxidation potential, current recovery, stability and resistance to fouling effects.

4.2.2 Electroanalysis of serotonin (SE)

Concentration study was carried out in PBS (pH 7.0) containing 5 x 10^{-6} µM to 2.30 µM serotonin (SE) using square wave voltammetry (SWV) measurements. The result obtained is represented with the Square wave voltammogrammes of GCE-MWCNT-Fe_3O_4 (Figure 4.21a). Inset in Figure 4.21a is plots of current (I) against concentration of SE using GCE-MWCNT-Fe_3O_4, while Figure 4.21b is the linear plots of current (I) against concentration of SE (5 x 10^{-6} µM to 2.30 µM) at GCE-MWCNT-NiO electrode.

From Figure 4.21, the dependence of the oxidation peak currents on the concentration of SE showed that the anodic peak current increased as the concentration of serotonin (SE) increases. The detection limit was calculated based on the relationship LoD = 3.3 δ /m where δ is the relative standard deviation of the intercept of y-coordinates from the line of best fit, and m is the slope of the same line [294]. The obtained limit of detection and the sensitivity of the modified electrodes are 50.8 nM (2.0 x 10^{-4} µA/µM), 60.6 x nM (42.468 µA/µM) and 10.9 x 10^{-8} M (10.248 µA/µM) for GCE-MWCNT-NiO, GCE-MWCNT-ZnO and GCE-MWCNT-Fe_3O_4 sensors respectively.

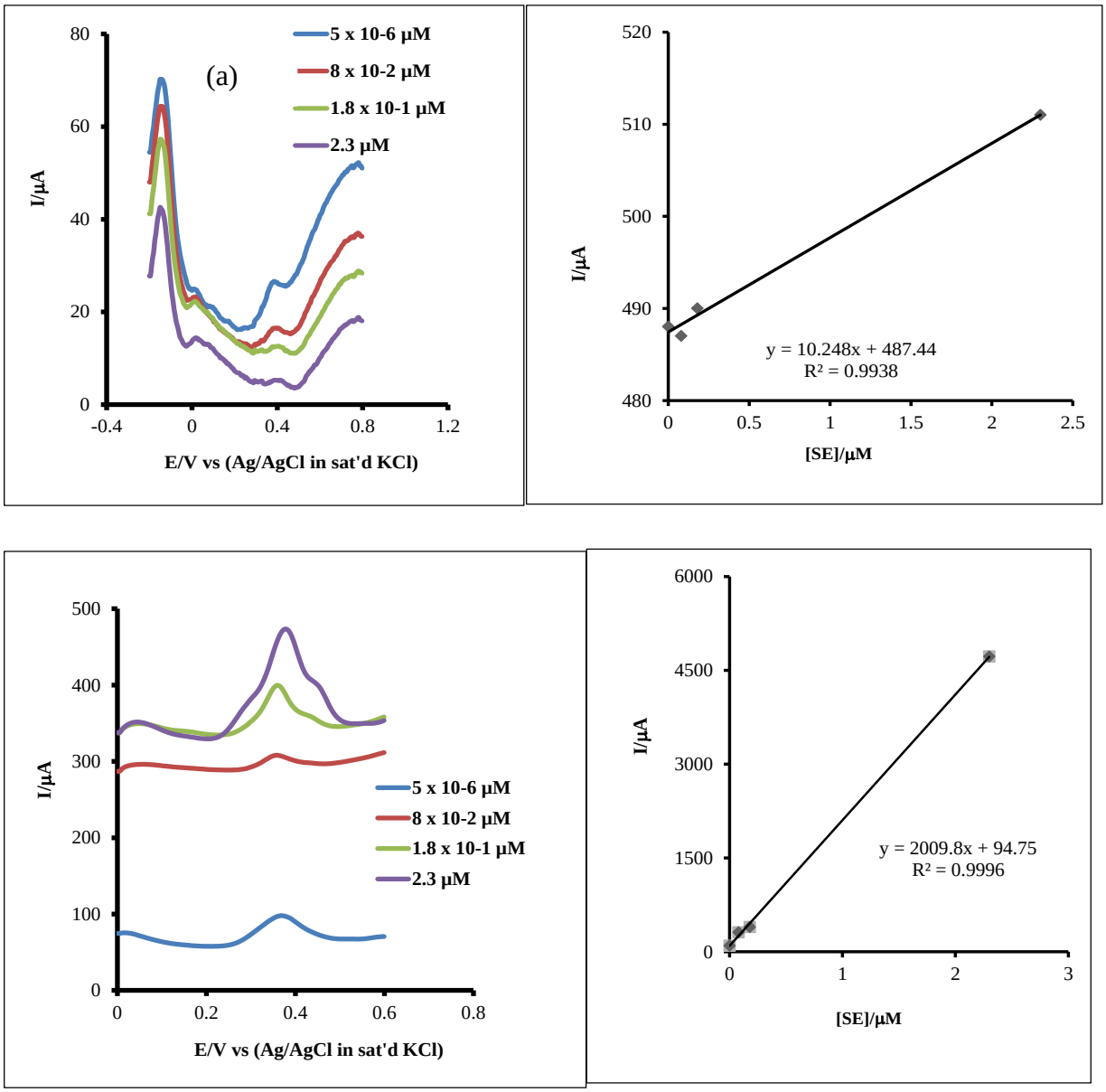

Figure 4.21: Square wave voltammogrammes of (a) GCE-MWCNT-Fe_3O_4 in PBS pH 7 containing 5 x 10^{-6} µM to 2.30 µM SE concentration (Inset is plots of current (I) against concentration of SE) and (b) GCE-MWCNT-NiO in PBS pH 7 containing 5 x 10^{-6} µM to 2.30 µM SE concentration (Inset is plots of current (I) against concentration of SE).

Table 4.6: Comparison of different electrochemical sensors for the determination of serotonin.

Electrode material	Techniques	Ep(V) (Ag/AgCl)	Detection Limit (M)	References
GCE(OX)	SWV	0.4	3×10^{-8}	[368]
TPyP-31P/FTO	CVs	0.2	2.2×10^{-4}	[369]
F-MWCNTs/BR9	DPV	0.21	9.0×10^{-6}	[370]
GN-SPEs	CVs	0.28	1.0×10^{-4}	[371]
GCE/MWCNT-NiO	SWV	0.36	50.8×10^{-9}	This work
GCE/MWCNT-ZnO	SWV	0.37	60.6×10^{-9}	This work
GCE/MWCNT-Fe_3O_4	SWV	0.38	10.9×10^{-8}	This work

The performances of the present electrochemical sensors were compared with those reported in the literatures (Table 4.6). The low-detection-limit (at nano molar SE concentration) obtained in the present study compare favourably and even better than previously reported limit of detection for SE using various electrochemical methods with different modified electrodes (Table 5.2) [355 – 358]. Since the concentration of serotonin in healthy human is in the range of 0.5 to 1.4 mM [359], the present sensor system with a low-detection-limit (at nano concentration) especially GCE-MWCNT-NiO and GCE-MWCNT-ZnO are well suitable for the analysis of serotonin in diluted physiological samples. The present sensor system was then subjected to stability and interference studies and for the determination of serotonin directly from physiological samples (urine).

4.2.3 Stability and reproducibility of the modified Electrodes

The stability of the modified electrodes (GCE-MWCNT-NiO, GCE-MWCNT-ZnO and GCE-MWCNT-Fe_3O_4) towards determination of serotonin (SE) was examined by measuring the current response at fixed concentration of SE (2×10^{-4} M) in pH 7.0 PBS (not shown). The

electrodes were repetitively scanned (20 scans) in a 2×10^{-4} M serotonin at 25 mVs^{-1}. A decrease in peak currents (<10%) was usually observed for the three composite modified electrodes after the first scan, which is a typical behaviour for a poisoned electrode. However, on rinsing the electrodes in a fresh PBS (pH 7.0) solution, the electrode surface was renewed and more than 95% of the initial catalytic current was obtained, indicating the electrochemical stability and reusability of the electrode after analysis. Similarly, after storage for four weeks in a refrigerator, no significant change in serotonin current was observed which confirmed the electrode stability towards the analyte.

4.2.4 Interference study

Since serotonin (SE), dopamine (DA) and ascorbic acid (AA) have similar oxidation potentials at most solid electrodes, separate determination of these species is a great problem due to their overlapping signals. In order to establish a sensitive and selective discrimination between SE, DA and AA on our developed sensor, the electrochemical oxidation of the mixture containing these three species at the MWCNT-MO modified GCE was studied. As shown in Figure 4.22, the CV of the mixture solution containing DA and AA shows broad and overlapped anodic peaks at bare GCE, so the peak potentials for SE, DA and AA are indistinguishable and therefore, it is impossible to separate the analytes from the broad and overlapped voltammetric peak. However, at the GCE-MWCNT-MO, the overlapped voltammetric peak is resolved into three well-defined anodic peaks at about 0.37, 0.2 and 0.07 V (A), corresponding to the oxidation of SE, DA and AA respectively. The separations of peaks were 300 mV, 170 mV and 130 mV between SE and AA, SE and DA, and DA and AA, respectively, which were large enough to determine SE, DA and AA individually and simultaneously. Thus, the GCE-MWCNT-MO electrodes can conveniently detect SE in physiological medium without interference from DA or AA.

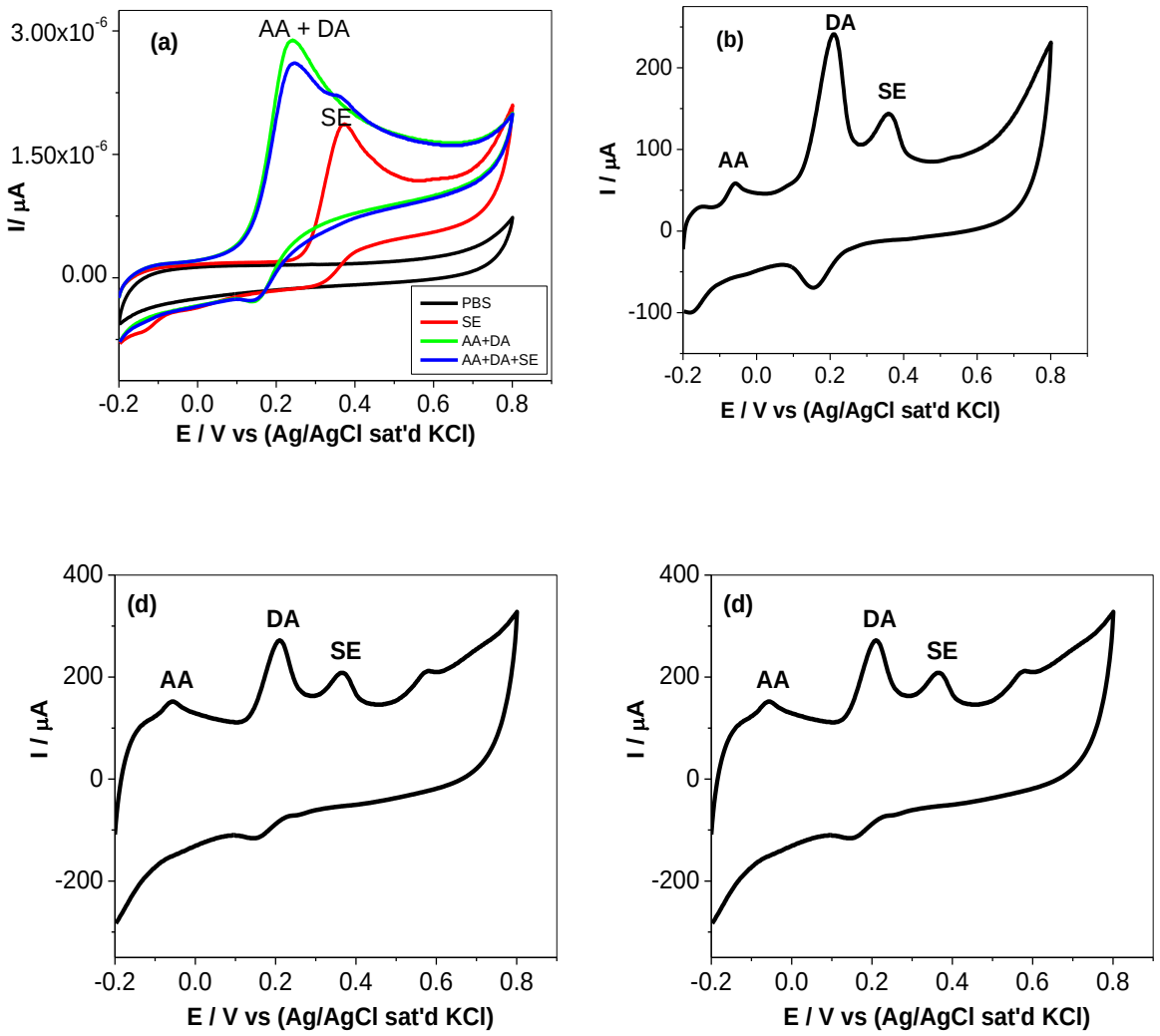

Figure 4.22: Cyclic voltammogram of $^{10\text{-}4}$ M of AA, DA and SE (in PBS pH 7.0) at (a) Bare GCE (b) GCE-MWCNT-NiO (c) GCE-MWCNT-ZnO and (d) GCE-MWCNT-Fe_3O_4 electrodes.

4.2.5 Determination of serotonin (SE) in human urine sample

Since SE concentration in urine is an important marker for various diseases and ageing related physiological conditions, it is considered necessary to detect these biomolecules in biological fluids [360] and therefore there are several literatures on its determination in urine samples [361, 362]. Also, whenever a compound is traceable in urine, sampling of urine always gets preference over blood sample due to its non-invasive nature. Hence the

developed method was applied for detection of SE in urine samples. For this purpose urine samples of laboratory personnel were collected for estimation of serotonin. Urine samples were diluted 200 times with 0.1 M phosphate buffer of pH 7.0 prior to analysis in order to reduce matrix complexity. Diluted urine samples were then spiked with different amounts of SE and the amounts of the analyte at GCE-MWCNT-NiO, GCE-MWCNT-ZnO and GCE-MWCNT-Fe_3O_4 were determined. The results obtained are presented in Table 5. 3. GCE-MWCNT-NiO and GCE-MWCNT-ZnO gave better recovery as compared with GCE-MWCNT-Fe_3O_4, and the result agreed with their detection limits towards SE. This result further confirmed the suitability and reliability of GCE-MWCNT-MO electrodes as a potential sensor for the analysis of SE.

Table 4.7: Recovery data for serotonin determination in human urine samples at modified GCE electrodes.

(A)

Sr.no/Electrode GCE-MWCNT-NiO	***Amount added* (mmol l^{-1})**	***Amount detected* (mmol l^{-1})**	***Recovery %***
1	2.00	2.28	114
2	2.00	2.20	110
3	2.00	2.08	104
4	2.00	2.20	110
The RSD % for n = 4 is 3.77%			

(B)

Sr.no/Electrode GCE-MWCNT-ZnO	**Amount added (mmol l^{-1})**	**Amount detected (mmol l^{-1})**	**Recovery %**
1	2.00	2.08	104
2	2.00	2.00	100
3	2.00	1.92	96
4	2.00	1.96	98
The RSD % for n = 4 is 3.43%			

(C)

Sr.no/Electrode GCE-MWCNT-Fe_3O_4	**Amount added (mmol l^{-1})**	**Amount detected (mmol l^{-1})**	**Recovery (%)**
1	2.00	1.92	96
2	2.00	1.84	92
3	2.00	1.92	96
4	2.00	1.96	98
The RSD % for n=4 is 2.64%			

4.3 METAL OXIDE NANOPARTICLES / Nylon 6, 6/MWCNT NANOCOMPOSITE MODIFIED ELECTRODE FOR THE DETECTION OF DOPAMINE AND SEROTONIN

4.3.1 Characterization of the electrodes

4.3.1.1 Morphological characterization

The surface morphology of the material was examined with SEM. The SEM images in Figure 4.23 show a change in morphology of the Nylon 6, 6 nanofibers before and after functionalization with zinc and iron oxide nanoparticles. From the images it is obvious that there is a change in the morphology and the diameter of the functionalized nylon nanofibers increases and varies from 298 nm to 350 nm compare to the unfunctionalized nylon 6,6 nanofibers [363]. The incorporation of multi-walled carbon nanotubes and metal oxide nanoparticles increased the viscosity and improved the conductivity of the solution. A more viscous solution produces thicker fibres and the increase in conductivity favours the stretching of thinner fibres [363].

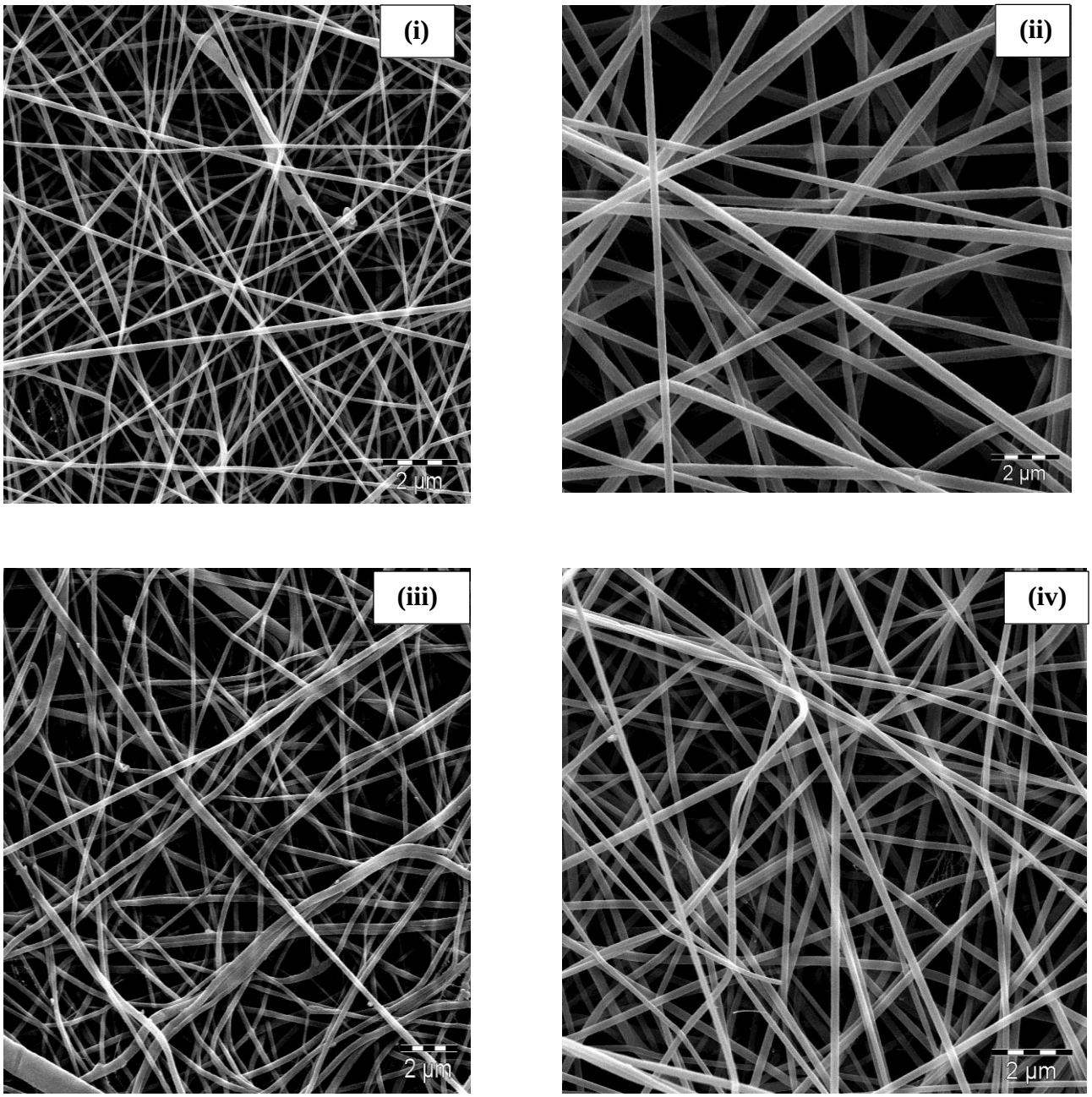

Figure 4.23: The typical SEM images of (i) Nylon 6,6 (ii) Nylon 6,6 /NiO (iii) Nylon 6,6 /ZnO and (iv) Nylon 6,6 /Fe_3O_4 nanofibers.

4.3.1.2 Fourier Transform Infra-Red Spectroscopy

The FTIR spectra for nylon 6, 6 nanofibers and their respective nanocomposites are shown in Figure 4.24 the Nylon 6, 6 nanofibers is characterized by O-H stretching vibration around 3950 cm^{-1}, N-H stretching vibration at 3317 cm^{-1}, C-H stretching vibration at 2939 cm^{-1} and CH_2 bond along with amide peaks at 1652, 1202, 1271 and 1363 cm^{-1} [364]. The band between 1582 – 1653 cm^{-1} can be attributed to vibration mode of C=C bonds of graphite in MWCNTs, while bands around 2920 and 2850 cm^{-1} are due to asymmetric and symmetric C–H stretching in the MWCNTs incoporated into the nylon 6,6/MO nanofiber [365]. The peaks between 700 - 500 cm^{-1} reveal the successful incorporation of NiO, ZnO and Fe_3O_4 nanoparticles in Nylon 6, 6 nanofibers [366].

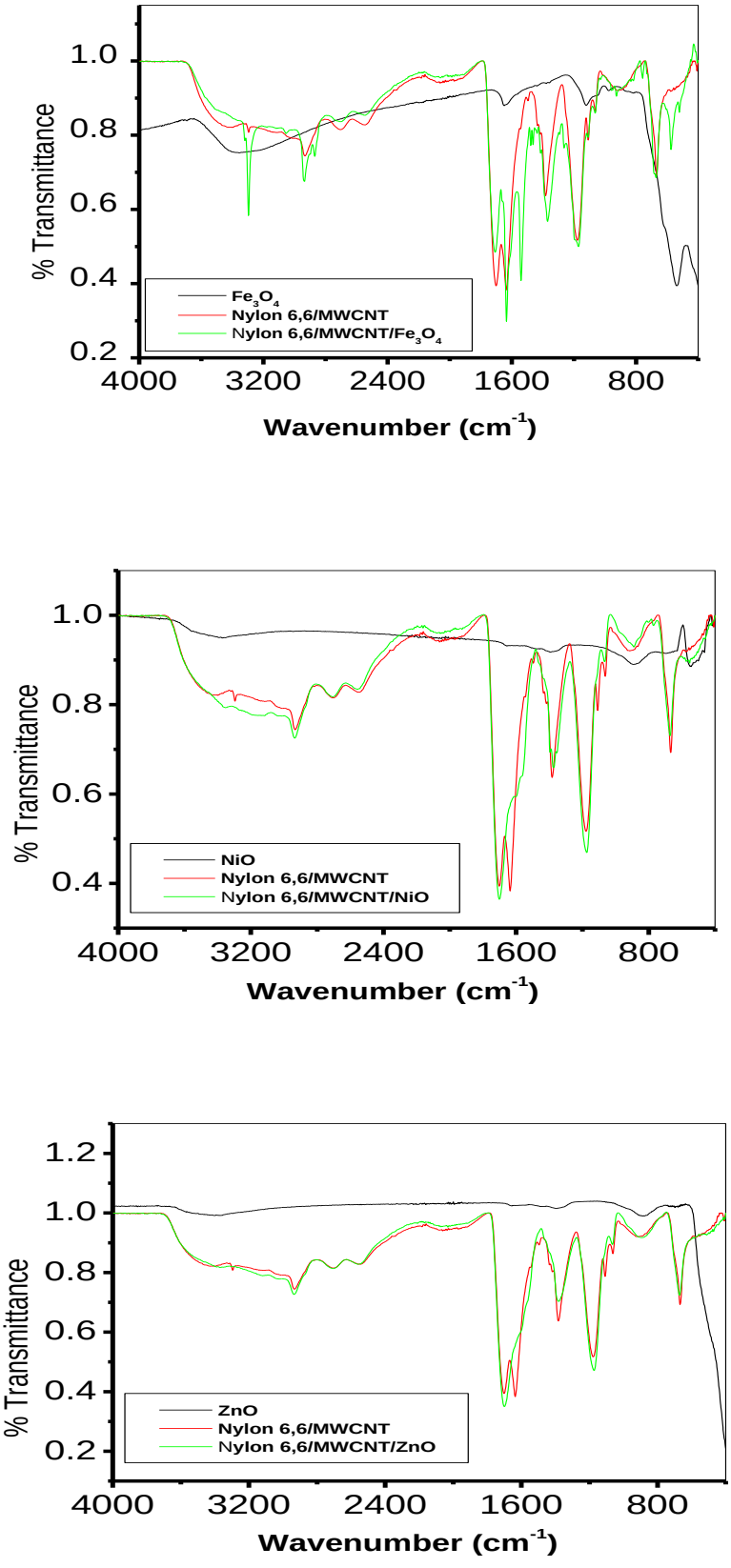

Figure 4.24: FTIR of Nylon 6,6/MWCNT, MO and Nylon 6,6/MWCNT/MO nanocomposites.

4.3.2 Electrochemical characterization of electrodes

To evaluate the charge transfer properties of the Nylon 6,6/MWCNT/MO modified electrodes where MO represents NiO, ZnO and Fe_3O_4 nanoparticles, we performed the cyclic voltammetry experiment for the modified electrodes in 5 mM $Fe(CN)_6]^{4-}/[Fe(CN)_6]^{3-}$ in 0.1 M PBS (scan rate, 25 mVs^{-1}) and the result is presented in Figure 4.25. Two pairs of redox peaks were observed at the modified electrodes (Figure 4.25). Only one redox peaks ranging from the regions of 0.0 to 400 mV is attributed to the $Fe(CN)_6]^{4-}/[Fe(CN)_6]^{3-}$ redox process. There were no observable peaks corresponding to Ni(II)/Ni(III), Zn(II)/Zn(III) and Fe(II)/Fe(III) redox processes on the nanocomposites of NiO, ZnO and Fe_3O_4 modified electrodes probably because of the faster electron transfer at the electrode, or overllap between the $Fe(CN)_6]^{4-}/[Fe(CN)_6]^{3-}$ peaks.

Therefore, the anodic current density of each electrode in $Fe(CN)_6]^{4-}/[Fe(CN)_6]^{3-}$ redox probe follows the order: Nylon 6,6/MWCNT/ZnO (17.80 $mAcm^{-2}$) > Nylon 6,6/MWCNT /NiO (16.97 $mAcm^{-2}$) > Nylon 6,6/MWCT/Fe_3O_4 (0.58 $mAcm^{-2}$). Therefore Nylon 6,6/MWCNT/ZnO has demonstrated the best electron transport properties with current density higher than that of Nylon 6,6/MWCNT /NiO and Nylon 6,6/MWCT/Fe_3O_4 electrodes.

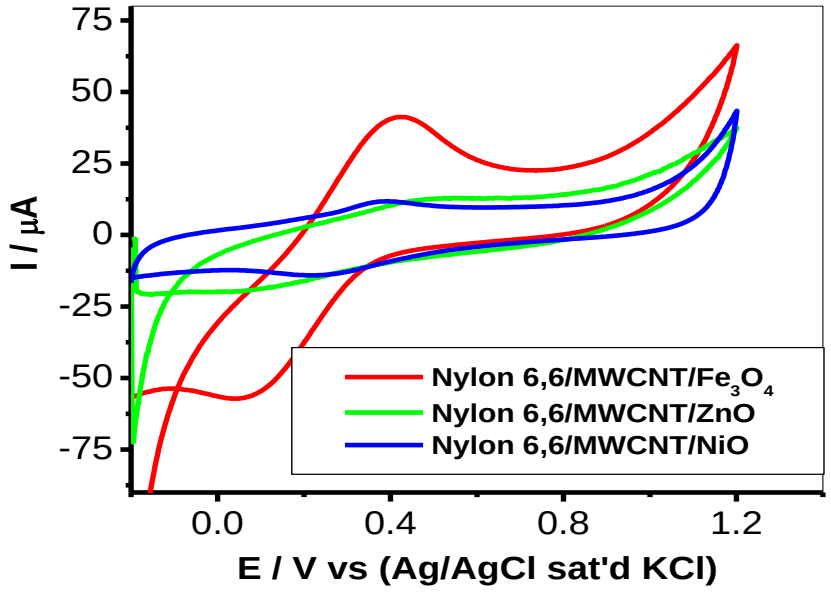

Figure 4.25: Comparative cyclic voltammogrammes for GCE/Nylon 6,6/MWCNT/NiO, GCE/Nylon 6,6/MWCNT/ZnO and GCE/Nylon 6,6/MWCNT/Fe_3O_4 at scan rate, 25 mVs^{-1} in 5 mM $Fe(CN)_6]^{4-}$/$[Fe(CN)_6]^{3-}$ solution prepared in 0.1M PBS (pH 7).

The scan rate study (scan rate, 25 – 1000 mVs^{-1}) of the Nylon 6,6 /MWCNT/MO electrode was carried out in 5 mM $Fe(CN)_6]^{4-}$/$[Fe(CN)_6]^{3-}$ solution prepared in 0.1M PBS (pH 7) using cyclic voltammetry experiment. Both anodic current (I_{pa}) and cathodic current (I_{pc}) increase with increase in scan rates (25 to 1000 mVs^{-1}) Figure 4.26.

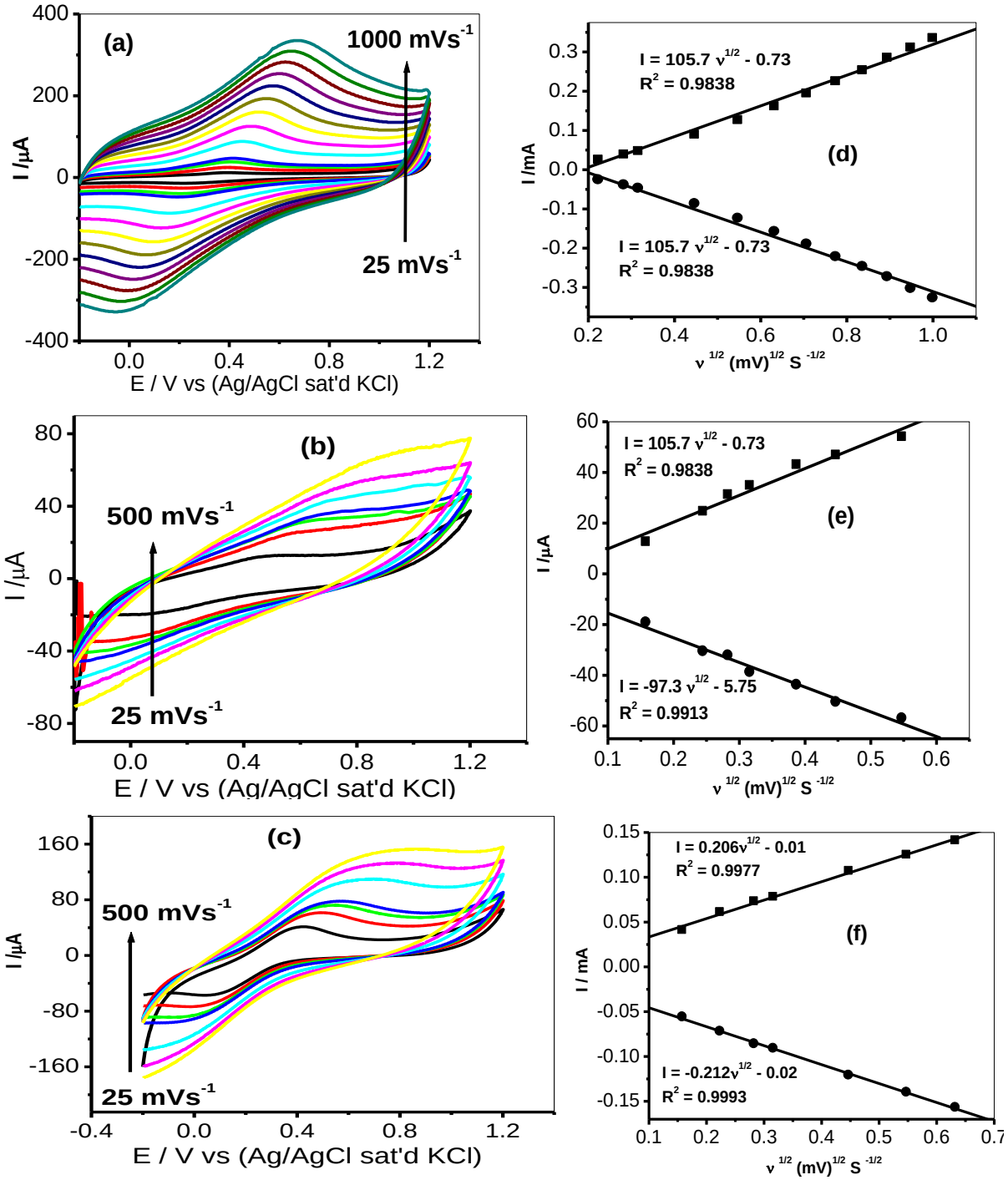

Figure 4.26: Effect of scan rate (25 – 1000 mVs^{-1}) on the cyclic voltammograms of (a) GCE/Nylon 6,6/MWCNT/NiO (b) scan rate (25 - 500 mVs^{-1}) GCE/Nylon 6,6/MWCNT/ZnO and (c) scan rate (25 – 500 mVs^{-1}) GCE/Nylon 6,6/MWCNT/Fe_3O_4 in 5 mM $Fe(CN)_6]^{4-}$/$[Fe(CN)_6]^{3-}$ solution prepared in 0.1M PBS (pH 7). (d-f) linear plots of Ipa/pc versus square root of scan rate for modified electrodes GCE/Nylon 6,6/MWCNT/NiO, GCE/Nylon 6,6/MWCNT/ZnO and GCE/Nylon 6,6/MWCNT/Fe_3O_4 respectively.

The apparent charge transfer rate constant (k_s) and the charge transfer coefficient (α) of a surface-confined redox couple can be evaluated from the cyclic voltammetric experiments by using the variation of anodic and cathodic peak potentials with logarithm of scan rate. The E_{pa} shifted to more positive values with increasing the scan rate (v). The transfer coefficient (i.e. α) and the number of electrons involved in the rate-determining step can be evaluated. Based on the slope of E_{pa} versus log (v), (1-α) $n\alpha$ was calculated to be 0.46, 0.38 and 0.40 for electrodes Nylon 6,6/MWCNT/NiO, Nylon 6,6/MWCNT/ZnO and Nylon 6,6/MWCNT/Fe_3O_4 respectively. The values of ks were evaluated to be 0.27, 0.067 and 0.069 cms^{-1} for electrodes Nylon 6,6/MWCNT/NiO, Nylon 6,6/MWCNT/ZnO and Nylon 6,6/MWCNT/Fe_3O_4 respectively using equation 4.2.

4.3.3 Electrochemical impedance spectroscopic (EIS) studies

EIS is a complex electrochemical process that gives insightful information about reaction at the electrode-electrolyte interface. The result obtained is presented in Nyquist plot, which includes a semi-circular portion corresponding to the electron-transfer-limited process and a linear part resulting from the diffusion process [367, 368]. The diameter of the semicircle corresponds to the electron transfer resistance (Rct) of the redox probe at the electrode interface. A smaller Rct value implies that the probe has a higher interfacial electron transfer rate.

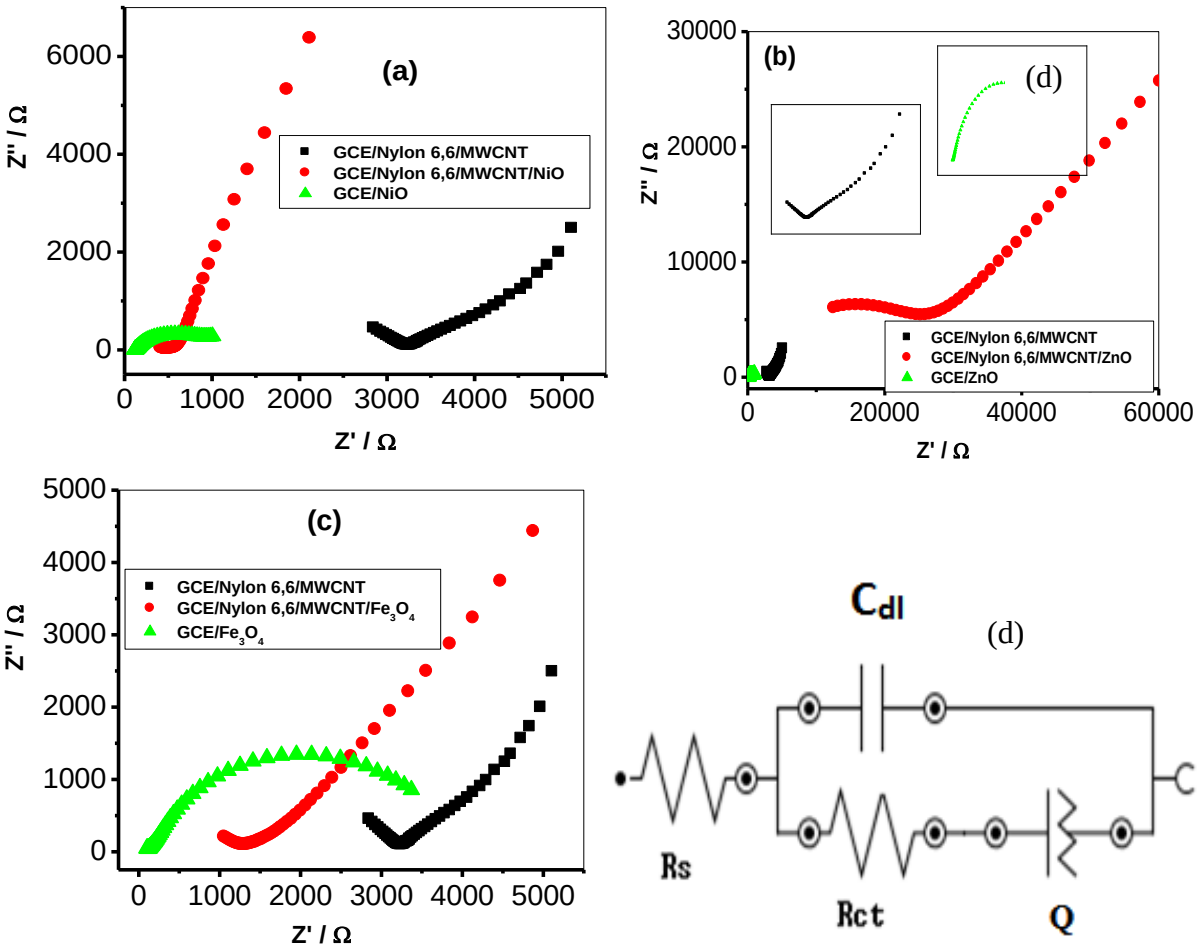

Figure 4.27: Typical Nyquist plots (a-c) obtained for the electrodes in in 5 mM $Fe(CN)_6]^{4-}$/$[Fe(CN)_6]^{3-}$ solution prepared in 0.1M PBS (pH 7) at a fixed potential of 0.2 V (vs. Ag|AgCl, saturated KCl) (d) Inset represents the circuit used in the fitting of the EIS data (a-c).

The Nyquist plots obtained from the impedance experiment (at fixed potential of 0.2 V vs Ag/AgCl, sat'd KCl) and between 10 KHz and 1 Hz are presented in Figure 4.27 a-c for modified electrodes Nylon 6,6/MWCNT/NiO, Nylon 6,6/MWCNT/ZnO and Nylon 6,6/MWCNT/Fe_3O_4 respectively. The circuit model used in the fitting of the impedance data is represented in Figure 4.27d. In this circuit model, R_s is the solution resistance, C_{dl} represents the double layer capacitance, Q or CPE is the constant phase element, and R_{ct} is the charge transfer resistance. The values obtained from the fitting of the raw impedance spectra with this circuit are presented in Table 4.8.

Table 4.8: Impedance data obtained for the bare GCE and the modified electrodes in 5 mM $Fe(CN)_6]^{4-}/[Fe(CN)_6]^{3-}$ solution at 0.2 V (vs. Ag|AgCl saturated KCl). All values were obtained from the fitted impedance spectra. The values in parentheses are percent errors of data fitting.

Electrodes	**Electrochemical impedance spectroscopy data**			
	R_s (Ω)	C_{dl} (n F)	R_{ct} (Ω)	Q (x 10^3)
GCE/Nylon 6,6/MWCNT	2396.00	21.56	784.00	0.41
GCE/Nylon 6,6/MWCNT/ NiO	448.00	0.032	126.60	0.23
GCE/Nylon 6,6/MWCNT Fe_3O_4	1009.00	130.20	321.00	0.25
GCE/Nylon 6,6/MWCNT/ZnO	9830.00	2.76	11190.00	89.98

From the R_{ct} values, the electron transport is faster for the Nylon 6,6/MWCNT/NiO and Nylon 6,6/MWCNT/Fe_3O_4 electrode compared to others. The R_{ct} value was very high at the Nylon 6,6/MWCNT/ZnO modified electrode, Nylon 6,6/MWCNT/NiO and Nylon 6,6/MWCNT/Fe_3O_4 modified electrode has a higher electron transport because of the low Rct value as shown in Table 4.8. The rapid electron transfer at the nanocomposite can be ascribed to the excellent conductivity of MWCNT, which acts as a good electron conducting wire between Nylon 6,6/MO and the electrode surface. The *n* values are less than the ideal 1.0 expected from an ideal capacitive behaviour, thus suggesting pseudo-capacitive properties for these electrodes.

4.3.4 Electrooxidation of DA and SE at the surface of the Electrodes

Figure 4.28 shows the electrochemical response of dopamine at bare Nylon 6,6/MWCNT /MO electrodes in 0.1M phosphate buffer solution (pH 7.0). The CV evolution of electrodes in DA is typical for DA oxidation process where the anodic peak corresponds to dopaminoquinone (DA+) (Figure 4.28a) and the cathodic peak corresponds to reduction of

dopaminoquinone to leucodopanoquinone [369]. On the other serotonin SE was as well successfully oxidized at the modified electrodes. The comparative results showed that DA and SE were oxidized with well-defined sharp DA and SE oxidation peak at lower potentials and significantly enhanced DA and SE oxidation current at the GCE/Nylon 6,6/MWCNT/MO electrodes investigated (Figure 4.28a,b) where MO is nickel oxide, zinc oxide and iron oxide nanoparticles.

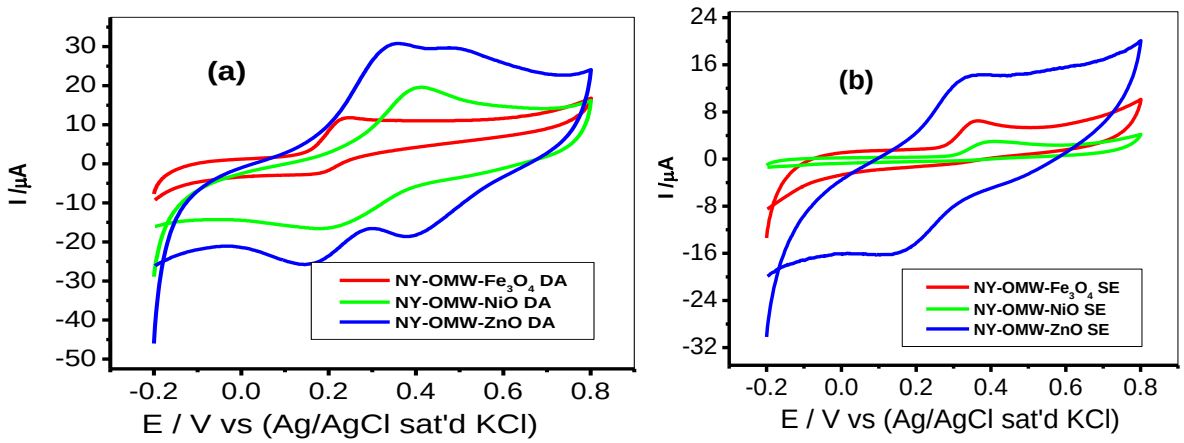

Figure 4.28: Comparative cyclic voltammogrammes of (a) 1 x 10^{-4} M DA and (b) SE on GCE/Nylon 6,6/MWCNT/NiO, GCE/Nylon 6,6/MWCNT/ZnO and GCE/Nylon 6,6/MWCNT/Fe_3O_4 at scan rate, 25 mVs^{-1} .

The exchange current density of an electrochemical reaction depends on the reaction and on the electrode surface on which the electrochemical reaction occurs. The DA oxidation current at the Nylon 6,6/MWCNT/MO electrodes follow the order: Nylon 6,6/MWCNT/ZnO (31.0 µA) > Nylon 6,6/MWCNT/NiO (19.5 µA) and Nylon 6,6/MWCNT/Fe_3O_4 (11.9 µA). For SE the oxidation current follows the order: Nylon 6,6/MWCNT/ZnO (14.3 µA) > Nylon 6,6/MWCNT/Fe_3O_4 (6.6 µA) and Nylon 6,6/MWCNT/NiO (2.97 µA). In terms of exchanged current density, the DA oxidation current at the electrode follows the order: GEC/Nylon 6,6/MWCNT/ZnO (43.85 $mAcm^{-2}$) > GCE/Nylon 6,6/MWCNT/NiO (27.86 $mAcm^{-2}$) and GCE?Nylon 6,6/MWCNT/Fe_3O_4 (16.83 $mAcm^{-2}$). Thus suggesting GEC/Nylon

6,6/MWCNT/ZnO electrode as the best electrode for DA oxidation in this study. While for SE the current density of the modified electrodes follows the order GCE/Nylon 6,6/MWCNT/ZnO (20.43 $mAcm^{-2}$) > GCE/Nylon 6,6/MWCNT/Fe_3O_4 (9.43 $mAcm^{-2}$) and GCE/Nylon 6,6/MWCNT/NiO (0.42 μ Acm^{-2}), this result, therefore, confirms GCE/Nylon 6,6/MWCNT/ZnO electrode as the best electrode for SE oxidation in this study. The higher DA and SE oxidation current at this electrode indicates that the Nylon/MWCNT has provided large surface area for effective diffusion of more DA and SE molecules in and out of the electrode surface for maximum electrocatalytic oxidation process [370].

4.3.4.1 Effect of varying scan rate at constant concentration (10^{-4} M) of dopamine in pH 7.0 PBS

Cyclic voltammetry experiments were carried out with the Nylon 6,6/MWCNT/MO to establish the impact of scan rate at constant concentration (10^{-4} M) of dopamine in pH 7.0 PBS solutions. In all cases, we observed a shift in potential with increase in scan rate (Figure 4.29). From the Randles–Sevˇcik equation for an anodic oxidation process equation (2.3, chapter 2), the plot of the peak currents (I_p) against the square root of scan rate ($v^{1/2}$) (Figure 4.29) for scan rate ranging from 25 to 300 mVs^{-1}, gave a linear relationship and approximately zero intercept, confirming a diffusion-controlled process but with some levels of adsorbed reaction intermediates. The linear relationship of the plot confirmed that the nanocomposites were electroactive, conducting and confined to the surface.

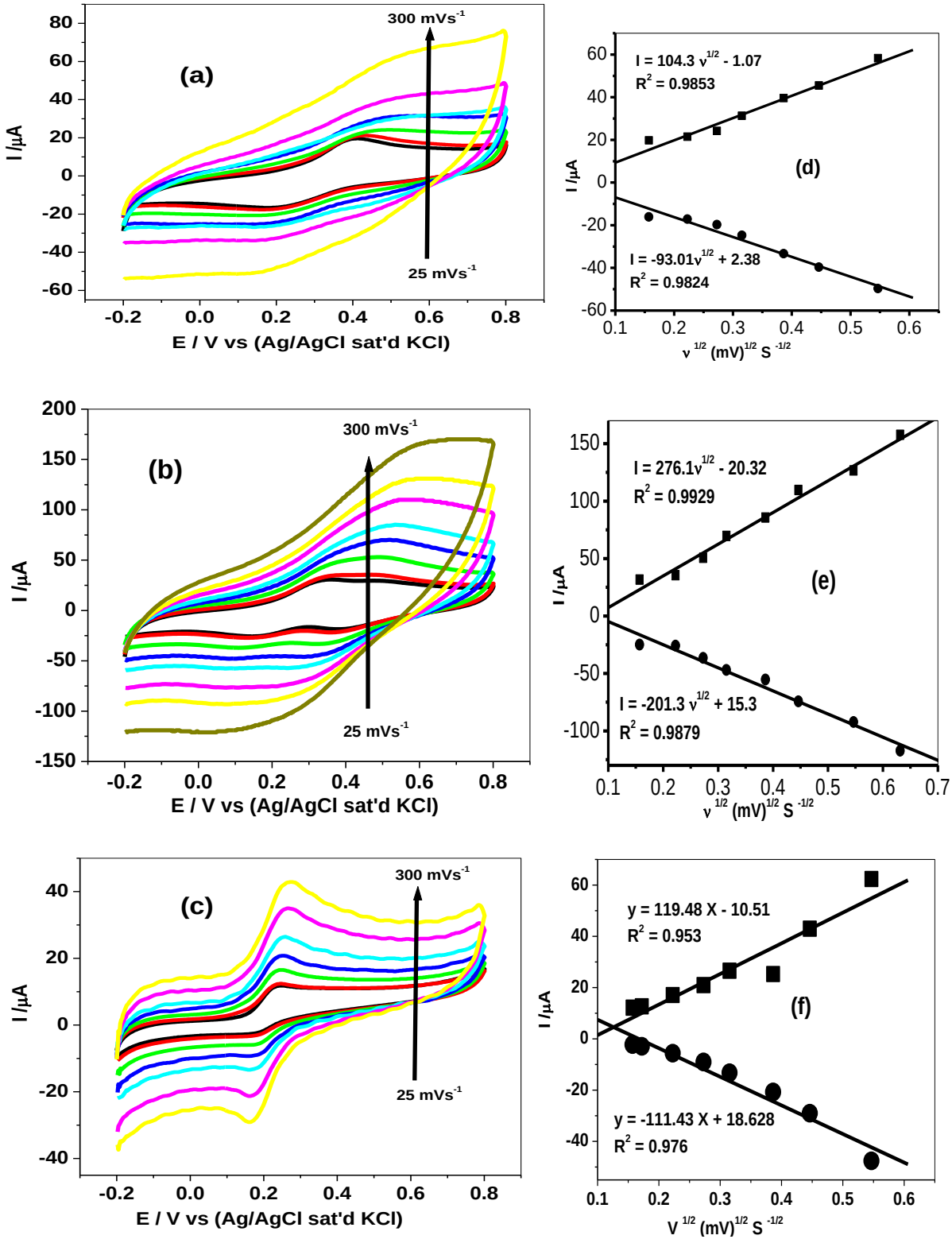

Figure 4.29: Effect of scan rate (25 – 300 mVs^{-1}) on the cyclic voltammograms of (a) GCE/Nylon 6,6/MWCNT/NiO (b) GCE/Nylon 6,6/MWCNT/ZnO and (c) GCE/Nylon 6,6/MWCNT/Fe_3O_4 in 1 x 10^{-4} M DA and their respective linear plots of current versus square root of scan rate (d-f).

The charge transfer coefficient (α) for the reaction can be evaluated from cyclic voltammetric experiments by using the variation of anodic and cathodic peak potentials with logarithm of scan rate. Based on the slope of E_{pa} with log (v), (1-α)nα was calculated to be 0.35, 0.34 and 0.47 for electrodes GCE/Nylon 6,6/MWCNT/NiO, GCE/Nylon 6,6/MWCNT/ZnO and GCE/Nylon 6,6/MWCNT/Fe_3O_4 respectively. In order to get information on the rate determining step, the peak potential, E_p, is proportional to log ν (graph not shown). The slopes of E_p *vs.* log v for the different electrodes were 0.117, 0.178, and 0.032 V for electrodes GCE/Nylon 6,6/MWCNT/NiO, GCE/Nylon 6,6/MWCNT/ZnO and GCE/Nylon 6,6/MWCNT/Fe_3O_4 respectively. The tafel slopes was estimated according to the equation 4.2, for the totally irreversible diffusion controlled process [324]. So, the respective values of b for these electrodes were obtained as 0.234, 0.356 and 0.064 $Vdec^{-1}$. Tafel values at GCE/Nylon 6,6/MWCNT/NiO and GCE/Nylon 6,6/MWCNT/ZnO are higher than the theoretical 0.118 V dec^{-1} for a one-electron process involved in the rate-determining step, while at GCE/Nylon 6,6/MWCNT/Fe_3O_4 the value is lower suggesting no adsorption on the surface of the electrode. Therefore, the high Tafel values suggest adsorption of dopamine or its reaction intermediate at the electrode surface since high Tafel values have been attributed to the adsorption of reactants or intermediates on the electrode surfaces and/or reactions occurring within a porous electrode structure [333]. Adsorption process at the electrode can be linked with the porous CNT layer [334]. The value of k_s was evaluated to be equal to 0.13, 0.24 and 0.49 cm s^{-1} for electrodes GCE/Nylon 6,6/MWCNT/NiO, GCE/Nylon 6,6/MWCNT/ZnO and GCE/Nylon 6,6/MWCNT/Fe_3O_4 respectively. According to the kinetics of electron process, when the rate constant is larger than 10^{-2} cm/s , the electron transfer process is very fast, and the electrode reaction is reversible, and when $10^{-4} < k_s < 10^{-2}$ cm/s, the electrode reaction is a quasireversible process. So the electrode reaction of DA on the proposed electrodes is reversible process.

4.3.4.2 Electrochemical impedance spectroscopic (EIS) studies

The Nyquist plots obtained from the impedance experiment (at fixed potential of 0.2 V vs Ag/AgCl, sat'd KCl) and between 10 KHz and 1 Hz are presented in Figure 4.30 a-c for modified electrodes Nylon 6,6/MWCNT/NiO, Nylon 6,6/MWCNT/ZnO and Nylon 6,6/MWCNT/Fe_3O_4 respectively. The circuit model used in the fitting of the impedance data is represented in Figure 4.30 d-e, where circuit Figure 4.30d represent the EIS data fitting for bare GCE, GCE/MO and GCE/ Nylon 6,6/MWCNT/NiO, GCE/ Nylon 6,6/MWCNT/Fe_3O_4 and Figure 4.30e represent that of GCE/ Nylon 6,6/MWCNT/ZnO and GCE/ Nylon 6,6/MWCNT modified GCE electrodes. In this circuit model, R_s is the solution resistance, C_{dl} represents the double layer capacitance, Q or CPE is the constant phase element, and R_{ct} is the charge transfer resistance, Zw is the Warburg impedance. The values obtained from the fitting of the raw impedance spectra with this circuit are presented in Table 4.9.

From the R_{ct} values, the electron transport is faster for the Nylon 6,6/MWCNT/NiO and Nylon 6,6/MWCNT/ZnO electrodes compared to others. The Rct value was higher at the bare GCE and GCE/Nylon 6,6/MWCNT/Fe_3O_4 when compared with the other modified electrodes. The rapid electron transfer at the nanocomposite can be ascribed to the excellent conductivity of MWCNT, which acts as a good electron conducting wire between Nylon 6,6/MO and the electrode surface. The *n* values are less than the ideal 1.0 expected from an ideal capacitive behaviour, thus suggesting pseudo-capacitive properties for these electrodes.

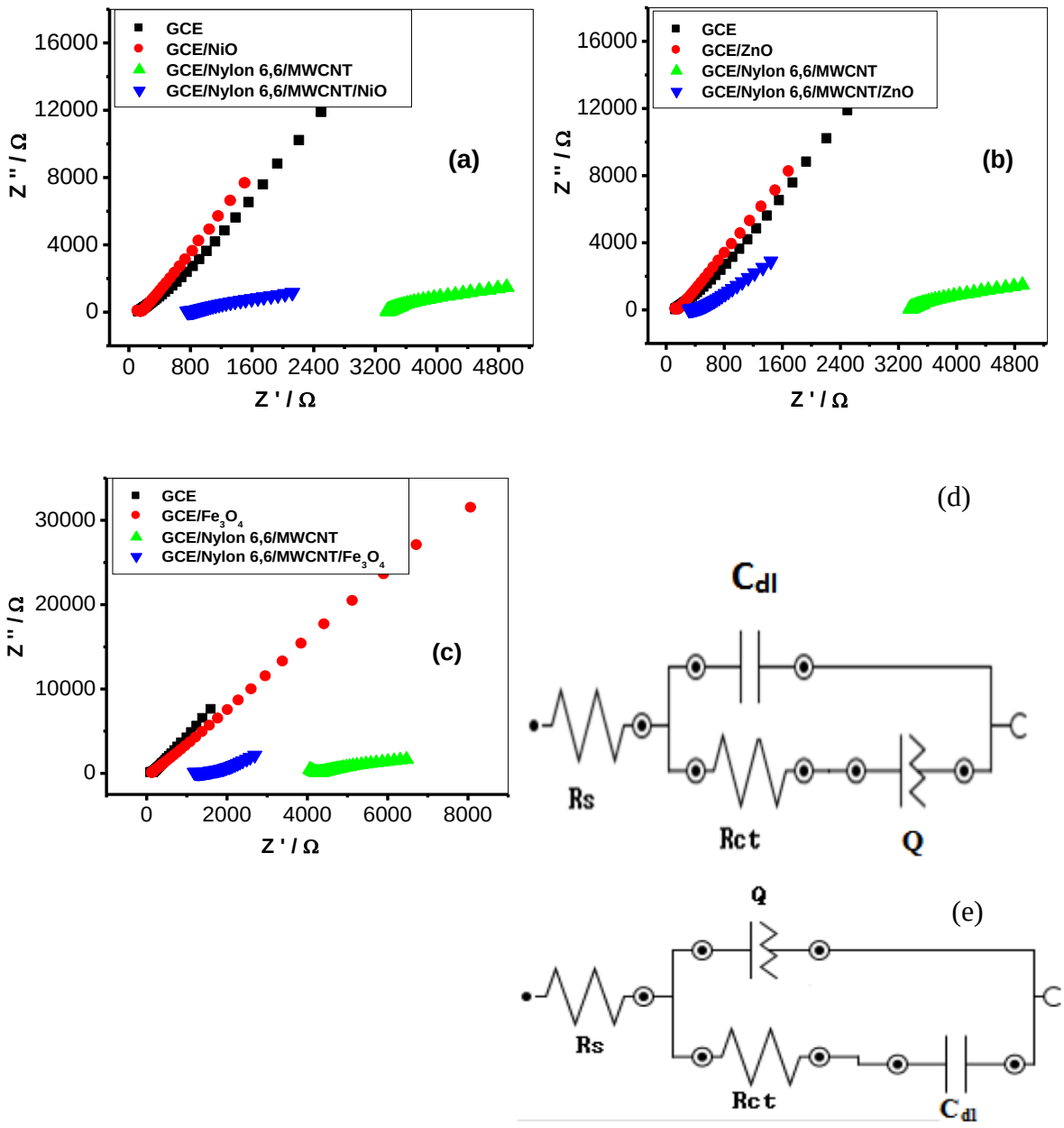

Figure 4.30: Typical Nyquist plots (a-c) obtained for the electrodes in in 1 mM dopamine solution prepared in 0.1M PBS (pH 7) at a fixed potential of 0.2 V (vs. Ag|AgCl, saturated KCl) (d -e) represents the circuit used in the fitting of the EIS data (a-c).

Table 4.9: Impedance data obtained for the bare GCE and the modified electrodes in 1 mM DA solution at 0.2 V (vs. Ag|AgCl saturated KCl). All values were obtained from the fitted impedance spectra. The values in parentheses are percent errors of data fitting.

Electrodes	Electrochemical impedance spectroscopy data			
	R_s (kΩ)	C_{dl} (μF)	R_{ct} (Ω)	Q (x 10^6 nF)
GCE/Nylon 6,6/MWCNT Fe_3O_4	1.19 (2.49)	0.32 ((17.93)	175.00 (8.63)	143.90 (2.52)
GCE/Nylon 6,6/MWCNT/NiO	0.72 (1.45)	0.28 ((13.70)	22.65 ((5.67)	222.00 ((1.56)
GCE	53700.00 (9.05)	0.15 (10.56)	103.30 (4.63)	27.50 (1.33)
GCE/NiO	61800.00 (8.53)	0.15 (10.70)	109.10 (4.72)	26.35 (1.31)
GCE/ZnO	80600.00 (7.95)	0.17 (16.73)	84.80 (7.47)	24.88 (1.36)
GCE/Fe_3O_4	117500.00 (0.78)	0.19 (17.95)	37.40 (2.58)	6.59 (3.04)

Electrodes	Electrochemical impedance spectroscopy data			
	R_s (kΩ)	C_{dl} (μF)	R_{ct} (Ω)	W x 10^3
GCE/Nylon 6,6/MWCNT	1.37 (1.98)	0.145 (35.82)	158.80 (15.44)	290.40 (0.94)
GCE/Nylon 6,6/MWCNT ZnO	0.35 (11.00)	14.75 (46.01)	0.30 (19.69)	0.12 (3.26)

4.3.4.3 Effect of varying scan rate at constant concentration (10^{-4} M) of serotonin in pH 7.0 PBS

Effect of varying scan rate at constant concentration (10^{-4} M) of serotonin in pH 7.0 PBS were also carried out with the Nylon 6,6/MWCNT/MO to establish the impact of scan rate at constant concentration (10^{-4} M) of serotonin in pH 7.0 PBS solutions. In all cases, we observed a shift in potential with increase in scan rate (Figure 4.31 a-c). From the Randles–Sevˇcik equation for an anodic oxidation process equation (2.3, chapter 2), the plot of the peak currents (I_p) against the square root of scan rate ($\nu^{1/2}$) (Figure 4.31 d-f) for scan rate

ranging from 25 to 300 mVs^{-1}, gave a linear relationship and approximately zero intercept, confirming a diffusion-controlled process but with some levels of adsorbed reaction intermediates. The linear relationship of the plot confirmed that the nanocomposites were electroactive, conducting and confined to the surface.

The charge transfer coefficient (α) for the reaction can be evaluated from cyclic voltammetric experiments by using the variation of anodic and cathodic peak potentials with logarithm of scan rate. Based on the slope of Epa with log (v), $(1-\alpha)n\alpha$ was calculated to be 0.36, 0.39 and 0.39 for electrodes GCE/Nylon 6,6/MWCNT/NiO, GCE/Nylon 6,6/MWCNT/ZnO and GCE/Nylon 6,6/MWCNT/Fe_3O_4 respectively. In order to get information on the rate determining step, the peak potential, Ep, is proportional to log ν (graph not shown). The slopes of Ep vs. log ν for the different electrodes were 0.076, 0.068, and 0.046 V for electrodes GCE/Nylon 6,6/MWCNT/NiO, GCE/Nylon 6,6/MWCNT/ZnO and GCE/Nylon 6,6/MWCNT/Fe_3O_4 respectively. The tafel slopes may be estimated according to the equation 4.2 in chapter 4 for the totally irreversible diffusion controlled process [332]. So, the respective values of b for these electrodes were obtained as 0.152, 0.136 and 0.092 $Vdec^{-1}$.

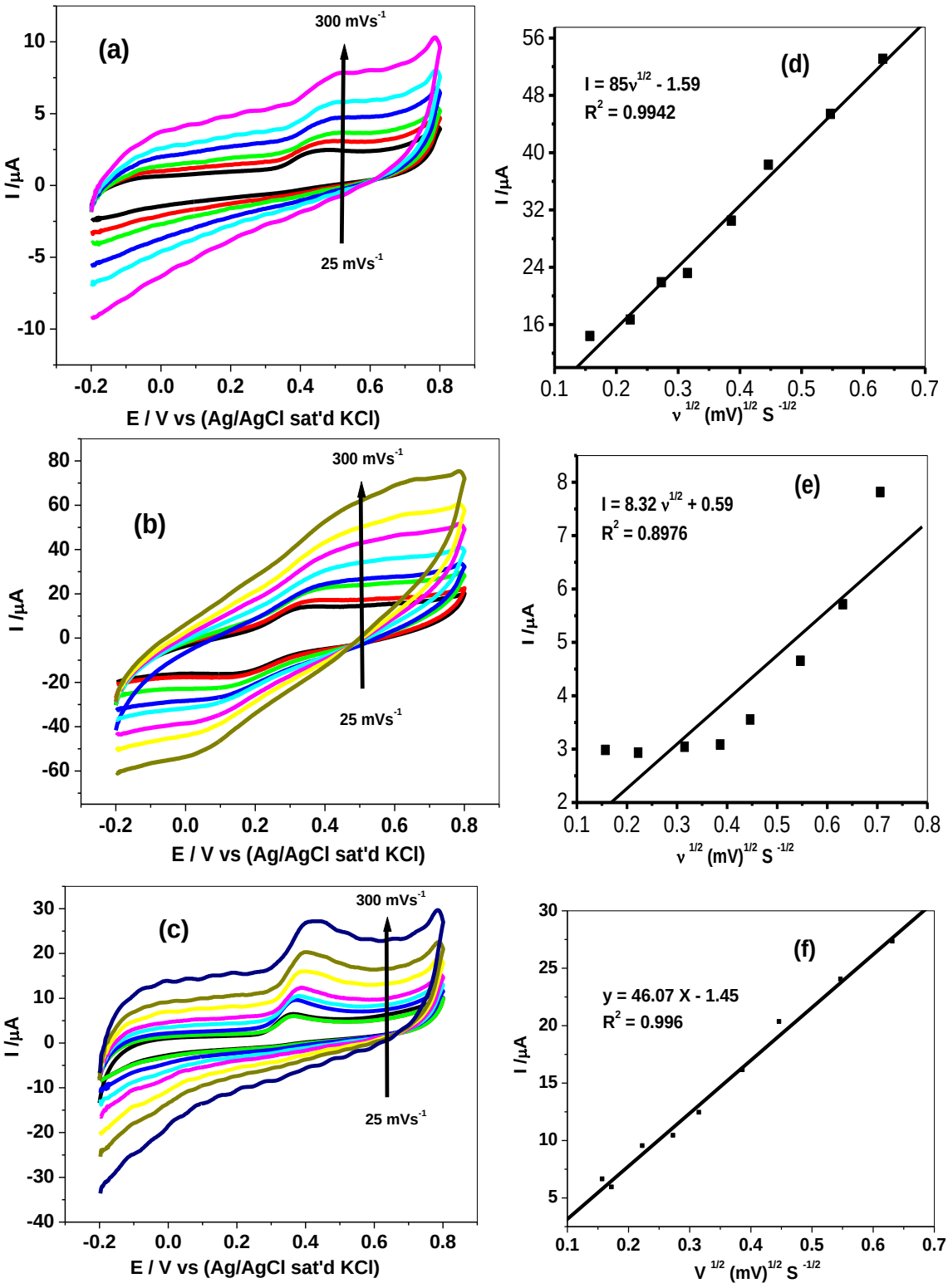

Figure 4.31: Effect of scan rate (25 – 500 mVs^{-1}) on the cyclic voltammograms of (a) GCE/Nylon 6,6/MWCNT/NiO (b) GCE/Nylon 6,6/MWCNT/ZnO and (b) GCE/Nylon 6,6/MWCNT/Fe_3O_4 in in 1 x 10^{-4} M SE. (d-f) linear plots of current versus square root of scan rate at modified electrodes GCE/Nylon 6,6/MWCNT/NiO, GCE/Nylon 6,6/MWCNT/ZnO and GCE/Nylon 6,6/MWCNT/Fe_3O_4 respectively.

Tafel values at GCE/Nylon 6,6/MWCNT/NiO and GCE/Nylon 6,6/MWCNT/ZnO were higher than the theoretical 0.118 V dec^{-1} for a one-electron process involved in the rate-determining step, while at GCE/Nylon 6,6/MWCNT/Fe_3O_4 the value is lower suggesting low adsorption process. Therefore the high Tafel values suggest adsorption of dopamine or its reaction intermediate at the electrode surface since high Tafel values have been attributed to the adsorption of reactants or intermediates on the electrode surfaces and/or reactions occurring within a porous electrode structure [325]. Adsorption process at the electrode can be linked with the porous CNT layer [371]. The value of ks was evaluated to be equal to 2.87, 2.7 and 2.7 cm s^{-1} for electrodes GCE/Nylon 6,6/MWCNT/NiO, GCE/Nylon 6,6/MWCNT/ZnO and GCE/Nylon 6,6/MWCNT/Fe_3O_4 respectively. According to the kinetics of electron process, when the rate constant is larger than 10^{-2} cm/s , the electron transfer process is very fast, and the electrode reaction is reversible, and when $10^{-4} < ks < 10^{-2}$ cm/s, the electrode reaction is a quasireversible process. So the electrode reaction of SE on the proposed electrodes is reversible process.

4.3.4.4 Electrochemical impedance spectroscopic (EIS) studies

The Nyquist plots obtained from the impedance experiment (at fixed potential of 0.2 V vs Ag/AgCl, sat'd KCl) and between 10 KHz and 1 Hz are presented in Figure 4.32 a-c for modified electrodes Nylon 6,6/MWCNT/NiO, Nylon 6,6/MWCNT/ZnO and Nylon 6,6/MWCNT/Fe_3O_4 respectively. The circuit model used in the fitting of the impedance data is represented in Figure 4.32 (d – e), where circuit Figure 4.32d represent the EIS data fitting for bare GCE, GCE/MO and GCE/Nylon 6,6/MWCNT/MO nanocomposites and Figure 4.32e represent that of GCE/Nylon 6,6/MWCNT modified electrode. In this circuit model, R_s is the solution resistance, C_{dl} represents the double layer capacitance, Q or CPE is the constant phase element, and R_{ct} is the charge transfer resistance. The values obtained from the fitting of the raw impedance spectra with this circuit are presented in Table 4.10.

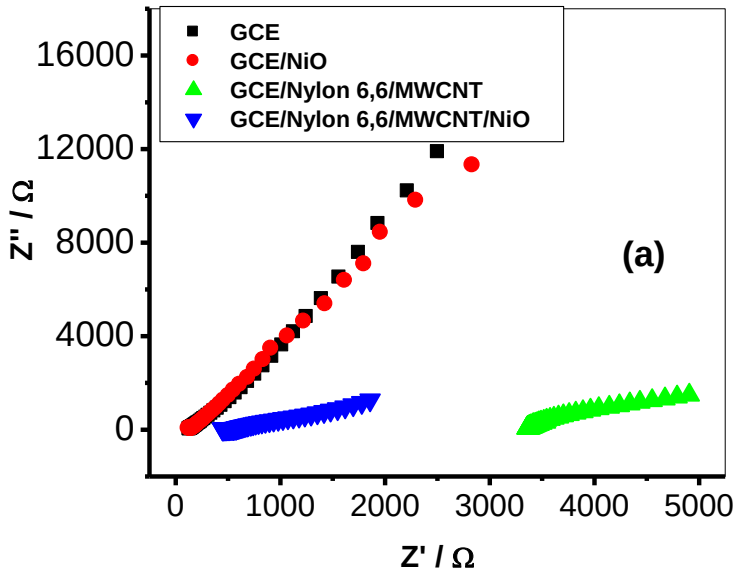
GCE
GCE/NiO
GCE/Nylon 6,6/MWCNT
GCE/Nylon 6,6/MWCNT/NiO
(a)
Z'' / Ω
Z' / Ω
16000
12000
8000
4000
0
0
1000
2000
3000
4000
5000

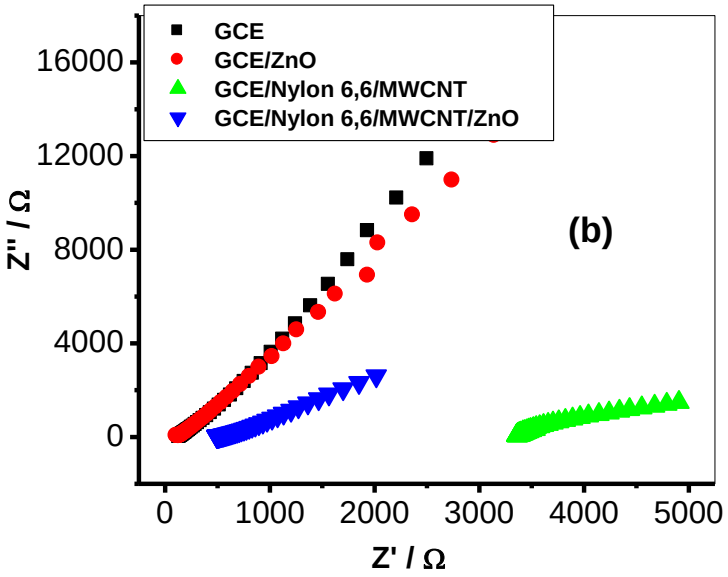
GCE
GCE/ZnO
GCE/Nylon 6,6/MWCNT
GCE/Nylon 6,6/MWCNT/ZnO
(b)
Z'' / Ω
Z' / Ω
16000
12000
8000
4000
0
0
1000
2000
3000
4000
5000

+

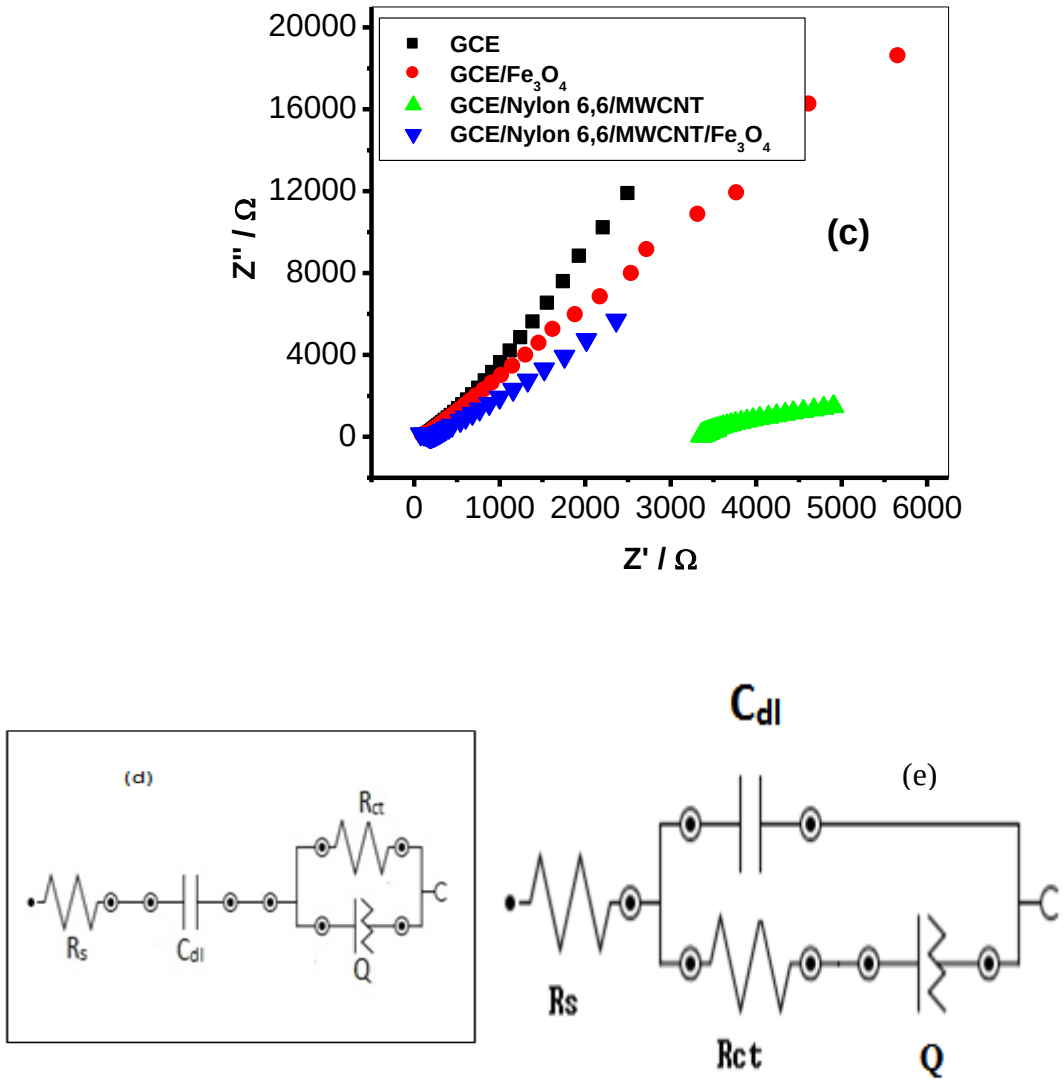

Figure 4.32: Typical Nyquist plots (a-c) obtained for the electrodes in in 1 mM serotonin solution prepared in 0.1M PBS (pH 7) at a fixed potential of 0.2 V (vs. Ag|AgCl, saturated KCl) (d -e) represents the circuit used in the fitting of the EIS data (a-c).

Table 4.10: Impedance data obtained for the bare GCE and the modified electrodes in 1 mM SE solution at 0.2 V (vs. Ag|AgCl saturated KCl). All values were obtained from the fitted impedance spectra.

Electrodes	Electrochemical impedance spectroscopy data			
	R_s (Ω)	Q (x 10^6 nF)	R_{ct} (Ω)	C_{dl} (nF)
GCE/Nylon 6,6/MWCNT/ ZnO	496.00 (0.61)	100.50 (1.82)	51.20 (14.34)	0.01 (19.78)
GCE/Nylon 6,6/MWCNT Fe_3O_4	92.1 (19.77)	44.20 (2.87)	280.30 (6.21)	4.48 (13.44)
GCE/Nylon 6,6/MWCNT/NiO	435.00 (1.74)	22.70 (2.61)	23.42 (40.34)	3.09 (75.64)
GCE	134.70 (1.28)	11.86 (2.52)	100.20 (16.23)	1.99 (8.39)
GCE/NiO	59.40 (12.36)	18.91 (1.08)	92.70 ((7.44)	123.30 ((16.28)
GCE/ZnO	49.60 ((14.05)	17.32 (1.13)	86.90 (7.47)	134.70 (16.51)
GCE/Fe_3O_4	45.10 (12.79)	12.06 (1.01)	84.20 ((6.23)	149.30 (14.17)

From the R_{ct} values, the electron transport is faster for the Nylon 6,6/MWCNT/NiO and Nylon 6,6/MWCNT/ZnO electrodes compared to others. The R_{ct} value was higher at the bare GCE and GCE/Nylon 6,6/MWCNT/Fe_3O_4 when compared with the other modified electrodes. The rapid electron transfer at the nanocomposite can be ascribed to the excellent conductivity of MWCNT, which acts as a good electron conducting wire between Nylon 6,6/MO and the electrode surface. The *n* values are less than the ideal 1.0 expected from an ideal capacitive behaviour, thus suggesting pseudo-capacitive properties for these electrodes.

4.3.4.5 Electroanalysis of Dopamine and Serotonin

Since the proposed Nylon 6,6/MWCNT/MO GCE electrodes have demonstrated favourable electrochemical response towards DA and SE, they have been used for determination of DA and SE. To improve the sensitivity of the developed sensors in detection of dopamine and serotonin, square wave voltemmetry (SWV) technique has been used. Figures 4.33 and 4.34 shows the square wave voltamogramme of the concentration range 2×10^{-14} mol/L to 9.9 ×

10^{-8} mol/L for electrodes GCE/Nylon 6,6/MWCNT/NiO, GCE/Nylon 6,6/MWCNT/ZnO and GCE/Nylon 6,6/MWCNT/Fe_3O_4 in dopamine and serotonin respectively. The respective detection limit for dopamine and serotonin on the electrodes were calculated based on the relationship LoD = 3.3 δ/m [294] where δ is the relative standard deviation of the intercept of the y-coordinates from the line of best fit, and m the slope of the same line to be 1.49 x 10^{-11}, 1.76 x 10^{-11}, and 4.28 x 10^{-11} mol/L (S/N = 3) for dopamine at modified electrodes GCE/Nylon 6,6/MWCNT/NiO, GCE/Nylon 6,6/MWCNT/ZnO and GCE/Nylon 6,6/MWCNT/Fe_3O_4 respectively. While for serotonin the limit of detection at modified electrodes were calculated to be 1.17x 10^{-10}, 3.39 x 10^{-7}, and 1.16 x 10^{-6} mol/L (S/N = 3) at GCE/Nylon 6,6/MWCNT/ZnO, GCE/Nylon 6,6/MWCNT/NiO and GCE/Nylon 6,6/MWCNT/Fe_3O_4 respectively. The best electrode for detection of dopamine was GCE/Nylon 6,6/MWCNT/NiO while for the detection of serotonin the best electrode to be considered is GCE/Nylon 6,6/MWCNT/ZnO due to their lowest limit of detections. A comparism of these results is given in Table 4.11 and 4.12 for dopamine and serotonin resprctively.

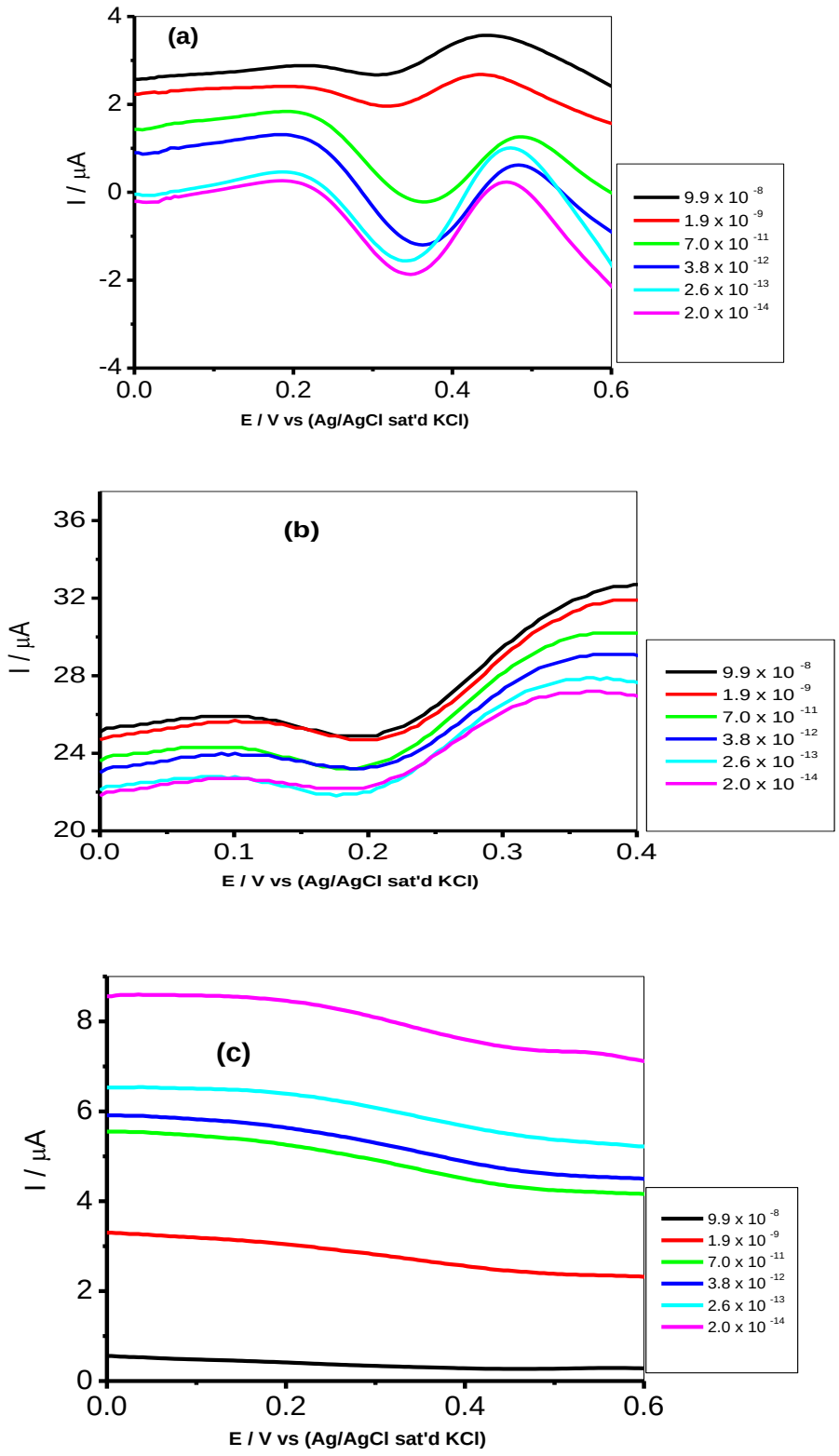

Figure 4.33: Square wave voltammogrammes of (a) GCE/Nylon 6,6/MWCNT/NiO (b) GCE/Nylon 6,6/MWCNT/ZnO and (c) GCE/Nylon 6,6/MWCNT/Fe_3O_4 in PBS pH 7 containing 2 x 10^{-14} M to 9.9 x 10^{-8} M DA concentration.

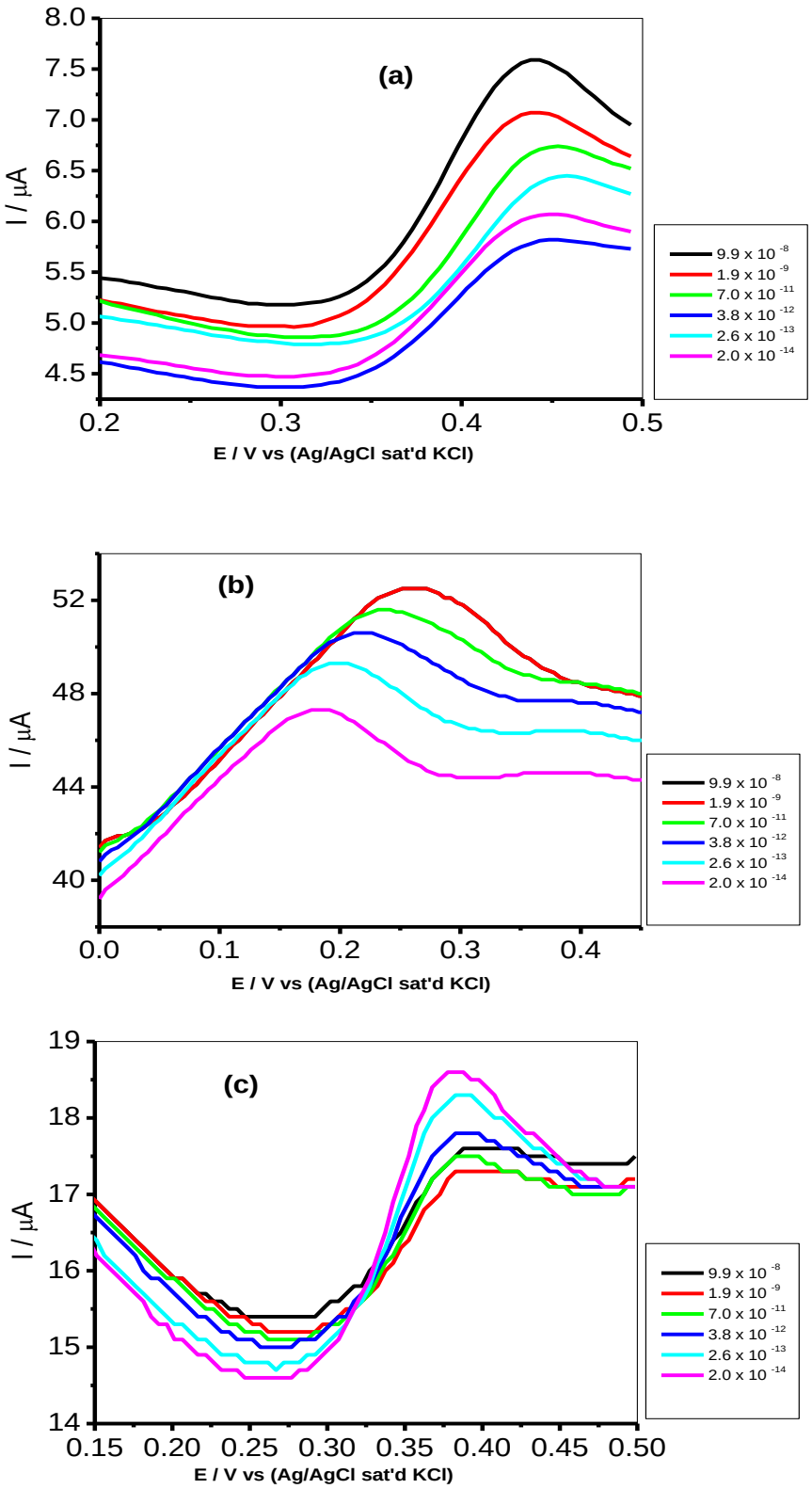

Figure 4.34: Square wave voltammogrammes of (a) GCE/Nylon 6,6/MWCNT/NiO (b) GCE/Nylon 6,6/MWCNT/ZnO and (c) GCE/Nylon 6,6/MWCNT/Fe_3O_4 in PBS pH 7 containing 2 x 10^{-14} M to 9.9 x 10^{-8} M SE concentration.

Table 4.11: Comparison of different electrochemical sensors for the determination of dopamine.

Electrode material	Techniques	Detection Limit (M)	References
Ni NPs@Poly1,5-DAN/GCEc	SWV	1.1×10^{-8}	[372]
TPyP-31P/FTO	DPV	1.4×10^{-7}	[373]
GCE/Nylon6,6/MWCNT/NiO	SWV	1.49×10^{-11}	This work
GCE/Nylon6,6/MWCNT/ZnO	SWV	1.76×10^{-11}	This work
GCE/Nylon6,6/MWCNT/Fe_3O_4	SWV	4.28×10^{-11}	This work

Table 4.12: Comparison of different electrochemical sensors for the determination of serotonin.

Electrode material	Techniques	Detection Limit (M)	References
TPyP-31P/FTO	CVs	2.2×10^{-4}	[374]
F-MWCNTs/BR9	DPV	9.0×10^{-6}	[375]
GCE/Nylon6,6/MWCNT/NiO	SWV	3.39×10^{-7}	This work
GCE/Nylon6,6/MWCNT/ZnO	SWV	1.17×10^{-10}	This work
GCE/Nylon6,6/MWCNT/Fe_3O_4	SWV	1.16×10^{-6}	This work

4.3.5 Interference study: Detection of DA and SE in the presence of AA

Figure 4.35 is the cyclic voltammetric responses of GCE/Nylon 6,6/MWCNT/NiO, GCE/Nylon 6,6/MWCNT/ZnO and GCE/Nylon 6,6/MWCNT/Fe_3O_4 in 0.1 M pH 7.0 PBS containing mixture of 10^{-2} M AA, approximately 1000 times concentration of DA and SE. The simultaneous detection of AA, DA and SE even at AA concentration (9.09 mM) which is 1000 times as high as DA and SE concentration (9.09 µM) was successful at the GCE/Nylon 6,6/MWCNT/MO electrodes with potential separation of about AA/DA 150,170,

250, DA/SE 200, 200, 250 mV, and AA/SE 350,370, 500 mV observed at GCE/Nylon 6,6/MWCNT/NiO, GCE/Nylon 6,6/MWCNT/ZnO and GCE/Nylon 6,6/MWCNT/Fe_3O_4 electrodes respectively.

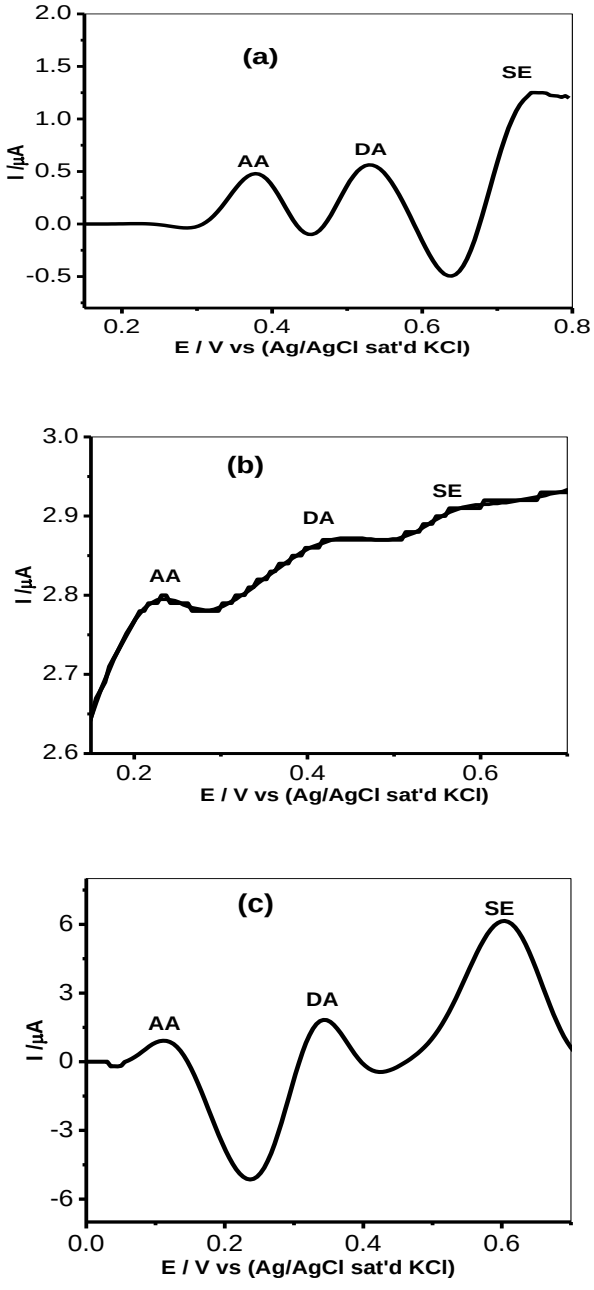

Figure 4.35: Cyclic voltammogram of 10^{-4} M of AA, DA and SE at (a) GCE/Nylon 6,6/MWCNT /NiO (b) GCE/Nylon 6,6/MWCNT/ZnO and (c) GCE/Nylon 6,6/MWCNT/Fe_3O_4 electrodes in PBS pH 7.0.

4.4 METAL OXIDE NANOPARTICLES / PANI NANOCOMPOSITE MODIFIED ELECTRODE FOR THE DETECTION OF DOPAMINE

4.4.1 Spectroscopic and microscopic characterisation

4.4.1.1 UV-vis spectroscopy result

UV–vis absorption spectroscopic analyses were performed to confirm the formation of the PANI-MO nanocomposites. UV–vis absorption spectra for mtal oxides nanoparticles [Figure 4.36] showed a strong absorption peak at 340, 370 and 398 nm which are characteristic peaks for nickel, zinc and iron oxide nanoparticles. The PANI-MO nanocomposites showed two strong absorption peaks at approximately 348 and 622 nm respectively. The absorption peak at 348 nm indicates a slight shift in the MO absorption bands suggesting the chemical interaction of the MO with the PANI molecules. This shift might be due to the benzenoid π-π* transition of the PANI molecules in the PANI-MO nanocomposites. This peak at 622 nm has been attributed to π-π* transition of quinine-imines group which also indicate the formation of emeraldine base. This result is similar to previously reported results for polyaniline powders, thin films, nanotubes, and nanofibers [376, 377].

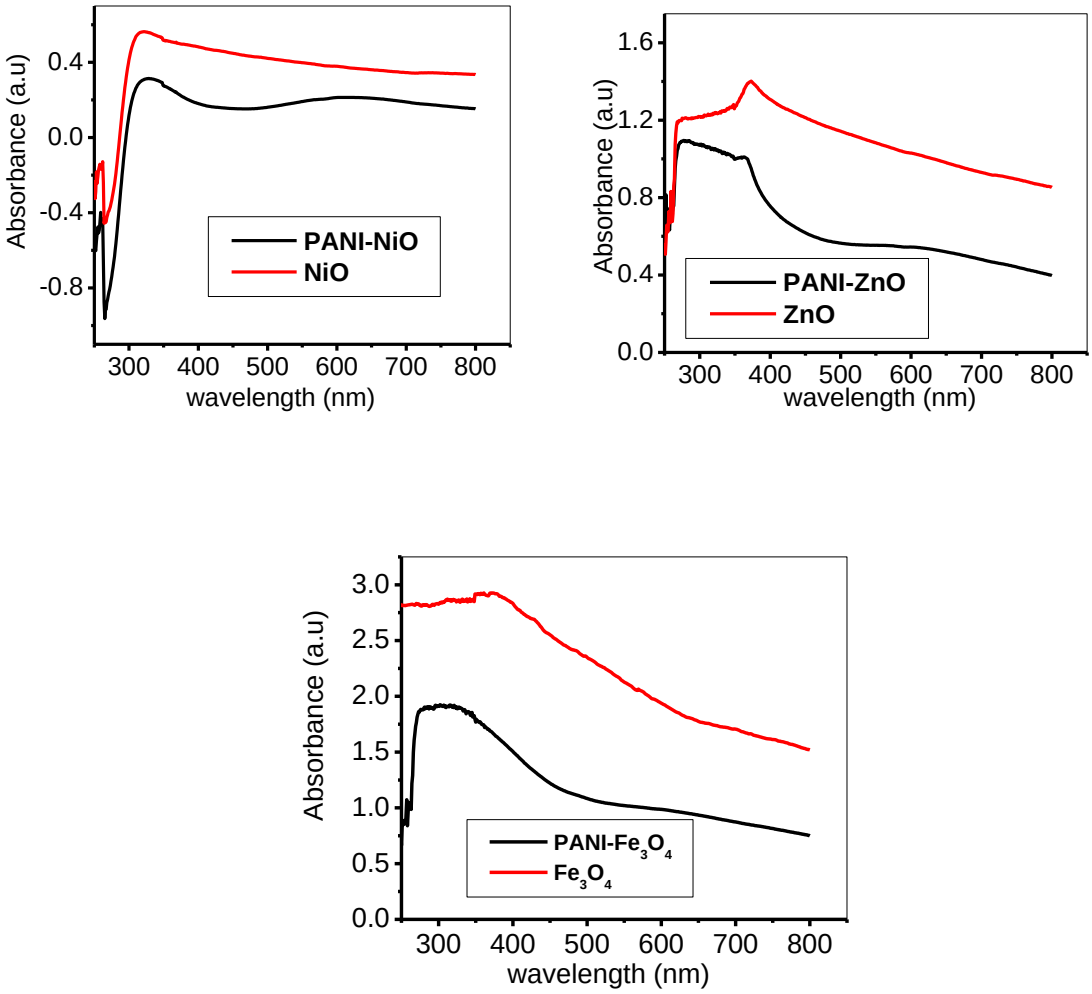

Figure 4.36: Uv-Vis spectra of (a) NiO, PANI and PANI-NiO (b) ZnO, PANI and PANI-ZnO and (c) Fe_3O_4, PANI and PANI-Fe_3O_4 nanocomposites.

4.4.1.2 Fourier Transform Infra-Red Spectroscopy

Figure 4.37, shows the FTIR spectra of MO, PANI and PANI-MO nanocomposites. The spectra of PANI show the main characteristic peaks at 1580, 1500, 1287, 1147 and 824 cm^{-1}. The bands at 1580 and 1500 cm^{-1} are attributed to stretching vibrations of N=N ring and N-N ring for benzenic rings and quinonic rings respectively, while the bands at 1287 cm^{-1} corresponds to NH bending, and 1147 cm^{-1} was assigned to C-N stretching of secondary aromatic amine [378]. The out-of-plane bending vibration of C-H on the 1, 4-disubstituted

aromatic rings was assigned to the peak at 824 cm^{-1} [379]. The reduction in the intensity of these PANI characteristic peaks in PANI-MO and the reduction in PANI broad band intensity at around 2400 cm^{-1} indicate successful transformation of the PANI molecule to PANI-MO nanocomposites. The peaks between 700 - 500 cm^{-1} indicate the presence of NiO, ZnO and Fe_3O_4 nanoparticles in the PANI molecules. The presence of the band at 1148 cm^{-1} in the FTIR spectra of the PANI-MO nanocomposites confirms the hydrogen bonding formed between the imine group of PANI and metal oxides nanoparticles.

In Figure 7.2c the peaks of PANI-Fe_3O_4 spectra shift towards lower wavenumber, probably due to the strong interaction of the 3d orbit of Fe_3O_4 with N atom in PANI to form a coordination bond [380-382].

4.4.1.3 SEM, TEM, EDX and XRD of PANI and PANI-NiO nanocomposites

4.4.1.3.1 Scanning Electron Microscopy

The SEM images of the MO, PANI nanofibers and PANI-MO nanocomposites are shown in Figure 4.38. Figure 4.38a is the SEM image for the PANI nanofibers which shows that PANI has a larger surface area due to its porous morphology. The PANI-MO SEM images (Figure 4.38 b-c) indicate a formation of aggregate porous layers with the metal oxide nanoparticles on PANI molecules. The successful formation of the PANI-MO nanocomposites can be attributed to ionic interaction between the PANI and the metal oxides nanoparticles. Similar reports on the successful formation of metal oxide/carbon nanomaterial based nanocomposites have been attributed to either π-π or electrovalent interaction between the metal oxide and the carbon based nano material [383].

.

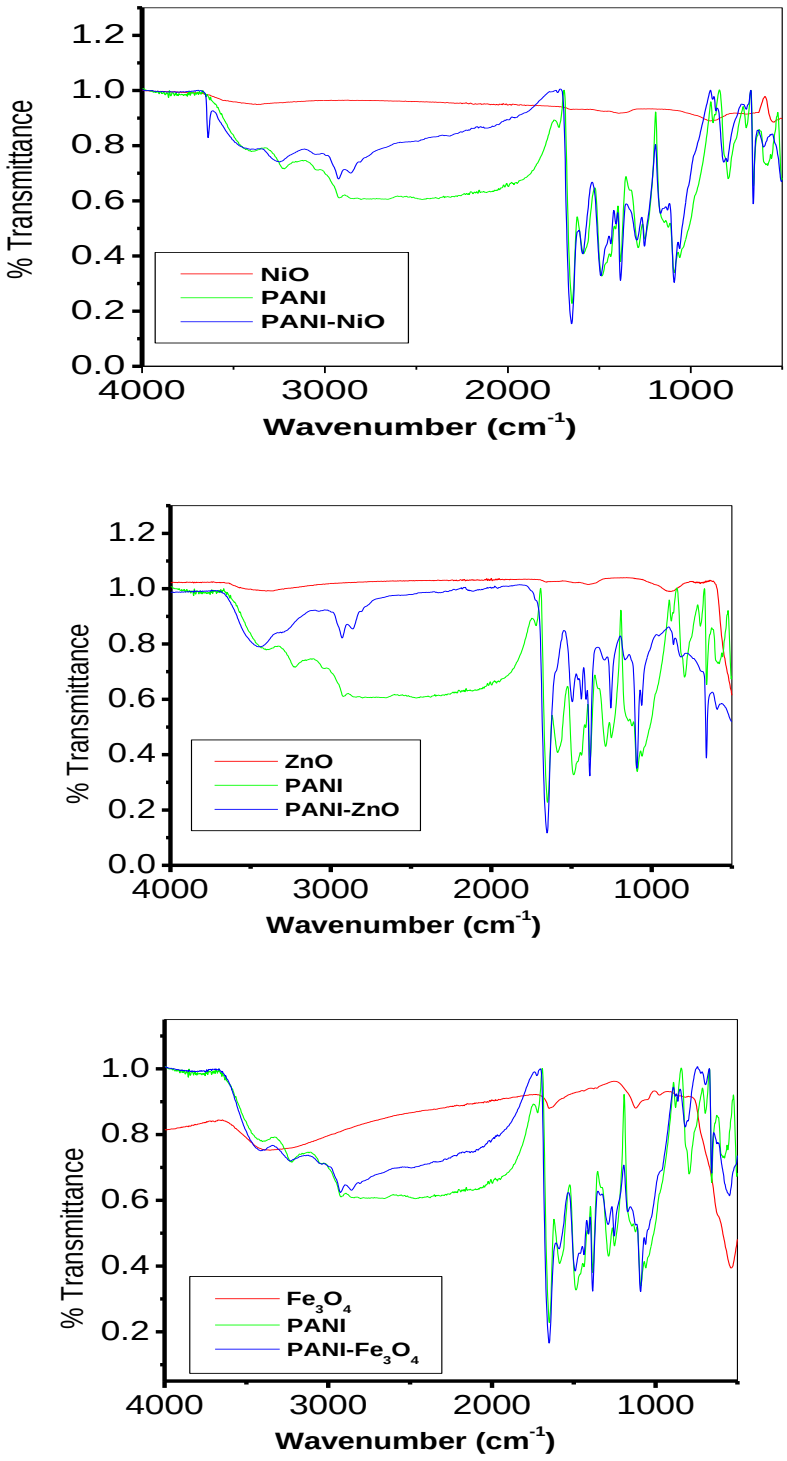

Figure 4.37: FTIR spectra of PANI, MO nanoparticles and PANI-MO nanocomposites.

From Figure 4.38a the SEM image of PANI-NiO represents formation of aggregate porous layers of PANI with well dispersed flower-like NiO nanoparticles embedded in it. The successful formation of the PANI-NiO nanocomposites can be attributed to ionic interaction between the two nanomaterials. Figure 4.38c shows the SEM for PANI-ZnO which indicate that the hexagonal particles of ZnO were hampered on addition of polyaniline after the formation of PANI-ZnO nanocomposite. The SEM images for the PANI-Fe_3O_4 showed a clustered morphology of Fe_3O_4 nanoparticles on multiwalled carbon nanotodes

4.4.1.3.2 Transmission Electron Microscope

The TEM images of PANI and PANI-MO nanocomposites are shown in Figure 4.39. The morphology of PANI nanofiber (Figure 4.39) shows small, spherical but closely packed particles probably due to π-π interactions between the PANI molecules. The estimated length of the PANI nanofibers was approximately 85 nm. The nanocomposites formed after doping NiO, ZnO and Fe_3O_4 into PANI nanofibers (PANI-NiO, PANI-ZnO and PANI-Fe_3O_4) (Figure 4.39 b-d) shows some form of aggregation probably due to π-π and electrovalent interaction between the metal oxides nanoparticles and PANI molecules [384, 385]. In addition the TEM image of PANI-Fe_3O_4 nanoparticles Figure 4.39d indicates the formation of spherical particles with an average diameter of 65 nm. The monodispersed dark region confirms the presence of Fe_3O_4 nanoparticles in the light colored region supposed PANI.

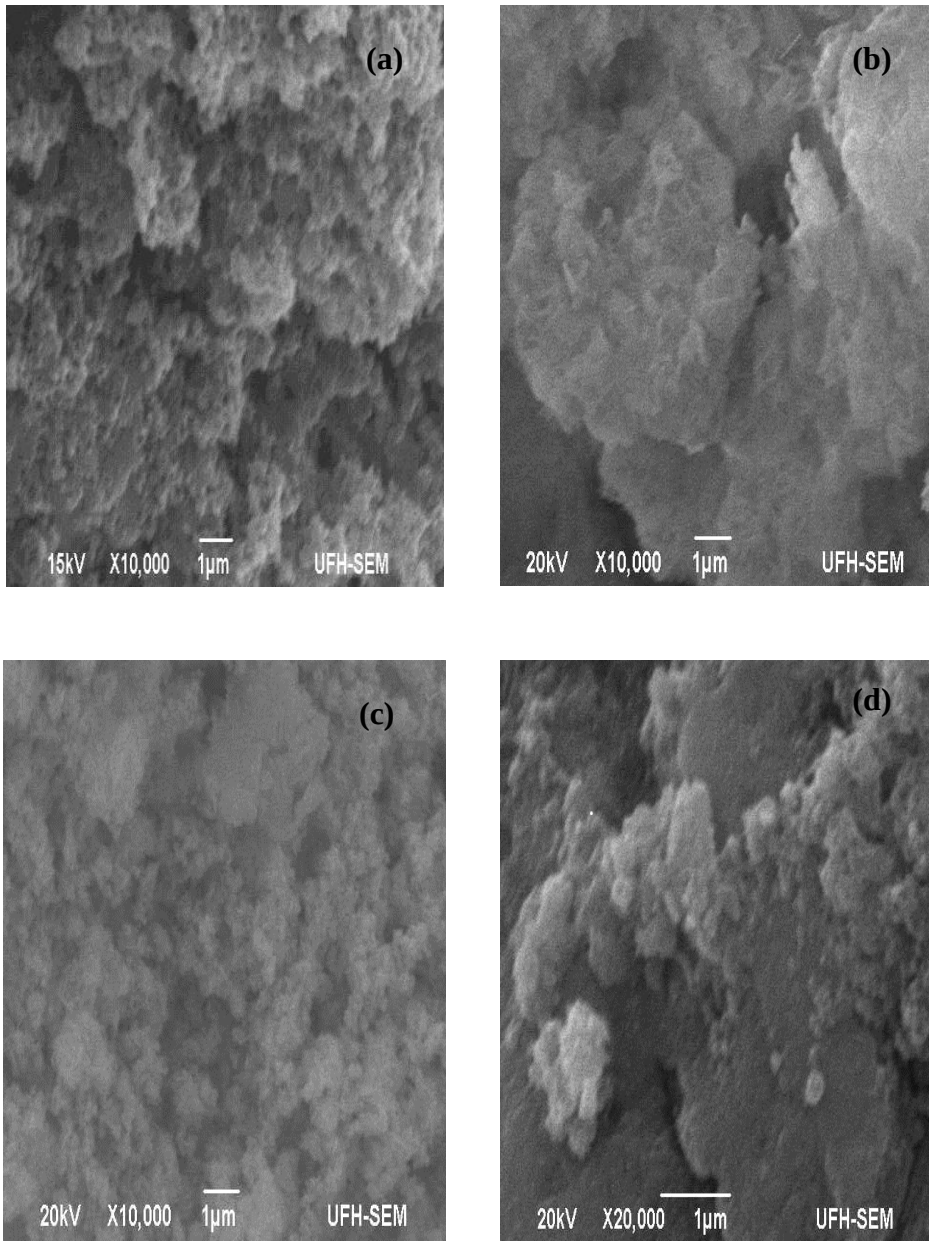

Figure 4.38: SEM images of (a) PANI nanofibers (b) PANI-NiO (C) PANI-ZnO and (d) PANI-Fe_3O_4 nanocomposites.

4.4.1.3.3 Energy Dispersed X-Ray

The EDX spectrum of the PANI-MO nanocomposites is presented in Figure 4.40. The prominence of the nickel, zinc and iron and oxygen (O ~ 36.88 %) peaks confirmed the presence of NiO, ZnO and Fe_3O_4 nanoparticles in the PANI-NiO, PANI-ZnO and PANI-Fe_3O_4. Generally, the presence of nitrogen (N = 7.94 %) and carbon (C = 6.47%) peaks though with lower peak intensity further reveals the presence of PANI molecules and the successful preparation of the PANI-MO nanocomposites.

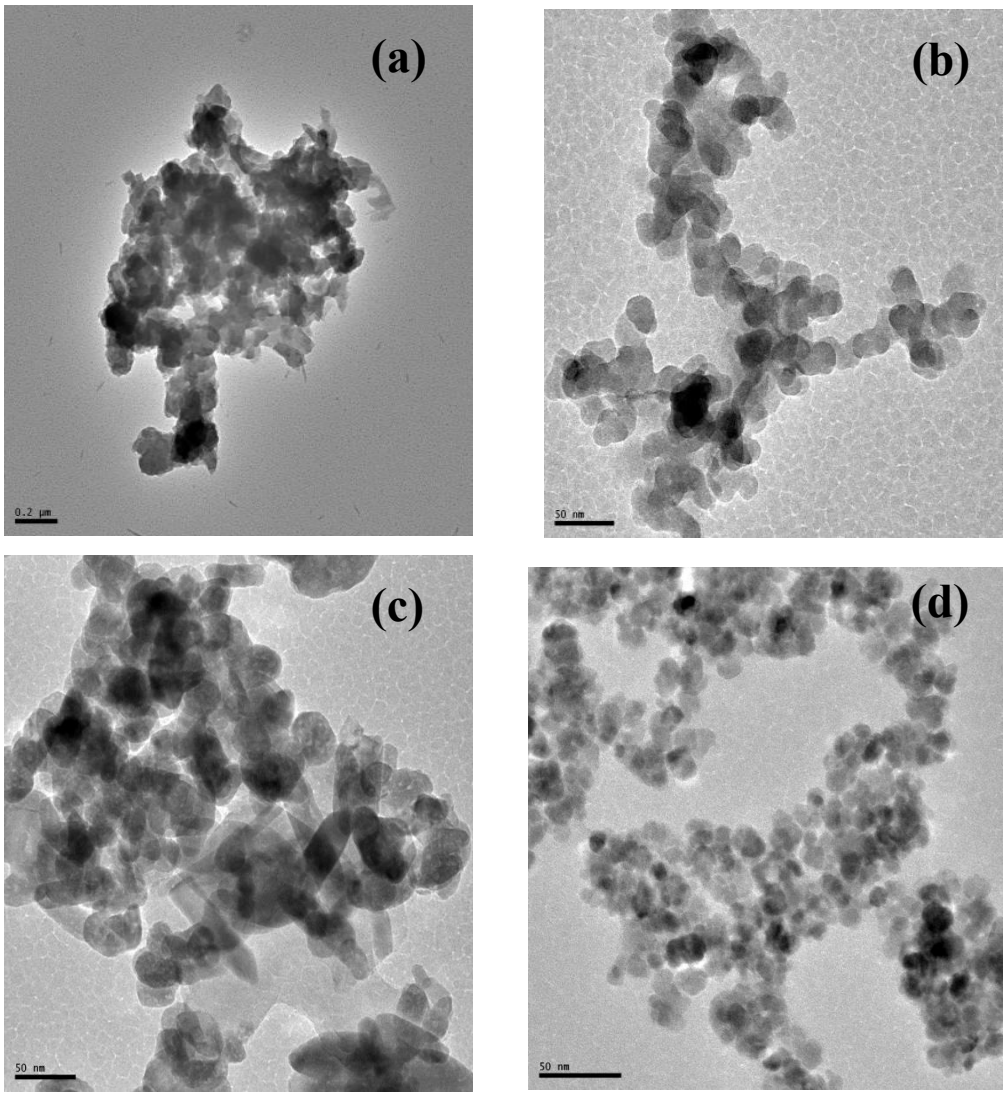

Figure 4.39: TEM images of (a) PANI nanofibers (b) PANI-NiO (C) PANI-ZnO and (d) PANI-Fe_3O_4 nanocomposites.

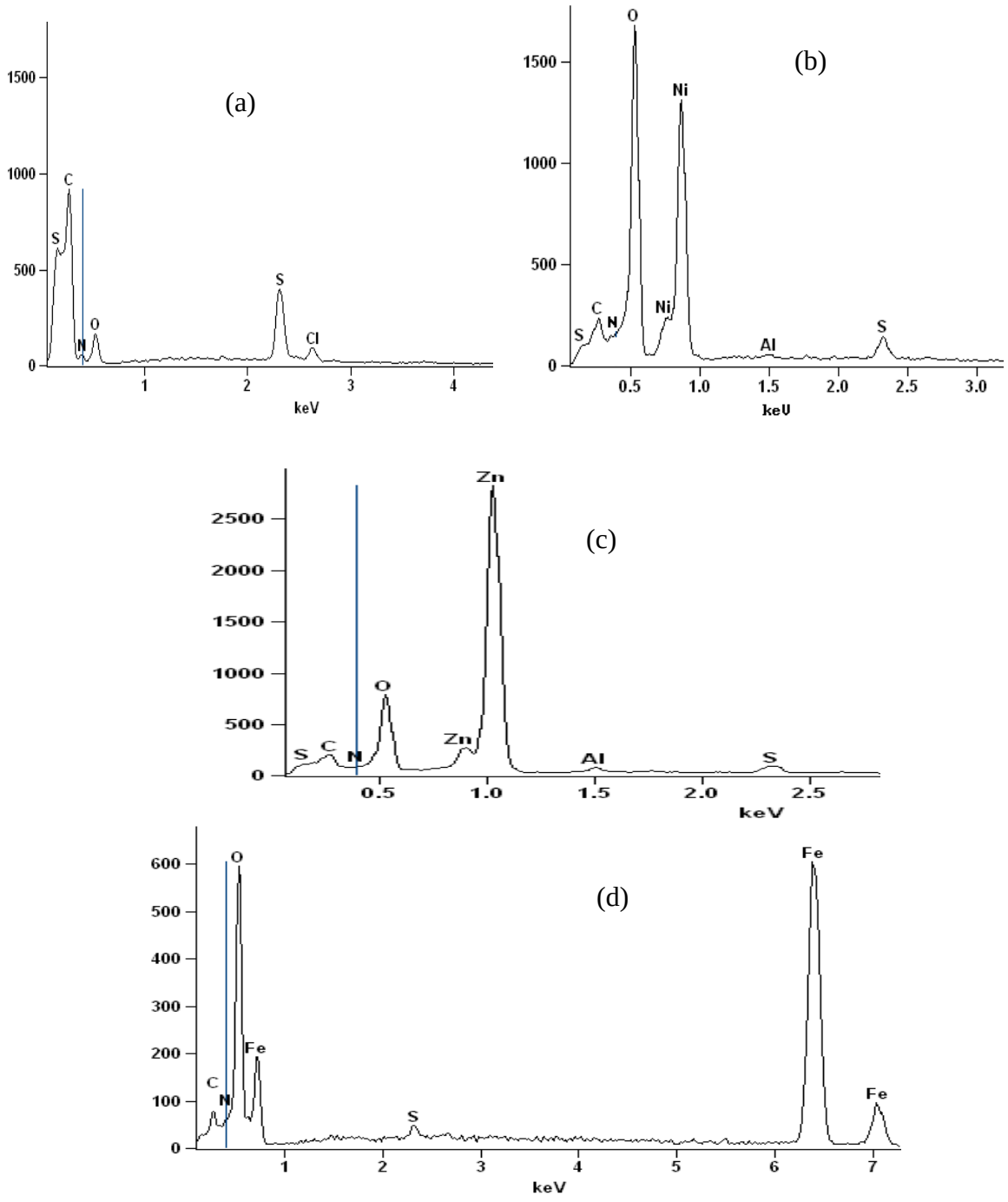

Figure 4.40: EDX spectra of (a) PANI-NiO (b) PANI-ZnO and (c) PANI-Fe_3O_4 nanocomposites.

4.4.1.3.4 X-Ray Diffraction

The XRD spectra of PANI and PANI-MO are shown in Figure 4.41. For polyaniline (PANI) Figure 4.41a, the characteristics peaks at $2\theta = 20^0$ and 26^0 correspond to (020) and (200) crystal planes of PANI [386]. After the incorporation of metal oxides nanoparticles into the PANI matrix to form PANI-MO composite, characteristics peaks that appear at $2\theta = 20^0$ and 30^0 for PANI has a reduced intensity and new peaks at $2\theta = 33^0$, 38^0, and 61^0 respectively in Figure 4.41b, corresponding to (111), (200), and (220) indices confirming the presence of NiO nanoparticles in the PANI-NiO nanocomposite formed, for PANI-ZnO nanocomposite characteristics peaks at $2\theta = 35^0$, 38^0, 62^0 and 68^0 respectively in Figure 4.41c, corresponding to (001), (101), (110) and (112) indices confirming the presence of ZnO nanoparticles. Figure 4.41c, reveals a diffused broad amorphous halo over the 2θ range of lower intensity which can be attributed to low crystallinity due to large fraction of PANI PANI-Fe_3O_4 nanocomposite. Peaks at 20° and 30° confirm the presence of PANI and the four reflection peaks around 35, 58, 65 and 72° corresponding to (311), (422), (440) and (620) indices also confirm the presence of iron oxide nanoparticles in PANI-Fe_3O_4 nanocomposite formed [384, 385]. After the incorporation of NiO into the PANI matrix to form PANI-NiO nanocomposite Figure 7.6b, characteristics peaks that appear at $2\theta = 33^0$, 38^0, and 61^0 respectively, corresponding to (111), (200), and (220) indices confirming the presence of NiO nanoparticles well dispersed in the PANI polymer matrix as observed from the SEM images. The XRD result further confirms the formation of the PANI-MO nanocomposites. Debye-Scherrer formula equation 4.3 below to calculate the crystal sizes of the nanoparticles [387].

$$d = \frac{K\lambda}{B\cos\theta} \tag{4.3}$$

where d is the average crystal size; K is a constant (0.89); λ is the wavelength (1.78901 nm) used; B is the full width at half maximum of the peak, θ is the Bragg's angle of the XRD peak, the crystal sizes of the NiO, ZnO and Fe_3O_4 nanoparticles were estimated from three prominent peaks to be ~ 50, 65 and 60 nm respectively.

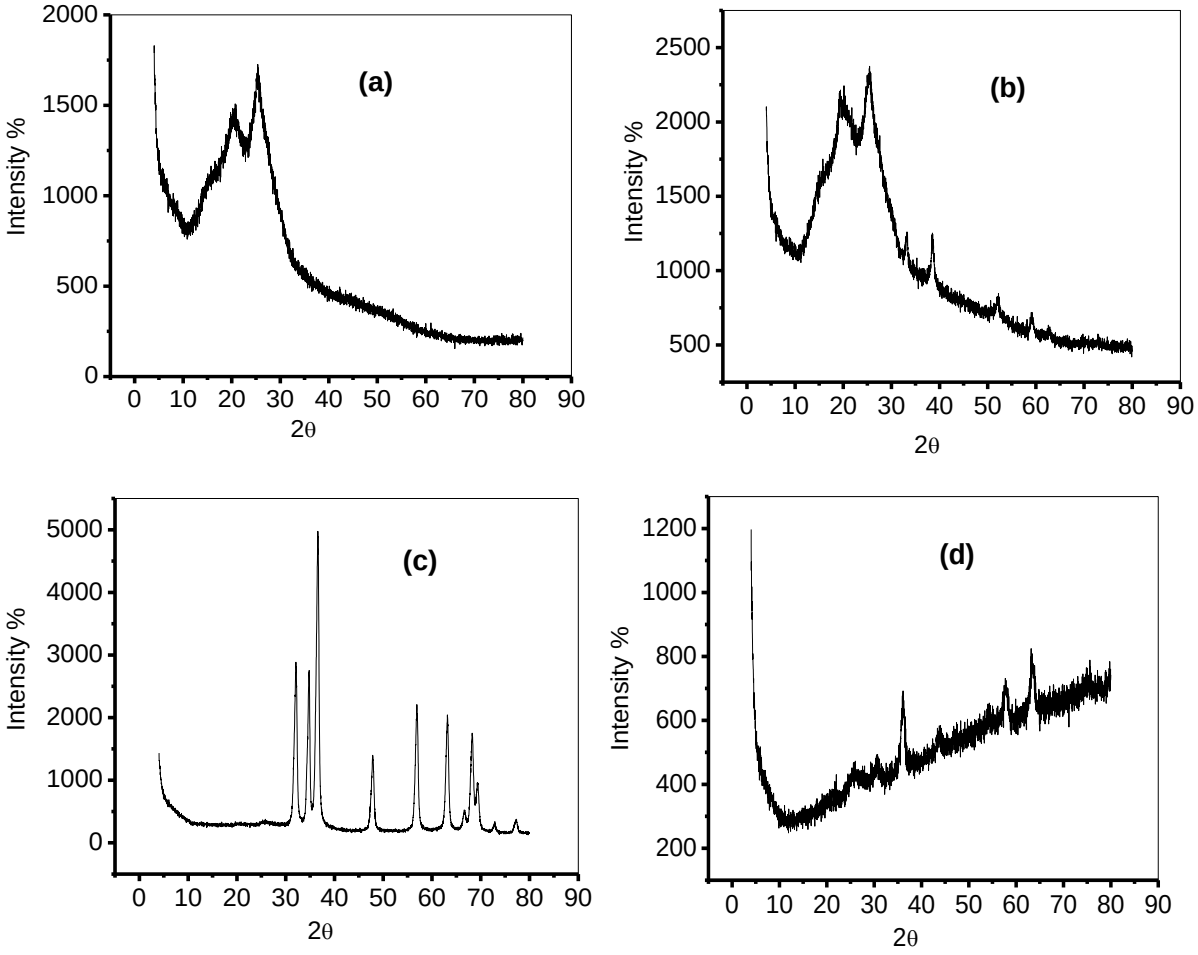

Figure 4.41: XRD spectra of (a) PANI (b) PANI-NiO (C) PANI-ZnO and (d) PANI-Fe_3O_4 nanocomposites.

4.4.2 Electrochemical characterization of electrodes

To evaluate the charge transfer properties of the PANI-MO modified electrodes where MO represents NiO, ZnO and Fe_3O_4 nanoparticles, we performed the cyclic voltammetry experiment for the modified electrodes in 5 mM $Fe(CN)_6]^{4-}/[Fe(CN)_6]^{3-}$ in 0.1 M PBS (scan rate, 25 mVs^{-1}) and the result is presented in Figure 4.42. Two pairs of redox peaks were observed at the modified electrodes (Figure 4.42). The first redox peaks ranging from the regions of 200 to 300 mV is attributed to the $Fe(CN)_6]^{4-}/[Fe(CN)_6]^{3-}$ redox process. There was no other observable peaks corresponding to Ni(II)/Ni(III), Zn(II)/Zn and Fe(II)/Fe(III) redox processes on the modified electrodes probably because of the faster electron transfer at the electrode, or overllap between the $Fe(CN)_6]^{4-}/[Fe(CN)_6]^{3-}$ peaks. Generally, the GCE-PANI-NiO, GCE-PANI-ZnO and GCE-PANI- Fe_3O_4 electrodes gave higher current response compared with bare GCE, and GCE-MO (MO = NiO, ZnO, Fe_3O_4) modified electrodes electrodes. Thus, the GCE-PANI--MO electrodes have demonstrated faster charge transport behaviour in this study.

Therefore, the anodic current density of each electrode in $Fe(CN)_6]^{4-}/[Fe(CN)_6]^{3-}$ redox probe follows the order: GCE-PANI-NiO (86.28 $mAcm^{-2}$) > GCE-PANI-ZnO (16.29 $mAcm^{-2}$) > GCE-PANI-/Fe_3O_4 (1.004 $mAcm^{-2}$). Therefore PANI-NiO has demonstrated the best electron transport properties with current density higher than that of PANI-ZnO and PANI-/Fe_3O_4 electrodes.

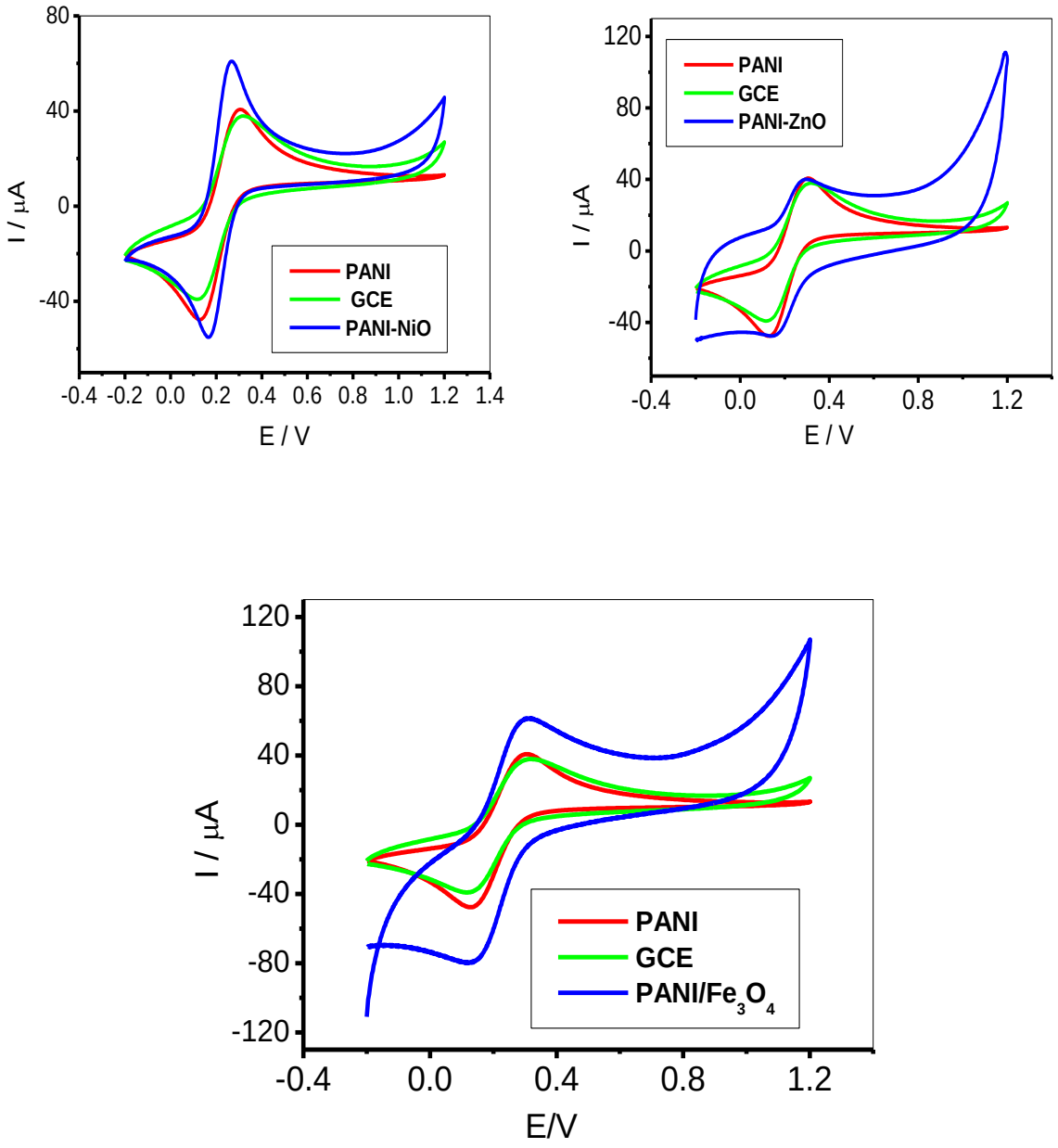

Figure 4.42: Comparative cyclic voltammogrammes for at scan rate, 25 mVs-1 in 5 mM $Fe(CN)_6]^{4-}$/$[Fe(CN)_6]^{3-}$ solution prepared in 0.1M PBS (pH 7).

The scan rate study (scan rate, 25 – 1000 mVs^{-1}) of the PANI-MO electrodes was carried out in 5 mM $Fe(CN)_6]^{4-}/[Fe(CN)_6]^{3-}$ solution prepared in 0.1M PBS (pH 7) using cyclic voltammetry experiment. Both anodic current (Ipa) and cathodic current (Ipc) increase with increase in scan rates (25 to 500 mVs^{-1}) (Figure 4.43)

The apparent charge transfer rate constant (ks) and the charge transfer coefficient (α) of a surface-confined redox couple can be evaluated from the cyclic voltammetric experiments by using the variation of anodic and cathodic peak potentials with logarithm of scan rate. The Epa shifted to more positive values with increasing the scan rate (v). The transfer coefficient (i.e. α) and the number of electrons involved in the rate-determining step can be evaluated. Based on the slope of Epa versus log (v), α was calculated to be 0.51, 0.40 and 0.38 for electrodes PANI-NiO, PANI-ZnO and PANI-Fe_3O_4 respectively. The values of ks were evaluated to be 1.58, 1.75 and 1.79 s^{-1} for electrodes PANI-NiO, PANI-ZnO and PANI-Fe_3O_4 respectively using equation 4.1.

4.4.2.1.1 Electrochemical impedance spectroscopic (EIS) studies

EIS is a complex electrochemical process that gives insightful information about reaction at the electrode-electrolyte interface. The result obtained is presented in Nyquist plot, which includes a semi-circular portion corresponding to the electron-transfer-limited process and a linear part resulting from the diffusion process [324]. The diameter of the semicircle corresponds to the electron transfer resistance (R_{ct}) of the redox probe at the electrode interface. A smaller Rct value implies that the probe has a higher interfacial electron transfer rate.

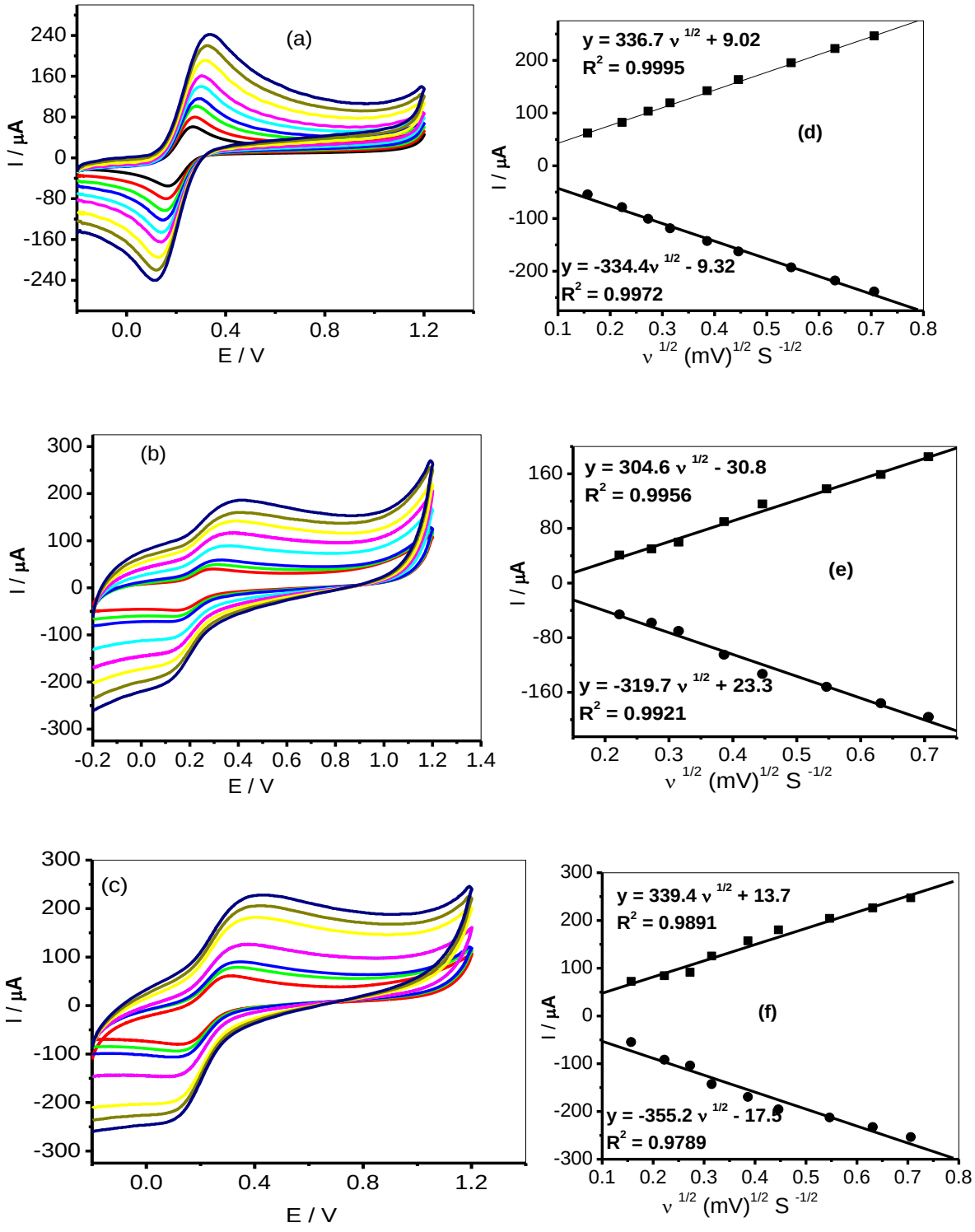

Figure 4.43: Effect of scan rate (25 – 500 mVs^{-1}) on the cyclic voltammograms of (a) PANI-NiO (b) PANI-ZnO and (C) PANI-Fe_3O_4 in 5 mM $Fe(CN)_6]^{4-}$/$[Fe(CN)_6]^{3-}$ solution prepared in 0.1M PBS (pH 7), (d-f) plot of current versus square root of scan rate at GCE-PANI- NiO, GCE-PANI-ZnO and GCE-PANI-Fe_3O_4 respectively.

The Nyquist plots obtained from the impedance experiment (at fixed potential of 0.2 V vs Ag/AgCl, sat'd KCl) and between 10 KHz and 1 Hz are presented in Figure 4.44 while the circuit model used in the fitting of the impedance data is represented in Figure 4.44 d-e. Where circuit in Figure 4.44d represent the EIS data fitting for bare GCE and Figure 4.44e represent that of the NiO, ZnO, Fe_3O_4, PANI, PANI-NiO, PANI-ZnO and PANI-Fe_3O_4 modified GCE electrodes. In this circuit model, R_s is the solution resistance, C_{dl} represents the double layer capacitance, Q or CPE is the constant phase element, and R_{ct} is the charge transfer resistance. The values obtained from the fitting of the raw impedance spectra with this circuit are presented in Table 4.13.

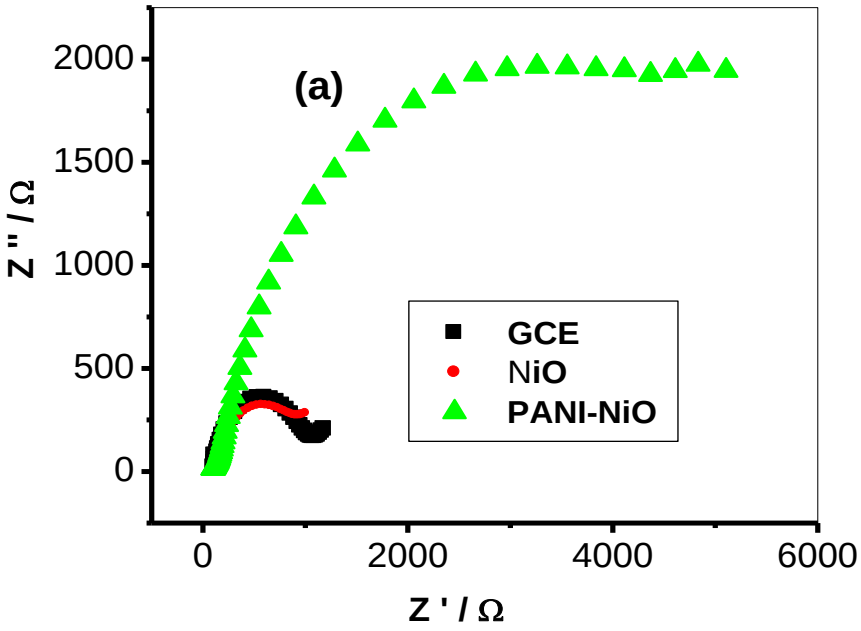
(a)
2000
1500
1000
500
0
Z '' / Ω
0
2000
4000
6000
Z ' / Ω
GCE
NiO
PANI-NiO

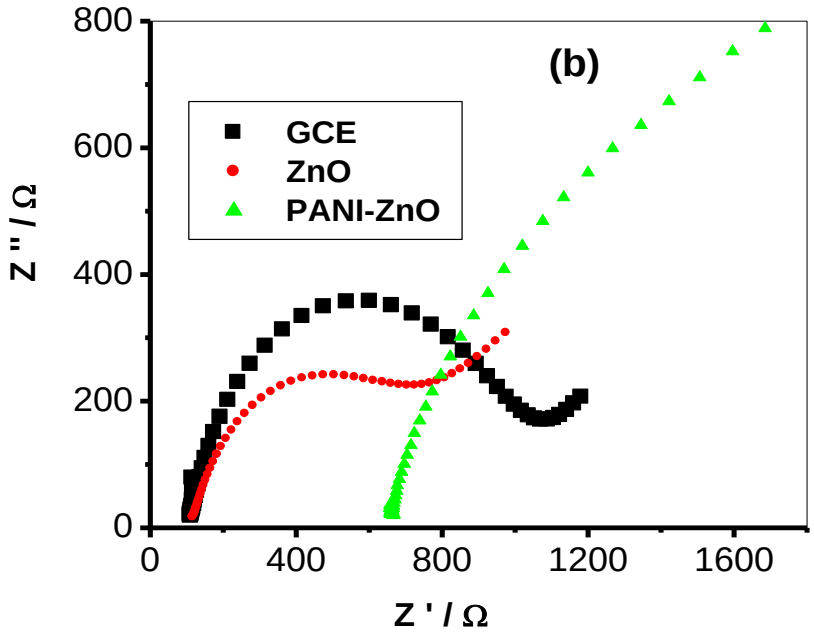
(b)
800
600
400
200
0
Z '' / Ω
0
400
800
1200
1600
Z ' / Ω
GCE
ZnO
PANI-ZnO

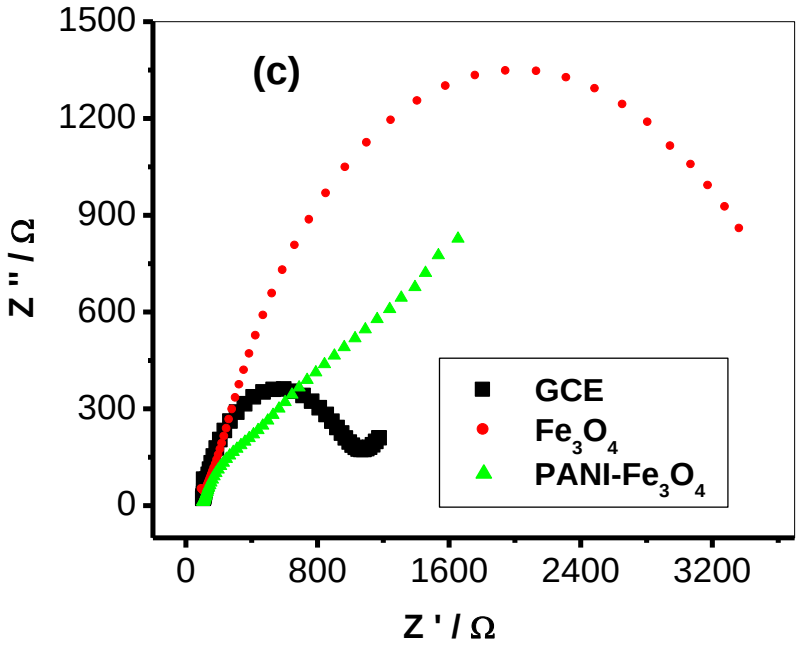

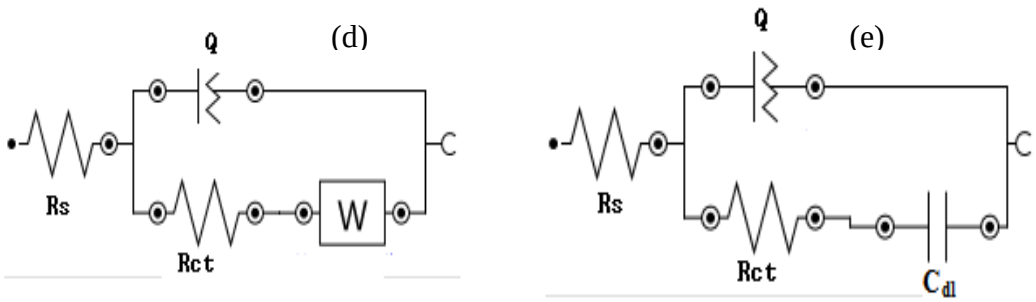

Figure 4.44: Typical Nyquist plots (a-c) obtained for the electrodes in 5 mM $Fe(CN)_6]^{4-}$/$[Fe(CN)_6]^{3-}$ solution prepared in 0.1M PBS (pH 7) at a fixed potential of 0.2 V (vs. Ag|AgCl, saturated KCl), (d –e) represents the circuit used in the fitting of the EIS data (a-c).

Table 4.13: Impedance data obtained for the bare GCE and the modified electrodes in 5 mM $Fe(CN)_6]^{4-}/[Fe(CN)_6]^{3-}$ solution at 0.2 V (vs. Ag|AgCl saturated KCl). All values were obtained from the fitted impedance spectra. The values in parentheses are percent errors of data fitting.

Electrodes	**Electrochemical impedance spectroscopy data**			
	R_s (Ω)	Q (x 10^6 nF)	R_{ct} (Ω)	C_{dl} (u F)
GCE	126.60 (0.04)	8.44 (1.19)	1237.00 (0.44)	2.13 (2.25)
GCE-NiO	104.60 (1.62)	940.00 (3.95)	442.00 (2.14)	22.63 (2.42)
GCE-ZnO	70.80 (1.10)	3200.00 (1.38)	38.20 (3.34)	83.30 (4.94)
GCE-Fe_3O_4	55.80 (8.93)	334.00 (9.50)	1915.00 (4.37)	10.61 (3.84)
GCE-PANI-NiO	51.20 (43.95)	196.00 (3.27)	276.40 (11.39)	17.20 (4.88)
GCE-PANI-ZnO	608.00 (2.85)	418.00 (2.00)	110.00 (50.75)	10.28 (15.78)
GCE-PANI-Fe_3O_4	69.40 (1.86)	634.20 (0.51)	111.40 (5.70)	3.51 (2.96)

From the R_{ct} values, the electron transport is faster for the PANI-MO electrode compared to others. The bare GCE exhibited a larger semicircle with an Rct value of 1.572 kΩ when compared with PANI-ZnO, PANI-NiO and PANI-Fe_3O_4 modified GCE (110, 276.4 and 111.4 Ω) respectively, revealing the fast electron transfer at PANI-MO modified electrode. The rapid electron transfer at the nanocomposite can be ascribed to the excellent conductivity of PANI which acts as a good electron conducting wire between MO and the electrode surface. The *n* values are less than the ideal 1.0 expected from an ideal capacitive behaviour, thus suggesting pseudo-capacitive properties for these electrodes.

4.4.3 Electrooxidation of DA at the surface of the Electrodes

Figure 4.45 shows the electrochemical response of dopamine at bare PANI-MO electrodes in 0.1M phosphate buffer solution (pH 7.0). The CV evolution of electrodes in DA is typical for DA oxidation process where the anodic peak corresponds to dopaminoquinone (DA+) (Figure 7.10) and the cathodic peak corresponds to reduction of dopaminoquinone to leucodopanoquinone [319]. The comparative results showed that DA was oxidized with less-defined DA oxidation peak at lower potentials and significantly enhanced DA oxidation current at the PANI-MO electrodes investigated (Figure 4.45a-c) where MO is NiO, ZnO and Fe_3O_4 nanoparticles.

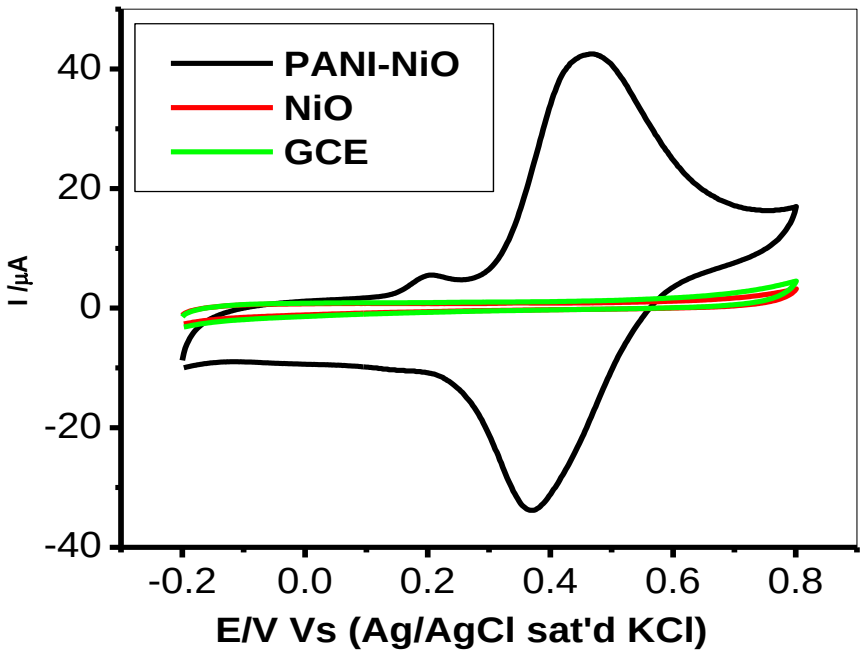

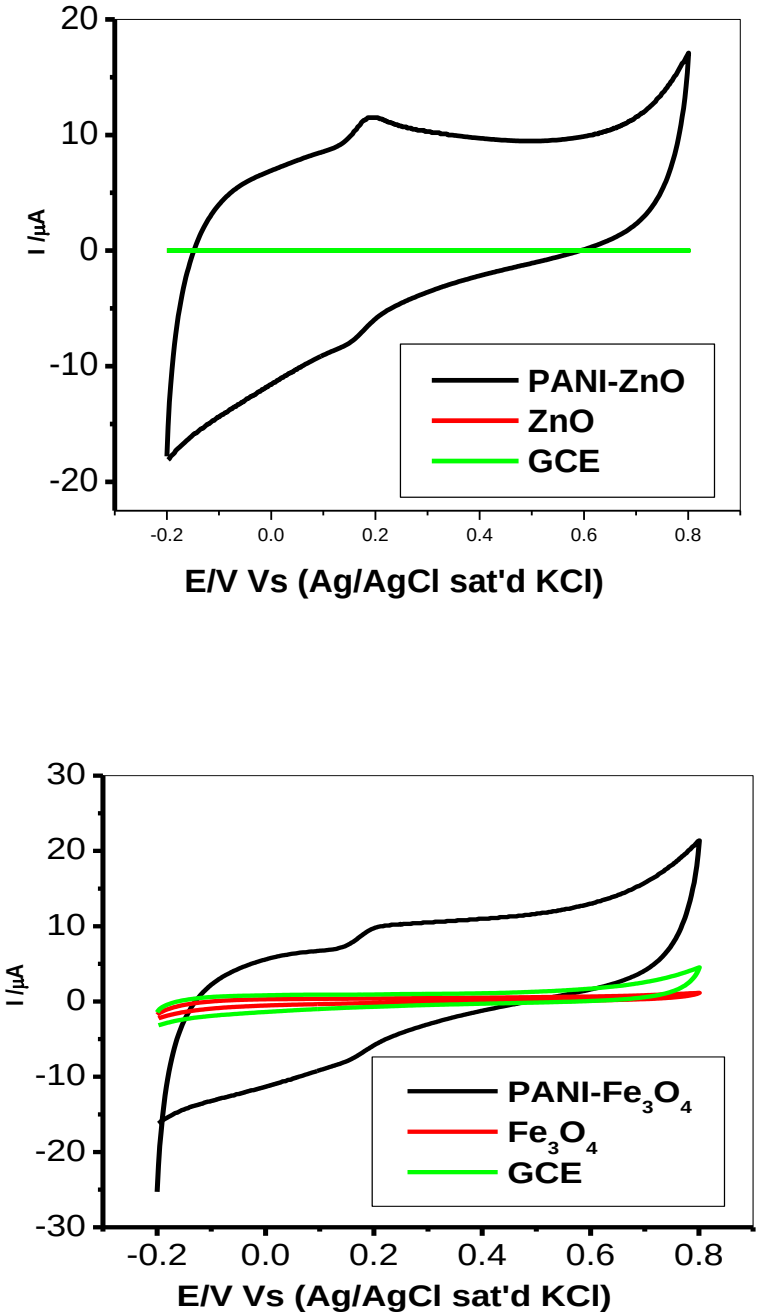

Figure 4.45: Comparative cyclic voltammogrammes of 1 x 10^{-4} M DA at 25 mVs^{-1} on bare GCE, GCE-MO and GCE modified electrodes PANI-NiO, PANI-ZnO and PANI-Fe_3O_4 respectively

The DA oxidation current at the PANI-MO electrodes follow the order: PANI-NiO (42.2 μA) > PANI-ZnO (19.4 μA) and PANI-Fe_3O_4 (9.8 μA). In terms of current density, the DA

oxidation current at the electrode follows the order: GCE- PANI-NiO (59.69 $mAcm^{-2}$) > GCE- PANI-ZnO (27.4 $mAcm^{-2}$) and > GCE- PANI-Fe_3O_4 (13.86 $mAcm^{-2}$) thus suggesting GCE- PANI-NiO electrode as the best electrode for DA oxidation in this study. The higher DA oxidation current at these electrodes indicates that the PANI has provided large surface area for effective diffusion of more DA molecules in and out of the electrode surface for maximum electrocatalytic oxidation process [388-390].

4.4.3.1 Effect of varying scan rate at constant concentration (10^{-4} M) of dopamine in pH 7.0 PBS

Cyclic voltammetry experiments were carried out with the PANI-MO to establish the impact of scan rate at constant concentration (10^{-4} M) of dopamine in pH 7.0 PBS solutions. In all cases, we observed a shift in potential with increase in scan rate (Fig. 4.46a-c). From the Randles–Sevˇcik equation for an anodic oxidation process equation (2.3, chapter 2), the plot of the peak currents (I_p) against the square root of scan rate ($\nu^{1/2}$) (Figure 4.46d-f) for scan rate ranging from 25 to 500 mVs^{-1}, gave a linear relationship and approximately zero intercept, confirming a diffusion-controlled process but with some levels of adsorbed reaction intermediates. The linear relationship of the plot confirmed that the nanocomposites were electroactive, conducting and confined to the surface.

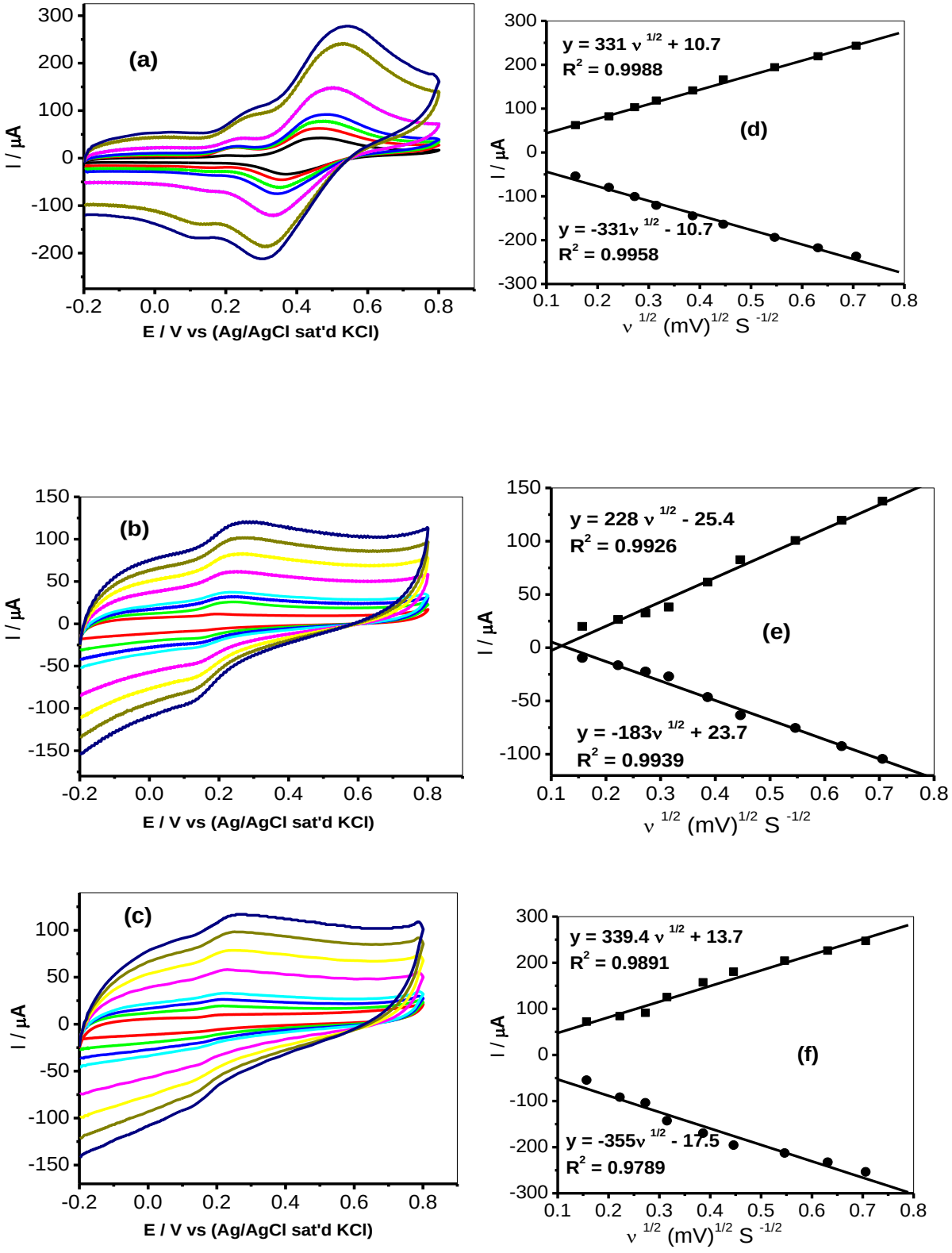

Figure 4.46: Effect of scan rate (25 – 300 mVs^{-1}) on the cyclic voltammograms of (a) GCE-PANI-NiO (b) GCE-PANI-ZnO and (b) GCE-PANI-Fe_3O_4 in 1 x 10^{-4} M DA. Where graphs (d-f) represent plot of current versus square root of scan rate at GCE-PANI- NiO, GCE-PANI-ZnO and GCE-PANI-Fe_3O_4 respectively.

The charge transfer coefficient (α) for the reaction can be evaluated from cyclic voltammetric experiments by using the variation of anodic and cathodic peak potentials with logarithm of scan rate. Based on the slope of E_{pa} with log (v), (1-α)nα was calculated to be 0.56, 0.52 and 0.96 for electrodes GCE-PANI-NiO, GCE-PANI-ZnO and GCE-PANI-Fe_3O_4 respectively. In order to get information on the rate determining step, The peak potential, E_p, is proportional to log ν (graph not shown). The slopes of E_p *vs.* log v for the different electrodes were 0.049, 0.022, and 0.078 V for electrodes GCE-PANI-NiO, GCE-PANI-ZnO and GCE-PANI-Fe_3O_4 respectively. The tafel slopes may be estimated according to the equation (4.2, chapter 4) for the totally irreversible diffusion controlled process [324]. So, the respective values of b for these electrodes were obtained as 0.098, 0.044 and 0.156 $Vdec^{-1}$. Tafel values at GCE-PANI-Fe_3O_4 was higher than the theoretical 0.118 V dec^{-1} for a one-electron process involved in the rate-determining step, while at GCE-PANI-NiO and GCE-PANI-ZnO modified electrodes the value was lower compared to the therotical value. Therefore the high Tafel values suggest adsorption of dopamine or its reaction intermediate at the electrode surface since high Tafel values have been attributed to the adsorption of reactants or intermediates on the electrode surfaces and/or reactions occurring within a porous electrode structure [325]. Adsorption process at the electrode can be linked with the porous polymer nanocomposite layer [325].

The value of k_s was evaluated to be equal to 1.51, 1.56 and 1.04 s^{-1} for electrodes GCE-PANI-NiO, GCE-PANI-ZnO and GCE-PANI-Fe_3O_4 respectively. According to the kinetics of electron process, when the rate constant is larger than 10^{-2} cm/s , the electron transfer process is very fast, and the electrode reaction is reversible, and when $10^{-4} < k_s < 10^{-2}$ cm/s, the electrode reaction is a quasireversible process. So the electrode reaction of DA on the proposed electrodes is reversible process

4.4.3.2 Electrochemical impedance spectroscopic (EIS) studies

The Nyquist plots obtained from the impedance experiment (at fixed potential of 0.2 V vs Ag/AgCl, sat'd KCl) and between 10 KHz and 1 Hz are presented in Figure 4.47. While the circuit model used in the fitting of the impedance data is represented in Figure 4.47d-f. Figure 4.47d represent the circuit used for the EIS data fitting for bare GCE and MO (MO: NiO, ZnO and Fe_3O_4 and PANI-NiO. Figure 4.47e represents that of PANI-ZnO and PANI-Fe_3O_4. In this circuit model, R_s is the solution resistance, C_{dl} represents the double layer capacitance, Q or CPE is the constant phase element, and R_{ct} is the charge transfer resistance. The values obtained from the fitting of the raw impedance spectra with this circuit are presented in Table 4.14.

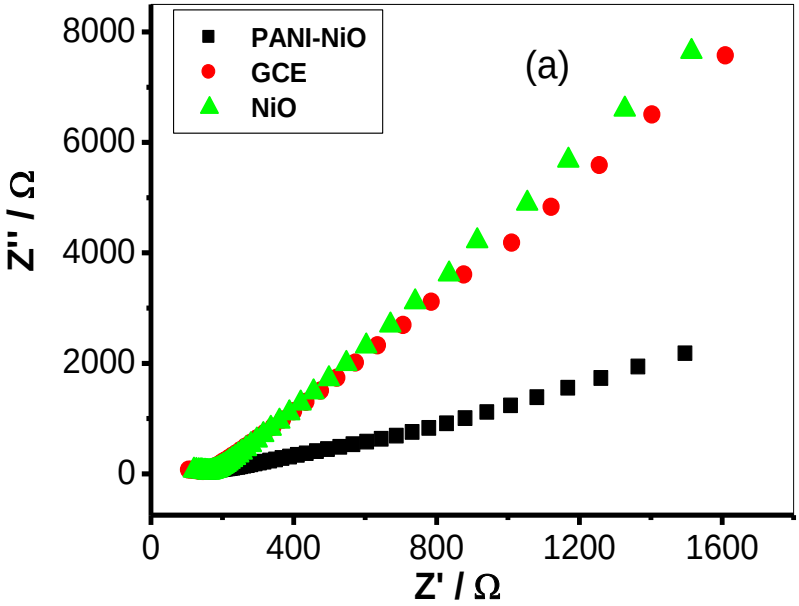
PANI-NiO
GCE
NiO
(a)
Z'' / Ω
Z' / Ω
0
2000
4000
6000
8000
0
400
800
1200
1600

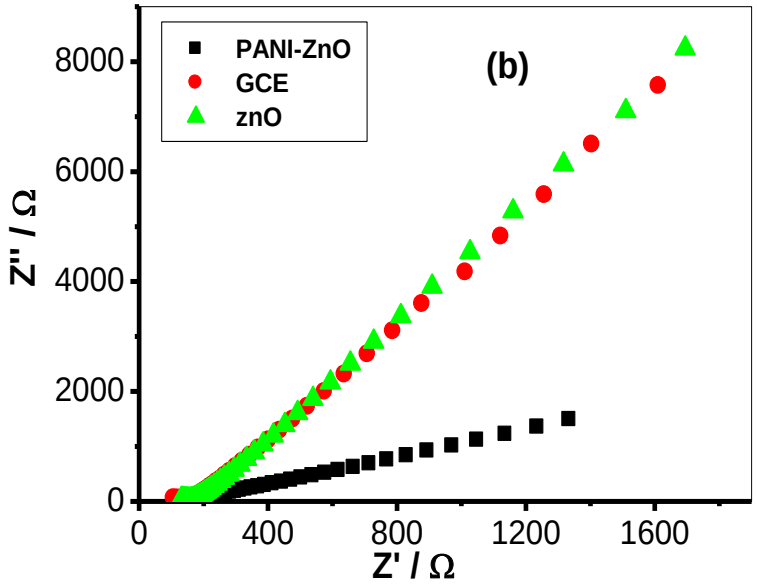
PANI-ZnO
GCE
znO
(b)
Z'' / Ω
Z' / Ω
0
2000
4000
6000
8000
0
400
800
1200
1600

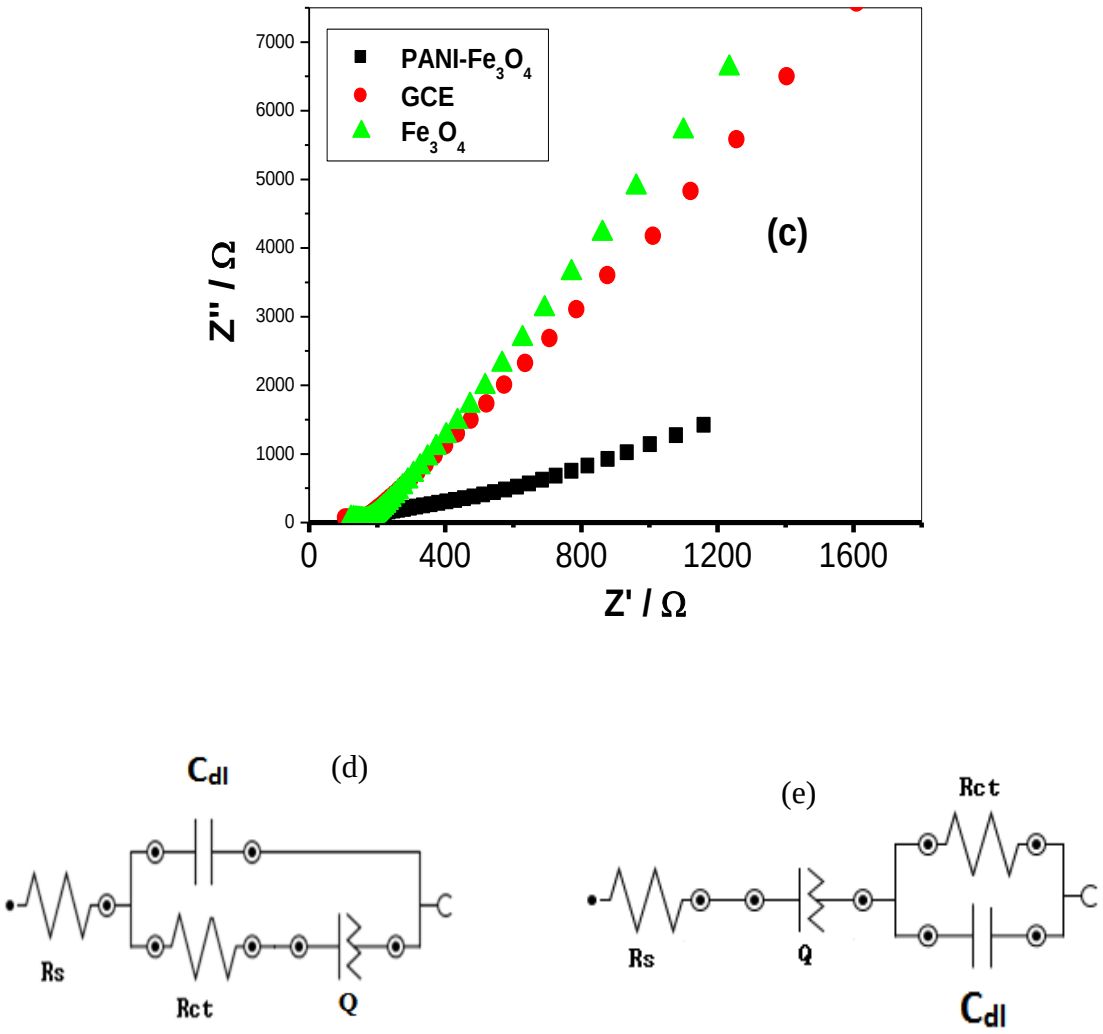

Figure 4.47: Typical Nyquist plots (a-c) obtained for the electrodes in 1 mM dopamine solution prepared in 0.1M PBS (pH 7) at a fixed potential of 0.2 V (vs. Ag|AgCl, saturated KCl). Figures 7.12 (d-e) represent the circuits used in the fitting of the EIS data (a-c).

Table 4.14: Impedance data obtained for the bare GCE and the modified electrodes in 1 mM dopamine solution at 0.2 V (vs. Ag|AgCl saturated KCl). All values were obtained from the fitted impedance spectra. The values in parentheses are percent errors of data fitting.

Electrodes	**Electrochemical impedance spectroscopy data**			
	R_s (Ω)	Q (x 10^6 nF)	R_{ct} (Ω)	C_{dl} (u F)
GCE	54.70 (9.05)	2.77 (1.33)	98.40 (4.63)	163.70 (10.56)
GCE-NiO	80.40 (0.50)	307.00 (3.25)	8.50 (7.77)	78.50 (15.72)
GCE-ZnO	62.60 (8.53)	2.65 (1.31)	104.80 (4.72)	152.30 (10.72)
GCE-Fe_3O_4	81.20 (7.95)	80.30 (3.04)	80.40 (7.47)	180.90 (16.73)
GCE-PANI-NiO	161.60 (1.16)	131.00 (1.89)	64.00 (10.48)	1.93 (9.34)
GCE-PANI-ZnO	143.60 (0.53)	187.40 (0.87)	13.08 (34.18)	253.80 (39..23)
GCE-PANI-Fe_3O_4	131.10 (0.79)	206.40 (1.38)	81.50 (8.24)	42.90 (9.39)

From the R_{ct} values, the electron transport is faster for the PANI-MO electrode compared to others. The bare GCE exhibited a larger semicircle with an Rct value of 1.572 kΩ when compared with PANI-ZnO, PANI-NiO and PANI-Fe_3O_4 modified GCE (13.08, 64 and 81.50 Ω) respectively, revealing the fast electron transfer at PANI-MO modified electrode. The rapid electron transfer at the nanocomposite can be ascribed to the excellent conductivity of PANI which acts as a good electron conducting wire between MO and the electrode surface. The *n* values are less than the ideal 1.0 expected from an ideal capacitive behaviour, thus suggesting pseudo-capacitive properties for these electrodes.

4.4.4 Electroanalysis of Dopamine at PANI-MO modified electrodes

Since the proposed PANI-MO glassy carbon electrodes have demonstrated favourable electrochemical response towards DA, they have been used for determination of DA. To improve the sensitivity of the developed sensors in detection of dopamine, square wave voltemmetry (SWV) technique has been used. Figure 4.48, is the square wave voltammogram

at the PANI-MO modified electrodes. The electrochemical oxidation current of dopamine at these electrodes is linearly proportional to its concentration in the range 2×10^{-14} mol/L to 9.9×10^{-8} mol/L. The respective detection limit for dopamine on the electrodes were calculated based on the relationship LoD = 3.3 δ/m [294] where δ is the relative standard deviation of the intercept of the y-coordinates from the line of best fit, and m the slope of the same line to be 6.33×10^{-10}, 1.15×10^{-10}, and 3.14×10^{-6} mol/L (S/N = 3) at modified electrodes GCE-PANI-NiO, GCE-PANI-ZnO and GCE-PANI-Fe_3O_4 respectively. The best modified electrode based on the limit of detection is the GCE-PANI-ZnO. The limit of detection obtained for GCE-PANI-NiO, GCE-PANI-ZnO and GCE-PANI-Fe_3O_4 were compared favourably and found to be better than the limit of detection reported for other electrodes in literature (see Table 4.15)

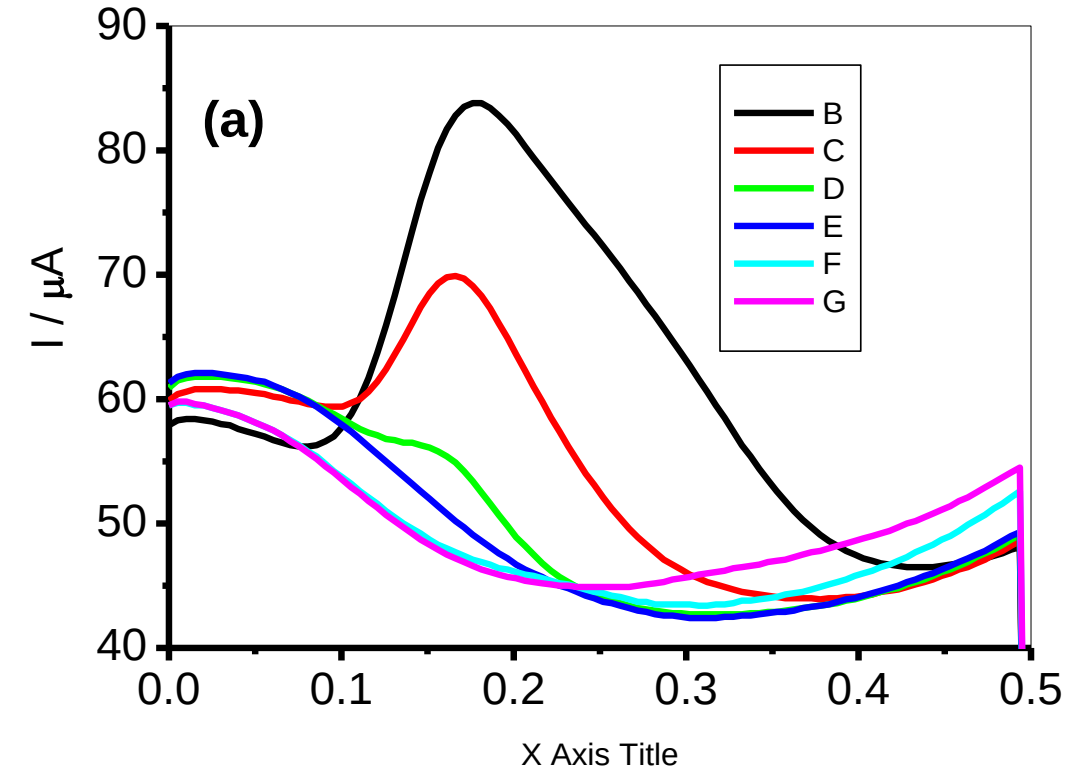
(a)
B
C
D
E
F
G
I / µA
90
80
70
60
50
40
0.0
0.1
0.2
0.3
0.4
0.5
X Axis Title

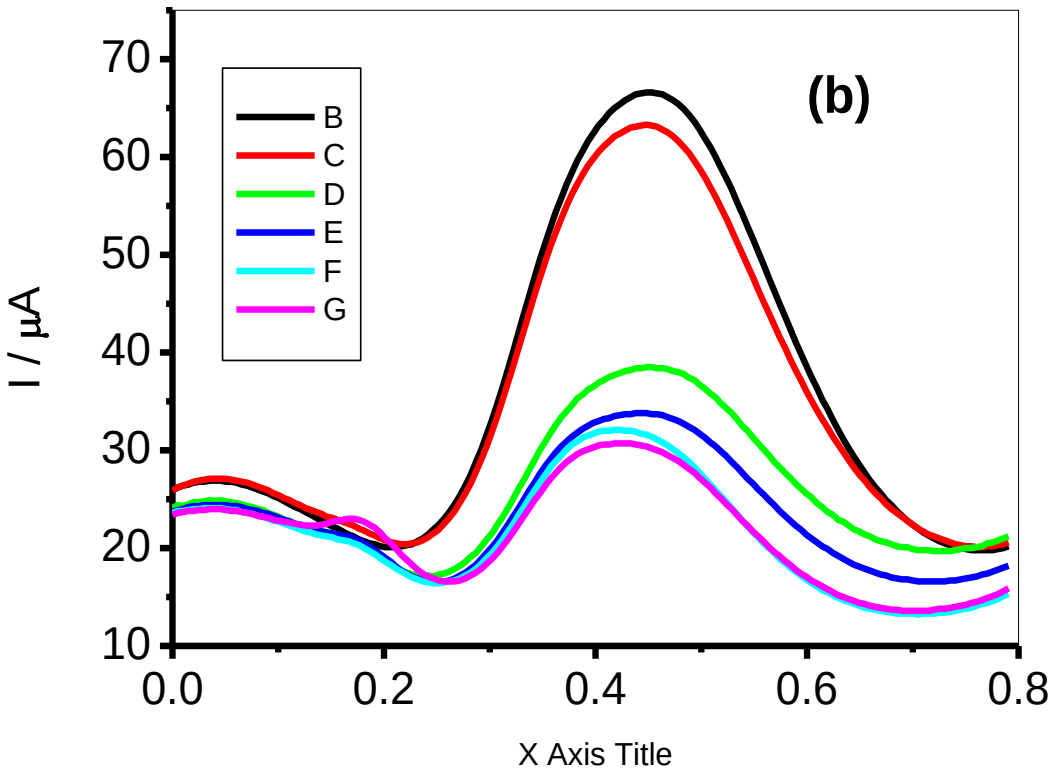
(b)
B
C
D
E
F
G
I / µA
70
60
50
40
30
20
10
0.0
0.2
0.4
0.6
0.8
X Axis Title

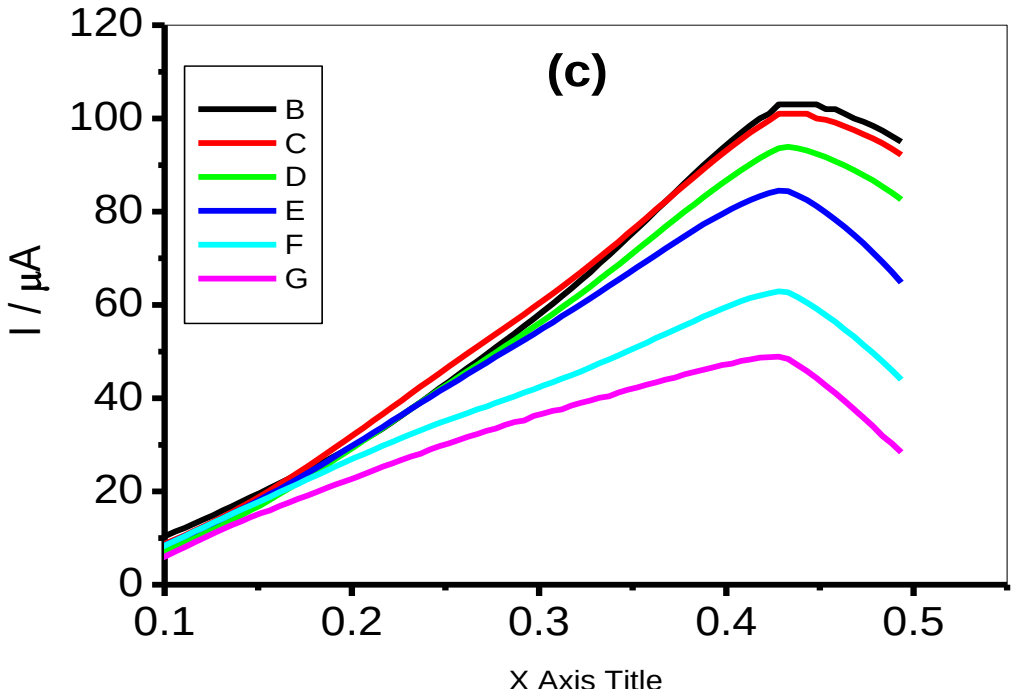

Figure 4.48: Square wave voltammogrammes of (a) GCE-PANI-NiO (b) GCE-PANI-ZnO and (c) GCE-PANI-Fe_3O_4 in PBS pH 7 containing 2 x 10^{-14} M to 9.9 x 10^{-8} M DA concentration represented as B-G.

Table 4.15: Comparison of different electrochemical sensors for the determination of dopamine.

Electrode material	Detection Limit (M)	References
CNS/Pt/PANI/GCE	0.6 x 10^{-6}	[391]
PANI-NF/Pt	33.3 x 10^{-6}	[392]
PANI/AgCl/GCE	5.4 x 10^{-8}	[393]
GCE-PANI-NiO	50.8 x 10^{-9}	This work
GCE-PANI-ZnO	60.6 x 10^{-9}	This work
GCE-PANI-Fe_3O_4	10.9 x 10^{-8}	This work

4.4.5 Interference study: Detection of DA and SE in the presence of AA

Figure 4.49 is the cyclic voltammetric responses of GCE-PANI-NiO, GCE-PANI-ZnO and GCE-PANI-Fe_3O_4 in 0.1 M pH 7.0 PBS containing mixture of 10^{-2} M AA, approximately 1000 times concentration of DA and SE. The simultaneous detection of AA, DA and SE even at AA concentration (9.09 mM) which is 1000 times as high as DA and SE concentration (9.09 µM) was successful at the GCE-PANI-MO electrodes with potential separation of about AA/DA 400, 350, 200 mV, AA/SE 600, 550, 350 mV and DA/SE 2000, 200,150 mV observed at GCE-PANI-NiO, GCE-PANI-ZnO and GCE-PANI-Fe_3O_4 electrodes respectively.

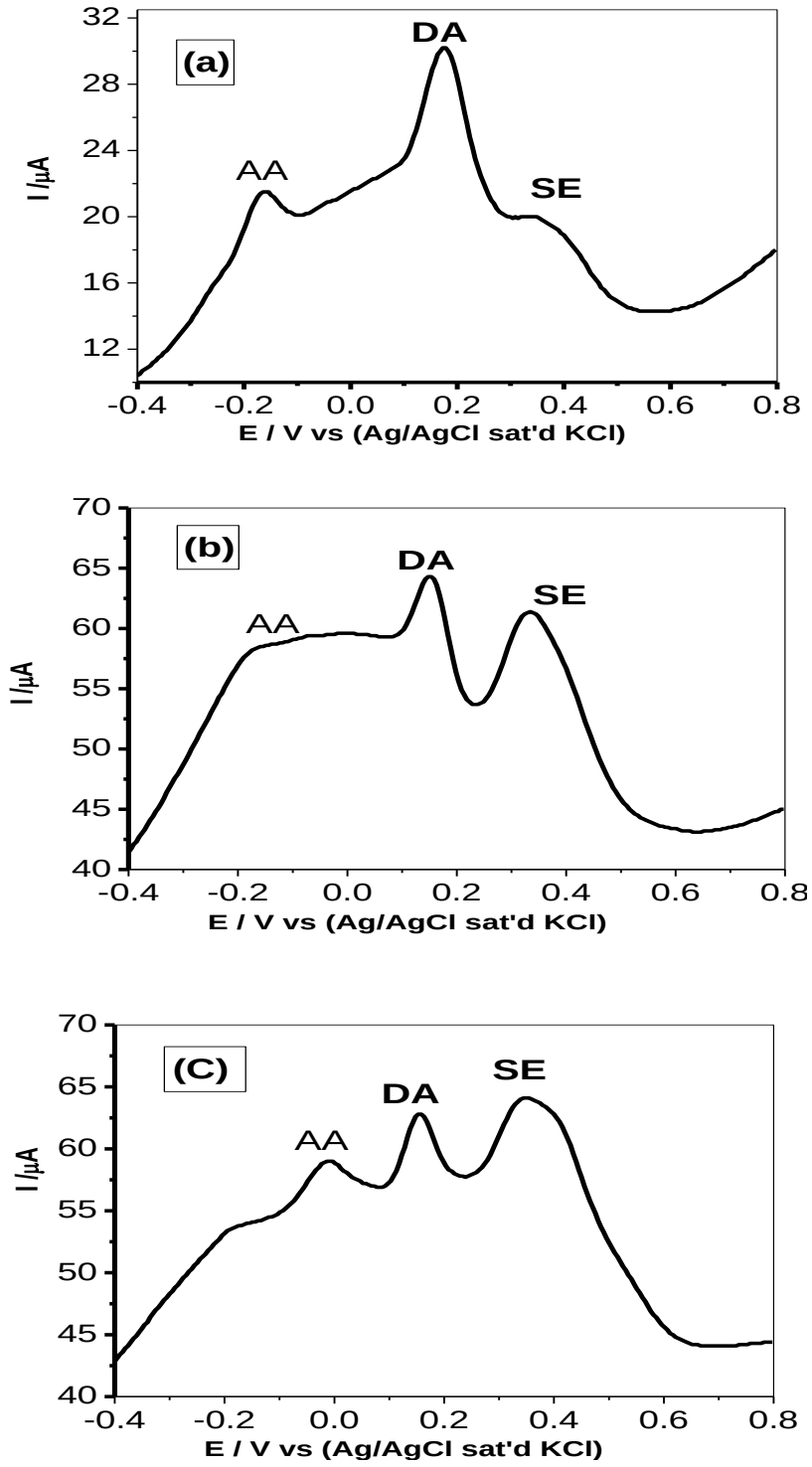

Figure 4.49: Cyclic voltammogram of 10^{-4} M of AA, DA and SE at (a) GCE-PANI-NiO (b) GCE-PANI-ZnO and (c) GCE-PANI-Fe_3O_4 electrodes in PBS pH 7.0.

4.5 Electrochemical Detection of Phenanthrene Using Nickel Oxide Doped PANI - based Modified Electrodes

The search for effective method in the determination and quantifications of contaminants in the environment has been a great concern in the heart of researchers. Pollution free environment is truly the desire of everyone. PAHs are among the organic pollutants that have been identified as teratogenic, mutagenic and carcinogenic in nature [394]. They have dangerous effects on both aquatic organisms and human beings through natural and anthropogenic activities, which are generated from industrial, agricultural and domestic waste. Examples of the PAHs are anthracene, phenanthrene, fluoranthene, pyrene [395, 396]. On the other hand nickel oxide (NiO) is an important transition metal oxide with cubic lattice structure. It has attracted variety of applications such as in catalysis [397], battery cathodes [398, 399], gas sensors [400], electrochromic films [401], and magnetic materials [402]. It possesses anodic electrochromism, excellent durability and electrochemical stability, large spin optical density and various manufacturing possibilities [403].

4.5.1 Spectroscopic and microscopic characterisation: see section 4.4.1

4.5.1.1 Electrochemical characterization of modified electrodes

Figure 4.50 is the cyclic voltammograms of polyaniline nanofibers on glassy carbon electrode (GCE-PANI) in 1 M H_2SO_4 solution at a scan rate of 25 mVs^{-1}. In this electrolyte, three redox peaks AA^1, BB^1 and CC^1 at (0.2/0.12 V), (0.4/0.32 V) and (0.52/0.42 V) oxidation/ reduction potentials respectively were observed. The oxidation state increases from completely reduced leucoemeraldine to emeraldine and to the fully oxidized form pernigraniline. However not all the possible PANI states are conductive, actually PANI emeraldine form is the only conductive form [394]. The first redox peak AA' is due to the conversion of leucoemeraldine to emeraldine salt while the third redox peaks CC' is due to the conversion of emeraldine salt

to pernigraniline form. The redox couple BB' at the centre is due to impurities such as the benzoquinone and the hydroquinone in the polyaniline [404, 405-406].

The current density increases with the number of cycles which indicates the transition of emeraldine to pernigraniline form as well as the uniform growth of the PANI layer [404, 407]. The variation of I_p with $v^{½}$ was carried out for the first oxidation peak to ensure the reversibility of the polymer. The peak current (I_p) depends linearly on the square root of scan rate ($v^{1/2}$) (not shown) indicating the diffusion-controlled process.

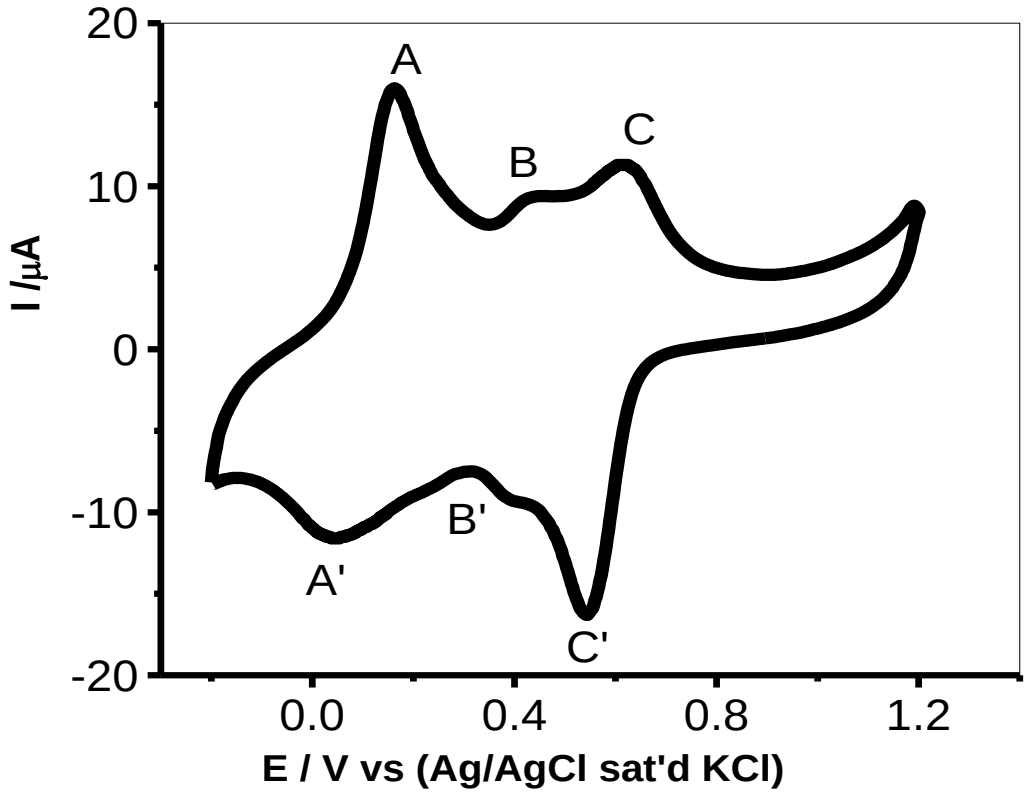

Figure 4.50: Cyclic voltammogram of GCE-PANI nanofibers modified electrode in 1 M H_2SO_4 at a scan rate of 25 mV s^{-1}.

A comparative cyclic voltammetry study was also performed on the modified electrode GCE, GCE/PANI and GCE/PANI-NiO in 1 M HCl at scan rate, 20 mVs^{-1}. The CV curve shows two sets of distinct redox activities for all the electrodes as indicated by the two pairs of anodic and cathodic current peaks (Figure 4.51a). The first redox couple which appears between 0 and 0.15 V (*vs.* Ag/AgCl) is associated with the conversion of the fully reduced leucoemeraldine base to the partially oxidized emeraldine, and the second couple occurring between 0.56 and 0.60 V *vs.* Ag/AgCl indicate the conversion of emeraldine to the fully oxidized pernigraniline form [404, 405-406]. From the overlaid cyclic voltammetry shown in Figure 4.51a. It is obvious that the GCE/PANI-NiO have a higher current response than the other electrodes. The result indicate that the modification of the PANI-NiO nanocomposites onto the GC electrode surface increase the peak current in 1 M HCl (I_{pa}: 59.8 μA) compared to GCE-PANI (I_{pa}: 17.8 μA) and the unmodified GC electrode (I_{pa}: 0.43 μA). This could be attributed to the aggregated layers of the PANI nanofilms with high surface area and good electrical conductivity which facilitate faster and more electron transport between the electrolyte and the base GC electrode. The embedded conducting NiO nanoparticles also form a synergy with the PANI nanofibers forming PANI-NiO nanocomposites with newer functionalities and enhanced electron transport behaviour than PANI or GC electrode alone. Similar results have been reported for modified electrodes in literature [404, 405-406]. Therefore to further investigate the kinetics of electrode reactions, cyclic voltammograms at different scan rates was obtained for the modified GCE-PANI-NiO electrode.

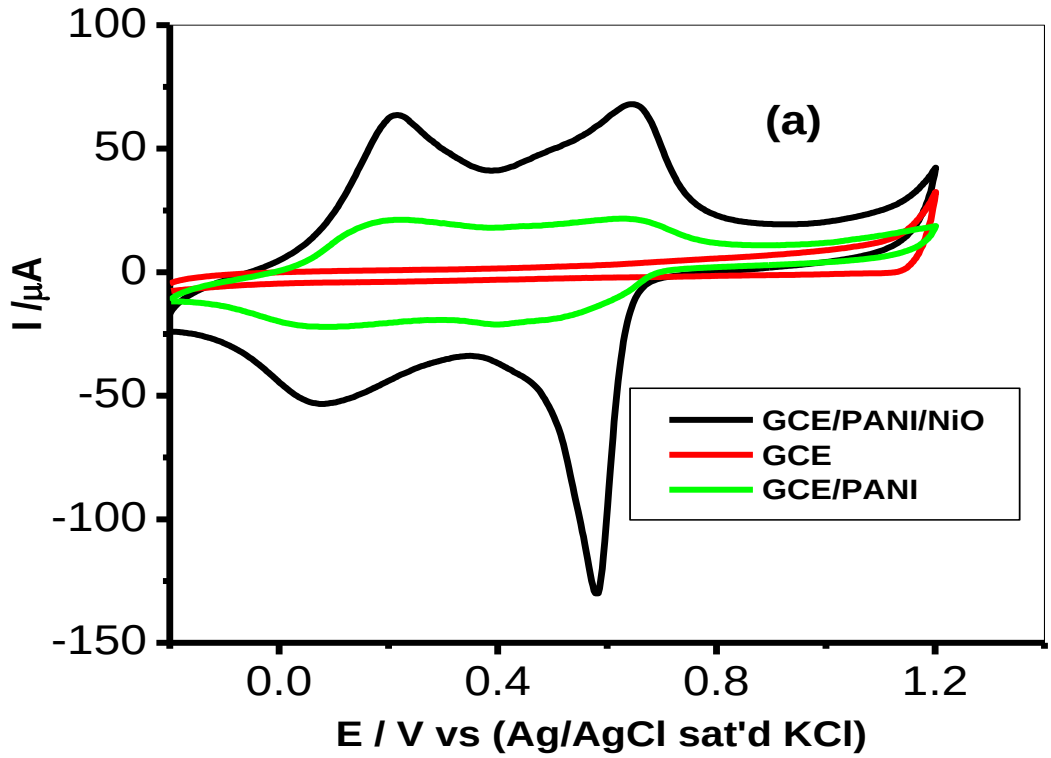
(a)
I /μA
E / V vs (Ag/AgCl sat'd KCl)
GCE/PANI/NiO
GCE
GCE/PANI
100
50
0
-50
-100
-150
0.0
0.4
0.8
1.2

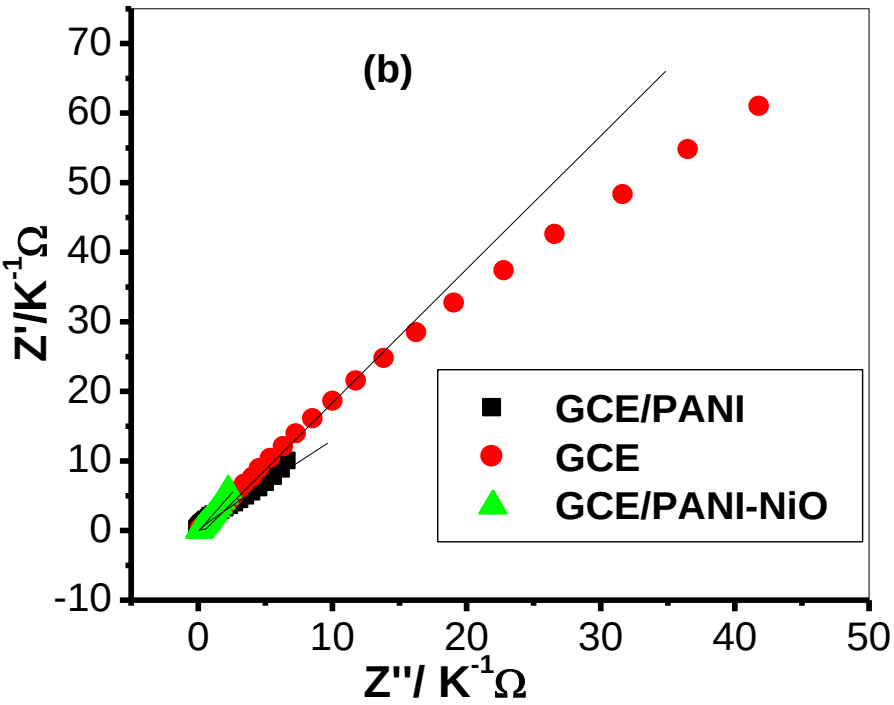
(b)
Z'/K-1Ω
Z''/ K-1Ω
GCE/PANI
GCE
GCE/PANI-NiO
70
60
50
40
30
20
10
0
-10
0
10
20
30
40
50

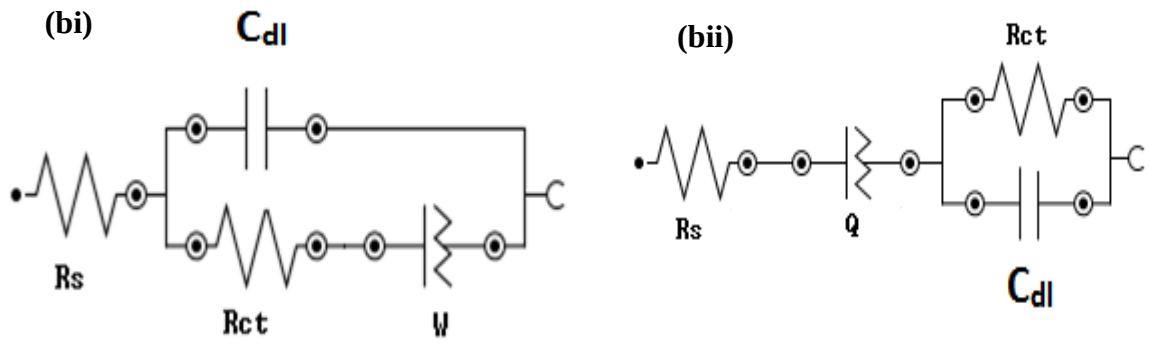

Figure 4.51: (a) Comparative cyclic voltammograms for GCE, GCE/PANI and GCE/PANI-NiO in 1 M HCl at scan rate, 20 mVs^{-1}. (b) Nyquist plot of the EIS measurement for GCE, GCE/PANI and GCE/PANI-NiO in 1 M HCl. (bi) the Randle's equivalent circuit used for fitting the Nyquist plots for GCE and (bii) the Randle's equivalent circuit used for fitting the Nyquist plots GCE/PANI and GCE/PANI-NiO respectively.

4.5.1.2 Electrochemical Impedance spectroscopy study

Electrochemical impedance spectroscopy (EIS) has been an important technique in investigating the complex electrochemical process taking place on the surface of an electrode or charge transfer process at the electrode/electrolyte interface. It is known to be an effective method of probing the extent of electron transport properties of the modified electrodes. Electrochemical impedance was used to investigate the charge transport process of the GCE, GCE/PANI and GCE/PANI-NiO electrodes in 1 M HCl electrolyte and this was done by monitoring charge transfer resistance (R_{ct}) at the electrode/electrolyte interface. The measurement was done in 1 M HCl solution (at fixed potential of 0.2 V vs Ag/AgCl, sat'd KCl) within a frequency range of 10 KHz to 0.1 Hz. The Nyquist plots obtained for the electrodes are presented in Figure 4.51b. The impedance data were fitted with an electrical circuit model represented as inset in Figure 8b where R_s is the solution resistance, C_{dl} is the double layer capacitance, R_{ct} is the charge transfer resistance and Q is the constant phase element. The circuit RC([RQ]) (i) was used for PANI and PANI-NiO, while R(C[RQ]) (ii)

was used for the bare GCE electrode. It is important to mention at this juncture that the two circuits look very the same except that in circuit (i), the solution resistance Rs is not in series to C_{dl} while in circuit (ii) it is directly in series. This slight change in circuit configuration is in response to changes in the electronic configuration of the GCE-PANI and GCE-PANI-NiO modified electrodes with newer functionalities and enhanced electron transport behaviour as compared to GC electrode alone. All the obtained spectra were first subjected to the Kramers–Kronig (K–K) test [408, 409]. Failure of the K–K test, signified by a large value of pseudo χ^2 is usually an indication that no good fit can be obtained using the electrical equivalent circuit's methods. It should be noted that aside from visual inspection of goodness of the fitting lines, two accurate ways to establish how well the modelling functions reproduce the experimental data sets are the relative error estimates (in %) and chi-square functions (χ^2) [410], which is the sum of squares of the relative residuals (i.e., sum of the real and imaginary χ^2), easily obtained from the K–K test.

The charge transfer resistance (Rct) values calculated after fitting the EIS data to the Randle's equivalent circuit in Table 8.1 confirms that NiO nanoparticles decreased the resistance of PANI by 172.5 Ω suggesting the suitability of GCE-PANI-NiO as a good conducting platform for electrocatalysis. This behaviour may be due to the synergy between the highly conducting nickel oxide nanoparticle and the porous conducting PANI nanofibers with large surface, thus facilitating more charge flow (at lower transfer resistance) between the electrolyte and the GC electrode. The result is further supported by the higher current response recorded at GCE-PANI-NiO electrode from the CV experiment. This result also agreed with other reports in literatures for enhanced electrochemical responses of chemically modified electrodes compared with unmodified electrodes [411, 412]. The exchange current can be thought of as a background current to which the net current observed at various over potentials is normalized. The exchange current was calculated using the equation 2.7 in

chapter 2. Where i_0 is the exchange current, R is the gas constant i.e. 8.314 J mol^{-1} K^{-1}, T is the absolute temperature (K), n is the number of moles of electron transfer, F is the Faraday constant and R_{ct} is the electron charge transfer. The highest value of exchange current i_0 for GCE-PANI-NiO electrode as shown in (Table 4.16), suggest that the electrochemical activity of the PANI-NiO is superior compared to that of other electrodes studied.

Table 4.16: Charge transfer resistance (R_{ct}), double layer capacitance (C_{dl}), and exchange current (i_0) for various electrodes in 1 M HCl solution.

Electrodes	**R_{ct}(Ω)**	**C_{dl} (μF)**	**i_0(A)**
GCE	147.4	5.25	1.742 x 10^{-4}
GCE/PANI	212.7	0.14	1.207 x 10^{-4}
GCE/PANI-NiO	40.2	0.32	6.386 x 10^{-4}

4.5.1.3 Effect of scan rate

The effect of scan rate (scan rate ranging from 20 – 300 mVs^{-1}) on the current response of PANI-NiO modified glassy carbon electrode (GCE-PANI-NiO) was investigated in 1 M HCl (Figure 4.52). Result showed there is an increase in anodic peak current as the scan rate increases (Figure 4.52a). Therefore the plot of the anodic (I_{pa}) and cathodic (Ipc) peak currents versus square root of scan rate ($V^{1/2}$) gave a linear relationship (Figure 4.52b) with the regression equations 1 and 2 as presented below.

$I_{p,a} = 2.97 \times 10^{-6} - 4.92 \times 10^{-6}$ x $v^{½}$ $(mV\ s^{-1})^{½}$ ($R^2 = 0.9965$) (1)

$I_{p,c} = -2.94 \times 10^{-5} + 5.46 \times 10^{-5}$ x $v^{½}$ $(mV\ s^{-1})^{½}$ ($R^2 = 0.9994$) (2)

The result suggests a diffusion controlled electrode reaction. In addition, with increasing scan rate, the peak potential (Ep) shifts to more positive values and there is a linear correlation between the peak potential and the logarithm of scan rate (log *v*) (graph not shown). In order to get information on the rate determining step. The peak potential, *E*p is plotted against log v (graph not shown). The slopes of *E*p *vs.* log *v* for the modified electrode GCE-PANI-NiO is 0.0279 V. From the slope obtained, the Tafel value (b) may be estimated according to the equation 4.2 for totally irreversible diffusion controlled process [324]. So, the value of *b* for this electrode was obtained as 55.8 $mVdec^{-1}$. The Tafel value falls within the range of normal values (~ 30-120 mV/dec) for a single-electron process involved in the rate determining step. This value indicates that a fast electron transfer is followed by a slow chemical step [325].

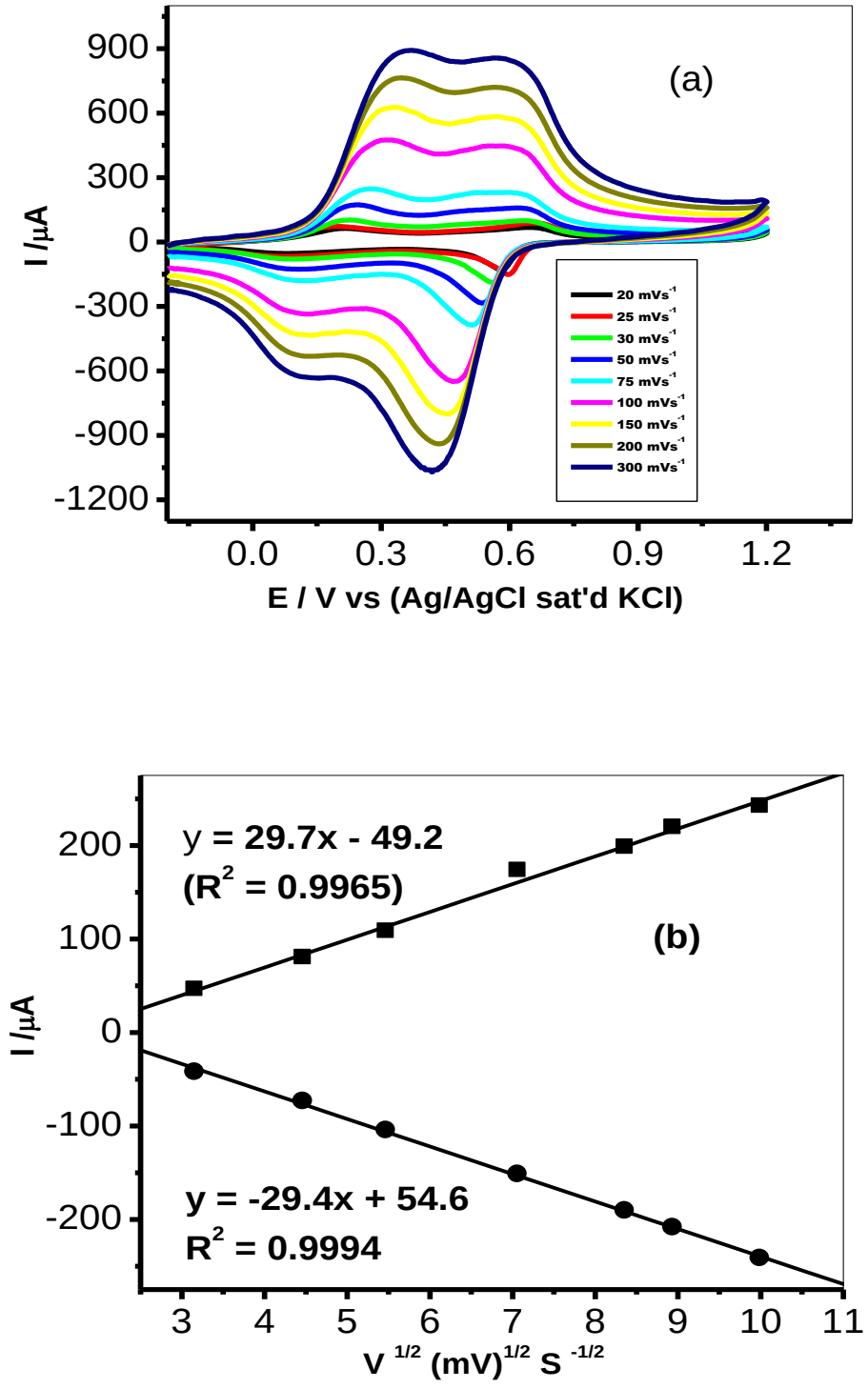

Figure 4.52: (a) cyclic voltammograms of GCE/PANI-NiO electrode in 1 M HCl solution (scan rate range 20 – 300 mVs^{-1}) and (b) Linear plots of I_{pa} vs $\nu^{1/2}$ and I_{pc} vs $\nu^{1/2}$ for GCE/PANI-NiO electrode in 1 M HCl solution.

4.5.2 Electrochemical response of the electrodes to phenanthrene oxidation

The polyaniline nanocomposites were developed to enhance the catalytic activity of the nanoparticles for the detection of phenanthrene. The electrochemical behaviour of different modified electrodes in the presence of 3 x 10^{-6} M phenanthrene in 1 M HCl was investigated by cyclic voltammetric (CV) technique at a scan rate of 20 mV/s. Figure 4.53 shows the CV responses obtained for the bare GCE, GCE/PANI and GCE/PANI-NiO electrodes in the presence of 3 x 10^{-6} M phenanthrene. At a bare GCE, GCE/PANI and GCE/PANI-NiO, a well-defined anodic peak was observed at 1540 mV, 1550 mV, and 1650 mV respectively corresponding to phenanthrene oxidation peak potential. This oxidation potential agreed closely with phenanthrene oxidation potential reported for some chemically modified electrodes [394, 413]. Among the three electrodes, GCE/PANI-NiO gave the best current response (750 μA) than the other electrodes, GCE/PANI (680 μA) and bare GCE (390 μA). The high phenanthrene current response at GCE/PANI-NiO electrode (~ 8 times that at bare GCE) is attributed to the synergy between PANI-NiO leading to the improved electrocatalytic properties of the surface nanocomposites material [412]. The lower phenanthrene oxidation potential on this electrode suggest large surface area created by the porous PANI material allowing easy contact between the analyte and the NiO catalyst thus faster reaction kinetics at lower energy. These results indicate that the GCE/PANI-NiO has high electrocatalytic activity towards the oxidation of phenanthrene. It is believed that the existence of NiO nanoparticles in the PANI nanofibers play an important role in the electron transfer between the surface electroactive catalyst and the base GC electrode after phenanthrene oxidation. The result obtained in this study agreed with similar observation for phenanthrene oxidation on graphenated polyaniline-doped tungsten oxide nanocomposites on glassy carbon electrode which was reported to be better compared to the bare GCE and other developed sensors signifying the importance of chemically modified electrodes in catalysis [394]. Since

GCE/PANI-NiO electrode demonstrated excellent catalytic properties towards phenanthrene oxidation in this study, further studies were carried out using this electrode unless otherwise stated.

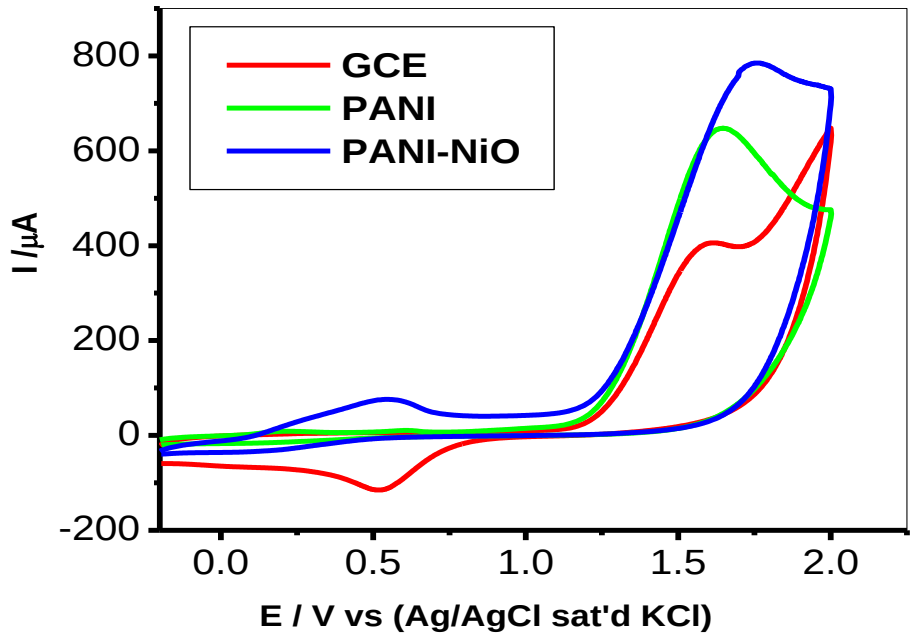

Figure 4.53: CyclicVoltammograms of GCE, GCE/PANI and GCE/PANI-NiO in 3 x 10^{-6} M phenanthrene in 1 M HCl at scan rate 20 mVs^{-1}.

4.5.2.1 Effect of scan rate

The effect of scan rate (scan rate, 10 - 300 mVs^{-1}) on the response of 3 x 10^{-6} M phenanthrene at PANI-NiO modified glassy carbon electrode was investigated in 1 M HCl (Figure 4.54a). Result showed that there is an increase in anodic peak current as the scan rate increases. The plot of the anodic peak current of phenanthrene against square root of scan rate ($v^{1/2}$) over the scan range study showed a linear relationship (Figure 4.54b) with a linear regression equation I_{pa} = 3.15×10^{-6} - 6.08$v^{½}$ (R^2 = 0.9985). This indicated that electrochemistry of the process was limited by rate of diffusion of phenanthrene from the solution to the surface of the

electrode. It was also observed that the oxidation peak potential were shifting to more positive potentials which further confirms that the electrode process was diffusion- controlled [412]. This indicated that the surface electrochemistry was limited by diffusion of solution of electrolyte/analyte to the surface of the electrode [412].

The slopes of *E*p *vs.* log *v* for the modified electrode GCE-PANI-NiO is 0.1135 V. The Tafel slopes (b) may be estimated according to the equation 4.2 for totally irreversible diffusion controlled process. So, the value of *b* for this electrode was obtained as 227 $mVdec^{-1}$. This Tafel value is higher than the theoretical value of 118 mV dec^{-1} for a one-electron process involved in the rate-determining step. Therefore higher Tafel values are attributed to the adsorption of reactants or intermediates on the electrode surfaces. These also indicates that the electrode surface is porous and despite this fact the modified electrodes still gave better performance towards phenanthrene in terms of oxidation potential, current recovery, stability and resistance to fouling effects.

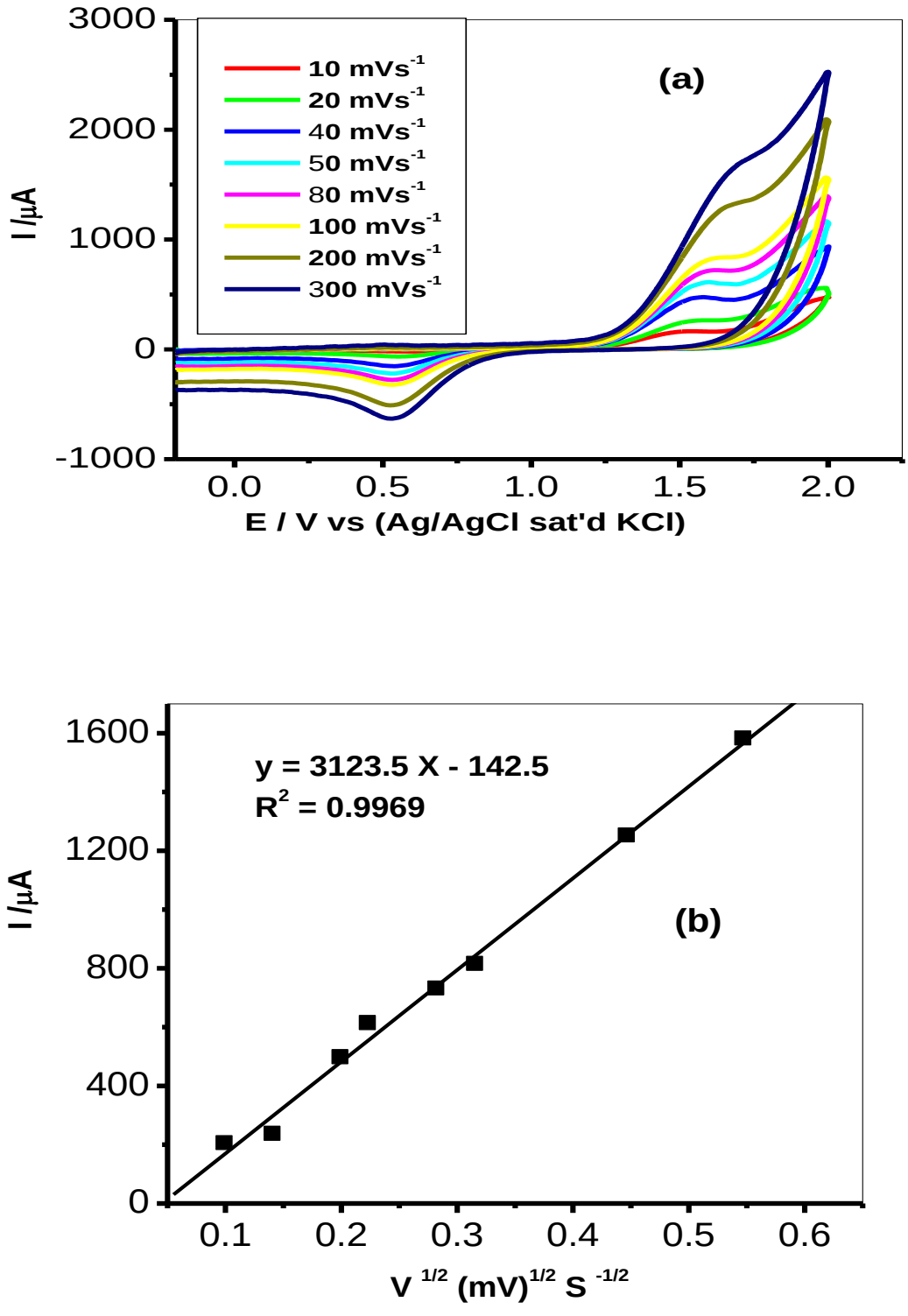

Figure 4.54: (a) Scan rate dependence cyclic voltammograms of GCE/PANI-NiO sensor in 1 M HCl containing 3 X10^{-6} M phenanthrene (b) linear plot of the anodic peak currents against square root of scan rate.

4.5.3 Electroanalysis of phenanthrene

A concentration study was carried out using square wave voltammetric (SWV) method. Result indicates that the electrochemical response of phenanthrene at GCE/PANI-NiO modified electrode gave phenanthrene oxidation peak current that is linearly proportional to its concentration in the range 7.6 pM – 1.4 $x10^{-11}$ M (Figure 4.55). The detection limit was calculated based on the relationship LoD = 3.3 δ/m [294] where δ is the relative standard deviation of the intercept of the y-coordinates from the line of best fit, and *m* the slope of the same line. The limit of detection and sensitivity of the GCE/PANI-NiO electrode in phenanthrene are 0.732 pM and 1.04 x 10^6 A/M respectively. The 0.732 pM reported for phenanthrene agreed closely with 5.0 x 10 $^{-13}$ M recently reported [394] but of higher magnitude lower compared with 19 nM reported on dendritic 7T-Polythiophene modified electrode [413].

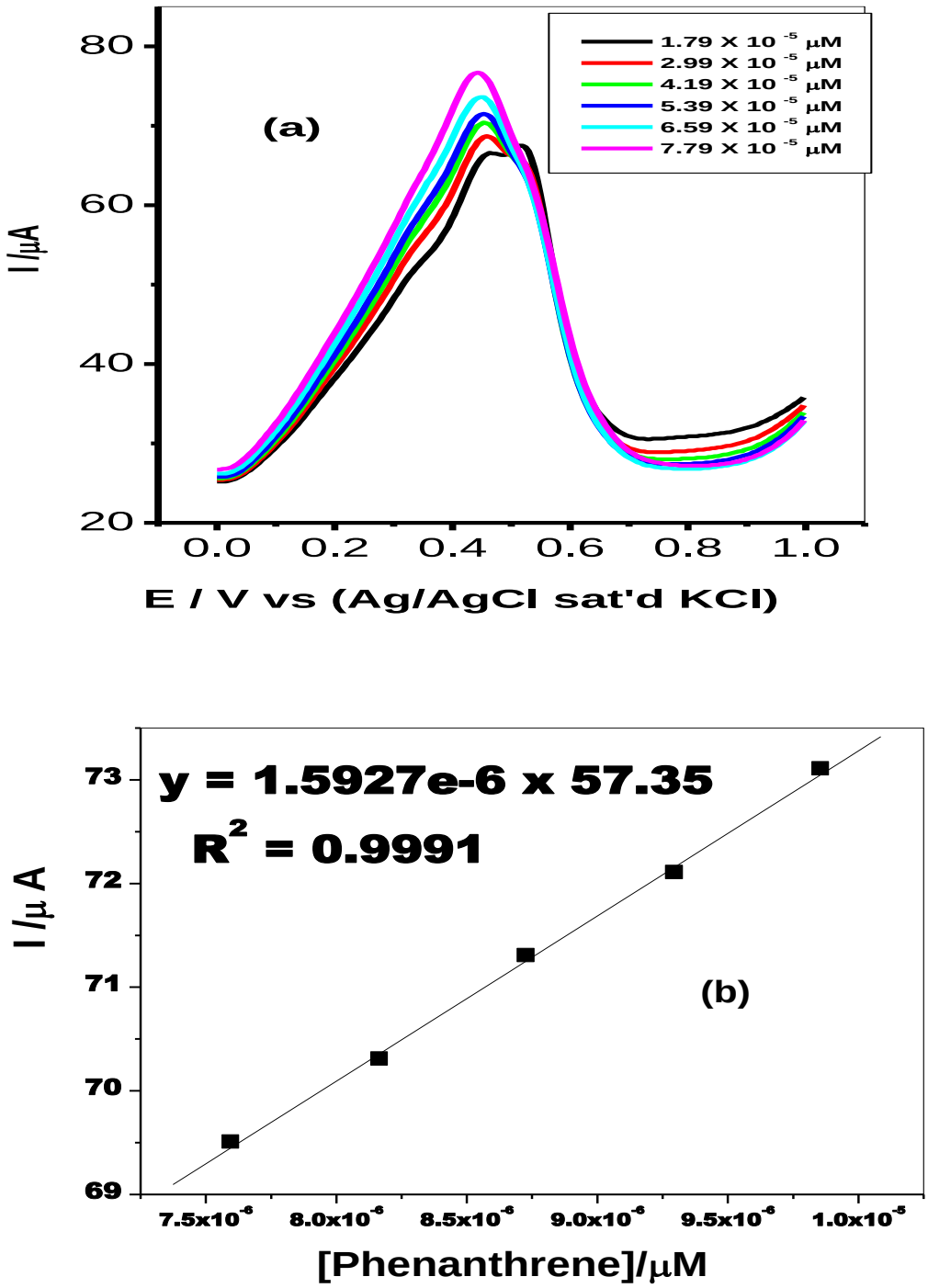

Figure 4.55: SWV of PANI-NiO in 1 M HCl containing different concentration of phenanthrene. (b) Is the plot of current (I) against phenanthrene concentration.

4.5.4 Stability, reproducibility and interference studies

Reproducibility of the PANI-NiO modified electrode was investigated towards the phenanthrene oxidation in the presence of 3×10^{-6} M phenanthrene in 1 M HCl solution. CV analysis was repeatedly performed (20 scans) and monitored in a solution of 1 M HCl containing 3×10^{-6} M phenanthrene. The phenanthrene oxidation current was stable with less than 10 % drop in the peak current between the 1st and 20th scan as shown in Figure 4.56. Thus, the GCE/PANI-NiO electrode has demonstrated good stability to electrode fouling effect during phenanthrene oxidation. However, on rinsing the electrodes in a fresh PBS (pH 7.0) solution, the electrode surface was renewed and more than 90% of the initial catalytic current was obtained, indicating the electrochemical stability and reusability of the electrode after analysis. Similarly, after storage for four weeks in a refrigerator, no significant change in serotonin current was observed which confirmed the electrode stability towards the analyte. Interference study was also carried out with the modified electrode in the presence of inorganic ions such as Cl^{-}, SO_4^{2-} and NO^{3-} which may probably present in water samples along phenanthrene. Result indicates no interference from these ions at 3×10^{-6} M phenanthrene concentration.

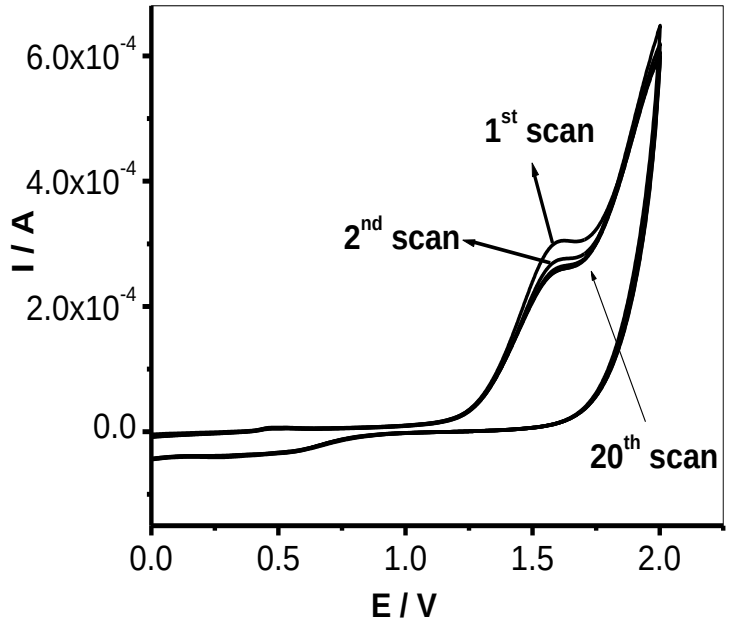

Figure 4.56: Repetitive cyclic voltammograms (20 scan) showing the current response and the stability of PANI-NiO modified electrode in 1 M HCl containing 3 x 10^{-6} M phenanthrene, scan rate 20 mVs^{-1}**.**

4.6 A SENSOR FOR DETERMINATION OF LINDANE USING PANI/, ZINC, IRON (III) OXIDES AND NYLON 6,6/MWCNT/ ZINC, IRON (III) OXIDES NANOFIBERS MODIFIED GLASSY CARBON ELECTRODE

Organochloride insecticides, such as hexachlorocyclohexane generally known as lindane are serious environmental pollutants and are normally extremely resistant to biodegradation [414]. Lindane (y-hexachlorocyclohexane) is also used in formulation of lotions and shampoos to treat lice and scabies [415]. Lindane has been known to cause immunotoxicity and retards reproduction and growth of animals, aquatic organisms and human [416]. Large scale production and application of this insecticide in agriculture deteriorates the environment owing to its long period of persistence [417] and the fact that there is no natural degradation of lindane. Moreover, it has moderate volatility and can be transported by air to remote locations [418]. It has deteriorating effects on the central nervous system of mammals, provoking seizures and in some cases causing death [419]. Microbial degradation of γ-HCH under aerobic conditions has been reported [420]. Anaerobic degradation of lindane with 95% removal efficiency has also been reported [421]. Different methods has been used for the detection and estimation of lindane such as colorimetric measurement of chloride ions [422, 423], phenol red based colorimetric method [424], colorimetric measurement using zinc in acetic acid [425], determination of complete mineralization to $14CO_2$ [426], thin-layer chromatography [422, 423] and gas chromatography [426,427]. The major demerits of these methods has to do with the use of rigorous approach involving solvent extraction, is time-consuming, very expensive, and also not suitable for on-site monitoring [427]. Therefore, quantitative analysis of lindane is an important area in the context of environmental protection.

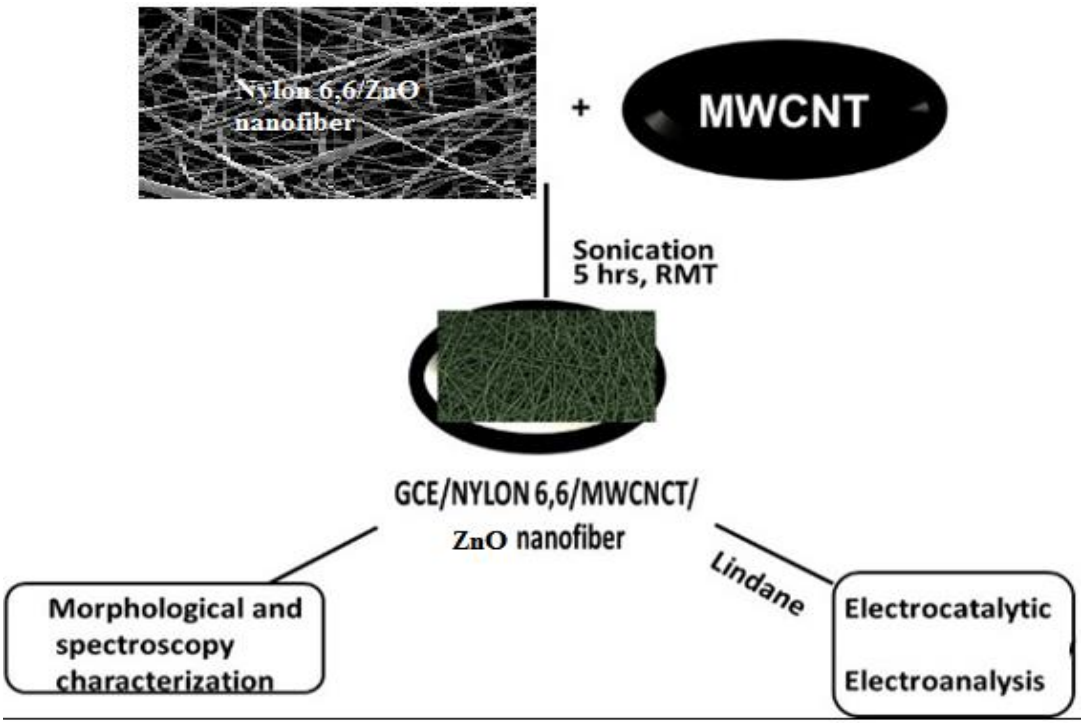

Scheme 4.4: Schamatic diagram of modification of electrode towards reduction of lindane.

4.6.1 Cyclic voltammetric response of lindane at PANI/Zn, Fe(III) and Nylon6,6/MWCNT/Ni, Zn, Fe(III) Oxides nanofibers modified electrodes:

PANI/Ni, Zn, Fe(III) and Nylon6,6/MWCNT/Ni, Zn, Fe (III) Oxides nanocomposites modified electrode was fabricated to obtained the optimized analysis parameter for lindane reduction. Scheme 4.4 is the schemmatic diagramm of the electrode modification of glassy carbon with Nylon 6,6/MWCMT/MO based nanocomposites. From the voltammogram in Figure 4.57 well defined irreversible reduction peaks around −1.61 and -0.89 V, were observed on the bare GCE, and there was a shift to more positive potential at the Nylon6,6/MWCNT/ Zn, Fe (III) Oxides nanofibers modified electrode in 500 μM lindane in 60:40 methanol/water containing 0.05 M TBAB. The measured reduction current was 12 μA on the bare GCE, while on the modified electrodes as shown in Table 4.17, there was an increase in reduction current for lindane. The comparative response at the modified electrodes studied reveal that the reduction peak current is higher at Nylon6,6/MWCNT/NiO,

Nylon6,6/MWCNT/ZnO modified electrode and more positive potential than the bare electrode which may be due to the enhanced diffusion of lindane molecules through the micropores of Nylon 6,6/MWCNT/MO nanofibers [428, 429]. The cyclic voltammetric response of 500 mM lindane at the modified electrodes. After 10 cycles of multiscans, only a small decrease in peak current is observed. This also further confirms that the reduction process of lindane at the modified electrodes is diffusion controlled. If the adsorbed species on the electrode surface completely block the mass transport, it then expected that there may be disappearance of the peak after multiscans. Therefore the absence of adsorption processes during the electroreduction of lindane at these modified electrodes is expected to improve the sensitivity of the sensor compared to the bare GCE sensor.

Table 4.17: Values obtained for the reduction potential (Epa) current (Ipa) and charge transfer coefficient (α) using cyclic voltammetry of the 500 μM lindane in 60:40 methanol/water containing 0.05 M TBAB, with PANI-Zn, Fe (III) and Nylon6,6/MWCNT/, Zn, Fe(III) Oxides nanocomposites.

Electrodes	Epa (mV)	Ipa (μA)	α
GCE-PANI-ZnO	-0.82	98	0.20
GCE-PANI-Fe_3O_4	-0.73	101	0.23
GCE/Nylon 6,6/MWCNT/ZnO	-0.58	258	0.25
GCE/Nylon 6,6/MWCNT/Fe_3O_4	-0.49	23	0.15

Figure 4.57: Comparative cyclic voltammogrammes for (a) GCE, GCE/Nylon 6,6/MWCNT/ZnO and GCE/Nylon 6,6/MWCNT/Fe_3O_4 and (b) GCE, GCE-PANI-ZnO and GCE-PANI-Fe_3O_4 at scan rate, 50 mVs^{-1} in 500 μM lindane in 60:40 methanol/water containing 0.05 M TBAB.

The cyclic voltammogram scan rate study of the modified GCE electrodes PANI- Zn, Fe (III) and Nylon6,6/MWCNT/Zn, Fe (III) Oxides nanofibers was studied. The Figures 4.58 and 4.59 show the scan rate study for Nylon 6, 6 and PANI based nanocomposites respectively The linear relationship between the peak current and square root of the scan rate as shown in Figures 4.58 and 4.59 obtained for modified GCE electrode of the PANI-Zn, Fe (III) and Nylon6,6/MWCNT/Zn, Fe(III) Oxides nanocomposites show that lindane undergoes a diffusion controlled reduction process. A high slope value is obtained which also indicate that the reduction process is electrotransfer (ET) [430]. The number of electrons transferred during the reduction of lindane is calculated from the Randles–Sevcik equation for irreversible reduction processes by substituting the diffusion coefficient value of 0.89 x 10^{-5} cm^2 s^{-1} for lindane reported in the literature [431].

In order to get information on the rate determining step, the peak potential, Ep, is proportional to log ν (not shown). The slopes of Ep vs. log ν whose relationship is shown by equation 4.2, for the different electrodes were 0.148, 0.131, 0.120 and 0.202 V for electrodes GCE/PANI-ZnO, GCE/PANI-Fe_3O_4, GCE/Nylon 6,6/MWCNT/ZnO and GCE/Nylon 6,6/MWCNT/Fe_3O_4 respectively. The value of α is calculated from the Tafel equation 4.4 below. From the slope of the Tafel plot the experimental electron transfer coefficient α is determined. The high value of α is clear evidence that a large double layer effect is present for the charge reactants [432].

$$slope = \frac{1.15RT}{F\alpha} \qquad (4.4)$$

Where T is the absolute temperature, R is the gas constant α is the so called "charge transfer coefficient", the value of which must be between 0 and 1 as shown in Table 4.17. Also from the table the smaller values of α further support the fact that electron transfer process (ET) and bond breaking are concerted [433]. Therefore the number of electrons (n) involved in the

reduction process is determined to be 6 which also support the earlier reports for benzene formation [434].

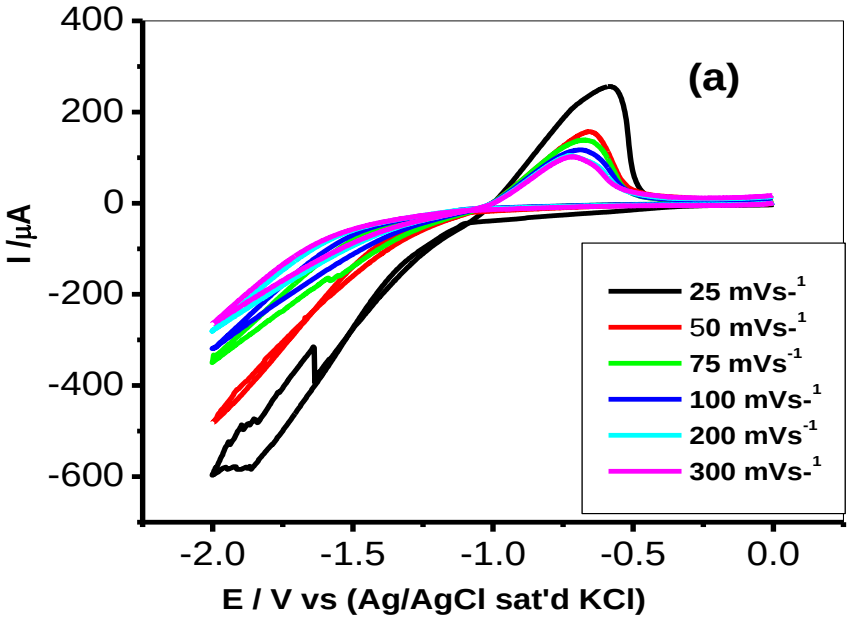

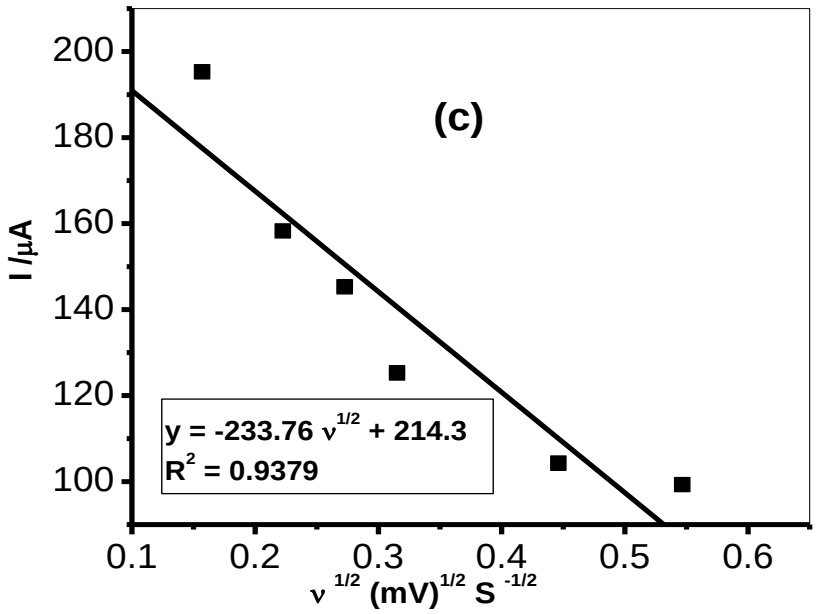

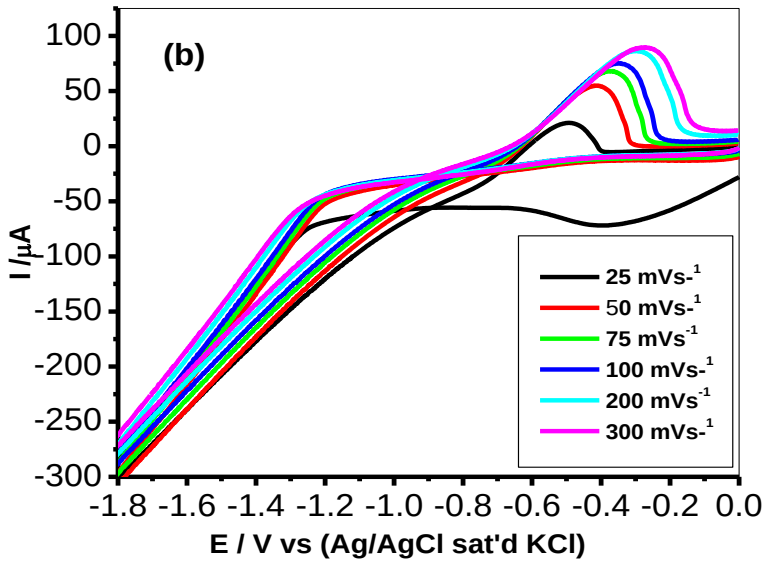

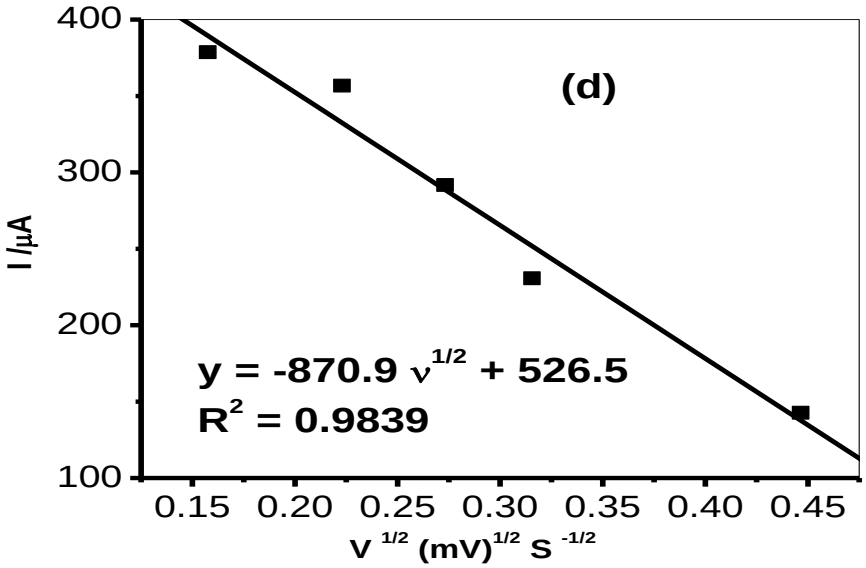

Figure 4.58: Effect of scan rate (25 – 300 mVs^{-1}) on the cyclic voltammograms of (a) GCE/Nylon 6,6/MWCNT/ZnO and (b) GCE/Nylon 6,6/MWCNT/Fe_3O_4 in 500 µM lindane in 60:40 methanol/water containing 0.05 M TBAB (c) and (d) are the plots of current (I) against square root of scan rate ν (mVs^{-1}) for GCE/Nylon 6,6/MWCNT/ZnO and (c) GCE/Nylon 6,6/MWCNT/Fe_3O_4 respectively.

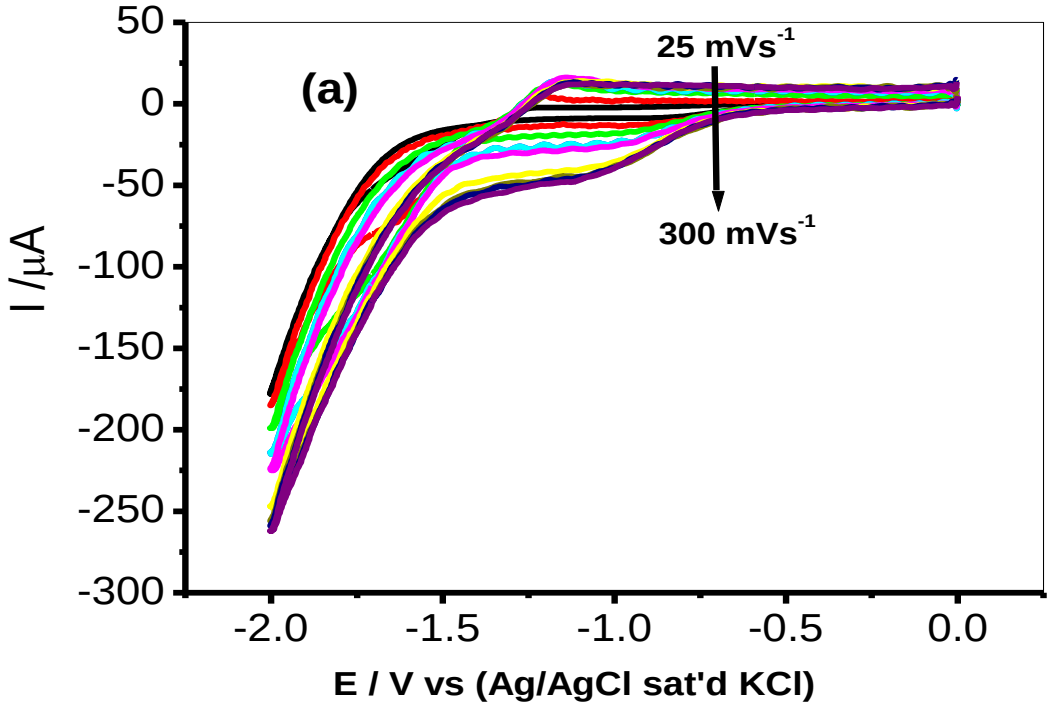
(a)
25 mVs-1
300 mVs-1
I /μA
E / V vs (Ag/AgCl sat'd KCl)
50
0
-50
-100
-150
-200
-250
-300
-2.0
-1.5
-1.0
-0.5
0.0

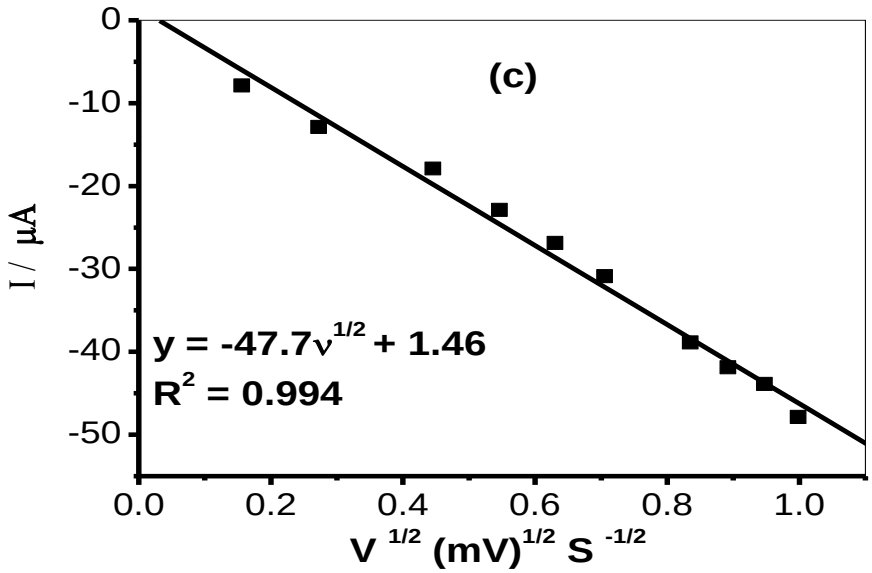
(c)
I / μA
y = -47.7ν1/2 + 1.46
R2 = 0.994
V 1/2 (mV)1/2 S -1/2
0
-10
-20
-30
-40
-50
0.0
0.2
0.4
0.6
0.8
1.0

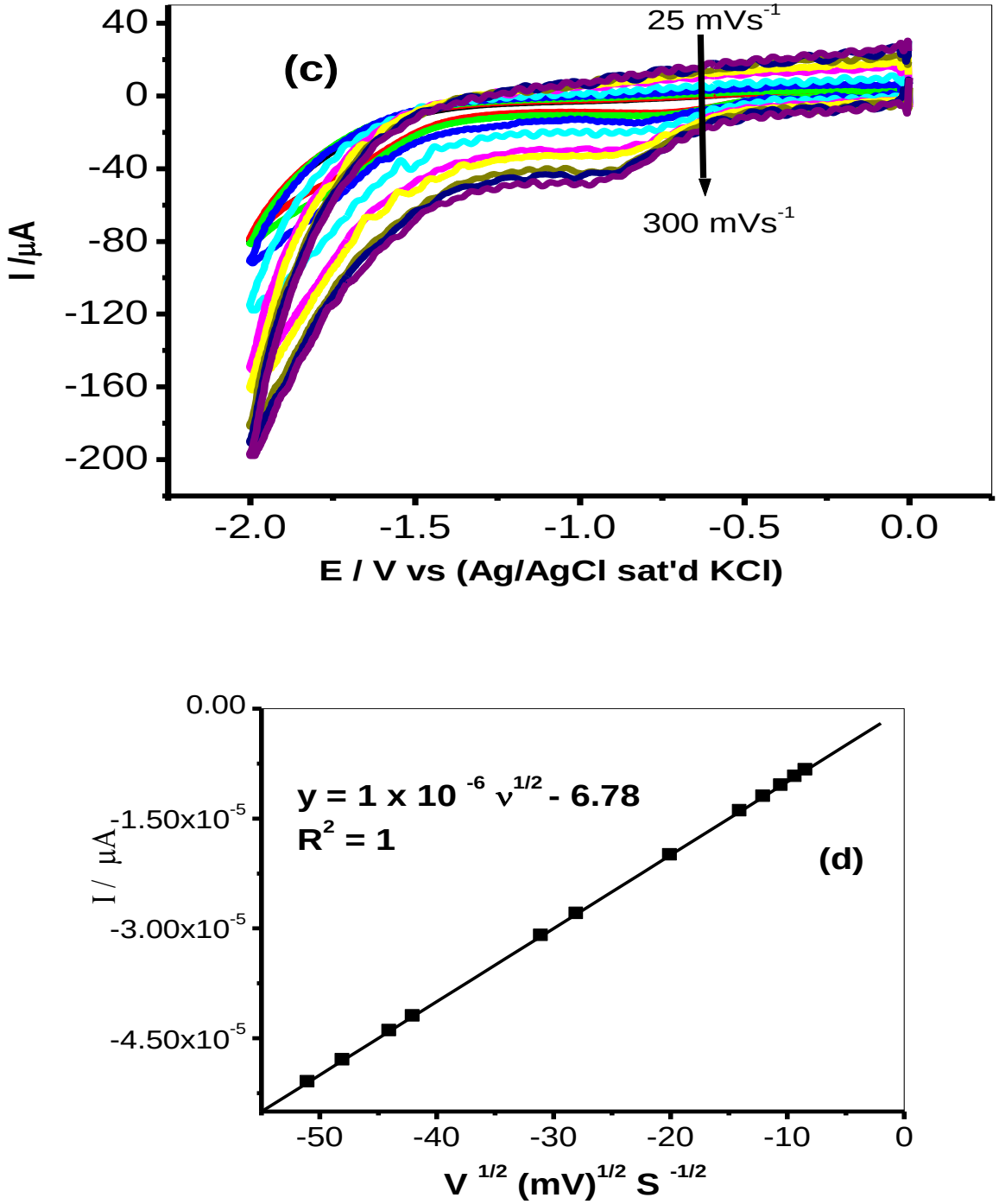

Figure 4.59: Effect of scan rate (25 – 300 mVs^{-1}) on the cyclic voltammograms of (a) GCE/PANI/ZnO and (b) GCE/PANI/Fe_3O_4in 500 μM lindane in 60:40 methanol/water containing 0.05 M TBAB (c) and (d) are the plots of current (I) against square root of scan rate ν (mVs^{-1}) for GCE/PANI/ZnO and GCE/PANI/Fe_3O_4 respectively.

4.6.2 Electroanalysis of Lindane

To improve the sensitivity of the proposed method in detection of lindane, square wave voltammetry (SWV) has been used. From Figure 4.60, it is found that the electrochemical reduction peak current is proportional to lindane concentrations in the range of 9.9×10^{-12} mol/L to 5×10^{-6} mol/L for modified PANI/Ni, Zn, Fe(III) and Nylon6,6/MWCNT/Ni, Zn, Fe(III) Oxides nanocomposites electrodes respectively. The detection limit was calculated based on the relationship LoD = 3.3 δ/m [294] where δ is the relative standard deviation of the intercept of the y-coordinates from the line of best fit, and m the slope of the same line. The respective detection limits for the electrodes are shown in Table 4.18. These values are found to be lower than LoD values reported at $NiCo_2O_4$ and cellulose acetate modified glassy carbon electrode [435, 436].

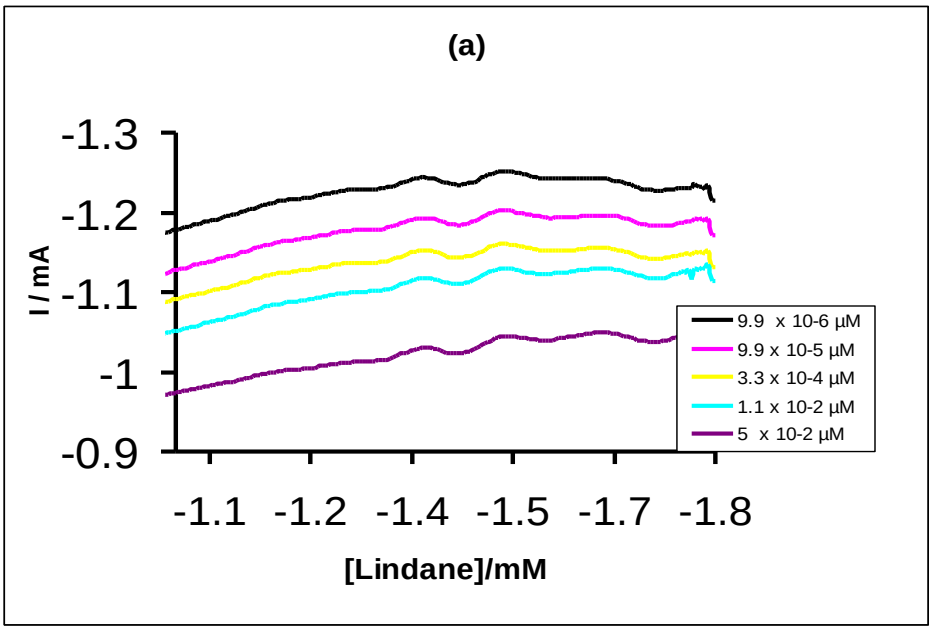

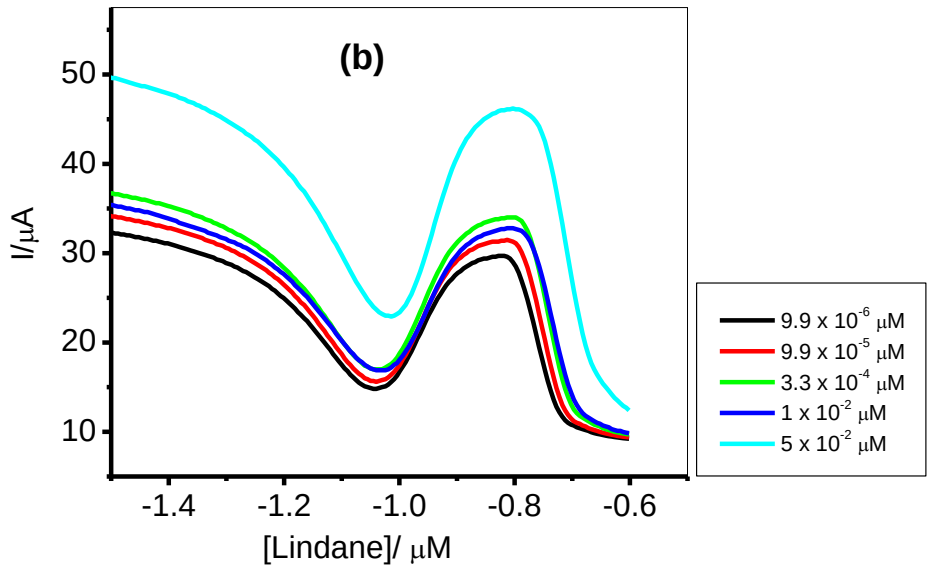
(b)
I/μA
50
40
30
20
10
-1.4
-1.2
-1.0
-0.8
-0.6
[Lindane]/ μM
9.9 x 10-6 μM
9.9 x 10-5 μM
3.3 x 10-4 μM
1 x 10-2 μM
5 x 10-2 μM

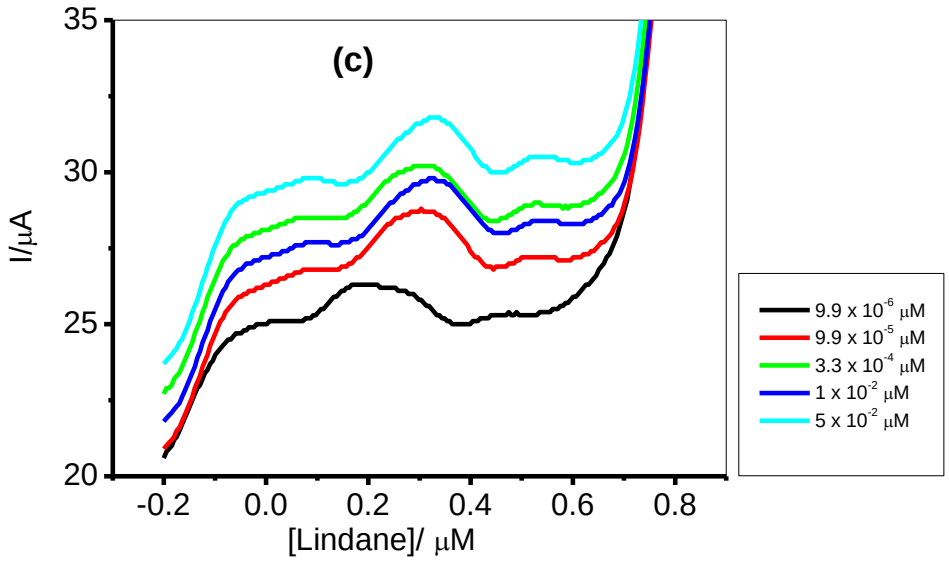
(c)
I/μA
35
30
25
20
-0.2
0.0
0.2
0.4
0.6
0.8
[Lindane]/ μM
9.9 x 10-6 μM
9.9 x 10-5 μM
3.3 x 10-4 μM
1 x 10-2 μM
5 x 10-2 μM

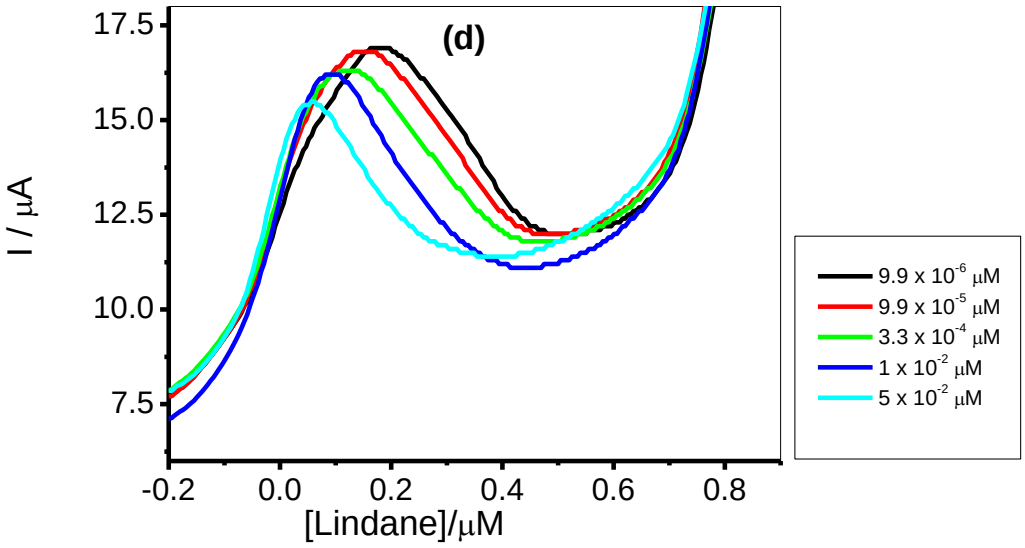

Figure 4.60: Square wave voltammogrammes of (a) GCE/ Nylon 6,6/MWCNT/ZnO (b) GCE/ Nylon 6,6/MWCNT/Fe_3O_4 (c) GCE/PANI/ZnO and (d) GCE/ PANI/Fe_3O_4 in 9.9 × 10^{-12} mol/L to 5 × 10^{-6} mol/L lindane in 60:40 methanol/water containing 0.05 M TBAB concentration.

Table 4.18: Comparative values obtained for the concentration study of 500 μM lindane in 60:40 methanol/water containing 0.05 M TBAB, at modified PANI/Ni, Zn, Fe(III) and Nylon6,6/MWCNT/Ni, Zn, Fe(III) Oxides nanocomposites electrodes using square wave voltammetry.

Electrodes	Concentration range (mol/L)	LoD	R^2
DME	-	Not reported	[437]
MWCNT-GCEs	-	0.1 mg L^{-1}	[438]
GCE/PANI-ZnO	9.9×10^{-12} - 5×10^{-6}	239.0 nM	0.9133
GCE/PANI-Fe_3O_4	9.9×10^{-12} - 5×10^{-6}	44.7 nM	0.8277
GCE/Nylon 6,6/MWCNT/ZnO	9.9×10^{-12} - 5×10^{-6}	51.0 nM	0.8349
GCE/Nylon 6,6/MWCNT/Fe_3O_4	9.9×10^{-12} - 5×10^{-6}	32.0 nM	0.9733
GCE/PANI-ZnO	9.9×10^{-12} - 5×10^{-6}	239.0 nM	0.9133

4.6.3 Interference studies

The interference study was carried out using cyclic voltammetry. The interfering substances considered in this work may be present in water or soil from industrial areas and agricultural land [439]. The possibility of the interference of several inorganic ions on the reduction of the signal of lindane was studied by analyzing concentrations of interfering substances and lindane at a ratio of 1: 1 (Figure 4.61). The variation of reduction signal for interfering substances with respect to lindane is represented as a percentage in the Figure 4.61. The inorganic ions such as NH^{4+}, Mn^{2+}, K^{+}, Na^{+}, $Fe^{2+}$and Co^{2+} did not interfere with lindane reduction signal.

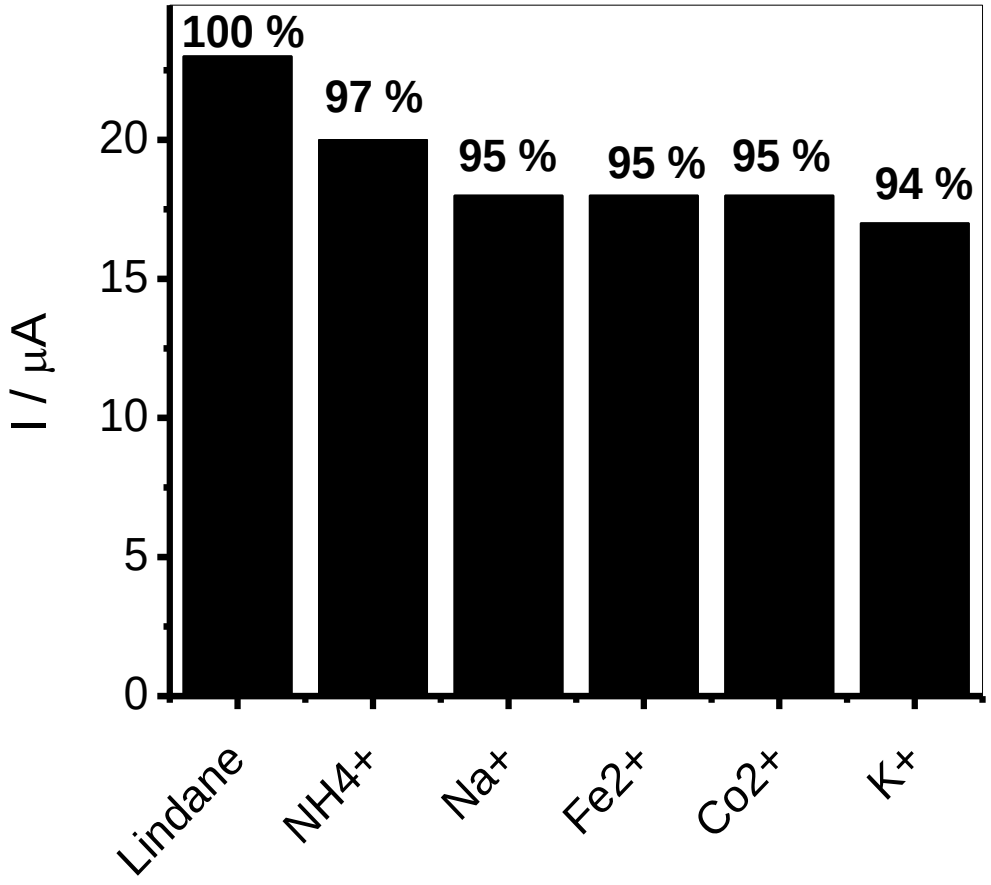

Figure 4.61: Interference study of 500 µM inorganic metal ions on the reduction signal of 500 µM lindane at the Nylon 6,6/MWCNT/Fe_3O_4 in 0.05 M TBAB 60 : 40 methanol–water scan rate 25 mVs^{-1}.

4.6.4 Real sample analysis

Real sample analysis was carried out by using Nylon6,6/MWCNT/Zn, Fe(III) Oxides nanocomposites sensors to determine the concentration of lindane in tap water samples. A sample containing different amounts of lindane was prepared in 60:40 (v/v) methanol–tap water (20 mL). The values of recovery were in the range from 99% to 102%, suggesting the accuracy of Nylon 6, 6/MWCNT/Fe_3O_4, and Nylon6, 6/MWCNT/ZnO nanofibers based sensor.

CHAPTER 5

●●●●●

CONCLUSIONS, FUTURE WORK AND RECOMMENDATION

5.1 Conclusion

This thesis describes the electron transport and electrocatalytic properties of chemically synthesized metal oxides MO (where MO = NiO, ZnO, Fe_3O_4) nanoparticles supported on multiwalled carbon nanotubes (MWCNT), polyaniline (PANI) and Nylon 6,6 nanofiber platforms towards the electrocatalytic oxidation of important molecules such as dopamine, serotonin, phenanthrene and lindane It has been demonstarted that glassy carbon electrode modified with funtionalised polymer nanocomposites exhibit enhanced electrochemical response towards electro-oxidation of these analytes.

The flowing conclusions can be drawn from this study:

5.1.1 Conclusion for section 4.1 and 4.2

It is shown that the GCE-MWCNT-MO nanocomposite modified electrode gave better electron transport as well as better dopamine and serotonin response compared with other electrodes investigated. Under the comparative studies with modified electrodes GCE-MWCNT-NiO, GCE-MWCNT-ZnO and GCE-MWCNT-Fe_3O_4, the modified electrode GCE-MWCNT-NiO has proven to be the best electrode in terms of dopamine and serotonin oxidation current and lower limit of detection. DA and ascorbic acid (AA) signal were well resolved using SWV and DPV techniques compared to CV techniques. Electrocatalysis of DA on the GCE-MWCNT-MO electrodes was through diffusion and surface-confined electrode process. The study also showed that the GCE/MWCNT/NiO modified electrode can be successfully used for the assay of dopamine in DA real life samples. Simultaneous voltammetric determination of serotonin (SE), ascorbic acid (AA) and dopamine (DA) was successful at the MWCNT-MO modified GCE electrodes without AA and DA signals interfering with serotonin. The present sensor system exhibited very good recovery limits for the determination of SE directly from urine sample. The method developed is simple, fast and

accurate and opens new avenues for quick simultaneous estimation of physiologically important compounds.

5.1.2 Conclusion for section 4.3

The comparative study at GCE/Nylon 6,6/MWCNT/NiO, GCE/Nylon 6,6/MWCNT/ZnO and GCE/Nylon 6,6/MWCNT/Fe_3O_4 nanocomposite modified electrode gave better electron transport as well as better dopamine and serotonin response compared with other electrodes investigated. GCE/Nylon 6,6/MWCNT/ZnO electrode has proven to be the best electrode in terms of DA and SE oxidation current and lower limit of detection. DA, SE and ascorbic acid (AA) signal were well resolved using SWV techniques compared to CV techniques, Electrocatalysis of DA and SE on the GCE/Nylon 6,6/MWCNT/MO electrodes was through diffusion and surface-confined electrode process. The study suggest that the GCE/Nylon 6,6/MWCNT/ZnO modified electrode can be successfully used for the assay of dopamine and serotonin in real life samples.

5.1.3 Conclusion for section 4.4

The comparative study at GCE-PANI-NiO, GCE-PANI-ZnO and GCE-PANI-Fe_3O_4 nanocomposite modified electrode gave better electron transport as well as better dopamine response compared with other electrodes investigated. GCE-PANI-ZnO electrode has proven to be the best electrode in terms of DA oxidation current and lower limit of detection. DA, SE and ascorbic acid (AA) signal were well resolved using SWV techniques. Electrocatalysis of DA on the GCE-PANI-MO electrodes was through diffusion and surface-confined electrode process. The study suggest that the GCE-PANI-ZnO modified electrode can be successfully used for the assay of dopamine in DA real life samples.

5.1.4 Conclusion for section 4.5

This work describes the electron transport and electrocatalytic properties of chemically-synthesized nickel oxide nanoparticles (NiO) supported on PANI nanofibers towards

phenanthrene oxidation. It is shown that the PANI–NiO nanocomposites modified GC electrode (GCE-PANI-NiO) yielded the fastest electron transport as well as the best electrocatalytic behaviour towards phenanthrene compared with the bare GCE and GCE-PANI electrodes investigated. The GCE-PANI-NiO electrode gave LoD of 0.732 pM towards phenanthrene. This enhancement and low LoD is associated with high electrical-conducting PANI which forms a synergistic behaviour with nickel oxide (NiO) nanoparticles. Electrocatalysis of phenanthrene on the PANI-NiO was predominantly diffusion-controlled, with some adsorption of reaction intermediates.

5.1.5 Conclusion for section 4.6

This work describes the electron transport and electrocatalytic properties of chemically-synthesized metal oxide nanoparticles (Fe_3O_4 and ZnO) supported on polyaniline and multi-walled carbon nanotubes-nylon 6,6 nanofibers platforms towards lindane reduction. It is shown that the PANI/Zn, Fe (III) and Nylon6,6/MWCNT/Zn, Fe(III) oxides nanocomposites modified electrode offers a high sensing current and lesser reduction potential for lindane than the bare GCE electrode. The Nylon6,6/MWCNT/Zn, Fe(III) Oxides nanocomposites modified electrode gave a lower limit of detection for lindane than the PANI/MO nanocomposites modified electrodes. It was also highly stable and reproducible with respect to time, so that the electrode can be used for multiple detection of lindane.

5.2 Future work

The following further investigations are recommended as a future work to the research activities.

1. Application of the fabricated sensors on real sample analysis.

2. Long shelf life properties of the fabricated sensors will be investigated.

3. Stability of the polyaniline based nanocomposites in dopamine will also be investigated

5.3 Recommendation

This work recommends the use of these polymer nanocomposites to researchers and they should take the subject of adsorption pheneomenon as a major concern, in reducing the effect on the limit of detection of fabricated sensors. Wider scope of application of these fabricated sensors for enviromental pollutant control and pharmaceutical applications should be maximized. The proposed method of preparation through chemical method has proven to be efficient. However, electrochemical method of preparation of the nanocomposite is recommended.

The development of the sensor devices using gold, platinum and printed electrodes should be explored in other to produce more specific and sensitive sensor devices.

Also, more electrocatalysis of other biological and enviromental molecules can be studied on these polymer nanocomposite.

REFERENCES

1. P. P. Joshi, S. A. Merchant, Y. D. Wang, and D. W. Schmidtke, Amperometric biosensors based on redox polymer-carbon nanotube-enzyme composites, *Anal. Chem*, 2005, **77**, 3183-3188.
2. M. Jacoby, Keepers of the gate, *Chem Engng News*, 2009, **87**, 10-13.
3. O. Zheng, R. J. Noll, R. G. Cooks, Handheld miniature ion trap mass spectrometers, *Anal Chem*, 2009, **81**, 2421-2425.
4. A. Hulanick, S. Geab and F. Ingman, Chemical sensors definition and classification, *Pure and App. Chern*. 1991, **63**, 1247-1250.
5. C. Nylander, Chemical Sensors and Biological Sensors, *J. Phys. Sci. Instr., Is*, 1985, **18**, 736-750.
6. J. Janata and A. Bezegh, Chemical sensors, *Anal. Chem*. 1988, **12**, 62R-64R.
7. J. Janata and R.J. Huber (eds.), Solid-state Chemical Sensors, *Academic Press*, New York, 1985, **66**, 205-211.
8. J. M. Giachino, Smart sensor, *Sensors and Actuators*, 1986, **10**, 239-248.
9. G. S. Wilson and R. Gifford, Biosensors for real-time in vivo measurements, *Biosens. Bioelectron.* 2005, **20**, 2388-2403;
10. T. Sakaguchi, Y, Morioka, M. Yamasaki, J. Iwanaga, K. Beppu, H. Maeda, Y. Morita and E. Tamiya, Rapid and onsite BOD sensing system using luminous bacterial cells-immobilized chip, *Biosens. Bioelectron*. 2007, **22**, 1345-1350.
11. S. M. Chen and W. Y. Chzo, W.Y. Simultaneous voltammetric detection of dopamine and ascorbic acid using didodecyldimethylammonium bromide (DDAB) film-modified electrodes, *J. Electroanal. Chem*. 2006, **587**, 226-234.
12. V. S. Vasantha and S. M. Chen, Electrocatalysis and simultaneous detection of dopamine and ascorbic acid using poly(3,4-ethylenedioxy)thiophene film modified electrodes, *J. Electroanal. Chem*. 2006, **592**, 77-87.
13. M. F. Simoyi, E. Falkenstein, K. V. Dyke, K. P. Blemings and H. Klandorf, Allantoin the oxidation product of uric acid is present in chicken and turkey plasma. Comparative, *Biochemistry and Physiology Part B*. 2003, **135**, 325-335.
14. K. Balasubramanian and M. Burghard, Biosensors based on carbon nanotubes, *Anal. Bioanal. Chem*. 2006, **385**, 452-468.
15. S. Zhang, N. Wang, Y. Niu and C. Sun, Immobilization of glucose oxidase on gold nanoparticles modified Au electrode for the construction of biosensor, *Sens. Act. B*. 2005, **109**, 367-374.

16. J. Wang, M. Musameh and Y. Lin, Solubilization of carbon nanotubes by nafion toward the preparation of amperometric biosensors, *J. Am. Chem. Soc.* 2003, **125**, 2408-2409.

17 C. C. Liu, Electrochemical Sensors, The Biomedical Engineering Handbook: Second Edition. Ed. Joseph D. Bronzino Boca Raton: *CRC Press LLC*, 2000.

19. B. Nigovic, M. Marusic and S. Juric, A highly sensitive method for determination of b-blocker drugs using a Nafion-coated glassy carbon electrode, *J. Electroanal. Chem*., 2011, **663**, 72-78.

20. A. F. Al-Ghamdi and M. M. Hefnawy Arab, Electrochemical determination of rosiglitazone by square-wave adsorptive stripping voltammetry method, *J. Chem.*, 2012, **5**, 383-389.

21. B. J. Sanghavi and A. K. Srivastava, Simultaneous voltammetric determination of acetaminophen and tramadol using Dowex50wx2 and gold nanoparticles modified glassy carbon paste electrode, Anal. Chim. Acta, 2011, 706, 246–254.

22. R. N. Goyal, V. K. Gupta, M. Oyama and N. Bachheti, Differential pulse voltammetric determination of Paracetamol at nanogold modified indium tin oxide electrode, *Electrochem. Commun*, 2005, **7**, 803-807.

23. C. Jeyaseelan, R. Jugade and A. P. Joshi, *Differential Pulse Polarographic* determination of nifedipine in pharmaceutical formulations, *Int J Pharm Sci Drug Res.* 2011, **3**, 253-255.

24. A. M. Sardar, C. Czudek, and G.P. Reynolds, Dopamine deficits in the brain: the neurochemical basis of parkinsonian symptoms in AIDS, *Neuro Report*, 1996, **7**, 910-912.

25. K. W. Perry, and R. W. Fuller, Effect of fluoxetine on serotonin and dopamine concentration in microdialysis fluid from rat striatum, *Life Sciences*, 1992, **50**, 1683-1690.

26. L. H. Parsons and J. B. Justice Jr., Perfusate serotonin increases extracellular dopamine in the nucleus accumbens as measured by in vivo microdialysis, *Brain Research*, 1993, **606**, 195-199.

27**.** M. T. Lin, H. J. Tsay, W. H. Su and F. Y. Chueh, Changes in extracellular serotonin in rat hypothalamus affect thermoregulatory function, *American Journal of Physiology*, 1998, **274,** 1260–1267.

28. L. Imeri, M. Mancia, S. Bianchi and M .R. Opp, 5-Hydroxytryptophan, but not L-tryptophan, alters sleep and brain temperature in rats, *Neuroscience*, 2000, **95**, 445–452.

29. G. K. Isbister, S. J. Bowe, A. Dawson and I. M. Whyte, Relative toxicity of selective serotonin reuptake inhibitors (SSRIs) in overdose, *J Toxicol Clin Toxicol*. 2004, **42**, 277–285.

30. J. Li and X. Lin, Simultaneous Determination of Dopamine and Serotonin on Gold Nanocluster/Overoxidized-Polypyrrole Composite Modified Glassy Carbon Electrode, *Sensors and Actuators B: Chemical*, 2007, **124**, 486–493.

31. S. Fatma Basyoni, Spectrophotometric and titrimetric determination of cate-cholamines, *Talanta*, 1987, **34**, 810-812.

32. T. Yoshitake, J. Kehr, K. Todoroki, H. Nohta, and M. Yamaguchi, Derivatization chemistries for determination of serotonin, norepinephrine and dopamine in brain microdialysis samples by liquid chromatography with fluorescence detection, *Biomedical Chromatography*, 2006, **20**, 267-281.

33. N. Shafi, J. M. Midgley, D. G. Watson, G. A. Smail, R. Strang, and R. G. Mac Farlane, Analysis of biogenic amines in the brain of the American cockroach (Periplaneta Americana) by gas chromatography-negative ion chemical ionisation mass spectrometry, *J. Chromatography B*, 1989, 490, 9-19.

34. J. Venugopal and S. Ramakrishna, Applications of polymer nanofibers in biomedicine and biotechnology, *Appl. Biochem. Biotechnol*, 2007, **125**, 147-157.

35. A. Bhattacharya, R. Advincula, R. Cook and I. Kosacki, TEG 474X – Nanotechnology and Corrosion, 2014, **5**, 1.

36. W. Richard, Siegel, Nanostructured materials, Argonne National Laboratory Argonne, Illinois 60439 U.S.A, *Materials Science Division*, 1992.

37. D. Chimene, D. L. Alge and A. K. Gaharwar, Two-Dimensional Nanomaterials for Biomedical Applications: Emerging Trends and Future Prospects, *Adv. Mater*. 2015,

38. S. Ramakrishna, R. Jose, P. S. Archana, A. S. Nair, R. Balamurugan, J. Venugopal and W. E. Teo, Science and engineering of electrospun nanofibers for advances in clean energy, water filtration, and regenerative medicine, *J. Mater. Sci.*, 2010, **45**, 6283–6312.

39. S. Chigome, G. Darko, U. Buttner, N. Torto. Semi-micro solid phase extraction with electrospun polystyrene fiber disks, *Anal. Methods*, 2010, **2**, 623-626.

40. S. Chigome, G. Darko and N. Torto, Electrospun nanofibers as sorbent material for solid phase extraction, *Analyst*, 2011, **136**, 2879-2889.
41. R. S. Walmsley, A. S. Ogunlaja, M. J. Coombes, W. Chidawanyika, C. Litwinski, N. Torto, T. Nyokong and Z. R. Tshentu, Imidazole-functionalized polymer microspheres and fibers – useful materials for immobilization of oxovanadium(iv) catalysts, *J. Mater. Chem*., 2012, **22**, 5792-5800.
42. T. Lin, D. Lukas and G. S. Bhat, Nanofiber Manufacture, Properties, and Applications, *J. Nanomater.* 2013, **2013**, 1.
43. M. Bognitzki, W. Czado, T. Frese, A. Schaper, M. Hellwig, M. Steinhart, A. Greiner and J. H. Wendorff, Nanostructured Fibers via Electrospinning, *Adv. Mater*., 2001, **13**, 70-72.
44. J. Dosh and D.H. Reneker, Electrospinning process and application of electrospun fibers, *J. Electrostat*., 1995, 35, 151-160.
45. R. Jaeger, M. Bergshoef, C. Martin-Batille, H. Schoenherr, and G. J. Vamsco. Electrospinning of ultra-thin polymer fibers, *Macromol Symp*, 1998, **127**, 141-150.
46. T. Grafe and K. Graham, Polymeric Nanofibers and Nanofiber Webs: A New Class of nonwovens. *Joint INDA TAPPI Conference, Atlanta, Georgia*, 2002, 24-26, 2002.
47. www.nano 21c.com, Nano Techniques Co., Ltd. "Mass production of Electrospun Nanofibers for filtration
48. M. H. Zheng, Z. Z. Ying, M. Kotaki and S. Ramakrishna, A review on polymer nanofibers by electrospinning and their applications in nanocomposites, *Comp. Sci. and Tech.* 2003, **63**: 2223-2253.
49. G. I. Taylor, Electrically driven jets, *Proc. Roy. Soc. London.* A. 1969, **313**, 453-475.
50. D. H. Reneker and I. Chun, Nanometre diameters of polymer, produced by Electrospinning, *Nanotechnology*, 1996, **7**, 216-223.
51. Y. Zhang, C.T. Lim, S. Ramakrishna and Z. M. Huang, Recent development of polymer nanofibers for biomedical and biotechnological application, *J. Mater. Sci. – Mater. Med*., 2005, **16**, 933-946.
52. S. Ramakrishna, K. Fujihara, W. E. Teo, T. Yong, Z. Ma and R. Ramaseshan, Electrospun nanofibers: solving global issues, *Materials today*, 2006, **9**, 40-50.
53. Z. Ma, M. Kotaki, R. Inai and S. Ramakrishna, Potential of nanofiber matrix as tissue-engineering scaffolds, *Tissue Eng*., 2005, **11**, 101-109.
54. S. Ramakrishna, K. Fujihara, W. E. Teo, T. C. Lim and Z. Electrospinning process, An Introduction to Electrospinning and Nanofibers, *World Scientific*, 2005, 135-137.

55. M. Raoufi, T. Das, I. Schoen, V. Vogel, D. Brüggemann and J. P. Spatz, Nanopore Diameters Tune Strain in Extruded Fibronectin Fibers, *Nano Lett*., 2015, **15**, 6357–6364.

56. F. Li, Y. Zhao and Y. Song, Core-Shell Nanofibers: Nano Channel and Capsule by Coaxial Electrospinning, Nanofibers, Ashok Kumar (Ed.), ISBN: 978-953-7619-86-2, InTech, DOI: 10.5772/8166, 2010.

57. M. Bognitzki, W. Czado, T. Frese, A. Schaper, M. Hellwig, M. Steinhart, A. Greiner and J. H. Wendorff, Nanostructured Fibers via Electrospinning, *Adv. Mater*, 2001, **13,** 70-72.

58. W, Cui, X. Li, S. Zhou and J. Weng, Investigation on process parameters of electrospinning system through orthogonal experimental design, *J. Appl. Polym. Sci*., 2007, **103**, 3105-3112.

59. S. H. Tan, R. Inai, M. Kotaki and S. Ramakrishna, Systematic parameter study for ultra-fine fiber fabrication via electrospinning process, *Polymer*, 2005, **46,** 6128-6134.

60. V. Thavasi, G. Singh and S. Ramakrishna, Electrospun nanofibers in energy and environmental applications, *Energy & Environmental Science,* 2008, **1**, 205-221.

61. K. S. Athira, P. Sanpui and K. Chatterjee, Fabrication of Poly(Caprolactone) Nanofibers by Electrospinning, *J. Polymer and Biopolymer Physics Chem.* 2014, **2**, 62-66.

62. M. M. Khin, A. S. Nair, V. J. Babu, R. Murugan and S. Ramakrishna, A review on nanomaterials for environmental remediation, *Energy & Environmental Science*, 2012, **5**, 8075-8109.

63. J. I. Kroschwitz, Encyclopedia of polymer science and engineering, 2nd Edn. *John Wiley & Sons*, New York, 1986, **6**, 812-815.

64. T. Ondarcuhu and C. Joachim, Drawing a single nanofibre over hundreds of microns, *Europhys. Let.* 1998, **42**, 215-220.

65. P. X. Ma and R. Zhang, Synthetic nano-scale fibrous extracellular matrix, *J. Biomed. Mater. Res*. 1999, **46**, 60-72.

66. A. Ndreu, Electrospun nanofibrous scaffolds for tissue engineering, MSc Thesis, Middle East Technical University, (2007).

67. S. Sukigara, M. Gandhi, J. Ayutsede, M. Micklus and F. and Ko, Regeneration of Bombyx morisilk by electrospinning-part 1: processing parameters and geometric properties, *Polymer*, 2003, **44**, 5721-5727.

68. J. M. Deitzel, J. Kleinmeyer, D. Harris and N. C. B. Tan, The effect of processing variables on the morphology of electrospun nanofibers and textiles, *Polymer*, 2001, **42**, 261-272.

69. R. S. Barhate, C. K. Loong and S. Ramakrishna, Preparation and characterization of nanofibrous filtering media., *J. Membr. Sci*. 2006, **283**, 209-218.

70. A. L. Yarin, S. Koombhongse and D. H. Reneker, Bending instability in electrospinning of nanofibers, *J. Appl. Phys*. 2001, **89**, 3018-3026.

71. M. Y. Shin, M. M.Hohman, M. Brenner and G. C .Ruteldge, Experimental Characterization of electrospinning: the electrically forced jet and instabilities, *Polymer*, 2001, **42**, 9955- 9967.

72. K. H. Lee, H. Y. Kim, Y. M. La, D. R. Lee and N. H. Sung, Influence of a mixing solvent with tetrahydrofuran and N,N-dimethylformamide on electrospun poly(vinyl chloride) nonwoven mats, *J. Polym. Sci.: Part B: Polym. Phys.*, 2002, **40**, 2259-2268.

73. M. D. Rajib Anwar, Electrospun nanofiber based biosensor for ultrasensitive proteion detection, 2011 MSc Thesis, Wichita State University.

74. X. J. Huang and Y. K Choi, Chemical sensors based on nanostructured materials, *Sens. Actuat*. B, 2007, **122**, 659-671.

75. A. K Wanekaya, W. Chen, N. V. Myung and A. Mulchandani, Nanowire-Based Electrochemical Biosensors, *Electroanalysis* 2006, **18**, 533-550.

76. X. Luo, A. Morrin, A. J. Killard and M. R. Smyth, Applications of nanoparticles in electrochemical sensors and biosensors, *Electroanalysis* 2006, **18**, 319-326.

77. A. A. Ansari, .A. Kaushik, P. R. Solanki and B. D. Malhotra, Electrochemical Cholesterol Sensor Based on Tin Oxide-Chitosan Nanobiocomposite Film, *Electrochem. Commun.* 2008, **10**, 1246-1249.

78. G. K. Kouassi, and J. Irudayaraj, Examination of Cholesterol oxidase attachment to magnetic nanoparticles, *J. Nanobiotechnology*, 2005, **3**, 1-9.

79. D. F. Cao, P. L. He and N. F.Hu. Electrochemical biosensors utilising electron transfer in heme proteins immobilised on Fe_3O_4 nanoparticles, *Analyst* 2003, **128**, 1268-1274.

80. A. Kaushik, R. Khan, P. R. Solanki, P. Pandey, J. Alam, S. Ahmad and B. D. Malhotra, Zinc oxide nanoparticles-chitosan composite film for cholesterol biosensor, *Biosens. Bioelectron.* 2008, **24**, 676-683.

81. J. Yu, T. Zhao and B. Zeng, Mesoporous MnO_2 as enzyme immobilization host for amperometric glucose biosensor construction*Electrochem. Commun.* 2008, **10**, 1318-1321.

82. J. J. Xu, X. L. Lu, Y. Du and H. Y. Chen, Application of MnO2 nanoparticles as an eliminator of ascorbate interference to amperometric glucose biosensors, *Electrochem. Commun.* 2004, **6**, 1169-1173.

83. A. S. Santos, N. Duran and L. T. Kubota, Biosensor for H_2O_2 Response Based on Horseradish Peroxidase: Effect of Different Mediators Adsorbed on Silica Gel Modified with Niobium Oxide, *Electroanalysis* 2005, **17**, 1103-1111.

84. A. Salimi, E. Sharifi, A. Noorbakhsh and S. Soltanian, Immobilisation of glucose oxidase on electrodeposited nickel oxide nanoparticles: direct electro transfer and electrocatalytic activity, *Biosens. Bioelectron.* 2007, **22**, 3146-3153.

85. S. Shrestha, C. E. Mills, J. Lewington and S. C. Tsang, Modified Rare Earth Semiconductor Oxide As a New Nucleotide Probe, *J. Phys. Chem. B,* 2006, **110**, 25633-25637.

86. S. Shrestha, C. M. Y. Yeung, C. E. Mills, J. Lewington and S. C. Tsang, Chemically immobilized single-stranded oligonucleotides on praseodymium oxide nanoparticles as an unlabeled DNA sensor probe using impedance, *Angew. Chem. Intern. Ed.* 2007, **46**, 3855-3860.

87. E. Topoglidis, Y. Astuti, F. Duriaux, F.; Gratzel, M.; Durrant (JR), Direct electrochemistry and nitric oxide interraction of heme proteins absorbed on nanocrystalline tin dioxide electrode,. *Langmuir*, 2003, **19**, 6894-6900.

88. E. Topoglidis, A. E. G. Cass, B. Oregan and J. R. Durrant, Immobilization and bioelectrochemistry of proteins on nanoporous TiO2 and ZnO films, *J. Electroanal. Chem.* 2001, **517**, 20-27.

89. S. Liu, A. Chen, Coadsorption of horseradish peroxidase with thionine on TiO2 nanotubes for biosensing, *Langmuir* 2005, **21**, 8409-8413.

90. A. Liu, M. Wei, I. Honma and H. Zhou, Direct electrochemistry of myoglobin in titanate nanotubes film, *Adv. Funct. Mater.* 2006, **16**, 371-376.

91. S. A. Kumar, P. H. Lo and S. M. Chen, Electrochemical synthesis and characterization of TiO2 nanoparticles and their use as a platform for flavin adenine dinucleotide immobilization and efficient electrocatalysis, *Nanotechnology* 2008, **19**, 255501-255508.

92. J. Yu and H. Ju, Preparation of porous titania sol-gel matrix for immobilization of horseradish peroxidase by a vapor deposition method, *Anal. Chem.* 2002, **74**, 3579-3583.

93. E. Topoglidis, C. J. Campbell, A. E. G. Cass and Durrant, Factors that affect protein adsorption on nanostructured titania films. A novel spectroelectrochemical application to sensing, J. R. *Langmuir*, 2001, **17**, 7899-7906.

94. G Zhao, Y. Lei, Y. Zhang, H. Li and M. Liu, Growth and Favorable Bioelectrocatalysis of Multishaped Nanocrystal Au in Vertically Aligned TiO2 Nanotubes for HemoproteinLiu, *J. Phys. Chem. C* 2008, **112**, 14786-14795.

95. F. Wu, J. Xu, Y. Tian, Z. Hu, L. Wang, Y. Xian and L. Jin, Direct electrochemistry of horseradish peroxidase on TiO2 nanotube arrays via seeded-growth synthesis, *Biosens. Bioelectron.* 2008, **24**, 198-203.

96. X. Xu, J. Zhao, D. Jiang, J. Kong, B. Liu and J. Deng, TiO2 sol-gel derived amperometric biosensor for H2O2 on the electropolymerized phenazine methosulfate modified electrode, *J. Anal. Bioanal. Chem.* 2002, **374**, 1261-1266.

97. J. Liu, C. Roussel, G. Lagger, P. Tacchini, H. H. Girault, Antioxidant Sensors Based on DNA-Modified Electrodes, *Anal. Chem.* 2005, **77**, 7687-7694.

98. S. A. Kumar and S. M. Chen, Nanostructured Zinc Oxide Particles in Chemically Modified Electrodes for Biosensor Applications, *Anal. Lett.* 2008, **41**, 141-158.

99. J. X. Wang, X. W. Sun, A. Wei, Y. Lei, X. P. Cai, C. M. Li and Z. L. Dong, Zinc Oxide Nanocomb Biosensor for Glucose Detection, *Appl. Phys. Lett.* 2006, **88**, 233106-3.

100. A. Wei, X. W. Sun, J. X. Wang, Y. Lei, X. P. Cai, C. M. Li, Z. L. .Dong and W. Huang, Enzymatic glucose biosensor based on ZnO nanorod array grown by hydrothermal decomposition, *Appl. Phys. Lett.* 2006, **89**, 123902-3.

101. P. R. Solanki, A. Kaushik, A. A. Ansari, G. Sumana and B. D. Malhotra, Zinc oxide-chitosan nanobiocomposite for urea sensor, *Appl. Phys. Lett.* 2008, **93**, 163903-3.

102. S. P. Singh, S. K. Arya, P. Pandey, B. D. Malhotra, S. Saha, K. Sreenivas and V. Gupta, Cholesterol biosensor based on rf sputtered zinc oxide nanoporous thin film, *Appl. Phys. Lett.* 2007, **91**, 063901-3.

103. R. Khan, A. Kaushik, P. R. Solanki, A. A. Ansari, M. K. Pandey and B. D. Malhotra, Zinc oxide nanoparticles-chitosan composite film for cholesterol biosensor, *Anal. Chim. Acta* 2008, **616**, 207-213.

104. Z. Deng, Q. Rui, X. Yin, H. Liu and Y. In Vivo Detection of Superoxide Anion in Bean Sprout Based on ZnO Nanodisks with Facilitated Activity for Direct Electron Transfer of Superoxide Dismutase, *Anal. Chem.* 2008, **80**, 5839-5846.

105. Z. Deng, Y. Tian, X. Yin, Q. Rui, H. Liu, and Y. Luo, Physical vapor deposited zinc oxide nanoparticles for direct electron transfer of superoxide dismutase, *Electrochem. Commun.* 2008, **10**, 818-820.

106. Y. F. Li, Z. M. Liu, Y. L. Liu, Y. H. Yang, G. L. Shen, and R. Q. Yu, A mediator-free phenol biosensor based on immobilizing tyrosinase to ZnO nanoparticles, *Anal. Biochem.* 2006, **349**, 33-40.

107. Z. Liu, Y. Liu, H. Yang, Y. Yang, G. Shen and R. Yu, A Mediator-Free Tyrosinase Biosensor Based on ZnO Sol-Gel Matrix, *Electroanalysis*, 2005, **17**, 1065-1070.

108. X. Lu, H. Zhang, Y. Ni, Q. Zhang and J. Chen, Porous nanosheet-based ZnO microspheres for the construction of direct electrochemical biosensors, *J. Biosens. Bioelectron.* 2008, **24**, 93-98.

109. Y. Yang, Z. Wang, M. Yang, J. Li, F. Zheng, G. Shen and R. Yu, Electrical detection of deoxyribonucleic acid hybridization based on carbon-nanotubes/nano zirconium dioxide/chitosan-modified electrodes, *Anal. Chim. Acta* 2007, **584**, 268-274.

110. Z. Tong, R. Yuan, Y. Chai, S. Chen and Y. Xie, Direct electrochemistry of horseradish peroxidase immobilized on DNA/electrodeposited zirconium dioxide modified, gold disk electrode, *Biotechn. Lett.* 2007, **29**, 791-795.

111. S. Zong, Y. Cao, Y. Zhou and H. Ju, *L A Comprehensive Review of Glucose Biosensors Based on Nanostructured Metal-Oxides, angmuir* 2006, **22**, 8915-8919.

112. S. Zong, Y. Cao, Y. Zhou and H. Ju, Hydrogen peroxide biosensor based on hemoglobin modified zirconia nanoparticles-grafted collagen matrix, *Anal. Chim. Acta* 2007, **582**, 361-366.

113. S. Zong, Y. Cao, Y. Zhou and H. Ju, Reagentless biosensor for hydrogen peroxide based on immobilization of protein in zirconia nanoparticles enhanced grafted collagen matrix, *Biosens. Bioelectron.* 2007, **22**, 1776-1782.

114. Z. Tong, R. Yuan, Y. Chai, Y. Xie and S. Chen, A novel and simple biomolecules immobilization method: Electro-deposition ZrO2 doped with HRP for fabrication of hydrogen peroxide biosensor, *J. of Biotechnology* 2007, **128**, 567-575.

115. B. Liu, Y. Cao, D. Chen, J. Kong and J. Deng, Amperometric Biosensor Based on a Nanoporous ZrO2 matrix, *J. Anal. Chim. Acta* 2003, **478**, 59-66.

116. S. Liu, Z. Dai, H. Chen and H. Ju, Immobilization of hemoglobin on zirconium dioxide nanoparticles for preparation of a novel hydrogen peroxide biosensor, *Biosens. Bioelectron.* 2004, **19**, 963-969.

117. Y. Yang, H. Yang, M. Yang, Y. Liu, G. Shen and R. Yu, Amperometric glucose biosensor based on a surface treated nanoporous ZrO2/Chitosan composite film as immobilization matrix, *Anal. Chim. Acta*, 2004, **525**, 213-220.

118. C. Xia, W. Ning and G. Lin, Facile synthesis of novel MnO2 hierarchical nanostructures and their application to nitrite sensing, *Sens. Actuators* B, 2009, **137**, 710-714.

119. W. J. R. Santos, P. R. Lima, A. A. Tanaka, S. M. C. N. Tanaka and L. T. Kubota, Determination of nitrite in food samples by anodic voltammetry using a modified electrode, *Food Chemistry* 2009, **113**, 1206-1211.

120. Z. Wang, Q. Liang, Y.Wang and G. Luo, Carbon nanotube-intercalated graphite electrodes for simultaneous determination of dopamine and serotonin in the presence of ascorbic acid, *J. Electroanal. Chem*. 2003, **540**, 129-134.

121. F. H. Wu, G. C. Zhou and X. W. Wei, Electrocatalytic oxidation of nitric oxide at multi-walled carbon nanotubes modified electrode, *Electrochem. Commun*. 2002, **4,** 690-694.

122. T. J. Jacobsson, Absorption and fluorescence spectroscopy of growing ZnO quantum dots: size and band gap correlation and evidence of mobile trap states, *Inorganic chemistry*, 2011, **50**, 9578-9586.

123. Y. Zhao, Z. Qiu, J. Huang, Preparation and Analysis of Fe3O4 Magnetic Nanoparticles Used as Targeted-drug Carriers, Chin. *J. Chem. Eng*. 2008, **16**, 451-455.

124. A. J. Bard and C. G. Zoski, Voltammetry Retrospective, *Analytical Chemistry*, 2000, **72**, 346 A-352 A.

125. A. J. Bard and L. R. Faulkner, Electrochemical Methods: Fundamentals and applications (2nd edition). New York, USA: John Willey & Sons, 2000.

126. K. David and J. Gosser, Cyclic voltammetry, simulation and Analysis of Reaction Mechanisms, *VCH publishers*, 1994, 42-43.

127. P. M, S. Monk, Fundamentals of electroanalytical chemistry. Newyork, USA: John Willey & Sons, 2001, 158-159.

128. P. Cervini, E. T. G. Cavalheiro, Determination of hydroquinone in a square wave voltammetry procedure using a graphite-polyurethane composite electrode, *Quím., São Paulo*, 2006, **31**, 59-62.

129. S. Devarajan, B. Vimalan and S. Sampath, Phase transfer of Au-Ag alloy nanoparticles from aqueous medium to an organic solvent: effect of aging of surfactant on the formation of Ag-rich alloy compositions. Journal of Colloid and Interface Science, 2004, **278**, 126-132.

130. X. M. Kang, Z. Z. Zhibin Zou and J. Peixiang Mo, A novel glucose biosensor based on immobilization of glucose oxidase in chitosan on a glassy carbon electrode modified with gold-platinum alloy nanoparticles/multiwall carbon nanotubes. *Analytical Biochemistry*, 2007, **369**, 71-79.

131. C. Fernàndez-Sańchez, C. J. McNeil and K. Rawson, Electrochemical impedance spectroscopy studies of polymer degradation: application to biosensor development. *Trends in Analytical Chemistry*, 2005, **24**, 37-48.

132. C. Buzea, I. I. P. Blandino, and K. Robbie, Nanomaterials and nanoparticles: Sources and toxicity, Biointerphases, 2007, 2, MR17 - MR172.

133. A. Chrissanthopoulos, S. Baskoutas, N. Bouropoulos, V. Dracopoulos, P. Poulopoulos, and S. N. Yannopoulos, *Photon. Nanostruct. Fundam. Appl*. 2011, **9**, 132.

134. K. Zhang, C. Rossi, P. Alphonse, C. Tenailleau, S. Cayez, and J. Chane-Ching, Integrating Al with NiO nano honeycomb to realize an energetic material on silicon substrate, *Appl. Phys. A Mater. Sci. Process*. 2009, **94**, 957.

135. P. Jarupoom, S. Eitssayeam, K. Pengpat, T. Tunkasiri, D. P. Cann, and G. Rujijanagul Effects of NiO nanoparticles on the magnetic properties and diffuse phase transition of BZT/NiO composites, *Nanoscale Res. Lett*. 2012, **7**, 59.

136. M. K. Singh, A. Agarwal, R. K. Swarnkar, R. Gopal, and R. K. Kotnala, Magnetic Properties of Ni/NiO Core–Shell Nanoparticles Synthesized by Nanosecond Laser Irradiance of Water Suspended Ni Particles, *Sci. Adv. Mater*. 2012, **4**, 532.

137. M. Tadic, M. Panjan, D. Markovic, I. Milosevic, and V. Spasojevic, Unusual magnetic properties of NiO nanoparticles embedded in a silica matrix, *J. Alloy. Compd*. 2011, **509**, 7134.

138. A. Kebede Agegnehu, C. Pan, J. Rick, J. Lee, W. Su, and B. Hwang, Enhanced hydrogen generation by cocatalytic Ni and NiO nanoparticles loaded on graphene oxide sheets, *J. Mater. Chem*. 2012, **22**, 13849.

139. Y. Wang, J. Zhu, X. Yang, L. Lu, and X. Wang, Preparation of NiO nanoparticles and their catalytic activity in the thermal decomposition of ammonium perchlorate *Thermochim. Acta*, 2005, **437**, 106.

140. M. Awais, M. Rahman, J. M. Don MacElroy, N. Coburn, D. Dini, J. G. Vos, and D. P. Dowling, Dowling Deposition and characterization of NiOx coatings by magnetron sputtering for application in dye-sensitized solar cells, *Surf. Coat. Technol*. 2010, **204**, 2729.

141. B. Liu, H. Yang, H. Zhao, L. An, L. Zhang, R. Shi, L. Wang, L. Bao, and Y. Chen, Synthesis and enhanced gas-sensing properties of ultralong NiO nanowires assembled with NiO nanocrystals, *Sens. Actuators B Chem*. 2011, **156**, 251.

142. N. Cho, I. Hwang, H. Kim, J. Lee, and I. Kim, Gas sensing properties of p-type hollow NiO hemispheres prepared by polymeric colloidal templating method, *Sens. Actuators B Chem*. 2011, **155**, 366.

143. Z. Chen, A. Xiao, Y. Chen, C. Zuo, S. Zhou, and L. Li, Template-directed preparation of two-layer porous NiO film via hydrothermal synthesis for lithium ion batteries, *Mater. Res. Bull*. 2012, **47**, 1987.

144. S. Hwang, G. Kim, S. Yun, and K. Ryu, NiO nanoparticles with plate structure grown on graphene as fast charge–discharge anode material for lithium ion batteries, *Electrochim. Acta*, 2012, **78**, 406.

145. D. Segets, J. Gradl, R. K. Taylor, V. Vassilev and W. Peukert, Analysis of optical absorbance spectra for the determination of ZnO nanoparticle size distribution, solubility, and surface energy, *ACS Nano*, 2009, **3**, 1703–1710.

146. X. Lou, Development of ZnO series ceramic semiconductor gas sensors, *J. Sens. Trans. Technol.* 1991, **3**, 1–5.

147. E. Bacaksiz, M. Parlak, M. Tomakin, A. Özcelik, M. Karakiz and M. Altunbas, The effect of zinc nitrate, zinc acetate and zinc chloride precursors on investigation of structural and optical properties of ZnO thin films, *J. Alloy. Compd.* 2008, **466**, 447–450.

148. J. Wang, J. Cao, B. Fang, P. Lu, S. Deng and H. Wang, Synthesis and characterization of multipod, flower-like, and shuttle-like ZnO frameworks in ionic liquids. *Mater. Lett.* 2005, **59**, 1405–1408.

149. Z. L. Wang, Splendid one-dimensional nanostructures of zinc oxide: A new nanomaterial family for nanotechnology, *ACS Nano* 2008, **2**, 1987–1992.

150. M. Chaari and A. Matoussi, Electrical conduction and dielectric studies of ZnO pellets, *Phys. B Condens. Matter*, 2012, **407**, 3441–3447.

151. U. Ozgur, Y. I. Alivov, C. Liu, A. Teke, M. A. Reshchikov, S. Doğan, V. Avrutin, S. J. Cho and H. Morkoc, A comprehensive review of ZnO materials and devices, *J. Appl. Phys*, 2005, **98**, doi:10.1063/1.1992666.

152. S. Bhattacharyya and A. Gedanken, A template-free, sonochemical route to porous ZnO nano-disks, *Microporous Mesoporous Mater*, 2007, **110**, 553–559.

153. B. Ludi and M. Niederberger, Zinc oxide nanoparticles: Chemical mechanism and classical and non-classical crystallization, *Dalton Trans*. 2013, **42**, 12554–12568.

154. D. Banerjee, J. Y. Lao, D. Z. Wang, J. Y. Huang, Z. F. Ren, D. Steeves, B. Kimball and M. Sennett, Large-quantity free-standing ZnO nanowires, *Appl. Phys. Lett*. 2003, **83**, 2061–2063.

155. Y. B. Hahn, Zinc oxide nanostructures and their applications, Korean, *J. Chem. Eng*. 2011, **28**, 1797–1813.

156. T. Frade, J. Melo, M. E. Jorge and A. Gomes, One-dimensional ZnO nanostructured films: Effect of oxide nanoparticles, *Mater. Lett*. 2012, **82**, 13–15.

157. R. Wahab, S. G. Ansari, Y. S. Kim, H. K. Seo and H. S. Shin. Room temperature synthesis of needle-shaped ZnO nanorods via sonochemical method, *Appl. Surf. Sci*. 2007, **253**, 7622–7626.

158. X. Kong, Y. Ding, R. Yang and Z. L. Wang, Single-crystal nanorings formed by epitaxial self-coiling of polar-nanobelts, *Science*, 2004, **303**, 1348–1351.

159. Z. W. Pan, Z. R. Dai and Z. L. Wang, Nanobelts of semiconducting oxides, *Science*, 2001, **291**, 1947–1949.

160. J. J. Wu, S. C. Liu, C. T. Wu, K. H. Chen and L. C. Chenm, Heterostructures of ZnO–Zn coaxial nanocables and ZnO nanotubes, *Appl. Phys. Lett*. 2002, **81**, 1312–1314.

161. W. J. Chen, W. L. Liu, S. H. Hsieh and T. K. Tsai, Preparation of nanosized ZnO using α brass, *Appl. Surf. Sci*. 2007, **253**, 6749–6753.

162. J. Liu, X. Huang, J. Duan, H. Ai and P. Tu, A low-temperature synthesis of multiwhisker-based zinc oxide micron crystals, *Mater. Lett*. 2005, **59**, 3710–3714.

163. Y. Huang, J. He, Y. Zhang, Y. Dai, Y. Gu, S. Wang and C. Zhou, Morphology, structures and properties of ZnO nanobelts fabricated by Zn-powder evaporation without catalyst at lower temperature, *J. Mater. Sci*. 2006, **41**, 3057–3062.

164. B. Nikoobakht, X. Wang, A. Herzing and J. Shi, Scable synthesis and device integration of self-registered one-di imensional zinc oxide nanostructures and related materials, *Chem. Soc. Rev*. 2013, **42**, 342–365.

165. L. C. Tien, S. J. Pearton, D. P. Norton and F. Ren, Synthesis and microstructure of vertically aligned ZnO nanowires grown by high-pressure-assisted pulsed-laser deposition. *J. Mater. Sci.* 2008, **43**, 6925–6932.

166. J. Cui, Zinc oxide naniwires, *Mater. Charact*. 2012, **64**, 43–52.

167. T. Xu, P. Ji, M. He and J. Li, Growth and structure of pure ZnO micro/nanocombs, *J. Nanomater*. 2012, 2012, doi:10.1155/2012/797935.

168. W. S. Chiua, P. S. Khiew, M. Clokea, D. Isaa, T. K. Tana, S. Radimanb, R. Abd-Shukorb, M. A. Abd–Hamid, N. M. Huangc and H. N. Limd, Photocatalytic study of two-dimensional ZnO nanopellets in the decomposition of methylene blue. *Chem. Eng. J.* 2010, **158**, 345–352.

169. M. Jose-Yacaman, C. Gutierrez-Wing, M. Miki, D. Q. Yang, K. N. Piyakis and E. Sacher, Surface diffusion and coalescence of mobile metal nanoparticles, *J. Phys. Chem. B*, 2005, **109**, 9703–9711.

170. V. Polshettiwar, B. Baruwati and R. S. Varma, Self-asssembly of metal oxides into three-dimensional nanostructures: Synthesis and application in catalysis, *ACS Nano* 2009, **3**, 728–736.

171. Q. Xie, Z. Dai, J. Liang, L. Xu, W. Yu and Y. Qian, Synthesis of ZnO three-dimensional architectures and their optical properties, *Solid State Commun*. 2005, **136**, 304–307.

172. J. Liu, X. Huang, Y. Li, K. M. Sulieman, F. Sun, and X. He, Selective growth and properties of zinc oxide nanostructures, *Scr. Mater*. 2006, **55**, 795–798.

173. M. Bitenc and Z. C. Orel, Synthesis and characterization of crystalline hexagonal bipods of zinc oxide, *Mater. Res. Bull*. 2009, **44**, 381–387.

174. N. Vigneshwaran, S. Kumar, A. A. Kathe, P. V. Varadarajan and V. Prasad, Functional finishing of cotton fabrics using zinc oxide-soluble starch nanocomposites. *Nanotechnology*, 2006, **17**, 5087–5095.

175. P. Sundara Venkatesh and K. Jeganthan, Investigations on the growth and characterization of vertically aligned zinc oxide nanowires by radio frequency magnetron sputtering, *J. Solid State Chem*. 2013, **200**, 84–89.

176. W. Water, S. E. Chen, T. H. Meen and L. W. Ji, ZnO thin film with nanorod arrays applied to fluid sensor, *Ultrasonics*, 2012, **52**, 747–752.

177. K. J. Kuo, C. M. Lin, C. L. Kuo and M. H. Huang, Growth of ultralong ZnO nanowires on silicon substrates by vapor transport and their use as recyclable photocatalysts, *Chem. Mater*. 2007, **19**, 5143–5147.

178. S. Janitabar Darzi and A. R. Mahjoub, Investigation of phase transformations and photocatalytic properties of sol–gel prepared nanostructured ZnO/TiO_2 composites, *J. Alloy. Compd.* 2009, **486**, 805–808.

179. C. Hariharan, Photocatalytic degradation of organic contaminants in water by ZnO nanoparticles: Revisited, *Appl. Catal. A Gen*. 2006, **304**, 55–61.

180. Q. Xiao and L. L. Ouyang, Photocatalytic photodegradation of xanthate over Zn1−xMnxO under visible light irradiation, *J. Alloy. Compd*. 2009, **479**, L4–L7.

181. M. Bizarro, High photocatalytic activity of ZnO and ZnO: Al nanostructured films deposited by spray pyrolysis, *Appl. Catal. B Environ*. 2010, **97**, 198–203.

182. M. Y. Guo, M. K. Fung, F. Fang, X. Y. Chen, A. M. C. Ng, A. B. Djurisic and W. K. Chan, ZnO and TiO_2 1D nanostructures for photocatalytic applications, *J. Alloy. Compd*. 2011, **509**, 1328–1332.

183. Q. Li, C. Wang, M. Ju, W. Chen and E. Wang, Polyoxometalate-assisted electrochemical deposition of hollow ZnO nanospheres and their photocatalytic properties, *Microporous Mesoporous Mater*, 2011, **138**, 132–139.

184. S. S. Ma, R. Li, C. P. Lv, W. Xu and X. L. Gou, Faciale synthesis of ZnO nanorod arrays and hierarchical nanostructures for photocatalysis and gas sensor applications, *J. Hazard. Mater*. 2010, **192**, 730–740.

185. G. Kenanakis and N. Katsarakis, Light-induced photocatalytic degradation of stearic acid by c-axis oriented ZnO nanowires, *Appl. Catal. A Gen*. 2011, **378**, 227–233.

186. R. M. Cornell and U. Schwertmann, The iron oxides. Structire, properties, reactions occurence and use, *VCH Publ*., Weheim, German, 1996.

187. H. Miyata and T. Kashimoto, Studies on the compounds Delated to PCB (IV). Investigation on polychlorodibenzofuran formation, *J. Food Hyg. Soc*. 1978, **19**, 78-84.

188. T. M. Lim, T. 3d. Sargent and N. Kusubov, Kinetics of trace element chromium (III) in the human body, *Am. J. Physiol*. 1983, **244**, R445,

189. M. P. Sharrock and R. E. Bodnar, Magnetic materials for recording: an overview with special emphasis on particles, *J. Appl. Phys*. 1985, **57**, 3919 – 3924.

190. R. A. Jacksona and C. R. A. Catlowa, Computer Simulation Studies of Zeolite Structure, *Molecular Simulation,* 1988, **1**, 207-224.

191. U. Schwertman and R. M. Taylor, Iron oxides. In: Dixon, J.B., Weed S.B. (Eds.), Minerals in Soil Environments, second ed. *Soil Sci. Soc. Am. J., Medison*, Wisconsin, USA, 1989, 379–428.

192. Vissokov and Pirgov, Plasma-chemical synthesis of ultradispersed iron oxides with pigment qualification, *Journal of Materials Science*, 1996, **31**, 4007-4016.

193. Dr. C. Sestier, M. F. Da-Silva, D. Sabolovic, J. Roger and J. N. Pons, Surface modification of superparamagnetic nanoparticles (Ferrofluid) studied with particle electrophoresis: Application to the specific targeting of cells, *Electrophoresis*, 2005, **19**, 1220–1226.

194. K. H. Choo and S. K. Kang, Removal of residual organic matter from secondary effluent by iron oxides adsorption, *Desalination*, 2003, **154**, 139–146.

195. K. Raj and R. Moskowitz, Commercial applications of ferrofluids, *J. Magnetism and Magnetic Materials*, 1990, **85**, 1990, 233-245.

196. J. Pieters and L. Balemans Light interception by condensation droplets on plastics: theoretical advances Actas del X11 congreso internacional de plasticos en agricultura, Granada (España), 1992, **1992**, 132–138.

197. J. Sun, T. Loboda, S. S. Sung and C. C. Black Jr. Sucrose Synthase in Wild Tomato, Lycopersicon chmielewskii, and Tomato Fruit Sink Strength, *Plant Physiology*, 1992, **98**, 1163-1169.

198. F. Z. Ronald, P. G. Emmanuel, A. W. Bernard, P. O. Michael, N. G. Bishwanath M. Vivek, W. R. Michael and R. H. Donald, Matrix-Mediated Synthesis of Nanocrystalline γ-Fe_2O_3: A New Optically Transparent Magnetic Material, *Science*, 1992, **257**, 219-223.

199. M. Safarík, S. J. Safarikova S. J. Forsythe, The application of magnetic separation in applied microbiology, *J. of Applied Bacteriology*, 1995, **78**, 578 – 585.

200. U. O. Hafeli, Magnetically modulated therapeutic systems, *Int. J. Pharmaceutics*, 2004, **277**, 19–24.

201. W. Schütt, C. Grüttner, U. Häfeli, M. Zborowski, J. Teller, H. Putzar, and C. Schümichen. Applications of Magnetic Targeting in Diagnosis and Therapy—Possibilities and Limitations: A Mini-Review, *Hybridoma*. 1997, **16**, 109-117.

202. F. Gazeaua, J. C Bacria, 1. F Gendrona, R. Perzynskia, Y. L Raikherb, V. I. Stepanovb and, E. Duboisc, Magnetic resonance of ferrite nanoparticles:: evidence of surface effects, *J. Magnetism and Magnetic Mater*. 1998, **186**, 175–187.

203. A. Denizlia and R. Say, Preparation of magnetic dye affinity adsorbent and its use in the removal of aluminium ions, *J. Biomater. Sci., Polymer Ed.* 2001, 12, 1059-1073.

204. U. Schwertman, R.M. Cornell Iron Oxides in the Laboratory: Preparation and Characterization, *WILEY–VCH*, New York, 2000, 11.

205. F. Rahma and S. Fellahi, Performance evaluation of synthesized acrylic acid grafted polypropylene with CaCO3/polyprolypele composites, *Polym. Comp*. 2000, **21**, 175-186.

206. J. Jancar and J. Kucera, Yield behavior of PP/$CaCO_3$ and PP($Mg(OH)_2$ composites, II: Enhanced interfacial adhesion, *Polym. Eng. Sci*. 1990, **30**, 714-720.

207. S. Iijima, Helical microtubules of graphitic carbon, *Nature*, 1991, **354**, 56-58.

208. H. Wang, Z. Li, K. Ghosh, T. Maruyama, S. Inoue and Y. Ando Synthesis of double-walled carbon nanotube films and their field emission properties, *Carbon*, 2010, **48**, 2882-2889.

209. E. D. Canto, K. Flavin, M. Natali, T. Perova and S. Giordani, Functionalization of single-walled carbon nanotubes with optically switchable spiropyrans, *Carbon* 2010, **48**, 2815-2824.

210. P. M. Ajayan, Nanotubes from Carbon, *Chem. Rev*. 1999, **99**, 1787-1800.

211. S. Piscanec, M. Lazzeri, J. Robertson, A. C. Ferrari, F. Mauri, Optical phonons in carbon nanotubes: Kohn anomalies, Peierls distortions, and dynamic effects, *Phys. Rev*. 2007, **75**, 035427.

212. A. S. Adekunle and K. I. Ozoemena, Electron transport and electrocatalytic properties of MWCNT/nickel nanocomposites: Hydrazine and diethylaminoethanethiol as analytical probes, *J. Electroanaly. Chem*. 2010, **645**, 41–49.

213. F. A. Usmani and M. Hasan, Carbon nanotube field effect transistors for high performance analog applications: An optimum design approach, *Microelectron. J.* 2010, **41**, 395–402.

214. G. Eduardo, S. Giovanni, P. Flavio, H. Niina, L. Juho, M. Jani, T. Ge za, K. Krisztian, J. Heli, T. Mauricio, H. Panu, S. Heikki, M. A. Pulickel and V. Robert, Electrical Transport and Field-Effect Transistors Using Inkjet-Printed SWCNT Films Having Different Functional Side Groups, *ACS Nano*, 2010, **4**, 3318–3324.

215. C. Wang, J. Zhang, K. Ryu, B. Alexander, G. Lewis and C. Zhou, Wafer-Scale Fabrication of Separated Carbon Nanotube Thin-Film Transistors for Display Applications, *Nano Lett*. 2009, **9**, 4285-4291.

216. A. Southard, V. Sangwan, J. Cheng, E. D. Williams and M. S. Fuhrer, Solution-processed single walled carbon nanotube electrodes for organic thin-film transistors, *Organic Electronics*, 2009, **10**, 1556–1561.

217. T. M. Barnes, J. D. Bergeson, R. C. Tenent, B. A. Larsen, G. Teeter, K. M. Jones, J. L. Blackburn and J. Lagemaat, Carbon nanotube network electrodes enabling efficient organic solar cells without a hole transport layer, *Appl. Phy. Lett.* 2010, **96**, 243309.

218. H. Wu, D. Wexler, A. Ranjbartoreh, H. Liu and G. Wang, Chemical processing of double-walled carbon nanotubes for enhanced hydrogen storage, *Int. J. Hydrogen Energy*, 2010, **35**, 6345 -6349.

219. L. Wang, W. Chen, D. Xu, B. S. Shim, Y. Zhu, F. Sun, L. Liu, C. Peng, Z. Jin, C. Xu and N. A. Kotov, Chemical processing of double-walled carbon nanotubes for enhanced hydrogen storage, *Nano Lett*. 2009, **9**, 4147-4152.

220. S. Mao, G. Lu, K., Yu and J. Chen, Specific biosensing using carbon nanotubes functionalized with gold nanoparticle–antibody conjugates, *Carbon*, 2010, **48**, 479-486.

221. S. Subramanian, K. I. Matsumoto, J. B. Mitchell, Radio frequency continuous-wave and time-domain EPR imaging and Overhauser-enhanced magnetic resonance imaging of small animals: instrumental developments and comparison of relative merits for functional imaging, *NMR in Biomedicine*, 2004, **17**,263–94.;

222. B. Geng, X. Zhou, J. Zhu, Y. S. Hung and S. T.Wong, Comparison of reversible-jump Markov-chain-Monte-Carlo learning approach with other methods for missing enzyme identification, *J Biomed Inform*, 1998, **41**, 272-281.

223. D. Zhao, J. Feng, Q. Huo, N. Melosh, G. H. Fredrickson, B. F. Chmelka and G. D. Stucky, Triblock Copolymer Syntheses of Mesoporous Silica with Periodic 50 to 300, *Angstrom Pores Science*, 1998, **279**, 548-552

224. Y. Dong, Y. Ma, T. Zhai, Y. Zeng, H. Fu, and J. Yao, A novel approach to the construction of core-shell gold-polyaniline nanoparticles, *Nanotechnology*, 2007, 18, 412001-419001.

225. A. R. B. M. Yusoff and S. A. Shuib, Metal-base transistor based on simple polyaniline electropolymerization, *Electrochimica Acta*, 2011, **58**, 417–421.

226. L. Geng, Y. Zhao, X. Huang, S. Wang, S. Zhang, and S. Wu, Characterization and gas sensitivity study of polyaniline/SnO_2 hybrid material prepared by hydrothermal route, *Sensors and Actuators B*, 2007, **120**, 568–572.

227. S. Yu, M. Xi, X. Jin, K. Han, Z. Wang, and H. Zhu, Preparation and photoelectrocatalytic properties of polyaniline-intercalated layered manganese oxide film, *Catalysis Communications*, 2010, **11**, 1125–1128.

228. C. C. Buron, B. Lakard, A. F. Monnin, V. Moutarlier, and S. Lakard, Elaboration and characterization of polyaniline films electrodeposited on tin oxides, *Synthetic Metals*, 2011, **161**, 2162–2169.

229. M. Deepa, S. Ahmad, K. N. Sood, J. Alam, S. Ahmad, and A. K. Srivastava, Electrochromic properties of polyaniline thin film nanostructures derived from solutions of ionic liquid/polyethylene glycol, *Electrochimica Acta*, 2007, **52**, 7453–7463.

230. C. L. Zhu, S. W. Chou, S. F. He, W.-N. Liao, and C. C. Chen, Synthesis of core/shell metal oxide/polyaniline nanocomposites and hollow polyaniline capsules, *Nanotechnology*, 2007, **18**,

231. D. Patil, P. Patil, Y. K. Seo, and Y. K. Hwang, Poly(o-anisidine)-tin oxide nanocomposite: synthesis, characterization and application to humidity sensing, *Sensors and Actuators B,* 2010, **148**, 41–48.

232. M. H. Tsai, C. J. Chang, P. J. Chen, and C. J. Ko, Preparation and characteristics of poly(amide-imide)/titania nanocomposite thin films, *Thin Solid Films*, 2008, **516**, 5654–5658.

233. X. Zhang and S. Wei, N. Haldolaarachchige, Magnetoresistive conductive polyaniline-barium titanate nanocomposites with negative permittivity, *J. Physic.Chem. C,* 2012, **16**, 15731–15740.

234. L. Song, Y. Hu, Q. He and F. You, Study on crystallization, thermal and flame retardant properties of nylon 66/organoclay composites by *in situ* polymerization, *J. Fire Sci.* 2008, ***26,*** 475–492.

235. D. J. Lin, C. L. ChangC. K. Lee and L. P. Cheng, Fine structure and crystallinity of porous nylon 66 membranes prepared by phase inversion in the water/formic acid/Nylon 66 system, *Eur. Polym. J.* 2006, **42**,356‑367.

236. A. Suzuki, Y. Chen and T. Kunugi, Application of a continuous zone-drawing method to nylon 66 fibres, *Polymer*, 1998, ***39,*** 5335–5341.

237. R. Nirmala, R. Navamathavan, H. S. Kang, M. H. El-Newehy and H. Y. Kim, Preparation of polyamide-6/chitosan composite nanofibres by a single solvent system

via electrospinning for biomedical applications, *Colloids Surf. B Biointerfaces,* 2011, **83**, 173–178.

238. A. Baji, Y. W. Mai, S. C. Wong, M. Abtahi and X. Du, Mechanical behavior of self-assembled carbon nanotube reinforced nylon 6,6 fibers, *Compos. Sci. Technol.* 2010, ***70,*** 1401–1409.
239. Z. M. Huang, Y. Z. Zhang, M. Kotaki and S. Ramakrishna, A review on polymer nanofibres by electrospinning and their applications in composites, *Compos. Sci. Technol.* 2003, ***63,*** 2223–2253.
240. C. Rong, G. Ma, S. Zhang, L. Song, Z. Chen, G. Wang and P. M. Ajayan, Effect of carbon nanotubes on the mechanical properties and crystallization behavior of poly(ether ether ketone), *Compos. Sci. Technol.* 2010, ***70,*** 380–386.
241. G. Mago, C. Velasco-Santos, A. L. Martinez-Hernandez, D. M. Kalyon and F. T. Tisher, Effect of functionalization on the crystallization behavior of MWNT-PBT composites, *Mater. Res. Soc. Symp. Proc.* 2008, ***1056,*** 295–300.

242. F. Zhang, X. Peng, W. Yan, Z. Peng and Y. Shen, Nonisothermal crystallization kinetics of *in situ* nylon 6/graphene composites by differential scanning calorimetry, *J. Polym. Sci. Part B Polym. Phys.* 2011, ***49,*** 1381–1388.
243. Y. S. Yun, Y. H. Bae, D. H. Kim, J. Y. Lee, I. J. Chin and H. J. Jin, Reinforcing effects of adding alkylated graphene oxide to polypropylene, *Carbon,* 2011, ***49***, 3553–3559
244. K. M. Sawicka and P. Gouma, Electrospun composite nanofibers for functional applications, *J. Nanopart. Res*, 2006, **8**, 769–781.
245. R. Sahay, P. S. Kumar, R. Sridhar, J. Sundaramurthy, J. Venugopal, S. Mhaisalkar and S Ramakrishna, Electrospun composite nanofibers and their multifaceted applications, *J. Mater. Chem*, 2012, **22**, 12953–12971.
246. L. Nikkola, K. Vapalahti, R. Huolman, J. Seppälä, A. Harlin and N. Ashammakhi, Multilayer implant with triple drug releasing properties, *J. Biomed. Nanotechnol*, 2008, **4**, 331–338.
247. N. Wang, H. Chen, L. Lin, Y. Zhao, X. Cao, Y. Song and L. Jiang, Multicomponent phase change microfibers prepared by temperature control multifluidic electrospinning, *Macromol. Rapid Commun*, 2010, **31**, 1622–1627.

248. J. Ayutsede, M. Gandhi, S. Sukigara, H. Ye, C. M. Hsu, Y. Gogotsi and F. Ko, Carbon nanotube reinforced bombyx mori silk nanofibers by the electrospinning process, B*iomacromolecules*, 2005, **7**, 208–214.

249. Y. H. Deng, H. Wang and H. S. Zhang, Determination of amino acid neurotransmitters in human cerebrospinal fluid and saliva by capillary electrophoresis with laser-induced fluorescence detection, *J. Sep. Sci.* 2008, **31**, 3088–3097.

250. B. W. Boyd, S. R. Witowski and R. T. Kennedy, Trace-level amino acid analysis by capillary liquid chromatography and application to in vivo microdialysis sampling with 10-s temporal resolution, *Anal. Chem*. 2000, **72**, 865–871.

251. N. E. A. Grova, Detection of polycyclic aromatic hydrocarbon level in milk collected near potential contamination sources, *J. Agricultural and Food chemistry*, 2002. **50**, 4640-4642.

252. S. Lundstedt, P. Haglud and L. Orberg, Degradation and formation of polycyclic aromatic compounds during bioslurry treatment of an aged gasworks soil, *J. Environmental Toxicological Chemistry*, 2003. **22**, 1413-1420.

253. (ATSDR). A.D.R., Public Health Statement, Polycyclic Aromatic Hydrocarbons. Atlanta, GA: U.S. Department of Health and Human Services, 1990.

254. R. A. Faust, Oak Ridge National Laboratory, Chemical Hazard Evaluation Group. Toxicity summary for Phenanthrene, Oak Ridge, 1993.

255. K. I. White, An overview of immunotoxicology and carcinogenic polycyclic aromatic hydrocarbons, *Environ. Carnog.Rev.C4*, 1986, 163-202.

256. R. C. Sims and O. M. R, Fate of polynuclear aromatic compounds (PNAs) in soilplant systems, *Residue Rev*. 1983, **88**, 1-68.

257. C. E. Cerniglia, Microbial metabolism of polycyclic aromatic hydrocarbons, *Adva. Appl. Microbiol*. 1984. **30**, 31-71.

258. L. H. Lim, R. M. H. R.M.H., Harrad, S., The contribution of traffic to atmospheric concentrations of polycyclic aromatic hydrocarbons, *Environ. Sci. Technol*., 1999, **33**, 3538-3542.

259. Centers for Disease Control and Prevention, Fourth National Report on Human Exposure to Environmental Chemicals – http://www.cdc.gov/exposurereport/pdf/FourthReport.pdf - Accessed 12/14/09

260. U. S. E. P. A. Consumer Factsheet on Lindane - http://www.epa.gov/safewater/dwh/c-soc/lindane.html - Accessed 12/14/09 ATSDR ToxFAQs – Chlordane 261. H.

Brandenberger and R. A. A. Maes, Analytical toxicology: for clinical, forensic, and pharmaceutical chemists, *Berlin: Walter de Gruyter*, 1997, 243.

262. S. J. Friedman, Lindane neurotoxic reaction in nonbullous congenital ichthyosiform erythroderma, *Arch Dermatol*, 1987, **123**, 1056-1058.
263. S. E. Aks, A. Krantz, D. O. Hryhorczuk, Acute accidental lindane ingestion in toddlers, *Ann Emerg Med*, 1995, **25**, 647-51.
264. M. Tenenbein, Seizures after lindane therapy, *J Am Geriatr Soc*, 1991,**39**, 394-395.
265. B. A. Solomon, S. R. Haut, E. M. Carr and A. R. Shalita, Neurotoxic reaction to lindane in an HIVseropositive patient: An old medication's new problem, *J Fam Pract.* 1995, **40**, 291-296.
266. T. F. Fischer, Lindane toxicity in a 24-year-old woman, *Ann Emerg Med* 1994, **24**, 972-974.
267. L. M. Solomon, L. Fahrner, and D. P. West, Gamma benzene hexachloride toxicity, *Arch Dermatol*, 1977, **113**, 353-357.
268. C. M. Ginsburg, W. Lowry, and J. S. Reisch, Absorption of lindane (gamma benzene hexachloride) in infants and children, *J Pediatr*, 1997, **91**, 998-1000.
269. E. Smith and G. Dent, Modern Raman spectroscopy: a practical approach, *Wiley. com*, 2005.
270. R. L. McCreery, Raman spectroscopy for chemical analysis, Wiley. com, 225, 2005
271. G. J. Fiechtner and J. R. Gord. Absorption and the dimensionless overlap integral for two-photon excitation, *J. Quantitative Spectroscopy and Radiative Transfer*, 2001, **68**, 543-557.
272. P. Griffiths and J. A. De Haseth, Fourier transform infrared spectrometry, *John Wiley & Sons*, 2007, 171.
273. H. Vogel, P. Rosén, B. Wagner, M. Melles and P Persson, Fourier transform infrared spectroscopy, a new cost-effective tool for quantitative analysis of biogeochemical properties in long sediment records, *J. Paleolimnology*, 2008, **40**, 689-702.
274. P. M. S. Monk, Fundamentals of electroanalytical chemistry. Newyork, USA: *John Willey & Sons*, 2001, 158-159.
275. E. A. Skoog, Principles of Instrumental analysis.6th ed, *Thomson Brooks/ Cole*, 2007: 169-173.
276. C. J. Buchko, L. C. Chen, Y. Shen and D. C. Martin, Conducting-polymer nanotubes for controlled drug release, *Polymer*, 40 (1999) 7397-7407.
277. G. I. Taylor, Electrically driven jets, *Proc. Roy. Soc. London*, 1969, **313**, 453-475.

278. J. Doshi, M. H. Mainz and G. S. Bhat, Proceedings of the tenth TANDEC Nonwoven Conference, *Knoxville*, *TN*, 2000.

279. J. M. Deitzel, W. Kosik, S. H. Mcknight, N. C. B. Tan, J. M. Desimone and S. Crette, Electrospinning of polymer nanofibers with specific surface chemistry, *Polymer*, 2002, **43**, 1025-1029.

280. M. Bognitzki, H. Hou, M. Ishaque, T. Frese, M. Hellwig, C. Schwarte, A. Shaper, J. H. Wendorff and A. Greiner, *Adv. Matter*, 2000, **12**, 637-640.

281. N. Alem, R. Erni, C. Kisielowski, M. D. Rossell, W. Gannett and A. Zettl, Atomically thin hexagonal boron nitride probed by ultrahigh-resolution transmission electron microscopy, *Physical review B*, 2009, **80**, 155425.

282. R. Jenkins and R. Snyder, Introduction to X-ray powder diffractometry, *John Wiley & Sons*, 2012, 2012.

283. B. B. He, Two-dimensional X-ray Diffraction, *John Wiley & sons NewYork*, 2011.

284. J. Als-Nielsen and D. McMorrow, Elements of modern X-ray physics, *John Wiley & Sons*, 2011.

285. J. B. Hudson, Surface Science: An Introduction, *John Wiley&Sons, New York*, 1998.

286. X. Jiang, T. Wang, Study on adsorption and reaction mechanism of preparation of TiO_2/SiO_2 by adsorption phase reactor technique, *Appl. Surf. Sci.* 2006, 252, 8029-8035.

287. D. Maryam, J. Tahoora, E. Mojdeh, B. Majedeh, S. Roya , K. Azadeh, N. Kobra, R.S. Mandana, B. Ali, M. Sepideh, *Int. J. Electrochem. Sci*. 2013,**8**, 8252 – 8263.

288. R. Essehli, B. El Bali, A. Faik, M. Naji, S. Benmokhtar, Y. R. Zhong and L. W. Su, Iron titanium phosphates as high-specific-capacity electrode materials for lithium ion batteries, *J. Alloys and Compds.* 2014, **585**, 434-441.

289. Y. Zhao, Z. Qiu, J. Huang, Preparation and Analysis of Fe_3O_4 Magnetic Nanoparticles Used as Targeted-drug Carriers, *Chin. J. Chem. Eng*. 2008, **16**, 451-455.

290. N. G. R. Mathebe and A. Morrin, E. I. Iwuoha, Electrochemical Properties of Nanotubes and Nanomicelles from Novel Polyaniline and Derivative, *Talanta*. 2004, **64**, 115-127.

291. N. P. Blanchard, R. A. Hatton, S. R. P. Silva, Tuning the work function of surface oxidized multi-wall carbon nanotubes via cation exchange, *Chem Phys Lett*.2007, **434**, 92–95

292. D. Giovanelli, N. S. Lawrence , S. J. Wilkins, L. Jiang, T. G. J. Jones and R. G. Compton, Anodic stripping voltammetry of sulphide at a nickel film: towards the development of a reagentless sensor, *Talanta*, 2003, 61,211-220.

293. J. Zagal, M. Paez, A. A. Tanaka, J. R. dos Santos Jr., and C. A Linkous C.A, Electrocatalytic activity of metal phthalocyanines for oxygen reduction, *J. Electroanal. Chem*, 1992, **339**, 13-30.

294. R. F. Aglan, G. G. Mohamed and H. A. Mohamed, Chemically modified carbon paste electrode for determination of cesium ion by potentiometric method, *Am. J. Anal. Chem.* 2012, **3**, 576-586.

295. S. E. Hyman and R. C. Malenka, Addiction and the brain: the neurobiology of compulsion and its persistence, *Nat. Rev Neurosci*. 2001, **2**, 695-703.

296. S. Nikolaus, C. Antke and H. W. Müller, Invivo imaging of synapstic function in the central nervous system: II, mental and affective disorder, *Behav. Brain. Res*. 2009, **204**, 32-66.

297. A. M. Sardar, C. Czudek and G. P. Reynolds, Dopamine deficits in the brain: the neurochemical basis of parkinsonian symptoms in AIDS, *Neuro Report*,1996, **7**, 910-912.

298. K. W. Perry and R. W. Fuller, Systemic administration of fluoxetine does not increase levels of dopamine in the striatum. *Life Sciences*. 1992, **50**, 1683-1690.

299. L. H. Parsons and J. B. Justice Jr, Perfusate serotonin increases extracellular dopamine in the nucleus accumbens as measured by in vivo microdialysis, *Brain Res*. 1993, **606**, 195-199.

300. A. Barakat, M. Al-Noaimi, M. Suleiman, A. S. Aldwyyan, B. Hammouti, T. B. Hadda S. F. Haddad, A. Boshaala and I. Warad, One step synthesis of NiO nanoparticles via solid-state thermal decomposition at low-temperature of novel *Aqua* (2,9-dimethyl-1,10-phenanthroline)$NiCl_2$ complex, *Int. J. Mol Sci*. 2013, **14**, 23941-23954.

301. N. Dharmaraj, P. Prabu, S. Nagarajan, C. H. Kimb, J. H. Park and H. Y. Kimb, Synthesis of nickel oxide nanoparticles using nickel acetate and poly(vinyl acetate) precursor, *Mater. Sci. Eng. B*. 2006, **128**, 111-114.

302. S. Talam, S. R. Karumuri and N. Gunnam, Synthesis, characterization, and spectroscopic properties of ZnO nanoparticles**,** ISRN *Nanotechnology*, 2012, Article ID 372505. doi:10.5402/2012/372505.

303. A. Ayodeji, O. Ilyas and A. M. Olabisi, Synthesis and characterization of ZnO nanoparticles with zinc chloride as zinc source, *Asian J. Natural Appl. Sci*. 2013, 2, 41- 43.

304. T. Koutzarova, S. Kolev, C. Ghelev, D. Paneva and I. Nedkov, Microstructural study and size control of iron oxide nanoparticles produced by microemulsion technique, *Phys. Stat. Sol.(c)*. 2006, **3**, 1302-1307.

305. X. J. Bard and L. R. Faulkner, Electrochemical Methods: Fundamentals and applications, 2nd ed. Wiley, New York 2000.

306. S. Ahmad, U. Riaz, A. Kaushik and J. Alam, Soft template synthesis of super paramagnetic Fe_3O_4 nanoparticles a novel technique, *J. Inorg. Organomet. Polym*. 2009, doi 10.1007/s10904-009-9276-6.

307. L. Bokobza and J. Zhang, Raman spectroscopic characterization of multiwall carbon nanotubes and of composites, *Express Polymer Letters*. 2012, **6**, 601-608.

308. L. Bokobza, J. L. Bruneel and M. Couzi, Raman spectroscopic investigation of carbon-based materials and their composites. Comparison between carbon nanotubes and carbon black, *Chem. Phys. Lett*. 2013, **590**, 153-159.

309. S. I. Cordoba-Torresi, G. A. Hugot-Le and S. Joiret, Electrochromic behavior of nickel oxide electrodes: II. Identification of the bleached state by Raman spectroscopy and nuclear reactions. *J. Electrochem. Soc*. 1991, **138**, 1554-1559.

310. L. Slavov, M. V. Abrashev, T. Merodiiska, C. Gelev, R. E. Vandenberghe, I. Markova-Deneva and I. Nedkov, Raman spectroscopy investigation of magnetite nanoparticles in ferrofluids, *J. Magn. Magn. Mater*. 2010, **322**, 1904-1911.

311. A. M. Hofmeister, E. Keppel and A. K. Speck, Absorption and reflection infrared spectra of MgO and other diatomic compounds, *Mon. Not. R. Astron. Soc.* 2003, **345**, 16-38.

312. S. Shahrokhian and S. Bozorgzadeh, Electrochemical oxidation of dopamine in the presence of sulfhydryl compounds: Application to the square-wave voltammetric detection of penicillamine and cysteine, *Electrochim. Acta* 2006, **51**, 4271-4276.

313. Y. Sahraoui, S. Chaliaa, A. Maaref, A. Haddad and N. Jaffrezic-Renault, An electrochemical nitrite sensor based on a multilayer film of polyoxometalate, *J. Sens. Technol.* 2013, **3**, 84-93.

314. S. Radhakrishnan, K. Krishnamoorthy, C. Sekar, J. Wilson and S. Kim, A highly sensitive electrochemical sensor for nitrite detection based on Fe_2O_3 nanoparticles decorated reduced graphene oxide nanosheets, *Appl. Catal., B* 2014, **148**, 22-28.

315. A. Y. Cui, C. Yang. W. Zeng. M. Oyama, W. Pu and J. Zhang, Electrochemical determination of nitrite using a gold nanoparticles-modified glassy carbon electrode prepared by the seed-mediated growth technique, *Anal. Sci*. 2007, **23**, 1421-1425.

316. A. S. Adekunle, S. Lebogang, P. L. Gwala, T. P. Tsele, L. O. Olasunkanmi, L. O.; O. E. Fayemi, D. Boikanyo, N. Mphuthi, J. A. O. Oyekunle, A. O. Ogunfowokan and E. E. Ebenso, Electrochemical response of nitrite and nitric oxide on graphene oxide nanoparticles doped with Prussian blue (PB) and Fe_2O_3 nanoparticles, *RSC Adv*. 2015, **5**, 27759-27774.

317. W. Lai and M. Sossina, Haile impedance spectroscopy as a tool for chemical and electrochemical analysis of mixed conductors: A case study of Ceria, *J. Am. Ceram. Soc.* 2005, **88**, 2979-2997.

318. O. Tovide, N. Jaheed, N. Mohamed, E. Nxusani, C. E. Sunday, A. Tsegaye, R. A. Ajayi, N. Njomo, H. Makelane, M. Bilibana, P. O. Baker, A. Williams, S. Vilakazi, R. Tshikhudo and E. I. Iwuoha, Graphenated polyaniline-doped tungsten oxide nanocomposite sensor for real time determination of phenanthrene, *Electrochim. Acta*, 2014, **128**, 138-148.

319. K. Min and Y. J. Yoo, Amperometric detection of dopamine based on tyrosinase-SWNTs-Ppy composite electrode, *Talanta*, 2009, **80**, 1007-1011.

320. G. A. Angeles, B. P. Lopez, M. P. Pardave, M. T. R. Silva, S. Alegret and A. Merkoci, A. Enhanced host–guest electrochemical recognition of dopamine using cyclodextrin in the presence of carbon nanotubes, *Carbon*, 2008, **46**, 898-906.

321. T. Peik-See, A. Pandikumar, H. Nay-Ming, L. Hong-Ngee and Y. Sulaiman, Simultaneous electrochemical detection of dopamine and ascorbic acid using an iron oxide/reduced graphene oxide modified glassy carbon electrode, *Sensors*, 2014, **14**, 15227-15243.

322. A. J. Bard and L. R. Faulkner, Electrochemical methods. 2nd ed, *John Wiley & Sons*, New York 2001.

323. J. N. Soderberg, A. C. Co, A. H. C. Sirk and V. I. Birss, Impact of porous electrode properties on the electrochemical transfer coefficient, *J. Phys. Chem. B* 2006, **110**, 10401-10.

324. M. Hasanzadeh, B. Khalilzadeh, N. Shadjou, G. Karim-Nezhad, L. Lotfali, I. Kazeman and M. H. Abnosi, A new kinetic-mechanistic approach to elucidate formaldehyde electrooxidation on copper electrode, *Electroanalysis*, 2010, **22**, 168-176.

325. Z. Xu, N. Gao, H. Chen and S. Dong, S. Biopolymer and carbon nanotubes interface prepared by self-assembly for studying the electrochemistry of microperoxidase-11, *Langmuir*, 2005, **21**, 10808-10813.

326. K. Min and Y. J. Yoo, Amperometric detection of dopamine based on tyrosinase-SWNTs-Ppy composite electrode, *Talanta*, 2009, **80**, 1007–1011.

327. G. A. Angeles, B. P. Lopez, M. P. Pardave, M. T. R. Silva, S. Alegret and A. Merkoci Enhanced host–guest electrochemical recognition of dopamine using cyclodextrin in the presence of carbon nanotubes, *Carbon*, 2008, **46**, 898-906.

328. T. Peik-See, A. Pandikumar, H. Nay-Ming, L. Hong-Ngee and Y. Sulaiman, simultaneous electrochemical detection of dopamine and ascorbic acid using an Iron Oxide/Reduced Graphene Oxide Modified Glassy Carbon Electrode, *Sensors*, 2014, **14**, 15227-15243.

329**.** M. T. Lin, H. J. Tsay, W. H. Su and F. Y. Chueh, Changes in extracellular serotonin in rat hypothalamus affect thermoregulatory function, *Am. J. Physiol*. 1998, **274**, 1260-1267.

330**.** L. Imeri, M. Mancia, S. Bianchi, and M.R. Opp, 5-Hydroxytryptophan, but not L-tryptophan, alters sleep and brain temperature in rats, *Neuroscience*, 2000, **95**, 445-452.

331**.** G. K. Isbister, S. J. Bowe, A. Dawson, and I. M. Whyte, Relative toxicity of selective serotonin reuptake inhibitors (SSRIs) in overdose, *Clinical Toxicology*, 2004, **42,** 277-285.

332. J. Li, and X. Lin, Simultaneous determination of dopamine and serotonin on gold nanocluster/overoxidized-polypyrrole composite modified glassy carbon electrode, *Sens. and Actuators B: Chemical*, 2007, **124**, 481-486.

333. Q. Jin, L. Shan, Spectrophotometric determination of total serotonin derivatives in the safflower seeds with Ehrlich's reagent and the underlying color reaction mechanism, J. Yue, and X. Wang, *Food Chem*., 2008, **108**, 779-783.

334. M. Mumtaz, N. Narasimhachari, R. O. Friedel, G. N. Pandey, and J. M Davis, Evaluation of fluorometric assay methods for serotonin in platelets. Plasma and whole blood samples by comparison with GC-MS-SIM Technique, *Res. Commun. Chem. Pathol. Pharmacol*. 1982, **36,** 45-60.

335. J. H. Thompson, Ch. A. Spezia, and M. Angulo, Fluorometric Detection of Serotonin Using O-Phthaldiadehyde: An Improvement, *Experientia*, 1970, **26**, 327-329.

336. T. Kato, A. Tokiyoshi, Y. Kashiwada, K. Miyachi, K. Moriyama, S. Morimoto, M. Asano, T. Yamaguchi, and Y. Fujita, Simple and Highly Sensitive Fluorometric Determination of Serotonin Using Propylene Glycol, *Bunseki Kagaku*, 2011, **60**, 685-686.

337. J. Chauveau, V. Fert, A. M. Morel, and M. A. Delagee, Rapid and specific enzyme immunoassay of serotonin, *Clin. Chem*. 1991, **37**, 1178-1184.

338. I. Hammel, Y. Naot, E. Ben-David, and H. Ginsburg, A simplified microassay for serotonin: modification of the enzymatic isotopic assay, *Anal. Biochem*. 1978, **90,** 840-843.

339. F. Engbaek, and B. Voldby, Radio immunoassay of serotonin (5-hydroxytryptamine) in cerebrospinal fluid, plasma, and serum, *Clin. Chem*. 1982, **28,** 624-628.

340. Z. D. Peterson, M. L. Lee, and S. W. Graves, Determination of serotonin and its precursors in human plasma by capillary electrophoresis-electrospray ionization-time-of-flight mass spectrometry, *J. Chromatogr. B. Analyt. Technol. Biomed. Life Sci*. 2004, **810**, 101-110.

341. J. J. Berzas Nevado, M. J. Villaseñor Llerena, Determination of fluoxetine, fluvoxamine, and clomipramine in pharmaceutical formulations by capillary gas chromatography, *J. Sep. Sci*. 2006, **29**, 103-113.

342. K. Tekes, HPLC Determination of Serotonin and Its Metabolites From Human Platelet-Rich Plasma; Shift to 5-Hydroxytryptophol Formation Following Alcohol Consumption, *J. Chromatogr. Sci*. 2008, **46**, 169-173.

343. S. Umeda, G. W. Stagliano, M. R. Borenstein, and R. B. Raffa, A reverse-phase HPLC and fluorescence detection method for measurement of 5-hydroxytryptamine (serotonin) in Planaria, *J. Pharmacol. Toxicological Methods*, 2005, **51**, 161-173.

344**.** N. G. Rajendra, K. G. Vinod, O. Munetaka, and B. Neeta, Gold nanoparticles modified indium tin oxide electrode for the simultaneous determination of dopamine and serotonin: Application in pharmaceutical formulations and biological fluids, *Talanta*, 2007, **72**, 557-976

345. Wu. Kangbing, F. Junjie, and Hu. Shengshui, Simultaneous determination of dopamine and serotonin on a glassy carbon electrode coated with a film of carbon nanotubes, *Anal. Biochem*. 2003, **318**, 100-106.

346. W. Zong-hua, L. Qiong-lin, W. Yi-ming, and Luo. Guo-an, Carbon nanotube-intercalated graphite electrodes for simultaneous determination of dopamine and serotonin in the presence of ascorbic acid, *J. Electroanal. Chem*. 2003, **540**, 129-134.

347. K. B. Wu, J. J. Fei, and S. S. Hu, Simultaneous determination of dopamine and serotonin on a glassy carbon electrode coated with a film of carbon nanotubes, *Anal. Biochem*. 2003, **318**, 100-106.

348. T. Selvaraju, and R. Ramaraj, Simultaneous determination of ascorbic acid, dopamine and serotonin at poly (phenosafranine) modified electrode, *Electrochem. Commun*. 2003, **5,** 667-672.

349. O. Joshua, and N. Tebello, Simultaneous voltammetric determination of dopamine and serotonin on carbon paste electrodes modified with iron(II) phthalocyanine complexes, *Anal. Chim. Acta*, 2001, **434**, 9-21.

350. Z. Jyh-Myng, C. I-Lang, and S. Ying, Fabrication and Characterization of Nanomaterials Modified Electrodes for the Electrochemical Sensor and Biosensor Applications, *Anal. Chim. Acta*, 1998, **369**, 103.

351**.** Y. Hans, Li. Shaoguang, T. Yuhai, C. Yan, C. Yuanzhong, and L. Xinhua, Clinical observation on electrothermic needle combined with acupoint sticking for the treatment in 80 cases of simple obesity, *Electrochim. Acta*, 2009, **54**, 4607-4936.

352**.** W. K. Lee, S. Chen, A. Chilkoti, and S. Zauscher, Fabrication of Gold Nanowires by Electric-Field-Induced Scanning Probe Lithography and In Situ Chemical Development, *Small*, 2007, **2**, 249-266.

353. H. Taekjip, A. Y. Ting, L. Liang, W. B. Caldwell, A. A. Deniz, D. S. Chemla, P. G. Schultz, and S. Weiss, Single-molecule fluorescence spectroscopy of enzyme conformational dynamics and cleavage mechanism, *Natl. Acad. Sci. U.S.A*, 1999, **96**, 893-898.

354. L. M. Bronstein, C. Linton, R. Karlinsey, B. Stein, D. I. Svergun, J. W. Zwanziger, and R. J. Spontak, Synthesis of Metal-Loaded Poly(aminohexyl) (aminopropyl)silses quioxane Colloids and Their Self-Organization into Dendrites, *Nano Lett*., 2002, **2**, 873-876.

355. S. K. Kim and S. Jeon, Simultaneous Determination of Serotonin and Dopamine at the PEDOP/MWCNTs–Pd Nanoparticle Modified Glassy Carbon Electrode, *J. Nanoscience and Nanotechnology*, 2012, **12**, 1903-1909.

356. Y. Q. Dai and K. K. Shiu, Glucose Biosensor Based on Multi-Walled Carbon Nanotube Modified Glassy Carbon Electrode, *Electroanalysis*, 2004, **16**, 1697–1703.

357. E**.** Laviron, Adsorption autoinhibition and autocatalysis in polarography and linear potential sweep voltammetry. *J. Electroanal. Chem*., 1974, **52**, 355-393.

358. M. J. Song, S. S. Kim, N. K. Min, and J. H. Jin, Electrochemical serotonin monitoring of poly(ethylenedioxythiophene):poly(sodium-4-styrenesulfonate)-modified fluorine-doped tin oxide by predeposition of self-assembled 4-pyridylporphyrin, *Biosens, Bioelectron.*, 2014, **52**, 411-416.

359. L. Ying, M. Ajinal Ali, S. M. Chen, S. Y. Yang, B. S. Lou, M. Fahad, and A. Al-Hemaid, Poly(basic red 9) doped functionalized multi-walled carbon nanotubes as composite films for neurotransmitters biosensors, *Colloids and Surfaces B: Biointerfaces*, 2014, **118,** 124-133.

360. K. Miyazaki, G. Matsumoto, M. Yamada, S. Yasui and H. Kaneko Simultaneous voltammetric measurement of nitrite ion, dopamine, serotonin with ascorbic acid on the GRC electrode, *Electrochim. Acta*, 1999, **44,** 3809–3820.

361. A. Babaei, and M. Babazadeh, A Selective Simultaneous Determination of Levodopa and Serotonin Using a Glassy Carbon Electrode Modified with Multiwalled Carbon Nanotube/Chitosan Composite, *Electroanalysis*, 2011, **23**, 1726-1735.

362. S. de Irazu, N. Unceta, M. Carmen Sampedro, M. Aranzazu Goicolea, and R. J. Barrio, Multimembrane carbon fiber microelectrodes for amperometric determination of serotonin in human urine, *Analyst*, 2001, **126**, 495-500.

363. A. El-Beqqali, A. Kussak, and M. Abdel-Rehim, Determination of dopamine and serotonin in human urine samples utilizing microextraction online with liquid chromatography/electrospray tandem mass spectrometry, *J. of Sep. Sci.*, 2007, **30**, 421-424.

364. F. Valentini, D. Romanazzo, M. Carbone and G. Palleschi, Modified Screen-Printed Electrodes Based on Oxidized Graphene Nanoribbons for the Selective Electrochemical Detection of Several Molecules, *Electroanalyis*, 2012, **24**, 872-881.

365. A. Babaei, A. R. Taheri and M. Aminikhah, Nanomolar simultaneous determination of levodopa and serotonin at a novel carbon ionic liquid electrode modified with $Co(OH)_2$ nanoparticles and multi-walled carbon nanotubes, *Electrochim. Acta*, 2013, **90**, 317-325.

366. L. L. Cho, Identification of textile fiber by Raman microspectroscopy. *J. Forensic Sci.* 2007, **6**, 55–62.

367. Z. M. Huang, Y. Z. Zhang, M. Kotaki and S. Ramakrishna, A review on polymer nanofibres by electrospinning and their applications in composites, *Compos. Sci. Technol*. 2003, **63**, 2223–2253.

368. F. Navarro-Pardo, G. Martínez-Barrera, A. L. Martínez-Hernández, V. M. Castaño, J. L. Rivera-Armenta, F. Medellín-Rodríguez and C. Velasco-Santos, Nylon 6,6 electrospun fibres reinforced by amino functionalised 1D and 2D carbon, *IOP Conf. Ser. Mater. Sci. Eng.* 2012, **40**, 012023:1–012023:6.

369. A. M. Hofmeister, E. Keppel, A. K. Speck, Absorption and reflection infrared spectra of MgO and other diatomic compounds, *Mon. Not. R. Astron. Soc*, 2003, **345**, 16–38.

370. H. R. Pant, M. P. Bajgai, C. Yi, R. Nirmala, K. T. Nam, W. Baek, Effect of successive electrospinning and the strength of hydrogen bond on the morphology of electrospun nylon-6 nanofibres. *Colloids Surf. A Physicochem. Eng. Asp*, 2010, **370**, 87–94.

371. A. Lasia, B. E. Conway, J. Bockris, and R.E. White, Edts, Electrochemical Impedance Spectroscopy and Its Applications, Modern Aspects of Electrochemistry, *Kluwer Academic/Plenum Publishers*, New York, 1999, **32**, 143-248.

372. W. Lai and M. Sossina, Haile impedance spectroscopy as a tool for chemical and electrochemical analysis of mixed conductors: A case study of Ceria. *J. Am. Ceram. Soc.* 2005, **88**, 2979-2997.

373. C. B. Jacobs, M. J. Peairs and B. J. Venton, Review: Carbon nanotube based electrochemical sensors for biomolecules, *Analytica Chimica Acta*, 2010, **662**, 105–127.

374. R. Ramachandran, S. M. Chen, G. P. G. kumar, P. Gajendran and N. B. Devi, An Overview of Fabricating Nanostructured Electrode Materials for Biosensor Applications, *Int. J. Electrochem. Sci*., 2015, **10**, 8607 – 8629.

375. A. A. Hathoot, U. S. Yousef, A. S. Shatla, M. Abdel-Azzem, Voltammetric simultaneous determination of glucose, ascorbic acid and dopamine on glassy carbon electrode modified by NiNPs@poly 1,5-diaminonaphthalene, *Electrochim. Acta*, 2012, **85**, 531–537.

376. K. Ghanbari and N. Hajheidari, Simultaneous electrochemical determination of dopamine, uric acid and ascorbic acid using silver nanoparticles deposited on polypyrrole nanofibers, *J. Polymer Research*, 2015, **22**,152.

377. F. Wang, Y. Y. Wu, K. Lu and B. X. Ye, Ni-coated Si microchannel plate electrodes in three-dimensional lithium-ion battery anodes, *Electrochem. Acta*, 2013, **87**, 251-256.

378. M. J. Song, S. S. Kim, N. K. Min and J. H. Jin, Electrochemical serotonin monitoring of poly (ethylenedioxythiophene), poly(sodium 4-styrenesulfonate)-modified fluorine-

doped tin oxide by predeposition of self-assembled 4-pyridylporphyrin, *Biosens. Bioelectron*, 2014, **52**, 367-411.

379. N. G. R. Mathebe, A. Morrin, and E. I. Iwuoha, E. I. Electrochemical Properties of Nanotubes and Nanomicelles from Novel Polyaniline and Derivative, *Talanta*. 2004, **64**, 115-127.

380. D. A. Li, A. Babel, A. Sanson, Y. Jenekhe and N. Xia, Nanofibers of conjugated polymers prepared by electrospinning with a two-capillary spinneret, *Adv. Mater*. 2004, **16**, 2062–2066

381. S. X. Xing, C. Zhao, S. Y. Jing and Z. C. Wang, Morphology and conductivity of polyaniline nanofibers prepared by 'seeding' polymerization, *Polymer*. 2006, **47**, 2305–2313.

382. G. Vaidyanathan, S. Sendhilnathan, and R. Arulmurgan, Structural and magnetic properties of $Co_{1-x}Zn_xFe_2O_4$ nanoparticles by co-precipitation method, *J. Magnetism and Magnetic Materials*, 2007, **313**, 293–299.

383. C. Caizer and M. Stefanescu, Magnetic characterization of nanocrystalline Ni-Zn ferrite powder prepared by the glyoxylate precursor method, *J. Physics D*, 2002, **35**, 3035–3040.

384. C. Dong, PowderX: windows-95-based program for powder X-ray diffraction data processing, J. *Applied Crystallography*, 1999, **32**, 838, 1999.

385. A. S. Adekunle, B. O. Agboola, J. Pillay and K. I. Ozoemena, Electrocatalytic detection of dopamine at single-walled carbon nanotubes–iron (III) oxide nanoparticles platform, *Sensors and Actuators B*, 2010, **148**, 93–102.

386. A. S. Adekunle and K. I. Ozoemena, Electron transport and electrocatalytic properties of MWCNT/nickel nanocomposites: Hydrazine and diethylaminoethanethiol as analytical probes, *J. Electroanaly. Chem*. 2010, **645**, 41–49.

387. X. H. Xia, X. H.J. P Tu, J. Zhang, X. L. Wang, W. K. Zhang and H. Huang, A highly porous NiO/polyaniline composite film prepared by combining chemical bath deposition and electro-polymerization and its electrochromic performance. *Nanotechnology,* 2008, **19**, 465701

388. Z. Jinli, W. Jiao, L. Yuanyuan, N. Ning, G. Junjie, Y. Feng and L. Wei, Potential of metal-free graphene alloy as electrocatalysts for oxygen reduction reaction, *J. Mater. Chem. A*. 2015, **3**, 2043-2049.

389. Y. Tang, K. Pan, X. Wang, C. Liu and Shenglian Luo, Enhancing electrochemical and electrocatalytic activities of polyaniline via co-doping with poly(styrene sulfonate) and gold, *J. Electroanal. Chem.* 2010, **639**, 123–129.

390. K. Min and Y. J. Yoo, Amperometric detection of dopamine based on tyrosinase-SWNTs-Ppy composite electrode. *Talanta*, 2009, **80**, 1007-1011.

391. G. A. Angeles, B. P. Lopez, M. P. Pardave, M. T, R. Silva, S. Alegret and A. Merkoci, Enhanced host–guest electrochemical recognition of dopamine using cyclodextrin in the presence of carbon nanotubes, *Carbon*, 2008, **46**, 898-906.

392. M. Bagherzadeh, S. A. Mozaffari and M. Momeni, Fabrication and electrochemical characterization of dopamine-sensing electrode based on modified graphene nanosheets, *Anal. Methods*, 2015, **7**, 9317-9323.

393. H. N. Yu, Y. C. Pang, J. Y. Tang, Polyaniline Nanofiber Modified Platinum Electrode Used to Determination of Dopamine by Square Wave Voltammetry Technique, *Int. J. Electrochem. Sci.* 2015, **10**, 8353 – 8360.

394. S. Zhou, M. Xie, X. Yuan, F. Zeng, W. Zou and D. Yuan Polyaniline/AgCl Hybrid Materials for Selective Determination of Dopamine by Electrochemical Methods, *Amer. J. Anal. Chem*. 2012, **3**, 385-391

395. T. Rengarajan, P. Rajendran, N. Nandakumar, B. Lokeshkumar and P. Rajendran, I. Nishigaki, Exposure to polycyclic aromatic hydrocarbons with special focus on cancer, *Asian Pacific J. Tropical Biomed.* 2015, **5**, 182–189.

396. V. Vestreng, H. Klein, Emission data reported to UNECE/EMEP: Quality Assurance and Trend Analysis & Presentation of WebDab, *MSc-W status report*, Norwegian Meteorological Institute, Oslo Norway, 2002.

397. S. Xu, W. Liu and S. Tao, Emission of Polycyclic Aromatic Hydrocarbons in China, *Environmental Science & Technology*, 2006, **40**, 702–708.

398. H. X. Yang, Q. F. Yang and X. H. Dong, Preparation and characterization of LiNiO 2 synthesized from $Ni(OH)_2$ and $LiOH•H_2O$, *J. Power Sources*, 1999, **79**, 256–261.

399. I. Hotovy, J. Huran, L. Spiess, R. Capkovic and S. Hascık, Preparation and characterization of NiO thin films for gas sensor application, Vacuum. 2000, **58**, 300–307.

400. E. L. Miller and R. E. Rocheleau, Electrochemical Behavior of Reactively Sputtered Iron-Doped Nickel Oxide. *J. Electrochem. Soc*. 1997, **144**, 3072–3077.

401. G. Wang, X. Lu, T. Zhai, Y. Ling, H. Wang, Y. Tong and Y. Li, Free-standing nickel oxide nanoflake arrays: synthesis and application for highly sensitive non-enzymatic glucose sensors, *Nanoscale*, 2012, **4**, 3123–3127.

402. Y. Ichiyanagi, N. Wakabayashi, J. Yamazaki, S. Yamada, Y. Kimishima, E. Komatsu and H. Tajima, Magnetic properties of NiO nanoparticles, *Physica B*, 2003, **329**, 862–863.

403. S. A. Makhlouf, F. T. Parker, F. E. Spada and A. E. Berkowitz, Magnetic anomalies in NiO nanoparticles, *J. Applied Physics*, 1997, **81**, 5561–5563.

404. S. Chakrabarty and K. Chatterjee, Synthesis and Characterization of Nano Dimensional Nickelous Oxide (NiO) Semiconductor, *J. Physical Science*, 2009, **13**, 245–250.

405. N. G. R. Mathebe, A. Morrin, and E. I. Iwuoha, Electrochemical Properties of Nanotubes and Nanomicelles from Novel Polyaniline and Derivative, *Talanta*, 2004, **64**, 115-127.

406. A. Morrin, O. Ngamna, A. J. Killard, S. E. Moulton, M. R. Smyth and G. G. Wallace, An amperometric enzyme biosensor fabricated from polyaniline nanoparticles, *Electroanalysis*, 2005, **17**, 423-430.

407. V. Somerset, J. Leaner, R. Mason, E. I. Iwuoha and A. Morrin, A. Development and application of a poly (2, 2′-dithiodianiline)(PDTDA)-coated screen-printed carbon electrode in inorganic mercury determination, *Electrochim. Acta*, 2010, **55**, 4240-4246.

408. M. Hasanzadeh, B. Khalilzadeh, N. Shadjou, G. Karim-Nezhad, L. Lotfali, I. Kazeman and M. H. Abnosi, A New Kinetic-Mechanistic Approach to Elucidate Formaldehyde Electrooxidation on Copper Electrode, *Electroanalysis*, 2010, **22**, 168-178.

409. A. J. Bard and L. R. Faulkner, Electrochemical Methods: Fundamentals and Applications, *Wiley*, New York, 2nd Ed. 2001.

410. B. A. Boukamp, A Nonlinear Least Squares Fit procedure for analysis of immittance data of electrochemical systems, *Solid State Ionics*, 1986, **20**, 31-44.

411. G. Nurk, H. Kasuk, K. Lust, A. Janes and E. Lust, Adsorption kinetics of dodecyl sulfate anions on the bismuth plane, *J. Electroanal. Chem.* 2003, **553**, 1-19.

412. Y. Wei, F. Fang, W.Yang, H. Guo, X. Niu and L. Sun, Preparation of a Nitrite Electrochemical Sensor Based on Polyaniline/ Graphene‐Ferrocenecarboxylic Acid

Composite Film Modified Glass Carbon Electrode and its Analytical Application, *J. Braz. Chem. Soc*. 2015, **26,** 2003-2013.

413. Z. Jinli, W. Jiao, L. Yuanyuan, N. Ning, G. Junjie, Y. Feng and L. Wei, Potential of metal-free ‘’graphene alloy” as electrocatalysts for oxygen reduction reaction, *J. Mater. Chem. A*. 2015, **3**, 2043-2049.

414. C. Rassie, R. A. Olowu, T. T. Waryo, L. Wilson, A. Williams, P. G. Baker and E. I. Iwuoha, Dendritic 7T-Polythiophene Electro-Catalytic Sensor System for the Determination of Polycyclic Aromatic Hydrocarbons, *Int. J. Electrochem. Sci*. **2011**, 6, 1949 – 1967.

415. T. M. Phillips, A. G. Seech, H. Lee and J. Trevors, Biodegradation of hexachlorocyclohexane (HCH) by microorganisms, *Biodegradation*, 2005, **16**, 363-392.

416. N. Manickam, R. Misra and S. Mayilraj, A novel pathway for the biodegradation of γ-hexachlorocyclohexane by a Xanthomonas sp. strain ICH12, *J. Appl. Microbiol*. 2007, **102**, 1468-1478.

417. B. R. Garrido, T. A. L. Chau, G. Feijoo, F. Macias and M. C. Monterrroso, Reductive Dechlorination of α-, β-, γ-, and δ-Hexachlorocyclohexane Isomers with Hydroxocobalamin, in Soil Slurry Systems, *Environ. Sci. Technol*. 2010, **44**, 7063-7069.

418. C. L. Willett, E. M. Ulrich and R. A. Hites, Differential Toxicity and Environmental Fates of Hexachlorocyclohexane Isomers, *Environ. Sci. Technol*. 1998, **32**, 2197-2207.

419. S. L. Simonich and R. A. Hites, Global distribution of persistent organochlo- rine compounds, *Science*, 1995, **269**, 1851-1854.

420. K. Walker, D. A. Vallero and R. G. Lewis, Ecological modelling and engineering of lakes and wetlands, *Environ. Sci. Technol*. 1999, **33**, 4373-4378.

421. R. V. Galiulin, V. N. Bashkin and R. A. Galiulina, Water, Air, The peculiarities of current pollution of river by the residues of DDT and HCH, *Soil Pollut*. 2002, **137**, 179-191.

422. H. M. Rajashekara Murthy and H. K. Manonmani, Aerobic degradation of technical hexachlorocyclohexane by a defined microbial consortium, *J. Hazard. Mater*. 2007, **149**, 18-25.

423. K. Senoo and H. Wada, Isolation and identification of an aerobic y- HCH-decomposing bacterium from soil, *Soil Sci. Plant Nutr*. 1989, **35**, 79−87.

424. C. M. Tu, Utilization and degradation of lindane by soil microorganisms, *Arch. Microbiol*. 1976, **108**, 259−263.

425. E. Lichtenstein, S. D. Beck and K. R. Schulz, Pesticide Analysis, Colorimetric Determination of Lindane in Soils and Crops, *J. Agric. Food Chem*. 1956, **4**, 936−936.

426. D. W. Kennedy and S. D. Aust, Bumpus, Comparative biodegradation of alkyl halide insecticides by the white rot fungus, Phanerochaete chrysosporium (BKM-F-1767), *J. A. Appl. Environ. Microbiol*. 1990, **56**, 2347−2353.

427. R. Imai, Y. Nagata, K. Senoo, H. Wada, M. Fukuda, M. Takagi and K. Yano, Dehydrochlorination of gamma-hexachlorocyclohexane (gamma-BHC) by gamma-BHC assimilating Pseudomonas paucimobilis, *Agric. Biol. Chem*. 1989, **53**, 2015−2017.

428. S. K. Sahu, K. K. Patnaik, M. Sharmila and N. Sethunathan, Degradation of α−, β−, γ- heaxachlorohexane by soil bacterium under aerobic condition, *Appl. Environ. Microbiol.* 1990, **56**, 3620−3622.

429. K. Ammasai, V. Susai and C. Maruthai, Development of an electroanalytical sensor for g-hexachlorocyclohexane based on a cellulose acetate modified glassy carbon electrode, *Anal. Methods*, 2013, **5**, 931

430. S. Wu, J. Liu, X. Bai and W. Tan, Stability Improvement of Prussian Blue by a Protective Cellulose Acetate Membrane for Hydrogen Peroxide Sensing in Neutral Media, *Electroanalysis*, 2010, **22**, 1906-1910.

431. M. M. Barsan, E. M. Pinto, M. Florescu, C. M. A. Brett, Development and characterization of a new conducting carbon composite electrode, *Anal. Chim. Acta* 2009, **635**, 71-78.

432. A. A. Isse, L. Falciola, P. R. Mussini, A. Gennaro, Relevance of electron transfer mechanism in electrocatalysis: the reduction of organic halides at silver electrodes, *Chem. Commun*. 2006, 344-346.

433. A. A. Isse, S. Gottardello, C. Durante and A. Gennaro, Dissociative electron transfer to organic chlorides: electrocatalysis at metal cathodes, *Phys. Chem. Chem. Phys.* 2008, **10**, 2409-2416.

434. P. R. Birkin, A. Evans, C. Milhano, M. I. Montenegro and D. Pletcher, The mediated reduction of lindane in DMF, *Electroanalysis*, 2004, **16**, 583-587.

435. J. M. Saveant, Electron transfer, bond breaking and bond formation, *Adv. Phys. Org. Chem*. 2000, **35**, 117-192.

436. M. U. Anu Prathap and R. Srivastava, Electrochemical reduction of Lindane (γ-HCH) at NiCo2O4 modified electrode, *Electrochim. Acta*, 2013, **108**, 145-152.

437. A. Kumaravel, S. Vincent and M. Chandrasekaran, Development of an electroanalytical sensor for γ-hexachlorocyclohexane based on a cellulose acetate modified glassy carbon electrode, *Anal. Methods*, 2013, **5**, 931-938.

438. M. Fayyad, M. Alawi and I. Issa, Differential pulse polarographic determination of organochlorine pesticides, *Anal. Lett*. 1989, **22**, 1939.

439. C. L. Huang, C. K. Tsai, F. Tan and C. W. Hsieh, Glassy Carbon Electrode Modified by Multi-walled Carbon Nanotubes for Detection Platform of Organochlorine Pesticides, *Adv. Biosensors and Bioelectronics (ABB)*, 2014, **3**, 2014.

APPENDIX

List of local and international conference presentations directly related to this thesis.

1. 2014 SACI conference Young Chemists symposium

   North-West University, Potchefstroom Campus, Tuesday 11th November 2014,

   "Electrochemical Properties of Multi-Walled Carbon Nanotube Doped with Nickel, Zinc and Iron Oxide Nanoparticles towards Dopamine Oxidation."

   Omolola E. Fayemi, Abolanle S. Adekunle Eno. E. Ebenso

   (**ORAL PRESENTATION BY O. E FAYEMI**)

2. MAM-14 7th International Symposium on Macro- and Supramolecular Architectures and Materials, November 23 - 27, 2014, Johannesburg - South Africa

   "Electrochemical Properties of Multi-Walled Carbon Nanotube Doped with Nickel, Zinc and Iron Oxide Nanoparticles towards Dopamine Oxidation."

   Omolola E. Fayemi, Abolanle S. Adekunle Eno. E. Ebenso

   (**ORAL PRESENTATION BY O. E FAYEMI**)

3. 16th Topical Meeting of the International Society of Electrochemistry in Angra dos Reis, Brazil. 24^{th} – 26^{th} of March 2015.

"A Sensor for Determination of Serotonin in Human Urine using a Multi-Walled Carbon Nanotube/Ni, Zn and Fe Oxides Composites Modified Glassy Carbon Electrode."

Omolola E. Fayemi, Abolanle S. Adekunle Eno. E. Ebenso

(**ORAL PRESENTATION BY O. E FAYEMI**)

4. 3^{rd} International Symposium on Electrochemistry, ElectrochemSA, SACI.

Bellville, Cape- Town, South Africa. 26^{th} – 28^{th} of May 2015.

"Electrochemical Detection of Phenanthrene Using Nickel Oxide Doped PANI - Nanofiber based Modified Electrodes."

Omolola E. Fayemi, Abolanle S. Adekunle Eno. E. Ebenso

(**ORAL PRESENTATION BY O. E FAYEMI**)

List of manuscripts based on this work:

1. Metal Oxide Nanoparticles/Multi-walled Carbon Nanotube Nanocomposite Modified Electrode for the Detection of Dopamine: Comparative Electrochemical Study

   Omolola E. Fayemi Abolanle S. Adekunle Eno. E. Ebenso

   J Biosens Bioelectron 2015, 6:4

   http://dx.doi.org/10.4172/2155-6210.10001902.

2. A Sensor for Determination of Serotonin in Human Urine using a Multi-Walled Carbon Nanotube/Ni, Zn and Fe Oxides Composites Modified Glassy Carbon Electrode.

   Omolola E. Fayemi, Abolanle S. Adekunle, Eno E. Ebenso

   Journal of Molecular Liquids (Under review)

3. Electrochemical Detection of Phenanthrene Using Nickel Oxide Doped PANI - Nanofiber based Modified Electrodes

   Omolola E. Fayemi, Abolanle S. Adekunle, Eno. E. Ebenso

   Journal of Nanomaterials, Volume 2016, Article ID 9614897, 12 pages

   http://dx.doi.org/10.1155/2016/96148974.

4. A Sensor For Determination of Lindane Using Pani/, Zn, Fe (Iii) Oxides and Nylon 6,6/Mwcnt/Zn, Fe(Iii) Oxides Nanofibers Modified Glassy Carbon Electrode

   Omolola E. Fayemi, Abolanle S. Adekunle, Eno. E. Ebenso.

   Journal of Nanomaterials Volume 2016, Article ID 4049730, 10 pages http://dx.doi.org/10.1155/2016/4049730